Subfilter Scale Modelling for Large Eddy Simulation of Lean Hydrogen-Enriched Turbulent Premixed Combustion

by

Francisco Emanuel Hernández Pérez

A thesis submitted in conformity with the requirements
for the degree of Doctor of Philosophy
Graduate Department of Aerospace Science and Engineering
University of Toronto

Abstract

Subfilter Scale Modelling for Large Eddy Simulation of Lean Hydrogen-Enriched Turbulent Premixed Combustion

Francisco Emanuel Hernández Pérez

Doctor of Philosophy

Graduate Department of Aerospace Science and Engineering

University of Toronto

2011

Hydrogen (H_2) enrichment of hydrocarbon fuels in lean premixed systems is desirable since it can lead to a progressive reduction in greenhouse-gas emissions, while paving the way towards pure hydrogen combustion. In recent decades, large-eddy simulation (LES) has emerged as a promising tool to computationally describe and represent turbulent combustion processes. However, a considerable complication of LES for turbulent premixed combustion is that chemical reactions occur in a thin reacting layer at small scales which cannot be entirely resolved on computational grids and need to be modelled.

In this thesis, subfilter-scale (SFS) modelling for LES of lean H_2-enriched methane-air turbulent premixed combustion was investigated. Two- and three-dimensional fully-compressible LES solvers for a thermally perfect reactive mixture of gases were developed and systematically validated. Two modelling strategies for the chemistry-turbulence interaction were pursued: the artificially thickened flame model with a power-law SFS wrinkling approach and the presumed conditional moment (PCM) coupled with the flame prolongation of intrinsic low-dimensional manifold (FPI) chemistry tabulation technique. Freely propagating and Bunsen-type flames corresponding to stoichiometric and lean premixed mixtures were considered. Validation of the LES solvers was carried out by comparing predicted solutions with experimental data and other published numerical results.

Head-to-head comparisons of different SFS approaches, including a transported flame surface density (FSD) model, allowed to identify weaknesses and strengths of the various models. Based on the predictive capabilities of the models examined, the PCM-FPI model was selected for the

study of hydrogen-enrichment of methane. A new progress of reaction variable was proposed to account for NO. The importance of transporting species with different diffusion coefficients was demonstrated, in particular for H_2. The proposed approach was applied to a Bunsen-type configuration, reproducing key features observed in the experiments: the enriched flame was shorter, which is attributed to a faster consumption of the blended fuel; and the enriched flame displayed a broader two-dimensional curvature probability density function. Furthermore, reduced levels of carbon dioxide (CO_2), increased levels of nitrogen monoxide (NO), and a slight increase in the carbon monoxide (CO) levels in areas of fully burned gas were predicted for the enriched flame.

Dedication

To you, the one who has been, is and will be always there with and for me, in different explicit or implicit forms.

To the memory of my grandmother Carmen, the most influential person in the early years of my life.

To my mother, Dora María, a single mother who has offered me unconditional love, comprehension, and encouragement.

To my families and relatives.

Acknowledgements

I extend my heartfelt gratitude to my thesis supervisors, Professors Clinton P. T. Groth and Ömer L. Gülder, for their guidance, support, and trust. I deeply appreciate their help and understanding, especially when I needed them the most.

I express my gratitude to Drs. Thierry Poinsot and Bénédicte Cuenot for giving me the opportunity to participate in the ECCOMET (Efficient and Clean Combustion Experts Training) project at CERFACS (Centre Européen de Recherche et Formation Avancée en Calcul Scientifique) in Toulouse, France. It was an invaluable experience!

I am grateful to Dr. Fabien Halter for providing experimental data from Centre National de la Recherche Scientifique (CNRS) at Orléans, France, to compare the predicted LES solutions with their experiments on hydrogen enrichment of methane. Similarly, I am grateful to Dr. Frank Yuen for his assistance with the experimental data from the University of Toronto Institute for Aerospace Studies (UTIAS).

I thank colleagues and friends who enriched my overall graduate experience over the years. Colleagues and friends I met through the UTIAS combustion lab: Mario Commodo, Frank Yuen, Peter Joo, Emre Karataş, Gorngrit Intasopa, Tayfun Aydin, David Pavé, Natalie Galley, Katie Bohan, Srivatsava Puranam, Frédéric Dandavino, Paul Mandatori, and Esen Cintosun. Through the UTIAS CFD lab: James McDonald, Pradeep Jha, Nasim Shahbazian, Lucian Ivan, Scott Northrup, Marc Charest, Jai Sachdev, Willem Deconinck, Tomoki Ohsawa, Jason Hicken, Anh Truong, Iordan Iordanov, and Mohammad Tabesh. Through CERFACS: Marco Maglio, Jean-Mathieu Senoner, Zafer Zeren, Ali Özel, Dirk Wunsch, Camilo Silva, Marta García, Bora Ucar, and Guillaume Albouze.

I extend my special thanks to Claudia Faccani, Tatiana Memisevic, and Irina Nanu, who have been very supportive friends. Special thanks are also due to Andreea O. Diaconescu and Mari-anne Hegström-Wojtowicz for sharing their joy of moving through life with me and cheering me up, even without noticing it.

I owe my deepest gratitude to my families, both maternal and paternal, for their support, encouragement, and inspiration, despite the distance and circumstances of life.

I owe an immense debt of gratitude to CONACyT (Mexican National Council for Science and Technology) for giving me the opportunity to pursue graduate studies abroad and providing the main funding of my research. Without their support, this thesis and overall experience would not have been possible. Supplemental financial assistance from UTIAS is also appreciated. I am

Francisco Emanuel Hernández Pérez

Toronto, 2011

Contents

List of Tables

List of Figures

List of Symbols

Alphanumeric Symbols

$\hat{\mathcal{A}}$	linearized flux Jacobian evaluated at a reference state $\hat{\mathcal{U}}$
A	area
a	speed of sound, absolute tolerance
$A_{i,j}$	area of computational cell i,j
B	pre-exponential factor
c	progress variable
$C_\epsilon, C_\nu, \zeta^*$	closure coefficients of the one-equation eddy-viscosity model
C_K	Kolmogorov constant
C_p	constant-pressure heat capacity
C_s	Smagorinsky coefficient
C_v	constant-volume heat capacity
c_v	subfilter-scale variance of the progress variable
$\mathrm{1D, 2D, 3D}$	one, two, and three spatial dimensions
$\mathcal{D}$	molecular diffusion coefficient
$\mathcal{D}_\mathrm{th}$	heat diffusivity
$\mathcal{D}_\mathrm{t}$	turbulent diffusion coefficient
$\mathcal{D}_{Y_\mathrm{c}}$	molecular diffusivity associated to Y_c
Da	Damköhler number
$\mathbf{e}_1, \mathbf{e}_2, \mathbf{e}_2$	unit vectors in the x_1, x_2 and x_3 coordinate directions
$\mathbf{e}_s$	unit vector along the direction of the distance between two adjacent cell centres
E	total energy, turbulent kinetic energy density
e	absolute internal energy
E_a	activation energy
E_F	efficiency factor
$\boldsymbol{\mathcal{F}}$	flux vector
$\boldsymbol{\mathcal{F}}^\mathbf{I}$	inviscid flux vector
$\boldsymbol{\mathcal{F}}^\mathbf{V}$	viscous flux vector
$\mathcal{F}$	Fourier transform
$\vec{\boldsymbol{\mathcal{F}}}$	flux dyad
F	thickening factor
F/O	fuel-oxidizer ratio

$\mathfrak{G}$	filter function
$\mathfrak{g}_i$	one-dimensional filter functions
G	Gibbs free energy, level surface of scalar field
g_i	gravitational acceleration
Δh_{f}^0	heat of formation
h	absolute enthalpy, grid spacing
h_{s}	sensible enthalpy
$\mathcal{J}_{i,\alpha}$	diffusive flux of species α in the ith direction
k	turbulent kinetic energy
k^{b}	backward reaction rate
K^{Eq}	equilibrium reaction rate constant
k^{f}	forward reaction rate
k_Δ	subfilter-scale turbulent kinetic energy
Ka	Karlovitz number
L_{t}	integral length scale
Le	Lewis number
$\dot{m}$	mass flux
$\mathcal{M}$	molecular mass
M	chemical symbol
M	Mach number
m	mass
M_0	reference Mach number
$\mathbf{n}$	unit vector normal to the flame
$\vec{n}$	unit vector normal to the cell face or edge
N	number of species
n	mole number
N_{R}	number of reactions
P	probability density function
p	pressure
Pr	Prandtl number
Q	criterion to identify coherent vortical structures
q_i	total heat flux
$\mathbf{r}$	distance vector
$\mathcal{R}$	universal gas constant, Riemann problem
R	gas constant
r	relative tolerance
R_{ij}	two-point correlation tensor
Re	Reynolds number
Re_{t}	turbulent Reynolds number
$\boldsymbol{S}$	source term vector
S	entropy
s_{L}	laminar flame speed

S_{ij}	strain rate tensor
Sc	Schmidt number
T	temperature
t	time
T_{b}	burnt mixture temperature
T_{u}	unburnt mixture temperature
$\boldsymbol{\mathcal{U}}$	conserved variable vector
u'	root-mean-square velocity or turbulent intensity
u'_{K}	Kolmogorov velocity
u_i	mixture velocity
V	volume
V_i^{c}	correction velocity
V_i	diffusion velocity
$V_{i,j,k}$	volume of computational cell i, j, k
$\boldsymbol{\mathcal{W}}$	primitive variable vector
$\mathcal{W}$	mean reaction rate
$\mathbf{x}$	position vector
x	coordinate normal to the flame front
x, y, z	Cartesian coordinates
X_α	mole fraction of species α
Y_α	mass fraction of species α
$Y_{\mathrm{c_v}}$	subfilter-scale variance of the progress of reaction variable
Y_{c}	progress of reaction variable
$Y_{\mathrm{c}}^{\mathrm{Eq}}$	equilibrium value of the progress of reaction variable
Z	mixture fraction
Z_{v}	subfilter-scale variance of the mixture fraction

Greek Symbols

γ	exponent of the power-law expression for the subfilter-scale wrinkling factor
$\Gamma_{\Delta_{\mathrm{o}}}$	efficiency function of Charlette *et al.*
$\boldsymbol{\Delta}$	LES filter vector
Δ	LES characteristic filter width
$\delta()$	Dirac delta function
δ_{i}	inner layer thickness
δ_{L}	laminar flame thickness
Δ_{o}	outer cutoff scale
δ_{ij}	Kronecker delta
ϵ	turbulent kinetic energy dissipation
ε	perturbation parameter used in the computation of numerical derivatives
η	Kolmogorov length scale
η_{i}	inner cutoff scale
θ	subfilter-scale heat flux

$\boldsymbol{\kappa}$	wavenumber vector
κ	scalar wavenumber
$\varkappa$	mole fraction of H_2 in the blended H_2-CH_4 fuel
λ	thermal conductivity
λ_i	eigenvalues
λ_{T}	Taylor microscale
μ	molecular viscosity
ν	kinematic viscosity, stoichiometric coefficient
ν_{t}	turbulent eddy viscosity
Ξ	wrinkling factor
Ξ_Δ	subfilter-scale wrinkling factor
ρ	mixture density
ρ_{r}	reactants density
Σ	flame surface density, flame surface per unit mass
τ_{K}	Kolmogorov time
τ_{ij}	viscous stress tensor
$\boldsymbol{\varphi}$	array of reactive scalars
ϕ	equivalence ratio
Φ_{ij}	velocity spectrum tensor
$\boldsymbol{\psi}$	array of statistical random variables associated with $\boldsymbol{\varphi}$
$\dot{\omega}$	net reaction rate

Superscripts

n	iteration index
T	transpose

Subscripts

α, β	species indices
b	burned gas
i, j, l	vector or tensor indices
Δ	subfilter-scale quantity
L	left solution state
p, q, r, s	number of atoms of a chemical element in the chemical symbol of a species
R	right solution state
r	reaction index
st	stoichiometric quantity
u	unburned gas
x, y, z	Cartesian coordinate directions

Other Symbols

$\bar{\varphi}$	LES filtered value of φ
$\check{\varphi}$	evaluated value of φ from filtered variables

$\hat{\varphi}$	flame-front conditioned value of φ, Roe's approximation variable and function, Fourier coefficient
$\langle\varphi\rangle$	average value of φ
$\tilde{\varphi}$	Favre-filtered LES value of φ
φ^*	statistical random variable associated with φ, complex conjugate of φ, specific value of φ

Abbreviations

AMR	adaptive mesh refinement
AUSM$^+$-up	advection upstream splitting method
CFD	computational fluid dynamics
CFL	Courant-Friedrichs-Lewy
CPU	central processing unit
DNS	direct numerical simulation
FSD	flame surface density
HLLE	Harten-Lax-van-Leer-Einfeldt
LEM	linear eddy model
LES	large eddy simulation
NKS	Newton-Krylov-Schwarz
ODE	ordinary differential equation
PDE	partial differential equation
PDF	probability density function
RANS	Reynolds averaged Navier-Stokes
SFS	subfilter-scale
UHC	unburnt hydrocarbon

Chapter 1

Introduction

1.1 Overview of Hydrogen-Hydrocarbon Combustion

Combustion involves the conversion of chemical bond energy contained in a fuel into heat and
light by chemical reactions between the fuel and an oxidizer. Fossil fuels constitute the primary
source of energy for domestic heating, power generation, and transportation. Alternative energy
sources such as nuclear, solar, and wind, supply less than 15% of the world energy demand [1].
The global energy needs are expected to rise, with fossil fuels remaining the dominant source in
the foreseeable future.

Besides generating heat, burning fossil fuels produces undesirable pollutants such as carbon
monoxide (CO), oxides of nitrogen (NO_x), oxides of sulfur (SO_x), soot, and unburnt hydrocar-
bons (UHC). Furthermore, emissions of carbon dioxide (CO_2) are virtually inherent to the oxi-
dation of hydrocarbon fuels since, for the majority of practical combustion devices, the oxidizer
is oxygen contained in air. Combustion-generated CO_2 accounts for nearly 80% of the anthro-
pogenic greenhouse-gas emissions of the Annex I [1] countries to the United Nations Framework
Convention on Climate Change (UNFCCC) [2]. At present, the increased level of anthropogenic
CO_2 in the atmosphere is widely considered to be a major factor in causing global warming, a
potentially devastating environmental and socioeconomic problem.

Global warming and security of energy supply are two significant challenges that society faces in
the twenty-first century. Combustion research is therefore committed to reducing the emissions
of pollutants and improving the efficiency of combustion devices. Since CO_2 is a by-product
of hydrocarbon combustion, it has been suggested to use hydrogen (H_2) as an alternative fuel,

---

[1]The Annex I to the UNFCCC includes Australia, Canada, United States and the majority of the European
nations.

which represents an environmentally cleaner energy source. However, there are considerable difficulties associated with hydrogen storage and distribution due to its high flammability limits, low ignition energy, and low volumetric energy content. In this context, hydrogen-hydrocarbon fuel blends appear as a promising option to synergistically pave the way towards pure hydrogen-based combustion systems and alleviate pollutant emissions related to fossil fuel combustion.

A number of studies have been conducted on the performance and emission characteristics of practical combustion devices using H_2-enriched hydrocarbon fuels [3, 4, 5, 6, 7, 8, 9, 10, 11, 12]. It has been found that hydrogen enrichment extends the lean stability limit and decreases emissions of CO, NO_x, and UHC in spark-ignition engines [7, 9], power-generation gas turbines [3, 8], and aircraft gas turbines [4]. There have also been several studies focused on fundamental aspects of hydrogen-hydrocarbon flames. It has been reported that H_2-enriched flames display higher laminar flame speeds, extended lean flammability limits, and augmented resistance to strain [13, 14, 15, 16, 17, 18, 19]. Moreover, experiments in swirl-stabilized burners [20, 21, 22] have been conducted to investigate the stabilization and blowout characteristics of H_2-enriched methane-air premixed flames. It has also been shown that the addition of H_2 to methane (CH_4) extends the flame lean stability limit, allowing stable burner operation at lower flame temperatures and reducing NO_x emissions.

1.2   Turbulent Premixed Combustion

Two of the most common classifications of combustion are based on the initial mixing condition of the reactants and whether the flow is laminar or turbulent. For most practical combustion applications, the flow is turbulent. In terms of mixing, combustion is classified in three categories: premixed, nonpremixed, and partially premixed. In premixed combustion, the fuel and oxidizer are homogeneously mixed at the molecular level before the chemical reactions occur. In nonpremixed combustion, the fuel and oxidizer mix and react during a continuous inter-diffusive process. In partially premixed combustion, the fuel and oxidizer partially mix and chemical reactions take place in a stratified medium [23].

Turbulent premixed combustion is encountered in practical devices such as gas turbines, spark-ignition engines, and domestic and industrial burners. Utilization of premixed combustion systems is advantageous as premixed systems provide greater control over combustion chemistry, flame temperatures, and pollutant emissions. Turbulent premixed combustion involves the interplay of complex phenomena such as turbulence, chemical reactions, mass and heat transfer, and radiation. Therefore, the complete description and understanding of turbulent premixed combustion processes are challenging tasks, requiring the interaction of different scientific dis-

ciplines (e.g., thermodynamics, chemical kinetics, fluid mechanics and so on) and the interplay between theory, experiment, and computation.

1.3   Turbulent Combustion Modelling

Recent developments in combustion theory, computational fluid dynamics (CFD), and high-performance computing hardware have made numerical combustion modelling a valuable and powerful instrument to assist in understanding observed combustion phenomena, simulate combustion processes, and guide the design of combustion experiments and practical systems. However, theoretical and computational models are unable to fully explain experimental observations and predict the behaviour of combustion systems in many instances. The relative role of the different physical and chemical phenomena in turbulent reacting flows is configuration dependent, plus the evolution of turbulent reacting flows is highly unsteady, involving complicated flow patterns. Reliable numerical models must thereby be able to predict unsteady turbulent-flow behaviour, in particular, that associated with turbulence-chemistry interaction.

The primary CFD approaches for computing chemically reacting turbulent flows are Direct Numerical Simulation (DNS), Reynolds-Averaged Navier-Stokes (RANS), and Large-Eddy Simulation (LES) [23, 24, 25]. DNS is potentially the most accurate approach in that all the scales of the turbulent flow field are completely resolved in the computation and no turbulence model is needed, solution errors are only related to the discretization errors of the numerical method. However, as DNS involves the solution of the governing equations down to the smallest physical scales, it is computationally expensive and currently impractical to obtain accurate solutions for the study of realistic engineering configurations. Nevertheless, DNS has proven to be a powerful research tool for the study of fundamental flame-turbulence interaction and specific combustion phenomena such as flame extinction, flame-wall interaction, differential diffusion of chemical species, and so forth [26, 27, 28, 29, 30].

The most commonly used approaches for engineering CFD applications fall into the category of Reynolds-averaged methods, simply called RANS. In RANS, averages of the flow variables are introduced and the governing equations are averaged. Averaging of the governing equations results in unclosed correlations. Whether they be based on time or ensemble averaging, RANS methods do not resolve any part of the turbulent fluctuations. These effects are entirely modelled. Additionally, RANS methods require that the time scales characterizing the mean flow unsteadiness and the turbulent fluctuations differ by orders of magnitude to be valid for unsteady problems [31]. For a detailed account of RANS approaches for turbulent combustion the reader is referred to the review by Veynante & Vervisch [24] and book by Poinsot & Veynante [25].

LES, a method based on a separation of scales via a low-pass filtering procedure, is considered an intermediate approach between DNS and RANS in that it directly resolves the large-scale motions of the flow (generally dependent on the geometry of the system under consideration), while the effects of the unresolved scales (having a potentially more universal structure) are modelled. Because of the explicit simulation of the large-scale motions, LES is inherently time dependent, and thereby, well suited to the prediction of unsteady flows. In spite of being computationally more demanding than RANS, LES offers substantial computational savings as compared to DNS [32].

1.4   Large Eddy Simulation of Turbulent Combustion

As mentioned above, LES is based on a separation of scales. In conventional LES, the separation of scales is achieved through a spatial low-pass filtering procedure of the governing equations [33], which generates additional unclosed terms. As the unclosed terms are related to physical processes occurring at scales smaller than the filter width, their modelling is called subfilter-scale (SFS) modelling. In the case of a reacting Newtonian fluid, the unclosed terms appearing in the filtered governing equations include the SFS stresses, SFS heat and species fluxes (scalar transport), and filtered reaction rates.

From the time LES emerged as an alternative approach to compute turbulent flows, most of the SFS modelling has been focused on the transport of momentum, while relatively little has been done concerning filtered reaction rates and scalar transport. The modelling of filtered reaction rates and SFS scalar transport can be more challenging because of the strong interactions between chemical reactions, diffusion, and convection even at the smallest scales of the flow. A remarkable complication for LES of turbulent premixed combustion is that chemical reactions occur in thin reacting layers at extremely small scales that are generally not resolved on typical LES grids. Thus, the role of SFS models in LES of premixed combustion is of significant importance. Presently, there is no universal SFS model and the accuracy and validity of models are subjects of debate. Different approaches that have been proposed for LES of combustion include the direct evaluation of Arrhenius law rates in terms of resolved variables [34], eddy break-up type modelling [35, 36], scale-similarity and dynamic evaluation of reaction rates [37, 38], probability density function (PDF) closure methods [39, 40, 41, 42, 43, 44, 45, 46, 47], conditional moment closure modelling [48, 49, 50, 51, 52], flame surface density [53, 54, 55, 56, 57] and flame wrinkling [58, 59, 60, 61, 62] descriptions of the flame front, level-set flame front tracking technique (G-equation) [23, 63, 64], artificially thickened flame modelling [65, 66, 67], and linear eddy modelling [68, 69, 70, 71, 72].

Although the theory needed for LES of combusting flows to reach its full predictive potential is far from complete yet, LES has been applied to diverse combustion problems with encouraging results. For instance, LES has been employed to study topics of practical interest which include, but are not limited to, aircraft [73, 74, 75] and reciprocating [76] engine combustion, blowoff and flashback in premixed gas turbines [77, 78, 79], and combustion instabilities [80, 81, 82].

1.5   H$_2$-Enriched Hydrocarbon Premixed Turbulent Combustion Modelling

It is well-known that the characteristics of lean hydrogen-air and hydrocarbon-air premixed flames differ substantially. For instance, Bell *et al.* [83] performed a two-dimensional study of Lewis number (Le) effects on lean premixed turbulent flames using DNS with detailed chemistry and transport (for a species α, the Lewis number is defined as the ratio of the mixture heat diffusivity to the molecular diffusivity of species α). The characteristics of fuel-lean propane, methane, and hydrogen flames were analysed and qualitatively compared with the experimental OH planar laser-induced fluorescence (PLIF) measurements of Bedat & Cheng [84]. The propane flame ($Le > 1$) displayed the smallest degree of wrinkling and peaks in the OH profile coincided with cusps of the flame surface. The methane flame ($Le \approx 1$) showed a somewhat larger degree of wrinkling than the propane flame, but less OH variation along the flame front. The hydrogen flame ($Le < 1$) was considerably more distorted than the propane and methane flames and the OH profile exhibited breaks, indicating local flame extinction.

Comprehensive measurements of flame-front structure for both hydrocarbon and lean hydrogen turbulent premixed Bunsen flames have been reported by Chen & Bilger [85, 86], presenting data that shows cellular burning structures in the hydrogen-air flame. Cellular patterns have been observed previously in nitrogen-diluted hydrogen-oxygen flames by Bregeon *et al.* [87] and Mitani & Williams [88]. Tip opening of Bunsen flames has been reported for lean hydrogen flames by Mizomoto *et al.* [89] and Katta & Roquemore [90]. Recently, Day *et al.* [91] have performed a three-dimensional numerical study of turbulent effects on cellular burning structures in lean premixed hydrogen flames. Even without any initial turbulence, a lean hydrogen premixed flame wrinkled and burned in cellular patterns in an initially uniform flow. All of these phenomena have been associated with non-unity Lewis number and preferential-diffusion of hydrogen.

Differences between the molecular diffusion coefficients of the fuel and oxidizer, and the heat diffusivity of the mixture, significantly affect the flame structure and propagation characteristics [92]. Thus, the incorporation of Lewis-number and preferential-diffusion effects is important in the modelling of lean hydrogen-enriched methane-air flames.

In this research, the hydrogen-enrichment of methane-air flames will be considered. A literature survey was carried out indicating that only a few computational studies of multidimensional H_2-enriched methane-air turbulent premixed flames have been conducted. Hawkes & Chen [93] performed two-dimensional (2D) DNS of freely propagating flames in decaying turbulence with complex reduced chemistry (15-step reaction mechanism). Mameri & Gökalp [94] carried out 2D RANS of Bunsen flames with reduced chemistry (1- and 2-step reaction mechanisms). Dunstan & Jenkins [95] simulated 2D premixed kernels in decaying turbulence using DNS and detailed chemistry. Day *et al.* [96] performed a 2D study to characterize lean methane-air flames with significant hydrogen addition, including detailed transport and chemical kinetics. Vreman *et al.* carried out three-dimensional DNS of slot Bunsen flames with tabulated chemistry [97]. In all the DNS simulations cited above, complex chemistry and preferential diffusion were taken into account and their relevance to characterize the flame behaviour were recognized.

1.6   Thesis Objective

As outlined above, hydrogen enrichment of hydrocarbon fuels in lean premixed systems is desirable since it can lead to a progressive reduction in greenhouse-gas emissions, while paving the way towards pure hydrogen combustion. Furthermore, the improved burning rates and increased lean stability limit resulting from hydrogen enrichment may lead to leaner burn systems, allowing for lower peak combustor temperatures and further reduction of CO_2, CO, and NO_x emissions. Hence, there is considerable interest in the investigation and prediction of the combustion and emission characteristics of H_2-enriched hydrocarbon turbulent premixed flames.

The main purpose of this doctoral research is the investigation of SFS modelling for LES of lean H_2-enriched methane-air turbulent premixed combustion. The prediction of carbon dioxide (CO_2), carbon monoxide (CO), and nitric oxide (NO) emissions in lean H_2-enriched flames is also contemplated as part of this investigation. To this end, theoretical and numerical modelling research, involving the implementation of different SFS models and fundamental flame studies, have been conducted.

In order to accomplish the research objective stated above, the following major tasks have been performed:

- development of both two- and three-dimensional fully-compressible LES solution methods for a thermally perfect reactive mixture of gases, based on an existing computational framework for fluids and combustion at UTIAS;

- implementation of the thickened flame model for LES of premixed combustion, coupled

with a power-law SFS flame wrinkling approach;

- implementation of the presumed conditional moment (PCM) SFS modelling approach, coupled with the flame prolongation of intrinsic low-dimensional manifold (FPI) chemistry tabulation technique;

- head-to-head comparisons of different SFS models for turbulent premixed combustion; and

- validation of results by comparing predicted solutions with experimental data and other published numerical results.

It is important to note that, although multi-phase flows are common in combusting applications, the scope of this thesis is limited to gaseous combustion. Also, under lean conditions NO can represent over 90% of the NO_x emissions [98]. Therefore, only emissions of NO will be accounted for and examined. In addition, methane will be used as the main fuel throughout this investigation. The reason is that methane is the primary component of natural gas, which is the fuel employed by most lean premixed systems of land-based gas turbines/engines.

1.7 Thesis Organization

The contents of the thesis are organized into 7 chapters. In this first Chapter, a general overview and introduction are provided. In Chapter 2, aspects of turbulent premixed combustion modelling and the governing equations for a compressible thermally perfect reactive mixture of gases are presented. In Chapter 3, the LES Favre-filtered governing equations are introduced and different subfilter-scale modelling strategies are reviewed. In Chapter 4, a detailed description of the thickened flame and PCM-FPI models is given. In Chapter 5, the numerical discretization and solution procedure are described. In Chapter 6, numerical LES results for the validation test cases including one-dimensional steady-state, two-dimensional freely propagating and three-dimensional Bunsen-type premixed flames are described and discussed. The results for the Bunsen-type flames are further compared with experimental data. Finally, in Chapter 7, concluding remarks are drawn and future research directions are suggested.

<div align="right">

Chapter 2

</div>

Turbulent Premixed Combustion Modelling

The essential elements required to mathematically describe combustion processes include the governing conservation equations, equation of state, chemical kinetic data, and thermodynamic and transport properties. This chapter presents the governing conservation equations and constitutive relations for a reactive mixture of thermally perfect gases and highlights fundamental aspects of turbulent premixed combustion modelling.

2.1 Background

Before presenting the governing equations for a reactive mixture of thermally perfect gases, some basic definitions required for the quantitative treatment of combustion processes will be introduced. To quantify the relative amount of species α in a mixture of N species, the species mass fraction, Y_α, and mole fraction, X_α, can be employed. They are defined by the following expressions:

$$Y_\alpha = \frac{m_\alpha}{\sum_{\beta=1}^{N} m_\beta}, \tag{2.1}$$

$$X_\alpha = \frac{n_\alpha}{\sum_{\beta=1}^{N} n_\beta}. \tag{2.2}$$

In Equations 2.1 and 2.2, m_α and n_α denote the mass and mole number of species α, respectively. From the definitions of Y_α and X_α, it follows that $\sum_{\alpha=1}^{N} Y_\alpha = 1$ and $\sum_{\alpha=1}^{N} X_\alpha = 1$. Furthermore,

species mass fractions can be converted to mole fractions and vice-versa through the relations

$$X_\alpha = \frac{Y_\alpha/\mathcal{M}_\alpha}{\sum_{\beta=1}^{N} Y_\beta/\mathcal{M}_\beta} = \mathcal{M}\frac{Y_\alpha}{\mathcal{M}_\alpha}\,, \tag{2.3}$$

$$Y_\alpha = \frac{X_\alpha\mathcal{M}_\alpha}{\sum_{\beta=1}^{N} X_\beta\mathcal{M}_\beta} = \frac{X_\alpha\mathcal{M}_\alpha}{\mathcal{M}}\,, \tag{2.4}$$

where $\mathcal{M}_\alpha$ is the molecular mass of species α and $\mathcal{M}$ is the mean molecular mass of the mixture, which is given by $\mathcal{M} = \sum_{\beta=1}^{N} X_\beta\mathcal{M}_\beta = \left(\sum_{\beta=1}^{N} Y_\beta/\mathcal{M}_\beta\right)^{-1}$.

Combustion intensity for a particular fuel and oxidizer depends upon their relative concentrations. The latter can be measured by defining the fuel-oxidizer ratio, $(F/O) = m_\mathrm{F}/m_\mathrm{O}$, where m_F and m_O are the mass of fuel and oxidizer, respectively, in the premixed mixture. Stoichiometric combustion occurs when all the reactants are completely consumed in the reaction and the products are in their most stable form. To quantify the deviation from stoichiometric conditions of the premixed mixture, the equivalence ratio, ϕ, is introduced and can be defined as

$$\phi = \frac{(F/O)}{(F/O)_\mathrm{st}}\,, \tag{2.5}$$

where $(F/O)_\mathrm{st}$ is the fuel-oxidizer ratio corresponding to a stoichiometric process. For fuel-lean (or simply lean) combustion $\phi < 1$, for stoichiometric combustion $\phi = 1$, and for fuel-rich (or simply rich) combustion $\phi > 1$.

2.2   Conservation Equations for a Reactive Mixture of Thermally Perfect Gases

The derivation of the conservation equations for mass, momentum, energy, and species mass fractions can be found in many standard textbooks such as those by Williams [99] and Kuo [100], and are summarized in the book by Poinsot and Veynante [25]. The form of the governing equations, under the assumptions of a Newtonian fluid, negligible bulk viscosity, valid Fick's law of diffusion, and negligible Soret, Duffour and radiation effects, is considered herein. The conservation equations for a thermally perfect reactive mixture of N chemical species evolving in time, t, and space, $\mathbf{x}$, can then be written using tensor notation as

$$\frac{\partial \rho}{\partial t} + \frac{\partial(\rho u_j)}{\partial x_j} = 0\,, \tag{2.6}$$

$$\frac{\partial(\rho u_i)}{\partial t} + \frac{\partial(\rho u_i u_j + \delta_{ij}p)}{\partial x_j} - \frac{\partial \tau_{ij}}{\partial x_j} = \rho g_i\,, \tag{2.7}$$

$$\frac{\partial(\rho E)}{\partial t} + \frac{\partial[(\rho E + p)u_j]}{\partial x_j} - \frac{\partial(\tau_{ij}u_i)}{\partial x_j} + \frac{\partial q_j}{\partial x_j} = \rho g_i u_i \,, \tag{2.8}$$

$$\frac{\partial(\rho Y_\alpha)}{\partial t} + \frac{\partial(\rho Y_\alpha u_j)}{\partial x_j} + \frac{\partial \mathcal{J}_{j,\alpha}}{\partial x_j} = \dot{\omega}_\alpha \,, \tag{2.9}$$

where

$$\tau_{ij} \;=\; \mu\left(\frac{\partial u_i}{\partial x_j} + \frac{\partial u_j}{\partial x_i}\right) - \frac{2}{3}\mu\delta_{ij}\frac{\partial u_l}{\partial x_l} \,, \tag{2.10}$$

$$q_j \;=\; -\lambda\frac{\partial T}{\partial x_j} - \rho\sum_{\alpha=1}^{N} h_\alpha \mathcal{D}_\alpha \frac{\partial Y_\alpha}{\partial x_j} \,, \tag{2.11}$$

$$\mathcal{J}_{j,\alpha} \;=\; -\rho\mathcal{D}_\alpha\frac{\partial Y_\alpha}{\partial x_j} \,, \tag{2.12}$$

with the indices $i, j, l = 1, 2, 3$ and $\alpha = 1, \ldots, N$. Einstein summation convention applies to the indices i, j, and l. In the expressions above, ρ is the mixture density, u_i is the mixture velocity, p is the mixture pressure, T is the mixture temperature, E is the total mixture energy (including chemical energy or heat of formation), Y_α is the mass fraction of species α, $\dot{\omega}_\alpha$ is the net reaction rate of species α, g_i is the acceleration due to gravity, τ_{ij} is the viscous stress tensor, q_j is the total heat flux (energy flux due to thermal conduction and energy flux due to the diffusion of species), and $\mathcal{J}_{j,\alpha}$ is the mass diffusive flux corresponding to species α. The coefficients μ, λ, h_α, and $\mathcal{D}_\alpha$ are the mixture viscosity, mixture thermal conductivity, enthalpy of species α, and molecular diffusivity of species α, respectively. Additionally, δ_{ij} is the Kronecker delta. The mixture is assumed to obey the ideal gas equation of state, which has the form

$$p = \rho\mathcal{R}T/\mathcal{M} = \rho R T \,, \tag{2.13}$$

where $\mathcal{R}$ is the universal gas constant ($8.314 \; \mathrm{J}\cdot\mathrm{mol}^{-1}\cdot\mathrm{K}^{-1}$) and R is the mixture gas constant given by $R = \mathcal{R}\sum_{\alpha=1}^{N} Y_\alpha/\mathcal{M}_\alpha = \sum_{\alpha=1}^{N} Y_\alpha R_\alpha$. The mixture total energy is expressed as

$$E = e + \frac{1}{2}u_i u_i = h - \frac{p}{\rho} + \frac{1}{2}u_i u_i \,, \tag{2.14}$$

where e is the mixture absolute internal energy and h is the mixture absolute enthalpy, which are related by the equation $e = h - p/\rho$. The mixture absolute internal energy and enthalpy can be determined as functions of the individual species absolute internal energy, e_α, and absolute

enthalpy, h_α, as follows:

$$e = \sum_{\alpha=1}^{N} Y_\alpha e_\alpha \,, \tag{2.15}$$

$$h = \sum_{\alpha=1}^{N} Y_\alpha h_\alpha \,. \tag{2.16}$$

For each species, e_α and h_α are taken as functions of temperature only. For a given temperature T^*, they are obtained via

$$e_\alpha = \int_0^{T^*} C_{v_\alpha}(T) \, dT \,, \tag{2.17}$$

$$h_\alpha = \int_0^{T^*} C_{p_\alpha}(T) \, dT \,, \tag{2.18}$$

where C_{p_α} and C_{v_α} are the species heat capacities at constant pressure and volume, respectively. The species e_α and h_α can be re-expressed in the form [25]

$$e_\alpha = \int_{T_0}^{T^*} C_{v_\alpha}(T) \, dT - R_\alpha T_0 + \Delta h_{f_\alpha}^0 = e_{s_\alpha} + \Delta h_{f_\alpha}^0 \,, \tag{2.19}$$

$$h_\alpha = \int_{T_0}^{T^*} C_{p_\alpha}(T) \, dT + \Delta h_{f_\alpha}^0 = h_{s_\alpha} + \Delta h_{f_\alpha}^0 \,, \tag{2.20}$$

where e_{s_α} is the species sensible internal energy, h_{s_α} is the species sensible enthalpy, and $\Delta h_{f_\alpha}^0$ is the species heat of formation (chemical energy) at a reference temperature T_0, which is generally 298 K.

2.3   Thermodynamic and Transport Data

Another basic element of combustion modelling is the determination of thermodynamic properties and transport coefficients of the individual species and the mixture. The thermodynamic and transport properties of each species are prescribed herein employing the database compiled by Gordon and McBride [101, 102], which provides curve fits for the species enthalpy, constant-pressure heat capacity, entropy, molecular viscosity, and thermal conductivity as functions of temperature. The database also includes properties such as molecular mass $\mathcal{M}_\alpha$ and heat of formation, $\Delta h_{f_\alpha}^0$. For each species, the expressions for enthalpy and constant-pressure heat

capacity have a polynomial form and are given by

$$
\begin{aligned}
h_\alpha &= R_\alpha T \left[-a_{1,\alpha}T^{-2} + a_{2,\alpha}T^{-1}\ln T + a_{3,\alpha} + \frac{a_{4,\alpha}T}{2} + \frac{a_{5,\alpha}T^2}{3} \right.\\
&\left. + \frac{a_{6,\alpha}T^3}{4} + \frac{a_{7,\alpha}T^4}{5} + b_1 T^{-1} \right] + \Delta h^0_{f_\alpha} ,
\end{aligned}
\tag{2.21}
$$

$$
C_{p_\alpha} = R_\alpha \left[a_{1,\alpha}T^{-2} + a_{2,\alpha}T^{-1} + a_{3,\alpha} + a_{4,\alpha}T + a_{5,\alpha}T^2 + a_{6,\alpha}T^3 + a_{7,\alpha}T^4 \right] , \tag{2.22}
$$

where $a_{m,\alpha}$ and $b_{m,\alpha}$ are the polynomial coefficients. The expressions for the species thermal conductivity, λ_α, and molecular viscosity, μ_α, have the form

$$
\Upsilon_\alpha = \exp\left(A_{\Upsilon,\alpha}\ln T + B_{\Upsilon,\alpha}T^{-1} + C_{\Upsilon,\alpha}T^{-2} + D_{\Upsilon,\alpha} \right) . \tag{2.23}
$$

Here, Υ stands for either μ or λ and $A_{\Upsilon,\alpha}$, $B_{\Upsilon,\alpha}$, $C_{\Upsilon,\alpha}$, and $D_{\Upsilon,\alpha}$ are the corresponding expression coefficients. Note that the transport properties of the individual species can also be computed using standard gas kinetic theory relations [103]. For a summary of those relations refer to the textbook by Law [104].

In the case of the mixture transport coefficients, Wilke's mixture rule [105] is used to compute the mixture viscosity and Mason and Saxena's [106] mixture rule is adopted to evaluate the thermal conductivity. The mixture viscosity and thermal conductivity are respectively given by the following expressions:

$$
\mu = \sum_{\alpha=1}^{N} \frac{\mu_\alpha Y_\alpha}{\mathcal{M}_\alpha \varphi_\alpha} , \tag{2.24}
$$

$$
\lambda = \sum_{\alpha=1}^{N} \frac{\lambda_\alpha Y_\alpha}{Y_\alpha + 1.065\mathcal{M}_\alpha(\varphi_\alpha - 1)} , \tag{2.25}
$$

where

$$
\varphi_\alpha = \sum_{\beta=1}^{N} \frac{Y_\beta}{\mathcal{M}_\beta} \left[1 + \left(\frac{\mu_\alpha}{\mu_\beta}\right)^{\frac{1}{2}} \left(\frac{\mathcal{M}_\beta}{\mathcal{M}_\alpha}\right)^{\frac{1}{4}} \right]^2 \left[8\left(1 + \frac{\mathcal{M}_\alpha}{\mathcal{M}_\beta}\right) \right]^{-\frac{1}{2}} . \tag{2.26}
$$

It should be noted that some important dimensionless numbers are commonly used to compare transport processes in combustion, namely the Lewis, Prandtl, and Schmidt numbers. They are respectively defined by the following relations:

$$
Le_\alpha = \frac{\lambda}{\rho \mathcal{D}_\alpha C_p} , \tag{2.27}
$$

$$
Pr = \frac{\mu C_p}{\lambda} , \tag{2.28}
$$

$$
Sc_\alpha = \frac{\mu}{\rho \mathcal{D}_\alpha} . \tag{2.29}
$$

In the expressions above, C_p is the mixture constant-pressure heat capacity, which is evaluated using the following expression: $C_\mathrm{p} = \sum_{\alpha=1}^{N} Y_\alpha C_{\mathrm{p}\alpha}$. Despite the large temperature variations found in combustion, the aforementioned non-dimensional numbers are almost constant and take on values near unity [104]. Unless otherwise stated, throughout this research the species mass diffusion coefficients are determined by prescribing the species Schmidt numbers.

2.4   Chemical Kinetics

2.4.1   Finite Rate Chemistry

For a chemical system consisting of N species reacting through N_R reactions represented by

$$\sum_{\alpha=1}^{N} \nu'_{\alpha,r} \mathrm{M}_\alpha \rightleftharpoons \sum_{\alpha=1}^{N} \nu''_{\alpha,r} \mathrm{M}_\alpha \,, \qquad r = 1, 2, \ldots, N_\mathrm{R} \,, \tag{2.30}$$
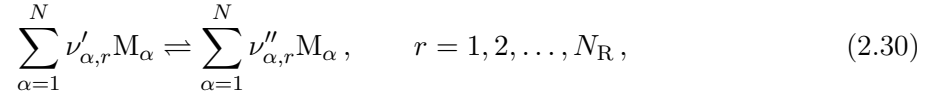
where $\nu'_{\alpha,r}$ and $\nu''_{\alpha,r}$ are the molar stoichiometric coefficients of species α in reaction r and M is the chemical symbol of species α, the time rate of change of the species concentration, $\dot{\omega}_\alpha$, can be determined using a general form of the law of mass action given by

$$\dot{\omega}_\alpha = \frac{d\left[\frac{\rho Y_\alpha}{\mathcal{M}_\alpha}\right]}{dt} = \frac{\mathcal{M}_\alpha}{\rho} \sum_{r=1}^{N_\mathrm{R}} \left(\nu''_{\alpha,r} - \nu'_{\alpha,r}\right) \left\{ k_r^\mathrm{f} \prod_{\beta=1}^{N} \left[\frac{\rho Y_\beta}{\mathcal{M}_\beta}\right]^{\nu'_{\beta,r}} - k_r^\mathrm{b} \prod_{\beta=1}^{N} \left[\frac{\rho Y_\beta}{\mathcal{M}_\beta}\right]^{\nu''_{\beta,r}} \right\} \,, \tag{2.31}$$

where k_r^f and k_r^b are the forward and backward reaction rate constants for the reaction r, respectively. In general, the reaction rate constants are temperature dependent and modelled using Arrhenius law:

$$k_r = A_r T^{B_r} \exp\left(\frac{E_{\mathrm{a}_r}}{\mathcal{R}T}\right) \,. \tag{2.32}$$

In Equation 2.32, A_r is the pre-exponential factor, B_r is the temperature exponent, and E_{a_r} is the reaction activation energy. The forward reaction rate data (A_r, B_r, and E_{a_r}) are usually provided in reaction mechanisms. If data for the backward rate constants are not provided, they can be obtained via the relation

$$k_r^\mathrm{b} = \frac{k_r^\mathrm{f}}{K_r^\mathrm{Eq} \left(\frac{1}{\mathcal{R}T}\right)^{\sum_{\gamma=1}^{N}(\nu''_\gamma - \nu'_\gamma)}} \,, \tag{2.33}$$

where the equilibrium constant, K_r^Eq, is given by

$$K_r^\mathrm{Eq} = \exp\left(\frac{-\Delta G_r^{p=1}}{\mathcal{R}T}\right) \,. \tag{2.34}$$

In the last equation, $\Delta G_r^{p=1}$ denotes the change in Gibbs free energy (products minus reactants) for the reaction r at atmospheric conditions. For each species, the Gibbs free energy is defined as $G_\alpha = h_\alpha - T S_\alpha$, where the species enthalpy, h_α, and entropy, S_α, are again found using the data compiled by Gordon and McBride [101, 102].

2.4.2   Reduced Mechanisms and Chemistry Tabulation

The use of detailed reaction mechanisms is computationally demanding and may be prohibitive for the simulation of turbulent flames. For example, a typical reaction mechanism for oxidation of methane, GRI-Mech 3.0 [107], contains 53 species and 325 reaction steps. Utilization of the aforesaid mechanism would involve the solution of 53 partial differential equations, in addition to the Navier-Stokes equations. In this thesis, reduced mechanisms and tabulated chemistry will be employed, instead. The tabulation of chemistry will be performed using the flame prolongation of intrinsic low-dimensional manifold technique (FPI), which will be described in Chapter 4. As for reduced chemical kinetic schemes, one-step and two-step mechanisms will be used for the oxidation of methane. They are summarized below.

Methane-Air, 1 step, 5 species (Westbrook and Dryer [108]):

$$CH_4 + 2O_2 \rightarrow CO_2 + 2H_2O$$
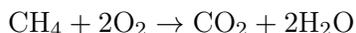
Methane-Air, 2 steps, 6 species (Westbrook and Dryer [108]):

$$CH_4 + \frac{3}{2}O_2 \quad \rightarrow \quad CO + 2H_2O$$
$$CO + \frac{1}{2}O_2 \quad \rightleftharpoons \quad CO_2$$
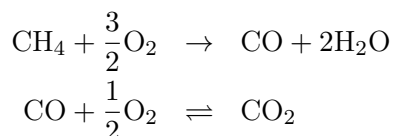
Nitrogen (N_2) is also included in both sets of species, but assumed to be inert. The one-step reaction only has an overall forward reaction rate given by:

$$k^{\circ} \quad = \quad A \exp\left(\frac{-E_a}{\mathcal{R}T}\right) [CH_4]^a [O_2]^b \ . \tag{2.35}$$

The two-step mechanism uses the same overall reaction rate for the methane and oxygen reaction, but has a forward and reverse reaction rate for the carbon monoxide and oxygen reaction. These

forward and reverse reaction rates are expressed as:

$$k^{\mathrm{f}} = A \exp\left(\frac{-E_{\mathrm{a}}}{\mathcal{R}T}\right) [\mathrm{CO}]^a [\mathrm{H_2O}]^b [\mathrm{O_2}]^c \tag{2.36}$$

$$k^{\mathrm{b}} = A \exp\left(\frac{-E_{\mathrm{a}}}{\mathcal{R}T}\right) [\mathrm{CO_2}]^a \,. \tag{2.37}$$

The coefficients used herein for each reaction mechanism are given in Table 2.1. The units for the concentrations are in $\mathrm{cm^3/mol}$ and the the overall units for the reaction rates are in $\mathrm{mol/(cm^3 s)}$.

Mechanism	Rate	A	E_{a} (J/(mol K))	a	b	c
One-step	k^{o}	22.11×10^{12}	2.0264×10^5	0.2	1.3	
Two-step	k^{o}	37.52×10^{12}	2.0464×10^5	0.2	1.3	
	k^{f}	$10^{14.6}$	1.6747×10^5	1.0	0.5	0.25
	k^{b}	5.0×10^8	1.6747×10^5	1.0		

Table 2.1: Methane-air reduced mechanism reaction rate coefficients.

2.5 Further Considerations on the Conservation Equations

Upon further consideration of the system of governing equations presented above, it can be seen that global conservation of mass needs special attention. Firstly, in addition to the N transport equations for N chemical species, the condition

$$\sum_{\alpha=1}^{N} Y_\alpha = 1 \,, \tag{2.38}$$

must be satisfied. Hence, the system of equations is overdetermined. This issue is resolved by solving transport equations for $N-1$ species and computing the remaining mass fraction using Equation 2.38. Secondly, if all the transport equations for the species are added together, global mass conservation requires that

$$\sum_{\alpha=1}^{N} Y_\alpha V_{j,\alpha} = 0 \,, \tag{2.39}$$

$$\sum_{\alpha=1}^{N} \dot{\omega}_\alpha = 0 \,, \tag{2.40}$$

where $V_{j,\alpha}$ is the jth component of the diffusion velocity of species α. When Fick's law of diffusion is used, the second condition above (Equation 2.39) is generally not automatically satisfied. To deal with this inconsistency, a diffusion velocity correction method is adopted [25].

The correction velocity is given by

$$V_j^c = \sum_{\alpha=1}^N \mathcal{D}_\alpha \frac{\partial Y_\alpha}{\partial x_j} \,, \tag{2.41}$$

and the corrected species diffussive flux takes the form

$$\mathcal{J}_{j,\alpha} = -\rho \left(\mathcal{D}_\alpha \frac{\partial Y_\alpha}{\partial x_j} - Y_\alpha V_j^c \right) \,. \tag{2.42}$$

It is important to mention that the correction velocity is also applied to the total heat flux q_j, appearing in the conservation equation for total energy. The heat flux can then be re-expressed as

$$q_j = -\lambda \frac{\partial T}{\partial x_j} + \sum_{\alpha=1}^N h_\alpha \mathcal{J}_{j,\alpha} \,. \tag{2.43}$$

2.6 Structure of a Laminar Premixed Flame

A premixed flame is regarded as a wave phenomenon in that the flame propagates towards the combustible mixture while consuming it. Two types of combustion waves can be identified, namely subsonic deflagration and supersonic detonation waves [100, 104]. In this research only deflagration waves are dealt with.

A sketch of a planar laminar premixed flame is shown in Figure 2.1. The combustible mixture (fresh or unburnt gas) and combustion products (burnt gas) are separated by a thin reacting interface, known as the flame front. Furthermore, the internal structure of a laminar premixed flame can be considered to consist of three layers [23]: a preheat layer governed by convection and diffusion, which is thicker than the other two; an inner layer where fuel is consumed, radicals are depleted, and most of the heat release takes place; and an oxidation layer where slow reactions occur with a minor heat release. The structure of a one-dimensional (1D) laminar premixed flame is illustrated in Figure 2.2.
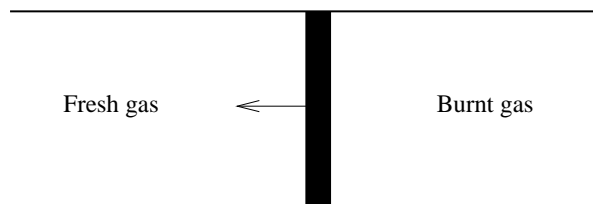
Figure 2.1: Sketch of a planar premixed flame.
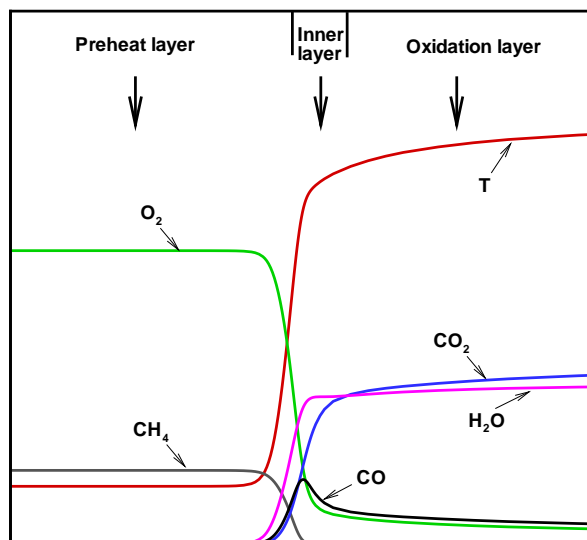
Figure 2.2: Structure of a 1D CH_4-air flame.

One of the most important parameters characterizing a laminar premixed flame is the propagation speed of the flame front normal to itself, which is referred to as the laminar flame speed or laminar burning velocity, s_L. It is a property that contains the physico-chemical information of the mixture and chiefly depends on the equivalence ratio, the temperature of the fresh gas, and pressure. From basic theory of laminar premixed flames, it is well established that

$$s_L \propto \sqrt{\mathcal{D}\omega}, \tag{2.44}$$

where $\mathcal{D}$ is a characteristic diffusivity of the flame and ω is the reaction rate. Another important parameter characterizing a laminar premixed flame is the laminar flame thickness, δ_L. Although different definitions of the laminar flame thickness exist, the two most common are the diffusive and the thermal thicknesses. The diffusive thickness can be written as

$$\delta_L = \frac{\mathcal{D}}{s_L}. \tag{2.45}$$

The thermal flame thickness, which is based on the temperature profile, is taken to have the form

$$\delta_L = \frac{T_b - T_u}{\max\left(\frac{dT}{dx}\right)}, \tag{2.46}$$

where T_u is the temperature of the unburnt mixture, T_b is the temperature of burnt gas, x is

the coordinate normal to the flame front, and $\max\left(\mathrm{d}T/\mathrm{d}x\right)$ stands for the maximum value of the gradient of temperature across the flame front. Unless otherwise stated, in the remainder of this thesis δ_L will denote the thermal laminar flame thickness, which will be employed for all the calculations.

A laminar flame front typical of hydrocarbon-air mixtures at atmospheric pressure has a thermal thickness in the range 0.1–1 mm, propagates with a speed between 0.1–1 m/s, and exhibits a steep temperature gradient with a burnt-to-fresh gas temperature ratio around 5–7 [24]. Moreover, the thicknesses of the different layers composing a methane-air premixed flame (see Figure 2.2) have been investigated by Peters and Williams [109]. For atmospheric pressure and $T_\mathrm{u} = 300$ K, they found that the thickness of the inner layer, δ_i, is about 10% of the diffusive flame thickness.

2.7   Scales of Turbulence and the Inertial Subrange

Turbulent flows are characterized by unsteady, irregular, and random motions having a wide range of scales. A turbulent flow is considered to be composed of eddies of different sizes. An eddy can be conceived as a turbulent motion that is, at least moderately, coherent within certain region [110]. Eddies of different sizes can overlap and larger eddies can carry smaller ones.

In a turbulent flow, the velocity and scalar properties display rapid and random fluctuations. To quantitatively describe turbulent flows, statistical analysis can be used and averages of the flow variables are taken. Different kinds of averaging are possible, for instance the time average (for statistically stationary flows), spatial average (for statistically homogeneous flows in one or more directions), and ensemble average (for replicable flows). Thus, the flow velocity and scalar quantities can be split or decomposed into mean and fluctuating components. For a relevant quantity ψ, the decomposition is written as

$$\psi = \langle \psi \rangle + \psi', \tag{2.47}$$

where $\langle \psi \rangle$ and ψ' are the mean and fluctuating components, respectively. To characterize the length scale distribution of the eddies, a two-point spatial correlation can be formed by measuring the velocity at two different locations in the flow, $\mathbf{x}$ and $\mathbf{x}+\mathbf{r}$, where $\mathbf{r}$ is the distance apart from $\mathbf{x}$. The two-point correlation (autocovariance) is expressed as

$$R_{ij}(\mathbf{x}, \mathbf{r}, t) = \langle u_i'(\mathbf{x}, t) u_j'(\mathbf{x} + \mathbf{r}, t) \rangle. \tag{2.48}$$

Representative lengths, called integral length scales, can then be defined such that

$$L_{11} = \frac{1}{R_{11}(\mathbf{x}, 0, t)} \int_0^\infty R_{11}(\mathbf{x}, \mathbf{e}_1 r, t) \, \mathrm{d}r = \frac{1}{\langle u_1'^2(\mathbf{x}, t)\rangle} \int_0^\infty R_{11}(\mathbf{x}, \mathbf{e}_1 r, t) \, \mathrm{d}r \, , \qquad (2.49)$$

$$L_{22} = \frac{1}{R_{22}(\mathbf{x}, 0, t)} \int_0^\infty R_{22}(\mathbf{x}, \mathbf{e}_2 r, t) \, \mathrm{d}r = \frac{1}{\langle u_2'^2(\mathbf{x}, t)\rangle} \int_0^\infty R_{22}(\mathbf{x}, \mathbf{e}_2 r, t) \, \mathrm{d}r \, , \qquad (2.50)$$

etc., where $\mathbf{e}_1$ and $\mathbf{e}_2$ are the unit vectors in the x_1 and x_2 coordinate directions, respectively. For isotropic turbulence the turbulent integral scale, L_t, is identified with the longitudinal integral scale, L_{11}, and indicates the size of the eddies that carry most of the turbulent kinetic energy, k. The latter is defined as

$$k = \frac{\langle u_1'^2 \rangle + \langle u_2'^2 \rangle + \langle u_3'^2 \rangle}{2} = \frac{3u'^2}{2} \, , \qquad (2.51)$$

where u' is the root-mean-square of the velocity fluctuations, often referred to as turbulent intensity.

Eddies of different sizes possess different amounts of kinetic energy. The turbulent kinetic energy contained in the large-scale eddies is continuously transferred to eddies of smaller and smaller sizes, until it is dissipated by viscous action (Richardson's energy cascade concept). Kolmogorov postulated that for sufficiently high Reynolds numbers the statistics of the small-scale turbulent motions are determined by the kinematic viscosity of the fluid, ν, and the rate of dissipation of the turbulent kinetic energy, ϵ. Dimensional analysis leads to appropriate expressions for the smallest scales of turbulence, which are named after Kolmogorov. The Kolmogorov length, time, and velocity are given by the following expressions:

$$\eta = \left(\frac{\nu^3}{\epsilon}\right)^{1/4} , \qquad \tau_\mathrm{K} = \left(\frac{\nu}{\epsilon}\right)^{1/2} , \qquad u_\mathrm{K}' = (\nu\epsilon)^{1/4} \, . \qquad (2.52)$$

Furthermore, Kolmogorov postulated that for sufficiently high Reynolds numbers there is a range of length scales ($L_\mathrm{t} \gg \ell \gg \eta$) through which the energy transfer rate is uniquely determined by ϵ. This range of length scales is called the inertial subrange. On dimensional grounds, the rate of energy transfer in this range is found to be

$$\epsilon \approx \frac{u'^3}{L_\mathrm{t}} \approx \frac{k^{3/2}}{L_\mathrm{t}} \, . \qquad (2.53)$$

It should be noted that a turbulent Reynolds number can be defined based on the integral length scale and the turbulent intensity,

$$Re_\mathrm{t} = \frac{u' L_\mathrm{t}}{\nu} \, , \qquad (2.54)$$

and the following relation holds for L_t and η:

$$\frac{L_t}{\eta} \approx Re_t^{3/4} \, . \tag{2.55}$$

Another length scale of interest, which is intermediate between L_t and η, is the Taylor microscale, λ_T. It can be understood as the distance that a large eddy convects an eddy of size η during the time τ_K [23], and is given by $\lambda_T = \left(15\nu u'^2/\epsilon\right)^{1/2}$.

For homogeneous turbulence the information contained in the two-point correlation can be re-expressed in terms of the wavenumber spectrum. The Fourier transform of the two-point correlation (Equation 2.48) defines the velocity spectrum tensor,

$$\Phi_{ij}(\boldsymbol{\kappa}, t) = \frac{1}{(2\pi)^3} \iiint\limits_{-\infty}^{\infty} e^{-\imath \boldsymbol{\kappa} \cdot \mathbf{r}} R_{ij}(\mathbf{r}, t) \, \mathrm{d}\mathbf{r} \, , \tag{2.56}$$

where $\boldsymbol{\kappa}$ is the wavenumber vector ($|\boldsymbol{\kappa}| = 2\pi/\ell$). In particular, the energy spectrum function is given by

$$E(\boldsymbol{\kappa}, t) = \iiint\limits_{-\infty}^{\infty} \frac{1}{2} \Phi_{ii}(\boldsymbol{\kappa}, t) \delta(|\boldsymbol{\kappa}| - \kappa) \, \mathrm{d}\boldsymbol{\kappa} \, . \tag{2.57}$$

Integration of Equation 2.57 over all scalar wavenumbers, κ, leads to the following relation:

$$\int_0^\infty E(\kappa, t) \, \mathrm{d}\kappa = \frac{1}{2} R_{ii}(0, t) = \frac{1}{2} \langle u_i' u_i' \rangle = k \, . \tag{2.58}$$

In the inertial subrange the energy spectrum has the form

$$E(\kappa) = C_K \epsilon^{2/3} \kappa^{-5/3} \, , \tag{2.59}$$

where C_K is the Kolmogorov constant. This is known as the $-5/3$ law. Figure 2.3 shows a schematic representation of the energy spectrum. For small wavenumbers (large scale eddies) the energy per unit wavenumber, E, increases with a power-law between κ^2 and κ^4. The spectrum peaks at a wavenumber that corresponds to the integral length scale. For larger wavenumbers, in the inertial subrange, E decreases following the $\kappa^{-5/3}$ law. For wavenumbers larger than the one corresponding to the Kolmogorov scale, E decreases exponentially due to viscous dissipation.
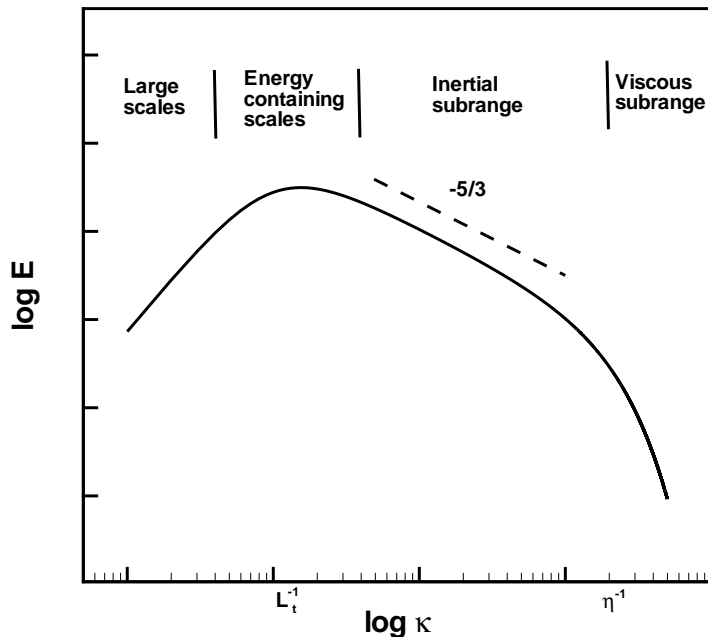
Figure 2.3: Schematic of the turbulent kinetic energy spectrum.

2.8 Turbulent Premixed Combustion Regimes

The derivation of models for turbulent premixed combustion is generally founded on physical analysis and comparisons of various time and length scales involved in combustion phenomena. These analyses have lead to turbulent premixed combustion diagrams, where different regimes can be defined in terms of representative length and velocity ratios and characteristic non-dimensional numbers. Besides the turbulent Reynolds number Re_t, two additional non-dimensional numbers are normally used to define the regimes, namely

- the Damkhöler number, Da, corresponding to the ratio of the turbulent integral time scale to the chemical time scale,

$$Da = \frac{L_t/u'}{\delta_L/s_L} \,, \qquad (2.60)$$

- and the Karlovitz number, Ka, corresponding to the ratio of the chemical time scale to the Kolmogorov time,

$$Ka = \frac{\delta_L/s_L}{\eta/u'_K} \,. \qquad (2.61)$$

Different regime diagrams of premixed combustion have been proposed by Borghi [111], Peters [112, 113], Abdel-Gayed and Bradley [114], Poinsot *et al.* [115], Pitsch and Duchamp de
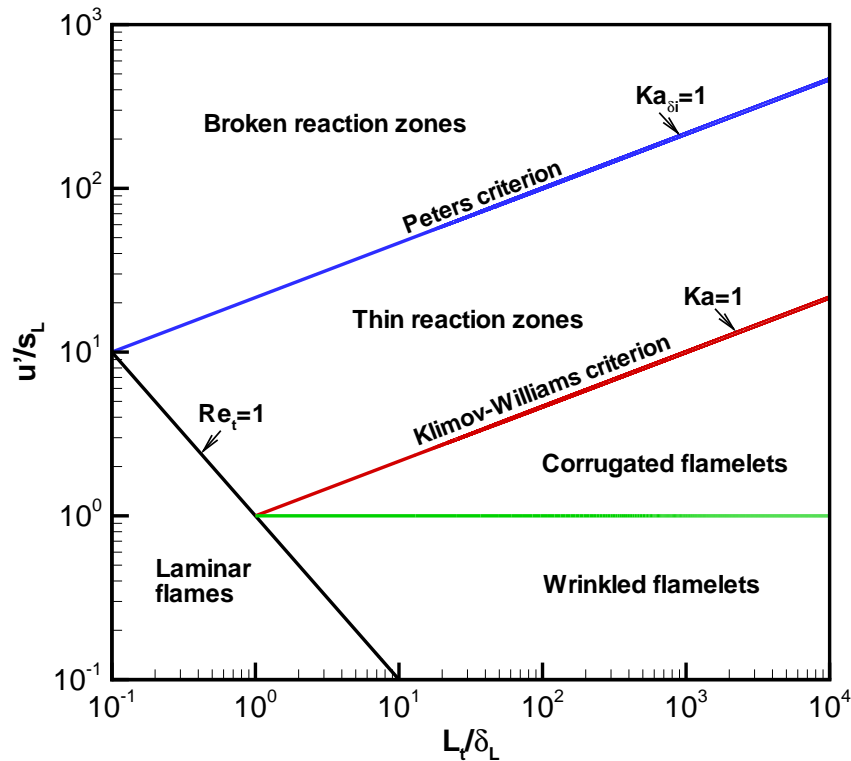
Figure 2.4: Diagram of turbulent premixed combustion regimes [113].

Lageneste [63], Düsing *et al.* [116], and others. The diagram proposed by Peters [113] is shown in Figure 2.4 and the various regimes with their respective features are summarized in Table 2.2. It should be pointed out that this diagram is based on scaling laws applicable to homogeneous isotropic turbulence without heat release and without consideration of any non-adiabatic, non-unity Lewis number, or non-unity Schmidt number effects. Nevertheless, the diagram provides an order-of-magnitude estimation of the regimes characterizing the flame-turbulence interaction. The lines $Re_t = 1$, $Ka = 1$ (Klimov-Williams criterion), $Ka_{\delta_i} = 1$ (Peters criterion), and $u'/s_L = 1$, set the boundaries between the various premixed combustion regimes. Note that Ka_{δ_i} is a Karlovitz number based on the thickness of the inner layer of the flame front. Using $\delta_i \approx 0.1\delta_L$, $Ka_{\delta_i} = 1$ corresponds to $Ka = 100$. Also note that a diffusive flame thickness is employed to construct the diagram.

For $Re_t < 1$ the flow and the flame are laminar. The flamelet region is bounded by $Re_t > 1$ and $Ka < 1$. In this region, $\delta_L < \eta$, therefore the flame structure is embedded within the smallest turbulent eddies where the flow is quasi-laminar. Turbulent edddies are not able to perturb the internal structure of the quasi-steady laminar flame. However, the flame front is wrinkled

$Ka < 1$ $(Da > 1)$	$100 > Ka > 1$ $(Da > 1)$	$Ka > 100$ $(Da \ll 1)$
Flamelets	Thin reaction zones	Broken reaction zones
Flame is thinner than all turbulent length scales	Small turbulent eddies may enter the preheat layer	All turbulent time scales are smaller than the chemical time scale

Table 2.2: Summary of turbulent premixed combustion regimes.

$(u'/s_\mathrm{L} < 1)$ or corrugated $(u'/s_\mathrm{L} > 1)$. Flame topology changes take place in the corrugated flamelet regime. The thin reaction zone regime is bounded by $Re_\mathrm{t} > 1$, $Ka > 1$, and $Ka_{\delta_\mathrm{i}} < 1$. For this regime, $\delta_\mathrm{L} > \eta > \delta_\mathrm{i}$, thereby small eddies can penetrate into the preheat layer, but not into the inner layer. Small eddies may distort the laminar structure of the flame front. The broken reaction zone regime is bounded by $Ka_{\delta_\mathrm{i}} > 1$. For this regime, $\delta_\mathrm{i} > \eta$, thus the smallest eddies are able to enter the inner layer and destroy the internal structure of the flame.

Since the corrugated flamelet and thin reaction zone regimes are commonly found in practical combustion applications (e.g., gas turbines and IC engines), both regimes are of particular interest. Despite the differences between these regimes, a flamelet approach (in which the turbulent flame is treated as an ensemble of quasi-laminar flames embedded in a turbulent flow) is often assumed to be valid in the modelling of turbulent premixed combustion for the two regimes [23]. As demonstrated by the experimental measurements of Kortschik *et al.* [117], conditional averages of the temperature ahead of the preheat zone show small variations suggesting that small eddies penetrating the preheat zone may not significantly alter the internal structure of the flame in the thin reaction zone regime and that a flamelet representation of the flame may be possible.

2.9 Lewis-Number and Preferential-Diffusion Effects

The turbulent flame speed and local structure are significantly affected by the differences between the molecular diffusion coefficients of the fuel, $\mathcal{D}_\mathrm{F}$, and the oxidizer, $\mathcal{D}_\mathrm{O}$, and the heat diffusivity of the mixture, $\mathcal{D}_\mathrm{th}$. An extensive discussion and review of molecular transport effects on turbulent flame propagation and structure has been provided by Lipatnikov & Chomiak [92].

To gain insight into flame front instabilities associated with Lewis-number and preferential diffusion effects, consider a positively curved (convex towards the reactants) bulge of a wrinkled laminar flame front. If the molecular diffusivity of the deficient reactant, $\mathcal{D}_\mathrm{d}$, is larger than $\mathcal{D}_\mathrm{th}$, the chemical energy supplied to the bulge by molecular diffusion exceeds the heat losses due to heat conduction leading to an increase in the local enthalpy and propagation speed. This process generates the so-called diffusive-thermal instability [118]. Furthermore, the concentration of a faster-diffusing reactant augments in the bulge. If the faster-diffusing reactant is the deficient one

($\mathcal{D}_d > \mathcal{D}_e$, where $\mathcal{D}_e$ is the molecular diffusivity of the excessive reactant), its local concentration tends to the stoichiometric value, the local propagation speed increases, the bulge grows, and the flame becomes unstable. The two physical processes described above are normally referred to as Lewis-number and preferential-diffusion effects, respectively.

Filtered Governing Equations and Subfilter-Scale Modelling

In this chapter, the LES filtering and Favre-filtered governing equations are introduced. Different subfilter-scale (SFS) models are reviewed for the SFS stresses, SFS scalar fluxes and filtered reactions rates. Particular emphasis is given to the modelling of the turbulence-chemistry interaction.

3.1 LES Filtering

As was previously mentioned in the introductory chapter, LES is a method based on a separation of scales. The large-scale energy-containing motions are directly computed, whereas the effects of the small scales are modelled. The conventional method to decompose flow variables into filtered (resolved) and residual (subfilter-scale) components is a low-pass spatial filtering procedure introduced by Leonard [33], but other approaches could be used (see, e.g., Meneveau & Katz [119]). For a relevant flow quantity φ, the spatial filtering is defined by

$$\bar{\varphi}(\mathbf{x}, t) = \int_{\mathrm{D}} \mathfrak{G}\left(\mathbf{x} - \mathbf{x}'; \boldsymbol{\Delta}(\mathbf{x})\right) \varphi(\mathbf{x}', t) \, \mathrm{d}\mathbf{x}' \,, \tag{3.1}$$

where $\bar{\varphi}$ is the filtered quantity (denoted by an overbar), $\mathfrak{G}$ is the filter function, and $\boldsymbol{\Delta}$ is the filter width associated with the size of the smallest scale retained by the filtering operation. The integration is performed over the flow domain D, where the filter function is non-zero. Additionally, the filter function satisfies the condition

$$\int_{\mathrm{D}} \mathfrak{G}(\mathbf{x} - \mathbf{x}') \, \mathrm{d}\mathbf{x}' = 1 \,. \tag{3.2}$$

The filter may be uniform (i.e., it is independent of the spatial position $\mathbf{x}$) or non-uniform. Also, it may be isotropic (i.e., it is independent of the spatial direction) or anisotropic. A three-dimensional (3D) filter can be expressed in terms of one-dimensional filter functions, $\mathfrak{g}_i$, and filter widths, Δ_i, as

$$\mathfrak{G}\left(\mathbf{x} - \mathbf{x}'; \boldsymbol{\Delta}(\mathbf{x})\right) = \prod_{i=1}^{3} \mathfrak{g}_i\left(x_i - x_i'; \Delta_i(\mathbf{x})\right) . \tag{3.3}$$

Various forms of standard filters exist, for instance a box or top-hat filter, a Gaussian filter, and a sharp spectral filter (cutoff filter in spectral space). The box filter has the form

$$\mathfrak{g}_i(x_i - x_i'; \Delta_i) = \begin{cases} 1/\Delta_i & \text{if } |x_i - x_i'| \leq \Delta_i/2 , \\ 0 & \text{otherwise} . \end{cases} \tag{3.4}$$

The Gaussian filter is given by

$$\mathfrak{g}_i(x_i - x_i'; \Delta_i) = \left(\frac{6}{\pi\Delta_i^2}\right)^{1/2} \exp\left(-\frac{6}{\Delta_i^2}(x_i - x_i')^2\right) . \tag{3.5}$$

And the sharp spectral filter can be written as

$$\mathfrak{g}_i(x_i - x_i'; \Delta_i) = \frac{\sin\left(\pi(x_i - x_i')/\Delta_i\right)}{\pi(x_i - x_i')} . \tag{3.6}$$

For a detailed discussion on the merits of each filter, the reader is referred to the book by Pope [110]. If the uniform isotropic 3D form of these filters is considered with a characteristic filter width Δ, the top-hat filter represents the volume average over a sphere of radius $\Delta/2$, the Gaussian filter represents the joint normal distribution with mean zero and covariance $\delta_{ij}\Delta^2/12$, and the sharp spectral filter removes all wavenumbers $|\boldsymbol{\kappa}| \geq \kappa_c$, with $\kappa_c = \pi/\Delta$ [110].

In reacting flows, a Favre filtering (density-weighted filtering) is further introduced

$$\tilde{\varphi}(\mathbf{x}, t) = \frac{\overline{\rho\varphi(\mathbf{x}, t)}}{\bar{\rho}} = \frac{1}{\bar{\rho}} \int_{\mathrm{D}} \rho\mathfrak{G}\left(\mathbf{x} - \mathbf{x}'; \boldsymbol{\Delta}(\mathbf{x})\right) \varphi(\mathbf{x}', t)\, \mathrm{d}\mathbf{x}' . \tag{3.7}$$

The Favre filtering has the advantage that when applied to the compressible form of the continuity equation, the equation is closed exactly without generating additional terms.

When the filtering procedure is applied to the system of governing equations, it is important that the differentiation and filtering operations commute. In general, these operations do not commute when a non-uniform filter is used. Ghosal & Moin [120] found that commutation errors are of the order $\mathcal{O}(\Delta^2)$. Thus, if a second-order accurate scheme is employed to solve the filtered equations, the commutation errors are of the order of the truncation error. However,

when higher-order schemes are employed, the commutation errors may lower the accuracy of the computation. A theory for constructing discrete high-order commutative filters already exists and was proposed by Vasilyev *et al.* [121].

In most LES approaches, implicit filtering is used, where the form of the filter is not explicitly given and the computational grid and the discretization operators act as the filter for the governing equations. Using an implicit approach, there is no need to specify a filter function, but neither can the filter function be determined exactly. It is a usual practice to take the filter width Δ to be proportional to the local cell size h (e.g., $\Delta = h$ or $\Delta = 2h$). For anisotropic filters, the characteristic filter width is generally taken to be $\Delta = (\Delta_1 \Delta_2 \Delta_3)^{1/3}$ [122]. Theoretical support for this choice and further discussion of the subject have been provided by Scotti and co-workers [123, 124].

3.2 Filtered Conservation Equations

The conservation equations introduced in Chapter 2 can be filtered to arrive at the corresponding equations for filtered or Favre-filtered variables, $\bar{\varphi}$ or $\tilde{\varphi}$. Assuming that the filtering and differentiation operations commute, the Favre-filtered form of the conservation equations for mass, momentum, total energy, and species mass fractions, along with the equation of state are given by

$$\frac{\partial \bar{\rho}}{\partial t} + \frac{\partial (\bar{\rho} \tilde{u}_j)}{\partial x_j} = 0 \,, \tag{3.8}$$

$$\frac{\partial (\bar{\rho} \tilde{u}_i)}{\partial t} + \frac{\partial (\bar{\rho} \tilde{u}_i \tilde{u}_j + \delta_{ij} \bar{p})}{\partial x_j} - \frac{\partial \check{\tau}_{ij}}{\partial x_j} = \bar{\rho} g_i + \underbrace{\frac{\partial \sigma_{ij}}{\partial x_j}}_{\mathbf{I}} + \underbrace{\frac{\partial (\bar{\tau}_{ij} - \check{\tau}_{ij})}{\partial x_j}}_{\mathbf{II}} \,, \tag{3.9}$$

$$\frac{\partial (\bar{\rho} \tilde{E})}{\partial t} + \frac{\partial [(\bar{\rho} \tilde{E} + \bar{p}) \tilde{u}_j]}{\partial x_j} - \frac{\partial (\check{\tau}_{ij} \tilde{u}_i)}{\partial x_j} + \frac{\partial \check{q}_j}{\partial x_j} = \bar{\rho} \tilde{u}_i g_i - \underbrace{\frac{\partial [\bar{\rho} (\widetilde{h_s u_j} - \check{h}_s \tilde{u}_j)]}{\partial x_j}}_{\mathbf{III}}$$

$$+ \underbrace{\frac{\partial (\overline{\tau_{ij} u_i} - \check{\tau}_{ij} \tilde{u}_i)}{\partial x_j}}_{\mathbf{IV}} - \underbrace{\frac{\partial (\bar{q}_j - \check{q}_j)}{\partial x_j}}_{\mathbf{V}}$$

$$- \underbrace{\frac{1}{2} \frac{\partial [\bar{\rho} (\widetilde{u_j u_i u_i} - \tilde{u}_j \widetilde{u_i u_i})]}{\partial x_j}}_{\mathbf{VI}}$$

$$- \underbrace{\frac{\partial [\sum_{\alpha=1}^{N} \Delta h_{f_\alpha}^0 \bar{\rho} (\widetilde{Y_\alpha u_j} - \tilde{Y}_\alpha \tilde{u}_j)]}{\partial x_j}}_{\mathbf{VII}} \,, \tag{3.10}$$

$$\frac{\partial(\bar{\rho}\tilde{Y}_\alpha)}{\partial t} + \frac{\partial(\bar{\rho}\tilde{Y}_\alpha\tilde{u}_j)}{\partial x_j} + \frac{\partial\check{\mathcal{J}}_{j,\alpha}}{\partial x_j} = -\underbrace{\frac{\partial[\bar{\rho}(\widetilde{Y_\alpha u_j} - \tilde{Y}_\alpha\tilde{u}_j)]}{\partial x_j}}_{\textbf{VIII}} - \underbrace{\frac{\partial(\bar{\mathcal{J}}_{j,\alpha} - \check{\mathcal{J}}_{j,\alpha})}{\partial x_j}}_{\textbf{IX}} + \underbrace{\bar{\dot{\omega}}_\alpha}_{\textbf{X}}, \tag{3.11}$$

$$\bar{p} = \bar{\rho}\check{R}\tilde{T} + \underbrace{\sum_{\alpha=1}^N R_\alpha\bar{\rho}(\widetilde{Y_\alpha T} - \tilde{Y}_\alpha\tilde{T})}_{\textbf{XI}}, \tag{3.12}$$

where

$$\sigma_{ij} = -\bar{\rho}\left(\widetilde{u_i u_j} - \tilde{u}_i\tilde{u}_j\right), \tag{3.13}$$

is the SFS stress tensor. The Favre-filtered total energy takes the form

$$\tilde{E} = \check{h}_s - \frac{\bar{p}}{\bar{\rho}} + \sum_{\alpha=1}^N \Delta h_{f_\alpha}^0 \tilde{Y}_\alpha + \frac{1}{2}\tilde{u}_i\tilde{u}_i + k_\Delta, \tag{3.14}$$

where

$$k_\Delta = \frac{1}{2}\left(\widetilde{u_i u_i} - \tilde{u}_i\tilde{u}_i\right), \tag{3.15}$$

is the SFS turbulent kinetic energy. The effects of the subfilter scales appear in the filtered total energy $\tilde{E}$, the filtered equation of state and the right-hand-sides of the governing continuity, momentum, energy and species mass fraction equations (i.e., terms **I**,...,**XI**). In the above equations, the check accent (ˇ) is used to denote quantities that are evaluated in terms of filtered variables. Therefore, $\check{R} = R(\tilde{Y}_\alpha)$, $\check{h}_s = h_s(\tilde{Y}_\alpha, \tilde{T})$, and so on. The fluxes $\check{\tau}_{ij}$, $\check{q}_j$, and $\check{\mathcal{J}}_{j,\alpha}$ are then expressed as

$$\check{\tau}_{ij} = 2\check{\mu}\left(\check{S}_{ij} - \frac{1}{3}\delta_{ij}\check{S}_{ll}\right), \tag{3.16}$$

$$\check{q}_j = -\check{\lambda}\frac{\partial\tilde{T}}{\partial x_j} - \bar{\rho}\sum_{\alpha=1}^N \check{h}_\alpha\check{D}_\alpha\frac{\partial\tilde{Y}_\alpha}{\partial x_j}, \tag{3.17}$$

$$\check{\mathcal{J}}_{j,\alpha} = -\bar{\rho}\check{D}_\alpha\frac{\partial\tilde{Y}_\alpha}{\partial x_j}, \tag{3.18}$$

where $\check{S}_{ij} = \frac{1}{2}(\partial\tilde{u}_i/\partial x_j + \partial\tilde{u}_j/\partial x_i)$, is the strain rate tensor corresponding to the Favre-filtered velocity. The molecular transport coefficients $\check{\mu}$, $\check{\lambda}$, and $\check{D}_\alpha$ are all evaluated at the temperature $\tilde{T}$.

3.3   Closures and Subfilter Scale Modelling

Modelling of the SFS terms is required to close the above system of equations. Term **II** is neglected under the assumption that the filtered viscous stresses, $\bar{\tau}_{ij}$, can be approximated to the

viscous stresses evaluated in terms of the Favre-filtered velocity, $\check{\tau}_{ij}$. Following similar assumptions for the total heat and species mass diffusion fluxes, terms **V** and **IX** may be neglected. Vreman *et al.* [125] performed a priori LES of a mixing layer at different Mach numbers and concluded that neglecting the non-linearities of the diffusion terms in the momentum and energy equations is acceptable. Regarding term **IV** (SFS viscous diffusion), it is generally much smaller than the other terms that require a model [126], and so is neglected. As for term **XI** (SFS temperature-species correlation), it is assumed to be small and generally neglected. Following the work of Knight *et al.* [127], term **VI** (the SFS turbulent diffusion) can be modelled in terms of the SFS stresses and the resolved velocity as

$$-\frac{\bar{\rho}\left(\widetilde{u_j u_i u_i} - \tilde{u}_j \widetilde{u_i u_i}\right)}{2} = \sigma_{ij}\tilde{u}_i\,. \tag{3.19}$$

Term **VII** involves the SFS species fluxes (term **VIII**) and is closed with the modelled SFS species fluxes. The remaining terms, which are the SFS stresses σ_{ij}, the SFS enthalpy flux $(\widetilde{h_s u_j} - \check{h}_s \tilde{u}_j)$, the SFS species fluxes $(\widetilde{Y_\alpha u_j} - \tilde{Y}_\alpha \tilde{u}_j)$, and the filtered reaction rates $\bar{\dot{\omega}}_\alpha$, are discussed below. Various approaches that have been employed for their modelling are also described.

3.3.1   Subfilter Scale Stresses

A number of strategies have been proposed to specifically model the SFS stresses. For detailed information on the existing modelling strategies, the reader is referred to the reviews by Rogallo & Moin [128], Lesieur & Métais [129], Piomelli [130], and Meneveau & Katz [119], the comparison of SFS models by Fureby *et al.* [131], or the textbooks by Pope [110] and Sagaut [132].

Two main categories of modelling approaches for σ_{ij} exist, namely functional modelling and structural modelling. The functional approach aims at representing the action of the subfilter scales on the resolved scales. The balance of the energy transfer between the resolved and unresolved scales suffices to describe the SFS effects. Models of this type make use of an eddy-viscosity. Examples of models that fall into this category are the Smagorinsky model [133], the one-equation eddy-viscosity model [134], the dynamic Smagorinsky model [135], and variants of the aforementioned models [136, 137, 138, 139]. These models suffer from the assumption that the principal axes (eigenvectors) of σ_{ij} are parallel to those of $\check{S}_{ij}$. The structural approach, on the other hand, aims at representing σ_{ij} without incorporating any knowledge of the detailed nature of the interactions between the resolved and unresolved scales. Examples of structural models are the scale-similarity and mixed model of Bardina *et al.* [140], the differential stress equation model of Deardorff [141], and the nonlinear anisotropic model of Lund & Novikov [142]. The advantage of structural models over functional models is that the principal axes of σ_{ij} and

$\check{S}_{ij}$ are not assumed to be parallel to each other.

It is worthwhile mentioning that alternative approaches also exist, for instance the monotone-integrated LES (MILES) approach [143, 144] (which implicitly models SFS effects through the numerical scheme for the inviscid flux), the approximate deconvolution model (ADM) [145, 146] (which involves the reconstruction of the unfiltered fields by inverting the filtering), the two-level simulation (TLS) approach [147, 148] (in which both the resolved and SFS motions are explicitly simulated, though the SFS motions evolve on embedded one-dimensional sub-domains), the homogenization-based LES model [149] (where homogenization by multiple-scale expansion is used and a micro-structure problem, involving a predefined stochastic process, is solved), etc.

In the following subsections, a description and discussion of the Smagorinsky and the one-equation eddy-viscosity models is provided. The constant-coefficient versions of both of these models have been implemented for use in this research.

Smagorinsky Model

The main role of this model is to remove energy from the resolved scales, mimicking the transfer of energy from the large to small scales and subsequent energy dissipation that is associated with the energy cascade. In the Smagorinsky model, the deviatoric part of the SFS stress tensor, for a compressible flow, is given by

$$\sigma_{ij} - \frac{1}{3}\delta_{ij}\sigma_{ll} = 2\bar{\rho}\nu_{\mathrm{t}}\left(\check{S}_{ij} - \frac{1}{3}\delta_{ij}\check{S}_{ll}\right),\tag{3.20}$$

where

$$\nu_{\mathrm{t}} = (C_{\mathrm{s}}\Delta)^2|\check{S}|,\tag{3.21}$$

and

$$|\check{S}| = \sqrt{2\check{S}_{ij}\check{S}_{ij}}.\tag{3.22}$$

The filter width, Δ, is taken as a characteristic length scale for the energy exchange between resolved and unresolved motions. The Smagorinsky coefficient, C_{s}, lies in the range between 0.1 and 0.23 [135], but there is no consensus on an optimal value. Yoshizawa [150] proposed an expression for the trace of the SFS stress tensor having the form

$$\sigma_{ll} = 2\bar{\rho}C_{\mathrm{I}}\Delta^2|\check{S}|^2.\tag{3.23}$$

The coefficient C_{I} is generally small. In Martín *et al.* [126] $C_{\mathrm{I}} = 0.09$ and Speziale *et al.* [151] found $C_{\mathrm{I}} \approx 0.0066$.

The Smagorinsky model has been widely utilized and produces reasonable results with a careful adjustment of the Smagorinsky coefficient. However, it has several limitations: the model assumes equilibrium between production and dissipation of SFS turbulence kinetic energy; the model is entirely dissipative and cannot predict backscatter (i.e., the transfer of energy from the small to the large scales); the model does not have the correct limiting behaviour near a wall; and modelling effects do not vanish in a fully resolved flow. Some deficiencies of the Smagorinsky model have been overcome by the dynamic model of Germano *et al.* [135], which assumes scale-similarity and uses information from the resolved scales to determine the Smagorinsky coefficient as part of the simulation.

SFS Turbulent Kinetic Energy Equation

One approach to improving the Smagorinsky model predictions is offered by a one-equation eddy-viscosity model, which is based on a transport equation for the SFS turbulent kinetic energy, k_Δ [134, 152]. The SFS stresses are modelled as

$$\sigma_{ij} = 2\bar{\rho}\nu_\mathrm{t}\left(\check{S}_{ij} - \frac{1}{3}\delta_{ij}\check{S}_{ll}\right) - \bar{\rho}\frac{2}{3}\delta_{ij}k_\Delta\,, \tag{3.24}$$

where

$$\nu_\mathrm{t} = C_\nu k_\Delta^{1/2}\Delta\,, \tag{3.25}$$

and the value of k_Δ is obtained from the modelled transport equation

$$\frac{\partial(\bar{\rho}k_\Delta)}{\partial t} + \frac{\partial(\bar{\rho}k_\Delta\tilde{u}_i)}{\partial x_i} = \sigma_{ij}\check{S}_{ij} - \frac{C_\epsilon\bar{\rho}k_\Delta^{3/2}}{\Delta} + \frac{\partial}{\partial x_i}\left[\bar{\rho}\left(\check{\nu} + \frac{\nu_\mathrm{t}}{\zeta^*}\right)\frac{\partial k_\Delta}{\partial x_i}\right]\,, \tag{3.26}$$

where $\check{\nu}$ is the mixture kinematic viscosity evaluated in terms of filtered variables ($\check{\nu} = \check{\mu}/\bar{\rho}$). The model coefficients C_ϵ and C_ν, can be adjusted to make the model consistent with the inertial subrange behaviour [153, 154] or determined dynamically from the simulation [139]. Schmidt & Schumann [154] used $C_\epsilon = 0.845$ and $C_\nu = 0.0856$, while Menon *et al.* [155] employed $C_\epsilon = 1.0$ and $C_\nu = 0.05$, which were suggested earlier by Yoshizawa [152]. As for ζ^*, a value of 1.0 has been adopted by Kim & Menon [139] and Fureby *et al.* [131], and 0.25 was used by Schmidt & Schumann [154].

Besides incorporating history and non-local effects, this model offers the advantages that non-equilibrium effects at the SFS level are taken into account and the eddy viscosity does vanish for a fully resolved flow. However, no backscatter is allowed ($k_\Delta \geq 0$). Menon *et al.* [155] and Fureby *et al.* [156] found a better performance of the constant-coefficient one-equation model over a variety of algebraic models in simulations of isotropic turbulence. Menon *et al.* [155] concluded

that models that do not assume local balance between energy production and dissipation are more suitable for modelling the SFS stresses in coarse grids even at relatively high Reynolds numbers. Additionally, Kim *et al.* [74] reported little difference between results obtained with constant-coefficient and dynamic versions of the k_Δ-equation for a gas turbine combustor flow using a relatively coarse grid.

3.3.2 Subfilter Scale Scalar Fluxes

In most of the work to date, a gradient transport assumption has been utilized to model SFS scalar fluxes [23, 25, 157, 32]. For a given scalar ψ, the gradient approximation to its SFS flux [158] can be written as follows:

$$\left(\widetilde{\psi u_j} - \tilde{\psi}\tilde{u}_j \right) = -\zeta_\mathrm{t} \frac{\partial \tilde{\psi}}{\partial x_j} \, . \tag{3.27}$$

In the above equation, ζ_t stands for an eddy-diffusivity, which is determined from the aforesaid eddy-viscosity and either the SFS Prandtl number, Pr_t, or the SFS Schmidt number, Sc_t. The SFS heat (enthalpy) flux is normally modelled using $\zeta_\mathrm{t} = \nu_\mathrm{t}/Pr_\mathrm{t}$, whereas the SFS species flux is modelled using $\zeta_\mathrm{t} = \nu_\mathrm{t}/Sc_\mathrm{t}$. Note that a similar gradient approximation, with $\zeta_\mathrm{t} = \nu_\mathrm{t}/Sc_\mathrm{t}$, is often used for other scalars employed in turbulent combustion models such as the progress variable (normalized temperature, species mass fraction or combination of species mass fractions) and the mixture fraction (ratio of local fuel mass to the sum of fuel and oxidizer mass). The SFS Prandtl and Schmidt numbers can be assumed to be constant (though there is no general consensus on their optimal values) or computed dynamically [159]. Domingo *et al.* [160] employed $Pr_\mathrm{t} = 0.9$ when modelling partially premixed flamelets. Using a dynamic formulation, Moin *et al.* [159] found values of Pr_t to be 0.4 and 0.85 in their study of compressible isotropic turbulence when two different initial pressure and temperature fluctuations were considered. In several LES studies, a value of 1.0 has been adopted for Sc_t [56, 161, 162]. Pitsch & Steiner [46] found that a constant value of 0.4 could be used after determining Sc_t with a dynamic procedure in their simulation of a turbulent diffusion flame.

An alternative approach to model SFS scalar fluxes was introduced by Speziale *et al.* [151] and Erlebacher *et al.* [163], which can be viewed as an analogue of the mixed model of Bardina *et al.* [140] for the SFS stresses, combining gradient and scale-similarity assumptions. However, application of this mixed model to LES of reacting flows has been limited to a few number of research works (e.g., Fureby & Möller [36] and Nogenmyr *et al.* [164]).

In this research, the commonly used gradient approximation is retained. Nevertheless, it should be noted that in premixed combustion counter-gradient transport exists, as it has been revealed

by experiments and DNS (see, e.g., Veynante *et al.* [165], Boger *et al.* [53], Tullis & Cant [166] and references therein). Counter-gradient transport is promoted by heat release, in particular, for low values of the ratio of turbulence intensity to laminar flame speed [165]. Boger *et al.* [53] found that, as compared to RANS, counter-gradient transport is lower in LES. Since the flame structure is partially resolved and part of the non-gradient phenomenon is included in the resolved scales, counter-gradient transport may be somewhat less important in LES. Models addressing counter-gradient transport have been proposed, for example, by Hawkes & Cant [55] and Tullis & Cant [166].

3.3.3 Filtered Reaction Rate Modelling

Modelling filtered reaction rates represents a major challenge in turbulent premixed combustion. Firstly, reaction rates are highly nonlinear functions of temperature and species mass fractions. Secondly, chemical reactions are confined to thin reacting layers at extremely small scales that cannot be resolved on typical LES grids. As a consequence, most of the turbulence-chemistry interaction needs to be modelled. A number of combustion models that have been proposed for LES follow concepts and modelling strategies originally developed for RANS (a detailed discussion of RANS approaches can be found, for example, in Veynante & Vervisch [24] and Poinsot & Veynante [25]). Different approaches that have been devised for LES of combustion include the direct evaluation of Arrhenius law rates in terms of resolved variables [34], eddy break-up type modelling [35, 36], scale-similarity and dynamic evaluation of reaction rates [37, 38], probability density function (PDF) closure methods [39, 40, 41, 42, 43, 44, 45, 46, 47], conditional moment closure modelling [48, 49, 50, 51, 52], flame surface density [53, 54, 55, 56, 57] and flame wrinkling [58, 59, 60, 61, 62] descriptions of the flame front, level-set flame front tracking technique (G-equation) [23, 63, 64], artificially thickened flame modelling [65, 66, 67], and linear eddy modelling [68, 69, 70, 71, 72].

In general, as pointed out by Veynante & Vervisch [24] and Janicka & Sadiki [157], two main views of the flame are employed in its modelling. The first view regards the flame as a geometrical entity. From the geometrical perspective, the study of scalar fields is based upon the dynamics and physical properties of iso-level flame surfaces. The flame is assumed to be thin compared to the flow scales. Further analysis along the normal direction to the flame surface uses a flamelet modelling, in which the local flame structure is associated with that of a one-dimensional laminar flame. The flame surface area per unit volume, also known as flame surface density, can be used to calculate the turbulent burning rate. Damköhler [167] first suggested that flame wrinkling is the main mechanism controlling the turbulent flame propagation. Accordingly, a larger turbulent flame speed, s_T, compared to the laminar flame speed, s_L, results from a larger wrinkled flame

surface area, A_T, compared to the cross-sectional flame area, A, in the direction of the flame propagation. Mathematically, this is expressed as $s_\mathrm{T}/s_\mathrm{L} = A_\mathrm{T}/A$.

The second view makes use of statistical analysis. Filtered values and correlations are extracted through filtered probability density functions (FPDF), which are determined either by presuming their shape or by solving a PDF transport equation. In the remainder of this section, a brief description of the main approaches used in LES of turbulent combustion is presented.

Flame Surface Density Model

One approach to model turbulent premixed flames is to ignore for the most part the internal structure of the flame and detailed chemical kinetics, and represent the combustion occurring at the flame front in terms of a reaction progress variable, c, such that $c = 0$ in the reactants and $c = 1$ in the combustion products. The progress variable quantifies the progress of reactions and may be defined as a reduced temperature or reduced fuel mass fraction:

$$c = \frac{T - T_\mathrm{u}}{T_\mathrm{b} - T_\mathrm{u}}, \tag{3.28}$$

$$c = \frac{Y_\mathrm{F} - Y_\mathrm{F}^\mathrm{u}}{Y_\mathrm{F}^\mathrm{b} - Y_\mathrm{F}^\mathrm{u}}, \tag{3.29}$$

where T, T_u, and T_b are respectively the local, the unburned, and burned gas temperatures. Similarly, Y_F, Y_F^u, and Y_F^u are the local, the unburned, and burned gas fuel mass fractions. In this approach, the transport equation for the progress variable

$$\frac{\partial(\rho c)}{\partial t} + \frac{\partial(\rho u_i c)}{\partial x_i} = \frac{\partial}{\partial x_i}\left(\rho \mathcal{D}_\mathrm{c}\frac{\partial c}{\partial x_i}\right) + \dot{\omega}_\mathrm{c} = \rho s_\mathrm{d}|\nabla c|, \tag{3.30}$$

is filtered. Here, s_d is the local displacement speed of the iso-surface c. The resulting filtered equation for the progress variable is

$$\frac{\partial(\rho \tilde{c})}{\partial t} + \frac{\partial(\rho \tilde{u}_i \tilde{c})}{\partial x_i} + \frac{\partial}{\partial x_i}[\rho\,(\widetilde{u_i c} - \tilde{u}_i \tilde{c})] = \frac{\partial}{\partial x_i}\left(\overline{\rho \mathcal{D}_\mathrm{c}\frac{\partial c}{\partial x_i}}\right) + \bar{\dot{\omega}}_\mathrm{c} = \overline{\rho s_\mathrm{d}|\nabla c|}. \tag{3.31}$$

The flame front displacement term, $\overline{\rho s_\mathrm{d}|\nabla c|}$, includes the reaction rate and may be modelled in terms of the flame surface density as

$$\overline{\rho s_\mathrm{d}|\nabla c|} \approx \rho_\mathrm{u} s_\mathrm{L}\Sigma = \rho_\mathrm{u} s_\mathrm{L}\Xi_\Delta|\nabla \bar{c}|, \tag{3.32}$$

where ρ_u is the density of the unburnt gas, s_L is the laminar flame speed, Σ is the SFS flame surface density (the flame surface per unit volume at the SFS level), and Ξ_Δ is the SFS wrinkling factor (ratio of SFS flame surface to its projection in the direction of propagation). Transport

equations have been proposed for Σ by Boger *et al.* [53] and Hawkes & Cant [55]. Alternatively, algebraic expressions have been provided by Boger *et al.* [53] and Charlette *et al.* [54]. A scale similarity model has also been proposed by Knikker *et al.* [57]. Models for Ξ_Δ include transport equations (Weller *et al.* [58], Fureby [59]) and algebraic equations (Charlette *et al.* [60, 61], Fureby [62]). Recently, Lin [168] successfully applied the FSD model of Hawkes & Cant to laboratory-scale burner configurations.

G-Equation Model

The G-equation, originally introduced by Markstein [169], provides a description of the flame front by an iso-level surface of a scalar field, G. The flame front is identified with $G = G_0$ and the values of G are typically chosen such that $G = 0$ at the flame front, $G < 0$ in the unburnt mixture, and $G > 0$ in the burnt gases. The G field is described by the following equation:

$$\frac{\partial G}{\partial t} + \mathbf{u} \cdot \nabla G = w |\nabla G| . \tag{3.33}$$

Here, w is the relative propagation speed of the flame front, which needs to be determined. A detailed discussion of the G-equation and the modelling of the propagation term, in particular within the RANS context, can be found in the book by Peters [23]. In the LES context, different approaches have been proposed for a modelled G-equation describing a filtered flame front (e.g., Im *et al.* [170], Piana *et al.* [171], Kim & Menon [74], Pitsch & Duchamp de Lageneste [63]). However, Oberlack *et al.* [172] showed that the G-equation has a special symmetry and pointed out that conventional ensemble or time averaging of the G-field cannot be performed, which has implications for LES. Accordingly, Pitsch [64] formulated a filtering procedure and G-equation consistent with the special symmetry of the G-field.

The new G-equation proposed by Pitsch [64], applicable to the corrugated flamelet and thin reaction zone regimes, has the form

$$\frac{\partial \check{G}}{\partial t} + \hat{\mathbf{u}} \cdot \nabla \check{G} = -\widehat{(s_\mathrm{L} + s_\kappa)} \, \mathbf{n} \cdot \nabla \check{G} , \tag{3.34}$$

where $\hat{\mathbf{u}}$ is the flame-front conditioned velocity, s_L is the laminar flame speed, s_κ describes the flame propagation by curvature effects, and $\mathbf{n}$ is the flame-front normal unit vector. The caret symbol ($\hat{\ }$) denotes a filtered quantity and $\check{G}$ is a level-set representation of the filtered flame front, not a filtered G-field. The conditioned velocity can be determined in terms of the unconditioned Favre-filtered velocity and the closure for the propagation term is expressed as [64]:

$$\widehat{(s_\mathrm{L} + s_\kappa)} \, \mathbf{n} = (\widehat{s_\mathrm{L}} - \mathcal{D}\check{\kappa} + s_\mathrm{T} - \mathcal{D}_{\mathrm{t},\kappa}\check{\kappa}) \, \check{\mathbf{n}} . \tag{3.35}$$

The first term describes the resolved part of the laminar burning velocity. The second term describes the interaction of molecular transport ($\mathcal{D}$ is a molecular diffusivity) with the resolved curvature, $\check{\kappa}$. The third term accounts for the SFS propagation by the laminar burning velocity and the interaction of SFS transport and SFS curvature. An expression to model this term can be obtained by deriving an equation for the SFS flame brush thickness and further assuming equilibrium between production and dissipation at the SFS level. The details are omitted here, but can be found in Pitsch [64]. The last term accounts for the interaction of SFS transport with the resolved flame-front curvature.

The diffusivity $\mathcal{D}_{t,\kappa}$ is given by [64]

$$\mathcal{D}_{t,\kappa} = \mathcal{D}_t Da_\Delta^{-2} \quad \text{for } Da > 1, \text{ and} \tag{3.36}$$

$$\mathcal{D}_{t,\kappa} = \mathcal{D}_t \quad \text{otherwise.} \tag{3.37}$$

In Equations 3.36 and 3.37, Da_Δ stands for the SFS Damköhler number, defined as $Da_\Delta = s_L \Delta/(u'_\Delta \delta_L)$, and $\mathcal{D}_t$ is a SFS diffusivity. This formulation of the G-equation has been recently coupled with a progress variable to describe the turbulent flame structure [173].

Although the G-equation model can be considered relatively simple in that the flame is only represented by an iso-surface, it has been widely employed. For instance, it was recently applied to perform LES of a low swirl stratified premixed flame [164]. One of the main challenges associated with the G-equation is the coupling of heat release effects with the G-field. In many formulations of the G-equation for LES, a turbulent flame speed is used to model the propagation term, but the turbulent flame speed alone evokes controversy in the combustion community and no universal model or correlation is available to predicted it [174].

Artificially Thickened Flame Model

The artificially thickened flame concept was first introduced by Butler & O'Rourke [175] for laminar flames. The basic idea of the thickened flame model is to artificially thicken the flame, so that it is resolvable on a relatively coarse mesh, but preserving its laminar flame speed. From basic theory of laminar premixed flames, the laminar flame speed, s_L, and the laminar flame thickness, δ_L, may be expressed as $s_L \propto \sqrt{\mathcal{D}\mathcal{W}}$ and $\delta_L \propto \frac{\mathcal{D}}{s_L}$, where $\mathcal{D}$ is the molecular diffusivity and $\mathcal{W}$ the mean reaction rate. An increase of the flame thickness δ_L by a factor F with a constant flame speed s_L can be achieved by replacing the thermal and molecular diffusivities $\mathcal{D}_{th}$ and $\mathcal{D}$ by $F\mathcal{D}_{th}$ and $F\mathcal{D}$, and the mean reaction rate $\mathcal{W}$ by $\mathcal{W}/F$. If F is sufficiently large (typically from 5 to 30), the thickened flame front may then be resolved on the LES computational mesh.

The thickened flame model was initially applied to LES by Veynante & Poinsot [176] and has been further developed by Angelberger *et al.* [65], Colin *et al.* [66], and Legier *et al.* [67]. The thickening of the flame front leads to a modified interaction between turbulence and chemistry because the Damkhöler number is decreased by a factor F. To account for this, an efficiency factor E_{F} is introduced. Then the balance equation for the chemical species takes the form

$$\frac{\partial(\bar{\rho}\tilde{Y}_\alpha)}{\partial t} + \frac{\partial(\bar{\rho}\tilde{Y}_\alpha\tilde{u}_j)}{\partial x_j} = \frac{\partial}{\partial x_j}\left(E_{\mathrm{F}}F\breve{\mathcal{D}}_\alpha\frac{\partial\tilde{Y}_\alpha}{\partial x_j}\right) + \frac{E_{\mathrm{F}}}{F}\bar{\dot{\omega}}_\alpha\,, \tag{3.38}$$

and the filtered reaction rate $\bar{\dot{\omega}}_\alpha$ is estimated using the Arrhenius laws. From the theoretical viewpoint, the thickened flame model is attractive in that it may be extended for complex chemistry because Equation 3.38 holds for any species α, at least when molecular fluxes remain described by Fick's law [66]. Also, phenomena such as ignition and flame-wall interaction can be accounted for. The thickened flame model has been used to simulate complex geometry combustors, study combustion instabilities and flashback, and simulate a complete ignition sequence in an annular combustion chamber [77, 78, 177, 178].

Linear Eddy Model (LEM)

The linear eddy model, originally proposed and developed by Kerstein [179, 180, 181, 182, 183, 184] and further developed into a SFS model by Menon *et al.* [69], is based on a one-dimensional (1D) stochastic description of turbulent stirring and diffusion. The model explicitly distinguishes the effects of turbulent stirring, molecular diffusion and chemical reactions at all scales of the flow.

Considering a species mass fraction, Y, and a decomposition of the velocity as $u_i = \tilde{u}_i + (u_i')^{\mathrm{R}} + u_i''$, the large-scale convection and SFS processes are respectively characterized by the following equations:

$$\frac{Y^* - Y^n}{\Delta t_{\mathrm{LES}}} = -\left[\tilde{u}_i + (u_i')^{\mathrm{R}}\right]\frac{\partial Y^n}{\partial x_i}\,, \tag{3.39}$$

$$Y^{n+1} - Y^* = \int_t^{t+\Delta t_{\mathrm{LES}}}\frac{1}{\rho}\left[-\rho u_i''\frac{\partial Y^n}{\partial x_i} - \frac{\partial}{\partial x_i}(\rho Y^n V_i^n) + \dot{\omega}\right]\,\mathrm{d}t\,. \tag{3.40}$$

In the above expressions, $(u_i')^{\mathrm{R}}$ is the LES-resolved SFS velocity (which can be obtained from k_Δ), u_i'' is the unresolved SFS velocity, t_{LES} is the LES time step, and V_i is the species diffusion velocity. The superscripts n and $n+1$ indicate two consecutive discrete times, and Y^* is an intermediate state after the large-scale convection is completed. Equation 3.40 describes the LEM model as viewed on the LES space and time scales. The molecular diffusion and chemical reaction contribution to the small-scale transport are resolved on an embedded 1D domain for

each LES cell and the 1D domain is aligned with the direction of the maximum scalar gradient. Equation 3.40 is re-expressed in the 1D LEM domain as

$$\rho\frac{\partial Y}{\partial t} + F^{\text{stir}} + \frac{\partial}{\partial s}(\rho Y V) = \dot{\omega}\,, \tag{3.41}$$

where F^{stir} represents the effect of the SFS turbulence on the scalar field and s is the spatial coordinate along the LEM domain. The SFS scalar field is discretized in each LES cell by $N_{\text{LEM}} = 6Re_\Delta^{3/4}$ sub-cells, where Re_Δ is the SFS Reynolds number (based on $(u_i')^{\text{R}}$ and Δ). The LEM scalar fields are ensemble-averaged to obtain LES-resolved scalar values. SFS stirring, F^{stir}, is implemented using stochastic re-arrangement events called triplet maps [180]. Each triplet map represents the action of an isotropic turbulent eddy on the SFS scalar field. The eddy size, ℓ, is randomly selected from a distribution function [180]

$$f(\ell) = \frac{5\ell^{-8/3}}{3\left(\eta^{-5/3} - \Delta^{-5/3}\right)}\,, \tag{3.42}$$

in the range Δ to η (Kolmogorov scale). Stirring events occur at a specified frequency, Υ, which has the form [180]

$$\Upsilon = \frac{54}{5}\frac{\nu Re_\Delta}{C_{\text{D}}\Delta^3}\frac{\left[(\Delta/\eta)^{5/3} - 1\right]}{\left[1 - (\eta/\Delta)^{4/3}\right]}\,, \tag{3.43}$$

where $C_{\text{D}} = 15$ and ν is the kinematic viscosity. The stirring time intervals are determined by the following relation: $\Delta t_{\text{stir}} = 1/(\Upsilon\Delta)$ [72].

The LEM model has been successfully applied to scalar mixing [70, 185, 161], nonpremixed combustion [186, 70], and premixed combustion [72, 187, 188, 162], among other applications. However, the model has some limitations. The computational burden associated with the LEM is much higher as compared to other models. Molecular diffusion across LES cells is not included. Also, in premixed combustion the flame-turbulence interaction is influenced by the flame front curvature, a missing effect in the the 1D LEM. Additionally, the triplet map assumes that eddies of all sizes affect the flame in the same way, which means that viscous dissipation is not taken into account properly.

Probability Density Function Methods

Many statistical approaches to model turbulent reacting flows are based on the use of probability density function (PDF) methods. PDF schemes provide a closed form representation of chemical source terms [189, 190] and are applicable to different combustion regimes. For a comprehensive description of the PDF approach to turbulent reacting flows, the reader is referred to the paper by Pope [190]. The application of PDF methods to LES was first suggested by Givi [26], and

has subsequently been explored by Pope [191], Madnia & Givi [192], Gao & O'Brien [39], Cook & Riley [41, 193], Cook *et al.* [43], Jiménez *et al.* [194], Réveillon & Vervisch [195], Colucci *et al.* [44], Jaberi *et al.* [45], Pierce & Moin [47], and others. PDF approaches have been mostly applied to nonpremixed combustion, but they can also be applied to premixed combustion (see, e.g., Möller *et al.* [42]).

If one considers a reaction rate $\dot{\omega}(\mathbf{x}, t) = \dot{\omega}\left(\boldsymbol{\varphi}(\mathbf{x}, t)\right)$, with $\boldsymbol{\varphi} = [\varphi_1, \varphi_2, \ldots, \varphi_{N_\mathrm{s}}]$ being the array of scalars (species mass fractions and temperature) and N_s denoting the number of scalars, the joint subfilter (or filtered) PDF is given by [191]

$$P(\boldsymbol{\psi}; \mathbf{x}, t) = \int \varrho[\boldsymbol{\psi} - \boldsymbol{\varphi}(\mathbf{x}', t)] \mathfrak{G}(\mathbf{x}' - \mathbf{x}) \, \mathrm{d}\mathbf{x}', \tag{3.44}$$

$$\varrho[\boldsymbol{\psi} - \boldsymbol{\varphi}(\mathbf{x}', t)] = \delta[\boldsymbol{\psi} - \boldsymbol{\varphi}(\mathbf{x}', t)] = \prod_{\beta=1}^{N_\mathrm{s}} \delta[\psi_\beta - \varphi_\beta(\mathbf{x}', t)], \tag{3.45}$$

where $\boldsymbol{\psi}$ is the array of statistical random variables associated with $\boldsymbol{\varphi}$, $\varrho[\boldsymbol{\psi} - \boldsymbol{\varphi}(\mathbf{x}', t)]$ is the fine-grained density function [189, 190], δ is the Dirac delta function, and $\mathfrak{G}$ is the filter function. For variable density flows, it is convenient to introduce a density-weighted PDF. The filtered reaction term can be closed through the relation

$$\bar{\dot{\omega}}(\mathbf{x}, t) = \int \dot{\omega}(\boldsymbol{\psi}) P(\boldsymbol{\psi}; \mathbf{x}, t) \, \mathrm{d}\boldsymbol{\psi}. \tag{3.46}$$

The subfilter PDF can be determined by the solution of a transport equation [39, 195, 44, 45] or modelled assuming its shape [41, 196, 43, 194, 193, 47]. Monte Carlo simulation techniques are commonly used in the implementation of transported PDF methods. Thus, application of transported PDF methods in LES generally requires high computational costs and robust solution algorithms. Assumed PDF methods, on the other hand, offer an inexpensive alternative to transported PDF methods [40]. A beta distribution is the usual choice for presuming PDFs and has been widely utilized for the mixture fraction. Its validity for the mixture fraction has been investigated by several authors [41, 194, 197], concluding that the beta distribution provides a good estimate of the PDF. Nevertheless, it has been shown that the filtered PDF often deviates from the beta-function PDF [198]. Other shapes for the PDF have been assumed, for instance, a delta-function PDF [47] or a multidimensional normal distribution [42].

Conditional Moment Closure Technique

Conditional moment closure (CMC) modelling was first proposed by Klimenko [199] and Bilger [200] in a RANS context. In CMC, transport equations are derived for conditioned averages

of the reactive scalars. Unconditional quantities are recovered from conditional averages by using a presumed PDF approach. Although initially developed for application to nonpremixed combustion, CMC modelling has also been extended to premixed combustion [201, 202].

The CMC approach has been formulated for LES by Kim & Pitsch [49] and Navarro-Martinez et al. [50]. A variant of the conditional moment closure technique, called conditional source estimation (CSE), was proposed by Bushe & Steiner [48] for LES. In CSE, conditionally filtered scalars are obtained by inverting integral equations and chemical source terms are closed by using conditionally averaged scalar values and presumed PDFs. It has been applied to study various nonpremixed flames with success [203, 204, 205]. In a recent work, the CSE closure was further investigated to close reaction rates in turbulent premixed flames, showing promising results when compared to DNS [206].

Presumed Conditional Moment Approach

Another approach, named presumed conditional moment (PCM), was proposed by Vervisch et al. [207] for RANS and initially applied to nonpremixed combustion. PCM combines presumed probability density functions with conditional moments, and has been used in conjunction with flamelet-based tabulated chemistry. PCM was further developed as a SFS model for LES by Domingo et al. [51] and applied to the simulation of a ducted premixed flame. The PCM model, coupled with flame prolongation of intrinsic low-dimensional manifold (FPI) [208] tabulation, has recently been employed to simulate a lifted jet flame in a vitiated coflow [52] and a fuel-lean premixed turbulent swirl flow [209] obtaining good agreement with experimental results. The combined PCM-FPI approach seems to be promising to model both premixed and nonpremixed combustion regimes, incorporating complex chemistry at relatively low computational costs.

<div align="right">Chapter 4</div>

PCM-FPI and Artificially Thickened Flame Models

The preceding chapter provided an overview of the mathematical modelling used herein for describing premixed combustion along with a brief review of SFS modelling approaches commonly used for treating the filtered reaction rate. The details of the two modelling approaches that have been adopted for the description of physical and chemical processes that occur in a premixed turbulent flame in this thesis are now described in this chapter. The first approach involves the presumed conditional moment closure coupled with flame prolongation of intrinsic low-dimensional manifold chemistry tabulation and the second approach couples the thickened flame model with a power-law wrinkling model. Additionally, a brief description of the transported FSD model of Hawkes & Cant is given, as this model has also been considered in the comparisons of different SFS models.

4.1   PCM-FPI Approach

The presumed conditional moment (PCM) [207, 51] combined with the flame prolongation of intrinsic low-dimensional manifold (FPI) [208] chemistry tabulation technique, called PCM-FPI hereafter, is a closure approach that presumes probability density functions (PDF) for fluctuating subfilter-scale quantities and incorporates tabulated complex chemistry from simple prototype combustion problems. When turbulent premixed combustion is considered, look-up tables of filtered terms associated with chemistry are built from laminar premixed flamelets.

4.1.1   FPI (Flame Prolongation of ILDM)

The main objective of the FPI tabulation technique is to reduce the cost of performing reactive flow computations with large detailed chemical kinetic mechanisms, but still retain the accuracy of detailed results, by building databases of relevant quantities based on detailed simulations of simple flames. Here, premixed steady-state one-dimensional laminar flames provide the basis for the tabulation. FPI features strong similarities with the FGM (flamelet-generated manifold) [210] method, where a few control variables are used to tabulate chemistry. For a given equivalence ratio (or mixture fraction), relevant chemical parameters such as species mass fractions or reaction rates are then related to a single progress of reaction variable, Y_c. For instance, any property φ_j (species mass fractions or reaction rates) of a steady-state laminar premixed flame at equivalence ratio ϕ_0 may be expressed as a function of position normal to the flame front, x, as $\varphi_j = \varphi_j(\phi_0, x)$, which can then be mapped to the progress of reaction variable, Y_c-space, eliminating x. The resulting FPI table may then be written:

$$\varphi_j^{\text{FPI}}(\phi_0, Y_c) = \varphi_j(\phi_0, x). \tag{4.1}$$

The progress of reaction variable Y_c is determined such that it increases monotonically and there is a one-to-one correspondence between Y_c and φ_j. In general, the progress of reaction can be defined as a linear combination of species mass fractions. Fiorina *et al.* [211] have shown that for methane-air combustion an appropriate choice is $Y_c = Y_{\text{CO}_2} + Y_{\text{CO}}$. Using this definition, the variations of temperature and major species mass fractions as functions of Y_c for methane-air premixed flames at different equivalence ratios are displayed in Figure 4.1. It can be observed that there is a one-to-one correspondence between the mass fractions of CH_4, O_2, and CO_2, under lean, stoichiometric, and rich conditions. As for temperature, a similar observation can be made, except for $\phi = 1.25$ when temperature is reaching its equilibrium value.

4.1.2   PCM (Presumed Conditional Moment)

Employing a statistical approach, the Favre-filtered reaction rate for a species α can be calculated by integrating the laminar reaction rate, $\dot{\omega}_\alpha$, with the joint subfilter PDF, $\tilde{P}$, as follows:

$$\tilde{\dot{\omega}}_\alpha = \int_{T^*}\int_{Y_1^*}\ldots\int_{Y_N^*} \dot{\omega}_\alpha(T^*, Y_1^*, \ldots, Y_N^*)\tilde{P}(T^*, Y_1^*, \ldots, Y_N^*)\,\mathrm{d}Y_N^*\ldots\mathrm{d}Y_1^*\mathrm{d}T^*. \tag{4.2}$$

The above description can be simplified if the laminar reaction rate is assumed to be characterized by two parameters: the mixture fraction, Z, and the progress variable, c, as provided by the FPI tabulated chemistry. The mixture fraction characterizes mixing between fuel and oxidizer

(a) Temperature trajectories

(b) CH$_4$ trajectories

(c) O$_2$ trajectories
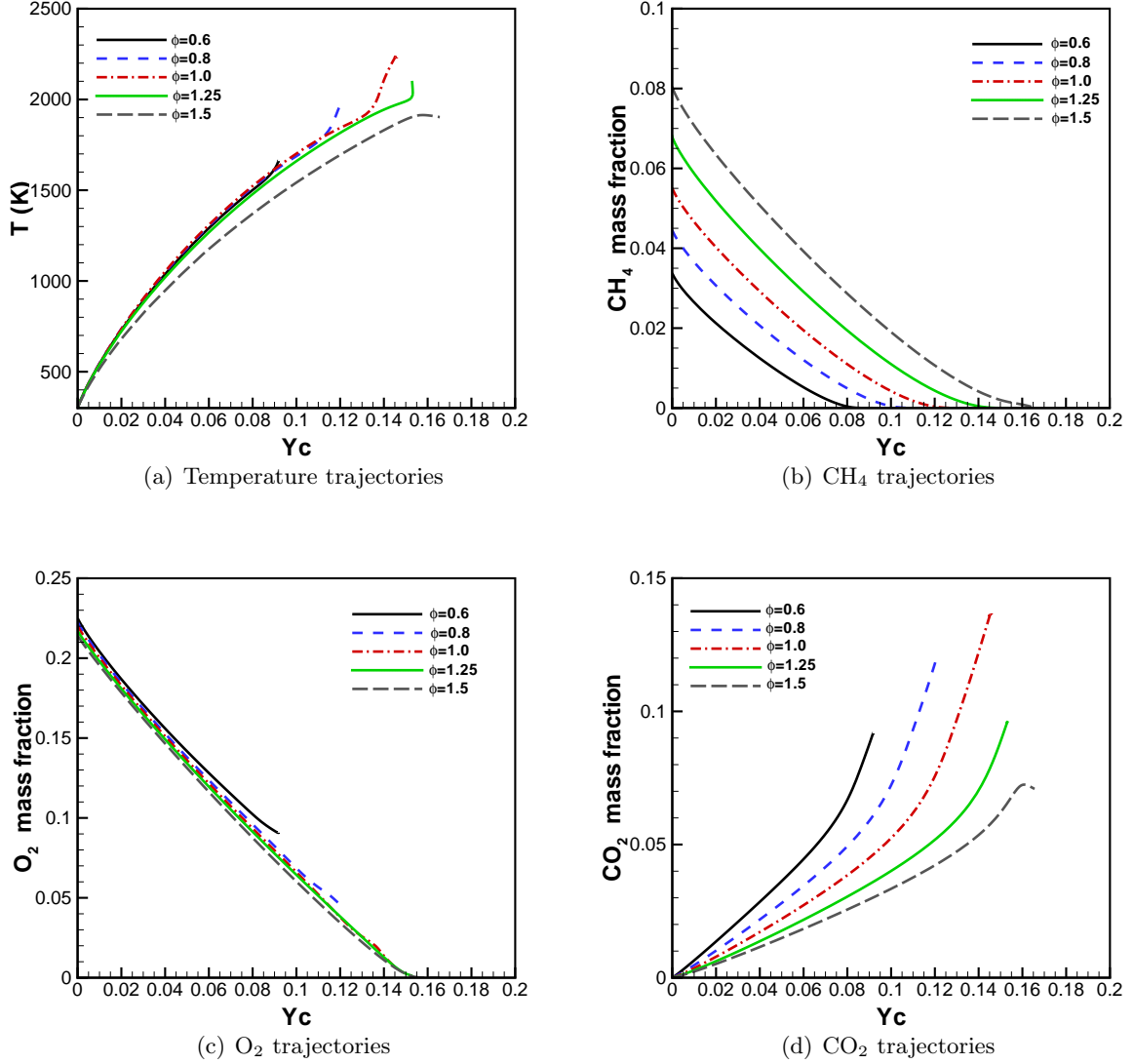
(d) CO$_2$ trajectories

Figure 4.1: Temperature and representative species trajectories in the progress of reaction space for $Y_c = Y_{CO_2} + Y_{CO}$, corresponding to lean, stoichiometric, and rich conditions.

(Z is related to the equivalence ratio, ϕ), whereas the progress variable quantifies the progress of reactions. Both variables take on values between zero and unity. The filtered reaction rate can then be re-expressed as

$$\tilde{\dot{\omega}}_\alpha = \int_0^1 \int_0^1 \dot{\omega}_\alpha(c^*, Z^*)\tilde{P}(c^*, Z^*)\, \mathrm{d}c^* \mathrm{d}Z^* . \tag{4.3}$$

On the other hand, the joint subfilter PDF can be also written as $\tilde{P}(c^*, Z^*) = \tilde{P}(c^*|Z^*)\tilde{P}(Z^*)$. By analyzing DNS data, Vervisch [212] found that the conditional PDF displays a weak dependence on the mixture fraction, suggesting that $\tilde{P}(c^*|Z^*) \approx \tilde{P}(c^*)$. The finding was further supported

by extracting the conditional PDF from the Sandia-D flame database [213], as shown by Vervisch *et al.* [207]. By assuming, $\tilde{P}(c^*|Z^*) = \tilde{P}(c^*)$, the filtered reaction rate can then be evaluated using

$$\tilde{\dot{\omega}}_\alpha = \int_0^1 \int_0^1 \dot{\omega}_\alpha(c^*, Z^*)\tilde{P}(c^*)\tilde{P}(Z^*)\,\mathrm{d}c^*\mathrm{d}Z^*\,. \tag{4.4}$$

It follows that the filtered conditional moment $\overline{(\dot{\omega}|Z^*)}$ is given by

$$\overline{(\dot{\omega}|Z^*)} = \int_0^1 \dot{\omega}_\alpha(c^*, Z^*)\tilde{P}(c^*)\mathrm{d}c^*\,. \tag{4.5}$$

In this sense, the PCM approach can be viewed as a simplified version of the CMC closure in that conditional moments are also employed, but instead of solving transport equations for the moments, they are presumed.

4.1.3 PCM-FPI for Premixed Combustion

In the context of LES of premixed combustion and FPI, any filtered quantity can be obtained via

$$\tilde{\varphi}_j = \int_0^1 \varphi_j^{\mathrm{FPI}}\tilde{P}(c^*)\,\mathrm{d}c^*\,. \tag{4.6}$$

Following Domingo *et al.* [52] and Galpin *et al.* [209], the subfilter PDF of c is assumed to have a beta distribution. The filtered PDF $\tilde{P}(c^*)$ is then calculated from the progress variable, $\tilde{c}$, and its SFS variance, $c_\mathrm{v} = \widetilde{cc} - \tilde{c}\tilde{c}$. The PDF has the form

$$\tilde{P}(c^*) = \frac{c^{*a-1}(1 - c^*)^{b-1}}{\int_0^1 c\star^{a-1}(1 - c\star)^{b-1}\mathrm{d}c\star}\,, \tag{4.7}$$

and the parameters a and b are determined with the following expressions:

$$a = \tilde{c}\left(\frac{\tilde{c}(1 - \tilde{c})}{c_\mathrm{v}} - 1\right) \geq 0, \qquad b = a\left(\frac{1}{\tilde{c}} - 1\right) \geq 0\,. \tag{4.8}$$

The two variables, $\tilde{c}$ and c_v, are linked to the progress of reaction $\tilde{Y}_\mathrm{c}$ and its SFS variance, Y_{c_v}. The filtered progress variable is defined as the filtered progress of reaction normalized by its value at equilibrium:

$$\tilde{c} = \frac{\tilde{Y}_\mathrm{c}}{Y_\mathrm{c}^{\mathrm{Eq}}(\phi_0)}\,. \tag{4.9}$$

The variance of c may be obtained from $\tilde{Y}_c$, $Y_c^{\mathrm{Eq}}(\phi_0)$ and the variance of the progress of reaction, $Y_{c_v} = \widetilde{Y_c Y_c} - \tilde{Y}_c \tilde{Y}_c$. The expression for c_v is

$$c_v = \frac{Y_{c_v}}{Y_c^{\mathrm{Eq}^2}(\phi_0)} . \tag{4.10}$$

It is worth mentioning that c_v can be normalized by its theoretical maximum leading to the introduction of the so called segregation factor or unmixedness, S_c, which takes on values ranging from zero to unity, and mathematically is expressed as

$$S_c = \frac{c_v}{\tilde{c}(1 - \tilde{c})} . \tag{4.11}$$

To determine Y_c and Y_{c_v}, modelled balance equations are utilized [51, 52, 209]. The derivation of both transport equations and relevant aspects related to their modelling are presented in Appendix B. The modelled transport equation for $\tilde{Y}_c$ has the form

$$\frac{\partial(\bar{\rho}\tilde{Y}_c)}{\partial t} + \frac{\partial(\bar{\rho}\tilde{u}_i\tilde{Y}_c)}{\partial x_i} = \frac{\partial}{\partial x_i}\left[\bar{\rho}(\check{\mathcal{D}}_{Y_c} + \mathcal{D}_t)\frac{\partial\tilde{Y}_c}{\partial x_i}\right] + \bar{\bar{\omega}}_{Y_c} , \tag{4.12}$$

where $\bar{\bar{\omega}}_{Y_c}$ is a source term due to chemistry, $\check{\mathcal{D}}_{Y_c}$ is the diffusion coefficient associated with Y_c, and $\mathcal{D}_t$ is the turbulent diffusion coefficient used to model SFS scalar transport. Both diffusion coefficients are obtained by prescribing the corresponding Schmidt numbers. The modelled transport equation for Y_{c_v} is given by [52]

$$\frac{\partial(\bar{\rho}Y_{c_v})}{\partial t} + \frac{\partial(\bar{\rho}\tilde{u}_i Y_{c_v})}{\partial x_i} = \frac{\partial}{\partial x_i}\left[\bar{\rho}(\check{\mathcal{D}}_{Y_c} + \mathcal{D}_t)\frac{\partial Y_{c_v}}{\partial x_i}\right] + 2\bar{\rho}(\check{\mathcal{D}}_{Y_c} + \mathcal{D}_t)\frac{\partial\tilde{Y}_c}{\partial x_i}\frac{\partial\tilde{Y}_c}{\partial x_i}$$
$$-2\overline{\rho\mathcal{D}_{Y_c}\frac{\partial Y_c}{\partial x_i}\frac{\partial Y_c}{\partial x_i}} + 2(\overline{Y_c\dot{\omega}_{Y_c}} - \tilde{Y}_c\bar{\bar{\omega}}_{Y_c}) . \tag{4.13}$$

In Equation 4.13 there is a term deserving particular attention, it is the scalar dissipation rate of Y_c, $\bar{\chi}_{Y_c} = 2\overline{\rho\check{\mathcal{D}}_{Y_c}\frac{\partial Y_c}{\partial x_i}\frac{\partial Y_c}{\partial x_i}}$, which may be decomposed into resolved and unresolved parts as follows [51]:

$$\overline{\rho\check{\mathcal{D}}_{Y_c}\frac{\partial Y_c}{\partial x_i}\frac{\partial Y_c}{\partial x_i}} = \bar{\rho}\check{\mathcal{D}}_{Y_c}\frac{\partial\tilde{Y}_c}{\partial x_i}\frac{\partial\tilde{Y}_c}{\partial x_i} + \bar{s}_{\chi_{Y_c}} . \tag{4.14}$$

The SFS component, $\bar{s}_{\chi_{Y_c}}$, requires modelling. This term can be closed using a linear relaxation hypothesis [51]

$$\bar{s}_{\chi_{Y_c}} = \frac{C_{\mathrm{D}}\bar{\rho}\mathcal{D}_t Y_{c_v}}{\Delta^2} , \tag{4.15}$$

with $C_{\mathrm{D}} \approx 1$, or using the combined linear relaxation hypothesis and bimodal limit closure proposed by Domingo *et al.* [52]. The latter takes into account that Y_c is a reactive scalar whose

gradient is influenced by chemistry. As this closure has been employed in this research, a brief description of the model is presented below.

By considering the balance equation for the product $c(1-c)$ [24] in the bimodal limit, $S_c \to 1$, it can be shown that

$$2\rho \mathcal{D}_c \frac{\partial c}{\partial x_i} \frac{\partial c}{\partial x_i} = 2c\dot{\omega}_c - \dot{\omega}_c. \tag{4.16}$$

By using $Y_c = cY_c^{Eq}$, $\mathcal{D}_{Y_c} = \mathcal{D}_c$, and filtering the above expression, one can arrive at

$$\bar{s}_{\chi Y_c} = -\bar{\rho} \check{\mathcal{D}}_{Y_c} \frac{\partial \tilde{Y}_c}{\partial x_i} \frac{\partial \tilde{Y}_c}{\partial x_i} + \overline{Y_c \dot{\omega}_{Y_c}} - \frac{\overline{Y_c^{Eq} \dot{\omega}_{Y_c}}}{2}. \tag{4.17}$$

Domingo *et al.* [52] combined Equations 4.15 and 4.17 to propose the following closure expression:

$$\bar{s}_{\chi Y_c} = (1 - S_c)\bar{\rho}\frac{\mathcal{D}_t}{\Delta^2}Y_{c_v} + S_c \left(-\bar{\rho}\check{\mathcal{D}}_{Y_c} \frac{\partial \tilde{Y}_c}{\partial x_i} \frac{\partial \tilde{Y}_c}{\partial x_i} + \overline{Y_c \dot{\omega}_{Y_c}} - \frac{\overline{Y_c^{Eq} \dot{\omega}_{Y_c}}}{2} \right). \tag{4.18}$$

It is important to remark that a reaction rate can be written as $\dot{\omega} = \rho \dot{\omega}^*$, therefore $\overline{\dot{\omega}} = \bar{\rho}\tilde{\dot{\omega}}^*$, $\overline{Y_c \dot{\omega}_{Y_c}} = \bar{\rho}\widetilde{Y_c \dot{\omega}_{Y_c}^*}$, and $\overline{Y_c^{Eq}\dot{\omega}_{Y_c}} = \bar{\rho}\widetilde{Y_c^{Eq}\dot{\omega}_{Y_c}^*}$. The terms $\tilde{\omega}_{Y_c}^*$ and $\widetilde{Y_c\dot{\omega}_{Y_c}^*}$ are included in the tabulated database, whereas the term $Y_c^{Eq}\dot{\omega}_{Y_c}^*$ is computed using $\widetilde{Y_c^{Eq}\dot{\omega}_{Y_c}^*} = Y_c^{Eq}\tilde{\omega}_{Y_c}^*$, since Y_c^{Eq} is constant for a premixed regime. With the introduction of the segregation factor, the PDF of c can be parametrized in terms of $\tilde{c}$ and S_c. Thus, a look-up table of filtered quantities $\tilde{\varphi}_j^{PCM}(\phi_0, \tilde{c}, S_c)$, can be pre-generated for use in subsequent LES calculations.

4.1.4 Tabulation of Chemistry

Species Selection

The premixed flamelet solutions are obtained with detailed chemical kinetics, which generally involves a large number of species and reactions. To tabulate chemistry, a reduced number of species, N_{FPI}, is considered for inclusion in the look-up tables. This can provide even greater computational efficiency and aids in reducing the table size, thereby reducing memory requirements for the tabulation. The species can be selected based on their contribution to the flamelet mass, energy, and heat release budgets [214]. A mass criterion is given by

$$\mathcal{I}_{m_\alpha} = \int_0^1 Y_\alpha \, dc, \tag{4.19}$$

where $\mathcal{I}_{m_\alpha}$ is the relative mass of species α in the premixed flamelet. Similarly, the energy criterion is expressed as

$$\mathcal{I}_{E_\alpha} = \frac{\int_0^1 Y_\alpha h_\alpha \, dc}{\sum_{\beta=1}^{N_T} \int_0^1 Y_\beta h_\beta \, dc} \,, \tag{4.20}$$

where $\mathcal{I}_{E_\alpha}$ is the relative energy of species, α, in the premixed flamelet and N_T is the total number of species present in the premixed flamelet. The heat release criterion is given by

$$\mathcal{I}_{HR_\alpha} = \frac{\int_0^1 \dot\omega_\alpha \Delta h_{f_\alpha}^0 \, dc}{\sum_{\beta=1}^{N_T} \int_0^1 \dot\omega_\beta \Delta h_{f_\beta}^0 \, dc} \,, \tag{4.21}$$

where $\mathcal{I}_{HR_\alpha}$ is the relative heat release of species α in the premixed flamelet. The species selected for tabulation are chosen such that they represent nearly 99% of the total mass and energy of the premixed flamelet. Application of the above criteria to select species for tabulation of methane-air and H_2-enriched methane-air flames will follow in subsections 4.1.5 and 4.1.6. The premixed flamelet solutions used in all of the present work, including the hydrogen enriched flames, have been computed using the Cantera package [215] in combination with the GRI-3.0 detailed chemical kinetic mechanism [107] containing 53 species and 325 reaction steps.

Mass Conservation

Since only a set of N_{FPI} ($N_{FPI} < N_T$) representative species is selected, the sum of their mass fraction differs from unity. To enforce conservation of mass, atom balances are carried out to adjust the mass fractions and/or reaction rates of certain species. Considering the oxidation of a hydrocarbon, which involves the elements C, H, O, and N, the chemical formula of a species α has the form $C_{p_\alpha} H_{q_\alpha} O_{r_\alpha} N_{s_\alpha}$, where $p, q, r,$ and s denote the subscripts of the four elements in the chemical symbol of this species. As there are four chemical elements, the mass fractions or reaction rates of four species can be determined by applying atom balances. The atom conservation of element C is expressed as:

$$\sum_{\alpha=1}^{N_{FPI}} p_\alpha \frac{Y_{C_{p_\alpha} H_{q_\alpha} O_{r_\alpha} N_{s_\alpha}}}{\mathcal{M}_{C_{p_\alpha} H_{q_\alpha} O_{r_\alpha} N_{s_\alpha}}} = \sum_{\alpha=1}^{N_{FPI}} p_\alpha \frac{Y_{C_{p_\alpha} H_{q_\alpha} O_{r_\alpha} N_{s_\alpha}}}{\mathcal{M}_{C_{p_\alpha} H_{q_\alpha} O_{r_\alpha} N_{s_\alpha}}}\bigg|_{c=0} \,, \tag{4.22}$$

where $\mathcal{M}$ is the molecular mass of the species α. Upon differentiation of the above equation with respect to time, one obtains:

$$\sum_{\alpha=1}^{N_{FPI}} p_\alpha \frac{\dot\omega^*_{C_{p_\alpha} H_{q_\alpha} O_{r_\alpha} N_{s_\alpha}}}{\mathcal{M}_{C_{p_\alpha} H_{q_\alpha} O_{r_\alpha} N_{s_\alpha}}} = 0 \,. \tag{4.23}$$

It follows that for element H

$$\sum_{\alpha=1}^{N_{\mathrm{FPI}}} q_\alpha \frac{Y_{\mathrm{C}_{p_\alpha}\mathrm{H}_{q_\alpha}\mathrm{O}_{r_\alpha}\mathrm{N}_{s_\alpha}}}{\mathcal{M}_{\mathrm{C}_{p_\alpha}\mathrm{H}_{q_\alpha}\mathrm{O}_{r_\alpha}\mathrm{N}_{s_\alpha}}} = \sum_{\alpha=1}^{N_{\mathrm{FPI}}} q_\alpha \left.\frac{Y_{\mathrm{C}_{p_\alpha}\mathrm{H}_{q_\alpha}\mathrm{O}_{r_\alpha}\mathrm{N}_{s_\alpha}}}{\mathcal{M}_{\mathrm{C}_{p_\alpha}\mathrm{H}_{q_\alpha}\mathrm{O}_{r_\alpha}\mathrm{N}_{s_\alpha}}}\right|_{c=0} , \tag{4.24}$$

$$\sum_{\alpha=1}^{N_{\mathrm{FPI}}} q_\alpha \frac{\dot{\omega}^*_{\mathrm{C}_{p_\alpha}\mathrm{H}_{q_\alpha}\mathrm{O}_{r_\alpha}\mathrm{N}_{s_\alpha}}}{\mathcal{M}_{\mathrm{C}_{p_\alpha}\mathrm{H}_{q_\alpha}\mathrm{O}_{r_\alpha}\mathrm{N}_{s_\alpha}}} = 0 , \tag{4.25}$$

for element O

$$\sum_{\alpha=1}^{N_{\mathrm{FPI}}} r_\alpha \frac{Y_{\mathrm{C}_{p_\alpha}\mathrm{H}_{q_\alpha}\mathrm{O}_{r_\alpha}\mathrm{N}_{s_\alpha}}}{\mathcal{M}_{\mathrm{C}_{p_\alpha}\mathrm{H}_{q_\alpha}\mathrm{O}_{r_\alpha}\mathrm{N}_{s_\alpha}}} = \sum_{\alpha=1}^{N_{\mathrm{FPI}}} r_\alpha \left.\frac{Y_{\mathrm{C}_{p_\alpha}\mathrm{H}_{q_\alpha}\mathrm{O}_{r_\alpha}\mathrm{N}_{s_\alpha}}}{\mathcal{M}_{\mathrm{C}_{p_\alpha}\mathrm{H}_{q_\alpha}\mathrm{O}_{r_\alpha}\mathrm{N}_{s_\alpha}}}\right|_{c=0} , \tag{4.26}$$

$$\sum_{\alpha=1}^{N_{\mathrm{FPI}}} r_\alpha \frac{\dot{\omega}^*_{\mathrm{C}_{p_\alpha}\mathrm{H}_{q_\alpha}\mathrm{O}_{r_\alpha}\mathrm{N}_{s_\alpha}}}{\mathcal{M}_{\mathrm{C}_{p_\alpha}\mathrm{H}_{q_\alpha}\mathrm{O}_{r_\alpha}\mathrm{N}_{s_\alpha}}} = 0 , \tag{4.27}$$

and for element N

$$\sum_{\alpha=1}^{N_{\mathrm{FPI}}} s_\alpha \frac{Y_{\mathrm{C}_{p_\alpha}\mathrm{H}_{q_\alpha}\mathrm{O}_{r_\alpha}\mathrm{N}_{s_\alpha}}}{\mathcal{M}_{\mathrm{C}_{p_\alpha}\mathrm{H}_{q_\alpha}\mathrm{O}_{r_\alpha}\mathrm{N}_{s_\alpha}}} = \sum_{\alpha=1}^{N_{\mathrm{FPI}}} s_\alpha \left.\frac{Y_{\mathrm{C}_{p_\alpha}\mathrm{H}_{q_\alpha}\mathrm{O}_{r_\alpha}\mathrm{N}_{s_\alpha}}}{\mathcal{M}_{\mathrm{C}_{p_\alpha}\mathrm{H}_{q_\alpha}\mathrm{O}_{r_\alpha}\mathrm{N}_{s_\alpha}}}\right|_{c=0} , \tag{4.28}$$

$$\sum_{\alpha=1}^{N_{\mathrm{FPI}}} s_\alpha \frac{\dot{\omega}^*_{\mathrm{C}_{p_\alpha}\mathrm{H}_{q_\alpha}\mathrm{O}_{r_\alpha}\mathrm{N}_{s_\alpha}}}{\mathcal{M}_{\mathrm{C}_{p_\alpha}\mathrm{H}_{q_\alpha}\mathrm{O}_{r_\alpha}\mathrm{N}_{s_\alpha}}} = 0 . \tag{4.29}$$

To illustrate the application of atom conservation, consider the set of species CH_4, O_2, N_2, H_2O, CO_2, CO, H_2, H, OH, and C_2H_2, where the mass fractions and/or reactions rates of C_2H_2, O_2, and H_2 are to be computed using atom balances of the elements C, O, and H, respectively. For C_2H_2, one obtains

$$2\frac{Y_{\mathrm{C_2H_2}}}{\mathcal{M}_{\mathrm{C_2H_2}}} = \left.\frac{Y_{\mathrm{CH_4}}}{\mathcal{M}_{\mathrm{CH_4}}}\right|_{c=0} - \left[\frac{Y_{\mathrm{CH_4}}}{\mathcal{M}_{\mathrm{CH_4}}} + \frac{Y_{\mathrm{CO_2}}}{\mathcal{M}_{\mathrm{CO_2}}} + \frac{Y_{\mathrm{CO}}}{\mathcal{M}_{\mathrm{CO}}}\right] , \tag{4.30}$$

$$2\frac{\dot{\omega}^*_{\mathrm{C_2H_2}}}{\mathcal{M}_{\mathrm{C_2H_2}}} = -\left[\frac{\dot{\omega}^*_{\mathrm{CH_4}}}{\mathcal{M}_{\mathrm{CH_4}}} + \frac{\dot{\omega}^*_{\mathrm{CO_2}}}{\mathcal{M}_{\mathrm{CO_2}}} + \frac{\dot{\omega}^*_{\mathrm{CO}}}{\mathcal{M}_{\mathrm{CO}}}\right] . \tag{4.31}$$

It follows that for O_2

$$2\frac{Y_{\mathrm{O_2}}}{\mathcal{M}_{\mathrm{O_2}}} = 2\left.\frac{Y_{\mathrm{O_2}}}{\mathcal{M}_{\mathrm{O_2}}}\right|_{c=0} - \left[2\frac{Y_{\mathrm{CO_2}}}{\mathcal{M}_{\mathrm{CO_2}}} + \frac{Y_{\mathrm{CO}}}{\mathcal{M}_{\mathrm{CO}}} + \frac{Y_{\mathrm{H_2O}}}{\mathcal{M}_{\mathrm{H_2O}}}\right] , \tag{4.32}$$

$$2\frac{\dot{\omega}^*_{\mathrm{O_2}}}{\mathcal{M}_{\mathrm{O_2}}} = -\left[2\frac{\dot{\omega}^*_{\mathrm{CO_2}}}{\mathcal{M}_{\mathrm{CO_2}}} + \frac{\dot{\omega}^*_{\mathrm{CO}}}{\mathcal{M}_{\mathrm{CO}}} + \frac{\dot{\omega}^*_{\mathrm{H_2O}}}{\mathcal{M}_{\mathrm{H_2O}}}\right] , \tag{4.33}$$

and for H_2

$$2\frac{Y_{H_2}}{\mathcal{M}_{H_2}} \quad = \quad 4\frac{Y_{CH_4}}{\mathcal{M}_{CH_4}}\bigg|_{c=0} - \left[4\frac{Y_{CH_4}}{\mathcal{M}_{CH_4}} + 2\frac{Y_{H_2O}}{\mathcal{M}_{H_2O}} + 2\frac{Y_{C_2H_2}}{\mathcal{M}_{C_2H_2}}\right], \tag{4.34}$$

$$2\frac{\dot{\omega}^*_{H_2}}{\mathcal{M}_{H_2}} \quad = \quad -\left[4\frac{\dot{\omega}^*_{CH_4}}{\mathcal{M}_{CH_4}} + 2\frac{\dot{\omega}^*_{H_2O}}{\mathcal{M}_{H_2O}} + 2\frac{\dot{\omega}^*_{C_2H_2}}{\mathcal{M}_{C_2H_2}}\right]. \tag{4.35}$$

4.1.5 Tabulation for Methane-Air Flames

First, an appropriate progress of reaction variable should be defined. Following Fiorina *et al.* [211], a suitable progress of reaction variable for the prediction of major species in methane-air flames is given by

$$Y_c = Y_{CO_2} + Y_{CO}. \tag{4.36}$$

To generate look-up tables, a database of 1D premixed methane-air flamelets was built employing Cantera and the GRI-Mech 3.0 mechanism. The database consists of 64 steady-state solutions for equivalence ratios in the range 0.4–2.0, at atmospheric pressure and a fresh gas mixture temperature of 300 K. These solutions were further postprocessed to determine the mass, energy, and heat release budgets, which were utilized to select the most representative species to be included in the look-up table. Figure 4.2 displays the relative contributions of species accounting for nearly 99.9% of total mass, energy, and heat release at equivalence ratios $\phi = 0.6$, $\phi = 0.8$, $\phi = 1.0$, and $\phi = 1.25$. Accordingly, the following 10 species were selected: CH_4, O_2, N_2, H_2O, CO_2,CO, H_2, H, OH, and C_2H_2. Note that Galpin *et al.* [209] have employed the same set of species previously. Although C_2H_2 does not appear in Figure 4.2, it was added to the set of selected species to absorb mass inconsistencies associated with carbon-containing species. Since there are four different chemical elements in the set of selected species, the mass fractions (or reaction rates) of six species can be tabulated from the Cantera solutions and the remaining four can be evaluated using atom balances, as previously discussed above. Of the 10 selected species, C_2H_2, O_2, and H_2 were computed via atom balances of the elements C, O, and H, respectively. Regarding element N, there is no need to apply atom balances since only N_2 contains it in the set of selected species.

4.1.6 Tabulation for H_2-Enriched Methane-Air Flames

As it was mentioned above, for a reduced number of 10 species the mass fraction of H_2 was determined via the atom-balance of element H. To improve the prediction of H_2, more species containing H need to be included in the set of tabulated species. Also, in the reduced set of 10 species, NO was not included. To determine an appropriate progress of reaction variable
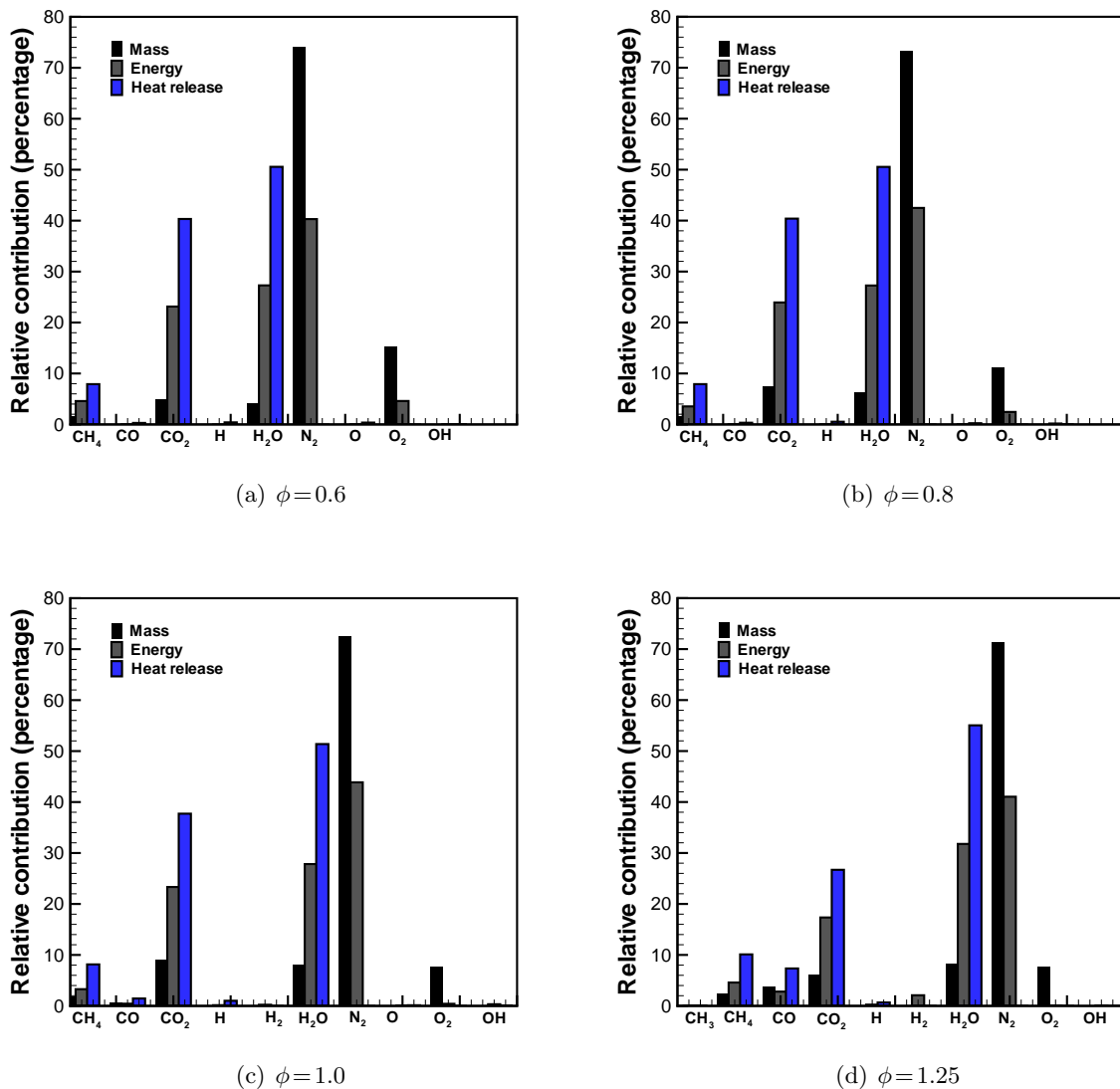
Figure 4.2: Relative mass, energy and heat release contributions of the most representative species in methane-air premixed flamelets at equivalence ratios $\phi{=}0.6$, $\phi{=}0.8$, $\phi{=}1.0$, and $\phi{=}1.25$.

and the species needed to properly account for H_2 and NO with FPI tabulated chemistry, it is required to analyse 1D premixed flamelets of H_2-enriched methane-air flames for different levels of H_2 addition at different equivalence ratios.

For a H_2-CH_4-air mixture, the equivalence ratio can be defined as

$$\phi = \frac{(n_{H_2}\mathcal{M}_{H_2} + n_{CH_4}\mathcal{M}_{CH_4})/(n_{O_2}\mathcal{M}_{O_2})}{[(n_{H_2}\mathcal{M}_{H_2} + n_{CH_4}\mathcal{M}_{CH_4})/(n_{O_2}\mathcal{M}_{O_2})]_{st}} , \tag{4.37}$$

where n and $\mathcal{M}$ are the species mole number and molecular mass, respectively. The subscript

st indicates that quantities are evaluated under stoichiometric conditions. A global combustion reaction for the H_2-CH_4-air mixture can then be expressed as

$$\varkappa H_2 + (1 - \varkappa)CH_4 + \frac{1}{\phi}\left(2 - \frac{3}{2}\varkappa\right)(O_2 + 3.76N_2) \rightarrow (1 - \varkappa)CO_2 + (2 - \varkappa)H_2O$$
$$+ \left(\frac{1}{\phi} - 1\right)\left(2 - \frac{3}{2}\varkappa\right)(O_2 + 3.76N_2) + 3.76\left(2 - \frac{3}{2}\varkappa\right)N_2, \quad (4.38)$$
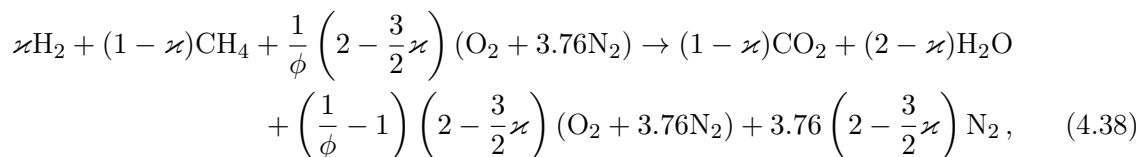
where $\varkappa$ is the mole fraction of H_2 in the blended fuel, given by

$$\varkappa = \frac{n_{H_2}}{n_{H_2} + n_{CH_4}}. \quad (4.39)$$

A database of 1D H_2-enriched methane-air premixed flamelets was first generated using Cantera with detailed chemistry for hydrogen-methane combustion provided by GRI-Mech 3.0. Validation of GRI-based mechanisms for hydrogen-methane-air blends has been carried out elsewhere [15, 216, 98, 18]. In particular, GRI-Mech 3.0 was used previously in References [15, 216, 98] to obtain good predictions of laminar flame speeds, profiles of major species, NO_x levels, and extinction strain rates in agreement with experimental values. More recently, Di Sarli & Di Benedetto [217] further validated GRI-Mech 3.0 against experimental data for hydrogen-methane-air blends and identified three regimes of laminar burning velocity in terms of the mole fraction of H_2 in the fuel: (i) methane-dominated combustion ($0 < \varkappa < 0.5$): transition regime ($0.5 \leq \varkappa \leq 0.9$); and (iii) methane-inhibited hydrogen combustion ($0.9 < \varkappa < 1$). The generated database was confined to the methane-dominated regime and includes different levels of enrichment up to a 40% mole fraction of H_2 in the blended fuel, with increments of 5%. The equivalence ratio was varied from values near the lean-flammability limit up to two. The resulting database contains 583 flamelets for atmospheric conditions.

Figure 4.3 shows the influence of H_2 addition on the burnt gas temperature, mass fraction of species CO_2, CO and NO, and laminar flame speed as a function of the global equivalence ratio. Figures 4.3(b) and 4.3(c) depict a decrease in CO_2 and CO emissions as the level of H_2 is increased in the blended fuel. The decrease is more pronounced for CO_2. On the other hand, Figure 4.3(d) shows that NO emissions increase slightly with H_2 addition and correlate with an increase in the burnt gas temperature, due to the thermal production of NO. Nevertheless, a drastic reduction of CO and NO is achieved when the equivalence ratio goes down. As the level of H_2 is increased in the enriched fuel, the flame speed increases (Figure 4.3(e)) and the flame becomes more resistant to quenching, which allows for leaner combustion.

It should be noted that errors in the prediction of NO mass fraction can be introduced when employing a progress variable defined in terms of major species only [218, 203, 219]. Minor
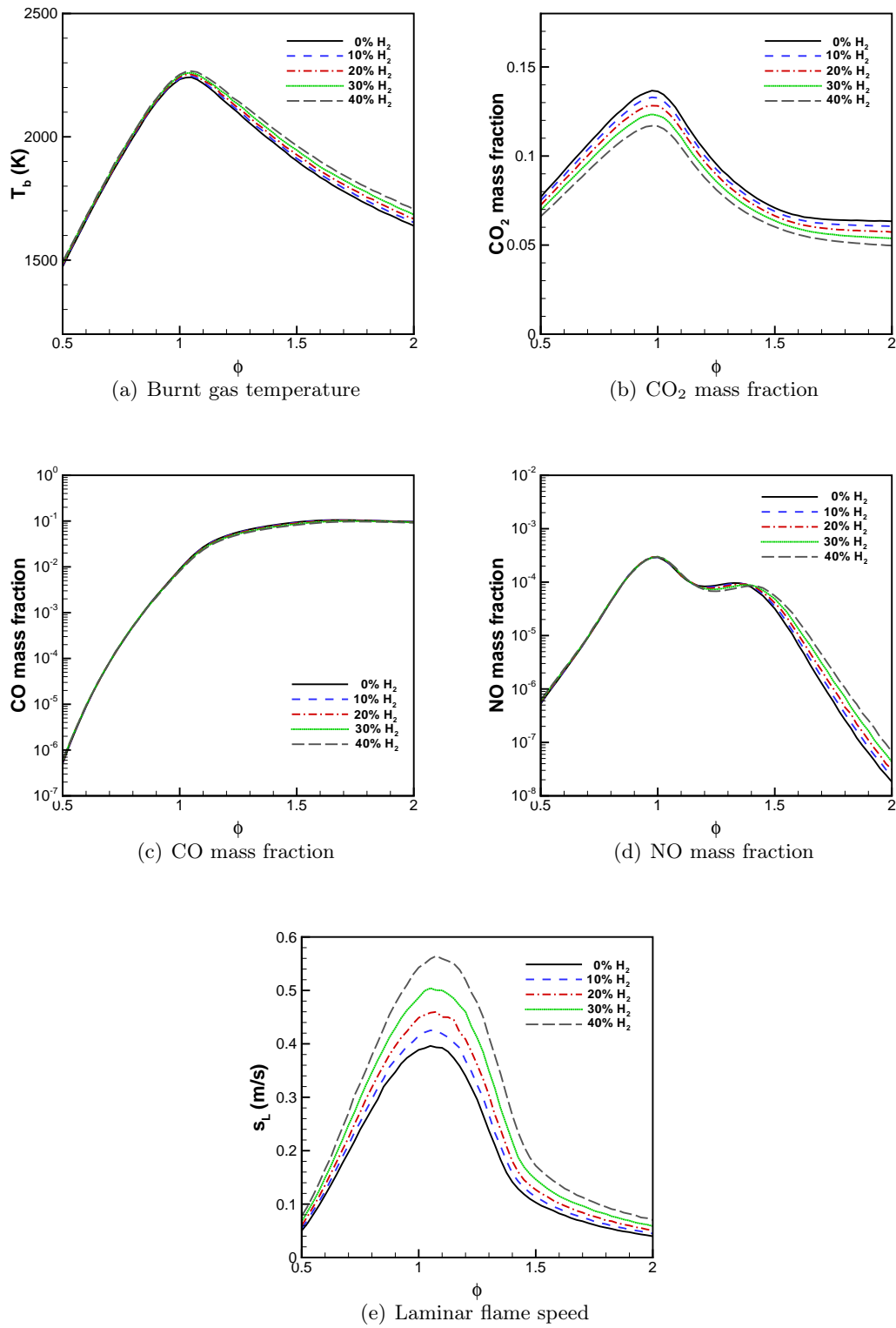
Figure 4.3: Influence of H_2 addition on the burnt gas temperature, mass fractions of species CO_2, CO, and NO, and laminar flame speed. 1D steady-state laminar premixed flame solutions obtained using Cantera.

species, such as NO, have characteristic time scales that differ from those of major species [220, 221, 222]. To account for the proper formation of NO via tabulated chemistry, the time scale associated with NO evolution must be included in the definition of the progress of reaction variable. Recently, Godel *et al.* [219] proposed a progress of reaction variable that takes into consideration NO_x. In their definition, Godel *et al.* added the mass fractions of NO_x species and N_2 to those of CO_2 and CO. In this thesis work, a modified progress of reaction variable is introduced for hydrogen-enriched methane combustion:

$$Y_c = Y_{CO_2} + Y_{NO} \,. \tag{4.40}$$

It was found that, with this definition, Y_c increases monotonically and accounts for slow chemistry associated with NO for lean and stoichiometric H_2-enriched methane-air premixed flamelets. Figures 4.4(a) and 4.4(b) display the NO mass fraction evolution in the progress variable space (normalized progress of reaction variable) corresponding to the proposed progress of reaction (Equation 4.40) and the progress of reaction variable used previously (Equation 4.36), for lean ($\phi = 0.8$) and stoichiometric H_2-enriched methane-air premixed flamelets. Magnified views of the regions where NO is reaching its equilibrium value are also displayed in Figures 4.4(c) and 4.4(d). The trajectories of NO mass fraction corresponding to Y_c based on major species (Equation 4.36) show larger slopes when NO is near its equilibrium value, which are almost vertical. This may lead to errors in the tabulated NO mass fraction. On the other hand, the NO trajectories corresponding to the new definition of Y_c show smoother and monotone transitions to the equilibrium values, as can be seen in Figures 4.4(c) and 4.4(d).

Temperature and representative species mass fractions trajectories in Y_c-space, associated with the proposed progress of reaction variable, are also depicted in Figure 4.5 for premixed flamelets enriched with H_2 by 20% (on a molar basis) and a range of equivalence ratios that includes fuel-rich conditions. It is apparent from the results shown in the figure that the novel Y_c is suitable for lean and stoichiometric conditions, ensuring a one-to-one correspondence between the representative mass fractions and Y_c. However, for the fuel-rich conditions (see Figures 4.5(c) and 4.5(e) for $\phi = 1.5$ and Figure 4.5(f) for $\phi = 1.25$ and $\phi = 1.5$), these desirable properties would no longer hold for the proposed progress of reaction variable. Nevertheless, since the scope of this research is limited to lean and stoichiometric flames, the newly defined Y_c (Equation 4.40) is adopted herein.

Another aspect of consideration is the selection of the number of species to be tabulated. Relative mass, energy, and heat release contributions of the most representative species in H_2-enriched methane-air premixed flamelets at equivalence ratios $\phi = 0.6$, $\phi = 0.8$, and $\phi = 1.25$ are shown
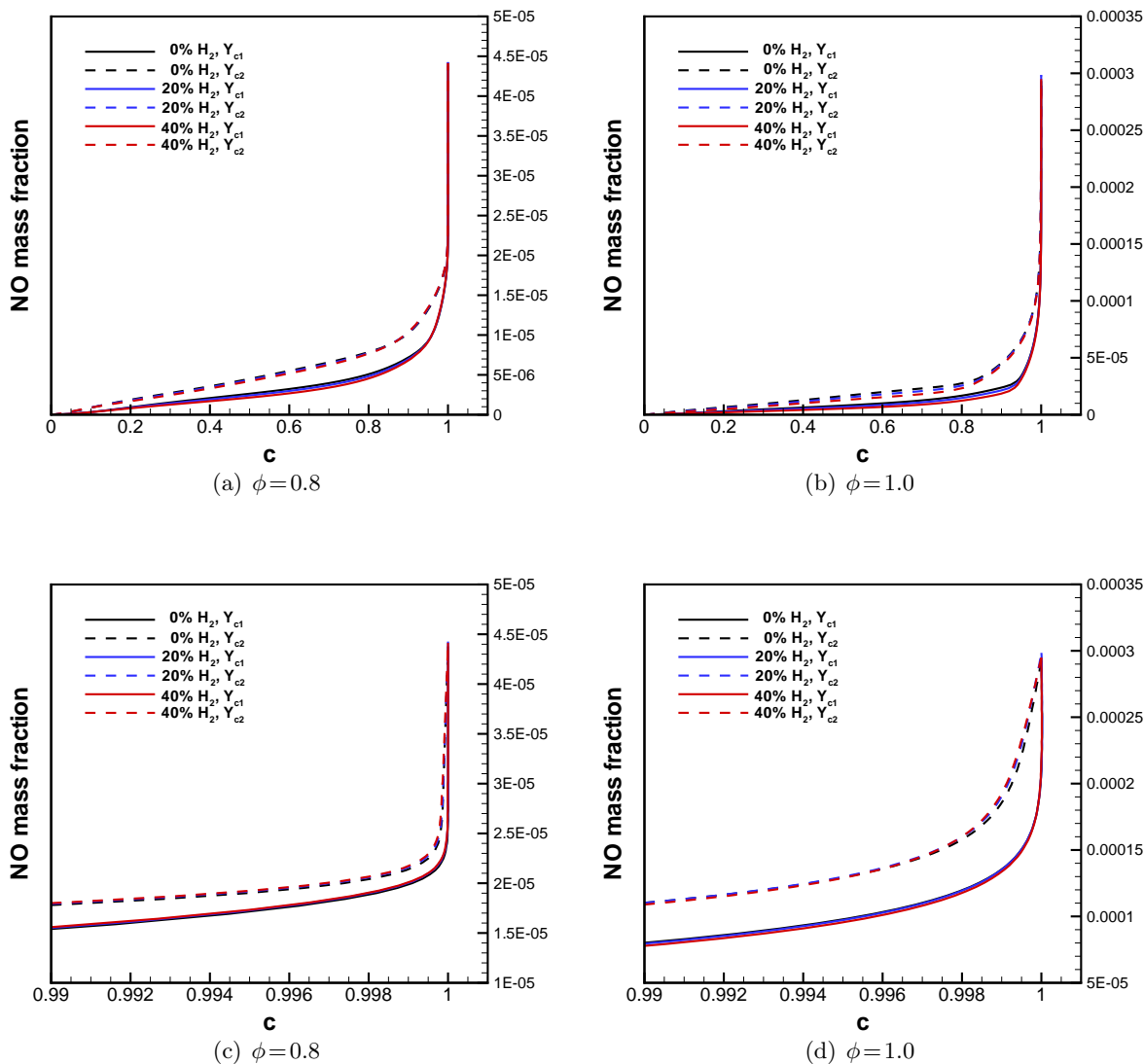
Figure 4.4: NO mass fraction evolution in the progress variable space for $Y_{c1} = Y_{CO_2} + Y_{CO}$ and $Y_{c2} = Y_{CO_2} + Y_{NO}$, corresponding to lean and stoichiometric conditions ($\phi = 0.8$ and $\phi = 1.0$) with different levels of H_2 (0%, 20%, and 40% on a molar basis) in the blended H_2-CH_4 fuel. 1D steady-state laminar premixed flames. Bottom: magnified views of the regions where NO is reaching its equilibrium value.

in Figure 4.6. Based on these contributions, the species CH_4, O_2, O, N_2, H_2O, CO_2, CO, H_2, H, and OH are selected. Since the prediction of NO is one of the objectives of this work, NO is also included in the set of selected species. Two more species are added to absorb mass inconsistencies when performing atom-balances for the elements C and H, namely C_2H_2 and NH_3. Consequently, the number of species to be included in a look-up table becomes 13. As there are four different chemical elements in the set of selected species, the mass fractions (or reaction rates) of nine species can be tabulated directly from the Cantera solutions and the

(a) Temperature trajectories

(b) CH$_4$ trajectories

(c) H$_2$ trajectories

(d) CO$_2$ trajectories

(e) CO trajectories
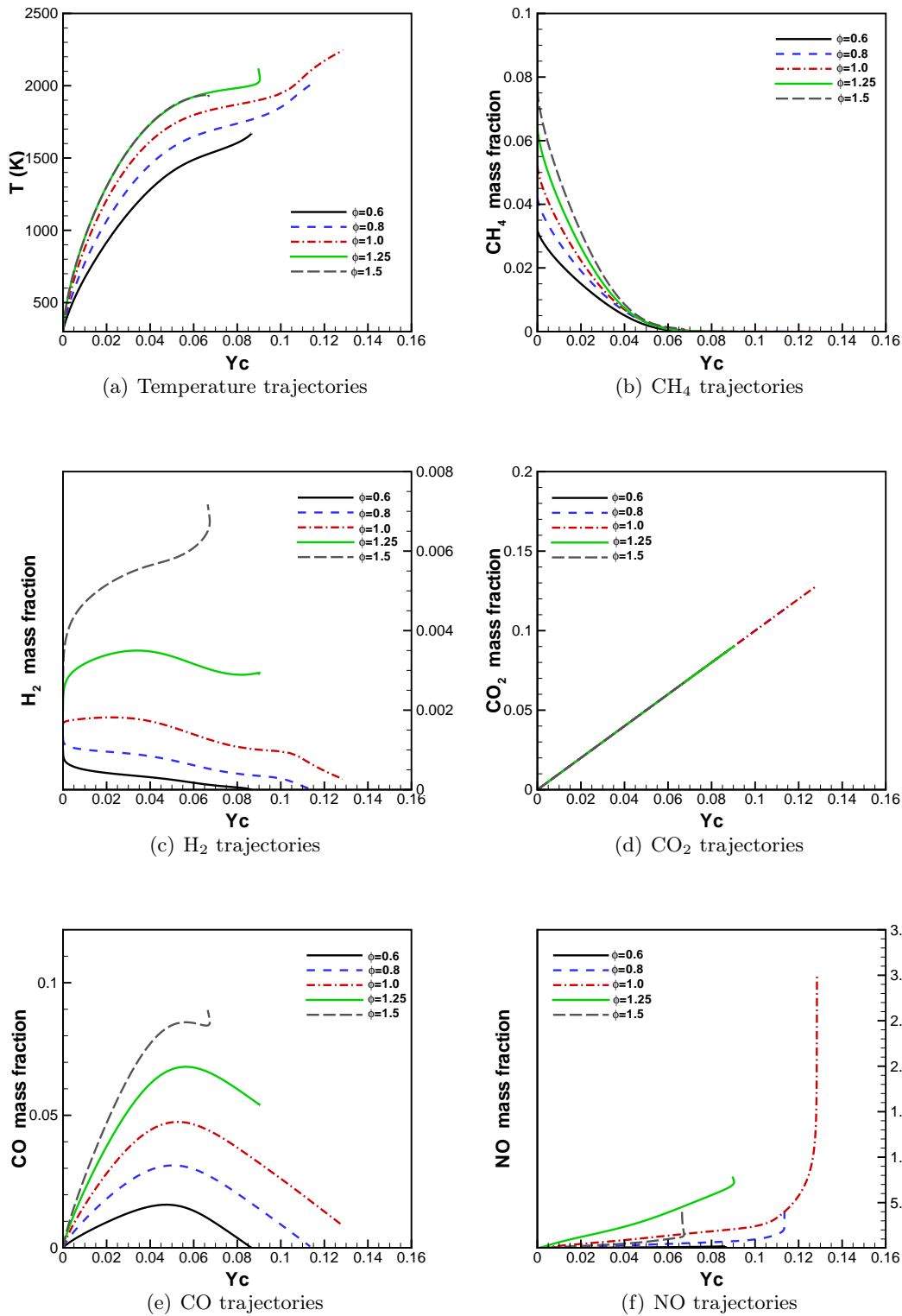
(f) NO trajectories

Figure 4.5: Temperature and representative species trajectories in the progress of reaction space for $Y_c = Y_{CO_2} + Y_{NO}$, corresponding to lean, stoichiometric, and rich conditions, and 20% H$_2$ in the blended H$_2$-CH$_4$ fuel. 1D steady-state laminar premixed flames.

remaining four can be evaluated using atom balances. In this case, the species C_2H_2, O_2, NH_3, and N_2 are computed via atom balances of the elements C, O, H, and N, respectively.
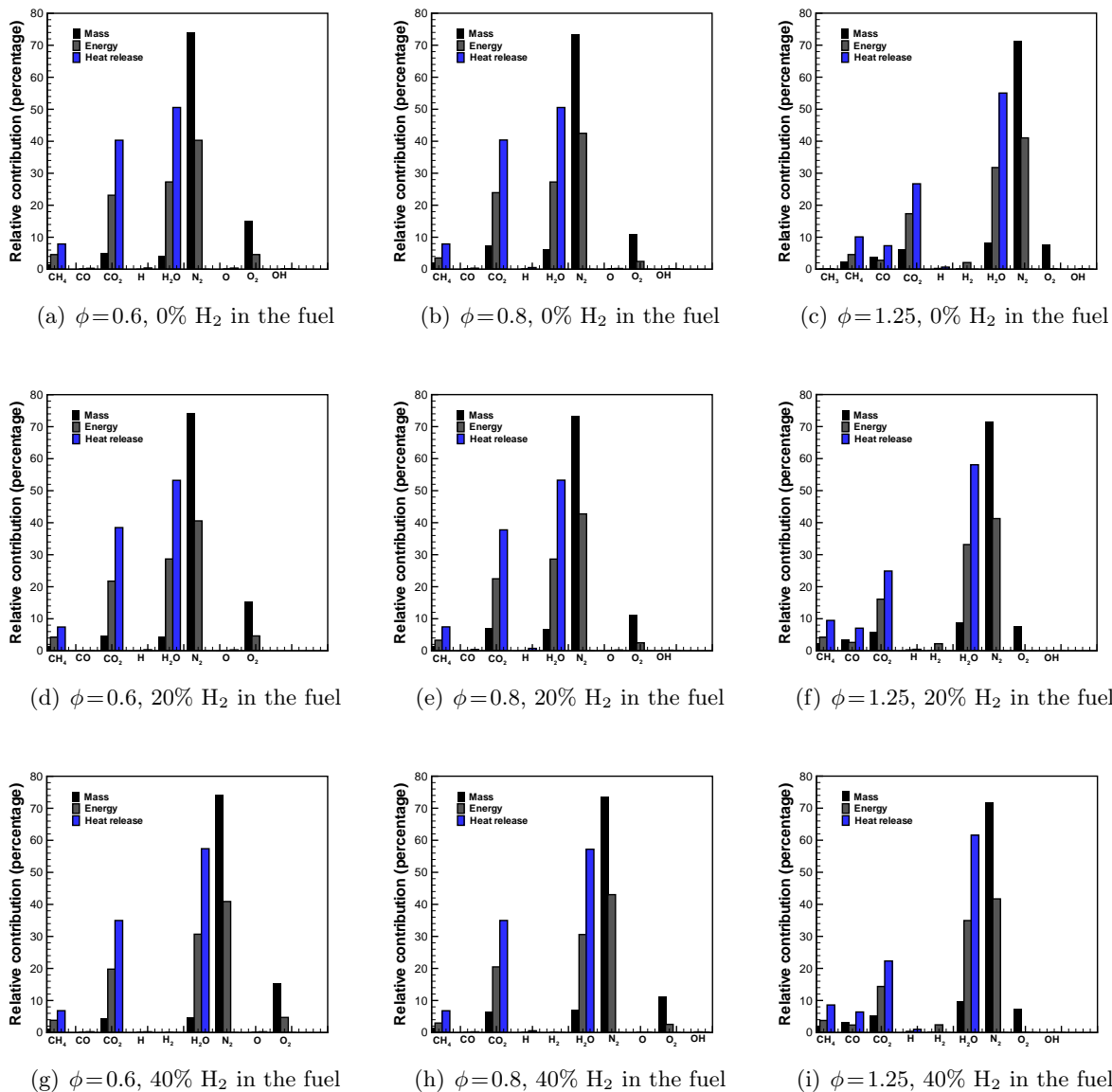
Figure 4.6: Relative mass, energy, and heat release contributions of the most representative species in H_2-enriched methane-air premixed flamelets at equivalence ratios $\phi=0.6$, $\phi=0.8$, and $\phi=1.25$.

4.1.7 LES Solution Method and PCM-FPI Look-Up Table Coupling

In the above description of the PCM-FPI approach, the premixed flamelet solutions were presented as functions of the equivalence ratio and progress variable only. Nevertheless, in section 2.6 of Chapter 2, it was mentioned that the properties of a premixed flame mainly depend on the equivalence ratio, the temperature of the fresh gas, and pressure. For more general com-

bustion processes involving heat losses, recirculation zones of burned gas and/or non-negligible pressure variations, the tabulation procedure would require incorporation of variable fresh gas temperature and/or multi-pressure conditions. In this research, heat losses have been neglected and essentially isobaric flames at atmospheric pressure have been considered. As a consequence, the tabulations have been carried out here for adiabatic flames at atmospheric pressure only.

There are different options to couple the fully compressible LES solver with the integrated FPI (PCM-FPI) look-up table: (i) a look-up table of species mass fractions $\tilde{Y}_\alpha$ can be employed, without solving transport equations for the species; (ii) a look-up table of reaction rates $\tilde{\dot{\omega}}_\alpha^*$ can be utilized, solving transport equations for the species; and (iii) a look-up table of species mass fractions $\tilde{Y}_\alpha$ can be used, solving transport equations for the species and reconstructing the reaction rates from the look-up table of mass fractions [209]. In all the cases, the Favre-filtered form of continuity, momentum, total energy, progress of reaction, and variance of the progress of reaction equations are solved, along with the transport equation for the SFS turbulent kinetic energy. The method to reconstruct the reaction rates from a look-up table of species mass fractions is described next.

Reconstruction of Reaction Rates

Under the assumption of equal molecular diffusivities of species and Y_c, it can be shown that the species trajectories in Y_c-space are governed by the equation [52]

$$\dot{\omega}_\alpha = \dot{\omega}_{Y_c} \left[\frac{\partial Y_\alpha}{\partial Y_c} - \frac{1}{Da} \frac{\partial^2 Y_\alpha}{\partial Y_c^2} \right] , \tag{4.41}$$

where Da is a Damköler number $(Da = \dot{\omega}_{Y_c}/(\rho\mathcal{D}|\nabla Y_c|^2))$, and $\mathcal{D}$ is the molecular diffusivity. If Da is sufficiently large so that the second-order term is negligible, the reaction rates of the species can be approximated as

$$\dot{\omega}_\alpha \approx \dot{\omega}_{Y_c} \frac{\partial Y_\alpha}{\partial Y_c} . \tag{4.42}$$

Based on the above approximation, Galpin *et al.* [209] have employed the approximate relation for the reaction rate of species α

$$\dot{\omega}_\alpha^* \approx \frac{Y_\alpha^{\mathrm{FPI}}(Y_c + \zeta\delta_t) - Y_\alpha}{\zeta\delta_t} , \tag{4.43}$$

where ζ was of the order of 5 and $\delta_t \approx 10^{-7}$, and a similar expression was employed to compute filtered reaction rates. In this thesis, Equation 4.42 is used and the derivative of the species

mass fraction Y_α with respect to Y_c is approximated using the relation

$$\frac{\partial Y_\alpha}{\partial Y_c} \approx \left[\frac{Y_\alpha^{\text{FPI}}(Y_c + \varepsilon) - Y_\alpha}{\varepsilon} \right] , \tag{4.44}$$

where ε is a small perturbation. Similarly, the filtered reaction rates are written as

$$\tilde{\dot{\omega}}_\alpha^* \approx \tilde{\dot{\omega}}_{Y_c}^* \frac{\partial \tilde{Y}_\alpha}{\partial \tilde{Y}_c} = \tilde{\dot{\omega}}_{Y_c}^* \left[\frac{\tilde{Y}_\alpha^{\text{PCM}}(\tilde{Y}_c + \varepsilon) - \tilde{Y}_\alpha}{\varepsilon} \right] . \tag{4.45}$$

The perturbation ε is determined by the relation $\varepsilon = a + r|Y_c|$ [223], where a and r are absolute and relative tolerances. After some preliminary tests, the absolute and relative tolerances were set to 10^{-5} (or 10^{-6}) and 10^{-3}, respectively, and yielded suitably accurate results.

4.2 Thickened Flame and Power-Law Formulation

4.2.1 Thickened Flame Model

Another approach to modelling the turbulence-chemistry interaction for premixed flames is offered by the so-called thickened flame model. This model is also considered in the present research. In the thickened flame model, the computed flame front structure is artificially locally thickened in such a way that it can be resolved on a relatively coarse LES mesh, but such that the flame speed remains unaltered [224, 66]. From the theory of laminar premixed flames, it is well established that the laminar flame speed, s_{L}, and the laminar flame thickness, δ_{L}, scale as

$$s_{\text{L}} \propto \sqrt{\mathcal{D}\mathcal{W}}, \qquad \delta_{\text{L}} \propto \frac{\mathcal{D}}{s_{\text{L}}} , \tag{4.46}$$

where $\mathcal{D}$ is the molecular diffusivity and $\mathcal{W}$ the mean reaction rate. Thus, an increase in flame thickness by a factor F with a constant flame speed, can be achieved by multiplying the molecular diffusivity by F, and the reaction rate $\mathcal{W}$ by $1/F$. Similarly, the thermal diffusivity, $\mathcal{D}_{\text{th}}$, is multiplied by F. It should be pointed out that, in the context of laminar flames, O'Rourke & Bracco [224] originally introduced a coordinate transformation to thicken the flame front, which lead to the modification of all the diffusive terms in the governing equations, including the transport of momentum. However, as outlined in Colin *et al.* [66], no modification is applied to the transport of momentum in the context of turbulent combustion. Besides, an efficiency factor, E_{F}, is introduced to account for the resulting decrease in the Damköhler number and incorporate the influences of the unresolved turbulent field on the chemical kinetics [66]. The

resulting filtered balance equation for chemical species takes the modified form

$$\frac{\partial(\bar{\rho}\tilde{Y}_\alpha)}{\partial t} + \frac{\partial(\bar{\rho}\tilde{Y}_\alpha\tilde{u}_i)}{\partial x_i} = \frac{\partial}{\partial x_i}\left(E_\mathrm{F}F\bar{\rho}\check{\mathcal{D}}_\alpha\frac{\partial\tilde{Y}_\alpha}{\partial x_i}\right) + \frac{E_\mathrm{F}\overline{\dot{\omega}}_\alpha}{F}\,,$$ (4.47)

where the filtered reaction rates, $\overline{\dot{\omega}}_\alpha$, are now calculated directly using Arrhenius law reaction rates evaluated in terms of resolved quantities. The heat flux appearing in the filtered energy equation is also modified and becomes

$$\check{q}_j = -E_\mathrm{F}F\check{\lambda}\frac{\partial\tilde{T}}{\partial x_j} - \bar{\rho}\sum_{\alpha=1}^{N}\check{h}_\alpha E_\mathrm{F}F\check{D}_\alpha\frac{\partial\tilde{Y}_\alpha}{\partial x_j}\,.$$ (4.48)

The efficiency factor is defined by the relation [66, 65]

$$E_\mathrm{F} = \frac{\Xi(\delta_\mathrm{L})}{\Xi(\delta_\mathrm{L}^1)}\,,$$ (4.49)

where $\Xi(\delta_\mathrm{L}^1)$ and $\Xi(\delta_\mathrm{L})$ are the SFS wrinkling factors corresponding to the thickened and un-thickened flames, respectively. The SFS wrinkling factor is defined as the ratio of SFS flame front area to its projection in the propagation direction. Colin *et al.* [66] estimated a maximum value of the efficiency factor $E_\mathrm{F} = F^{2/3}$. In this research, the wrinkling factor is evaluated using a power-law wrinkling model [60, 61], which is described below.

4.2.2 Power-Law Flame Wrinkling Model

Assuming that the internal structure of the flame is not significantly altered by the turbulence, as in the wrinkled flamelets, corrugated flamelets, and thin reaction zones premixed combustion regimes [23], and that the increased flame surface area due to the flame front wrinkling by the SFS turbulence leads to an increase in the flame speed, the power-law expression for the wrinkling factor is taken to have the form [60, 61]

$$\Xi_{\Delta_\mathrm{o}} = \left(1 + \frac{\Delta_\mathrm{o}}{\eta_\mathrm{i}}\right)^\gamma\,,$$ (4.50)

where Ξ_{Δ_o} is the SFS wrinkling factor associated to Δ_o (the outer cutoff scale), η_i is the inner cutoff scale, and γ is the power of the expression, which can be prescribed to be constant [60] or determined dynamically [61]. It is taken to be 0.5, as suggested by Charlette *et al.* [60]. The inner cutoff is associated with the maximum of the laminar flame thickness and the mean curvature of the flame, which can be estimated by assuming equilibrium between production and destruction of flame surface density as $|\langle\nabla\cdot\mathbf{n}\rangle_\mathrm{s}| = \Delta_\mathrm{o}^{-1}(u'_{\Delta_\mathrm{o}}/s_\mathrm{L})\Gamma_{\Delta_\mathrm{o}}$, where $\Gamma_{\Delta_\mathrm{o}}$ is the efficiency

function proposed by Charlette *et al.* [60] to account for the net straining of all relevant scales smaller than Δ_o. The SFS turbulence intensity, u'_{Δ_o}, is calculated using the expression proposed by Colin *et al.* [66], $u'_{\Delta_o} = c_2\Delta_x^3 \mid \nabla^2(\nabla \times \tilde{\mathbf{u}}) \mid$. The model constant c_2 is set to 2.0 in this work for three-dimensional simulations [66]. The SFS wrinkling factor can then be rewritten as

$$\Xi_{\Delta_o} = \left(1 + \min\left[\frac{\Delta_o}{\delta_L} , \Gamma_{\Delta_o}\frac{u'_{\Delta_o}}{s_L}\right]\right)^\gamma . \tag{4.51}$$

The efficiency function proposed by Charlette *et al.* [60] has the form

$$\Gamma_{\Delta_o}\left(\frac{\Delta_o}{\delta_L^*}, \frac{u'_{\Delta_o}}{s_L}, Re_{\Delta o}\right) = \{[(f_u^{-a} + f_{\Delta o}^{-a})^{-1/a}]^{-b} + f_{Re}^{-b}\}^{-1/b} , \tag{4.52}$$

where

$$f_u = 4\left(\frac{27C_K}{110}\right)^{1/2}\left(\frac{18C_K}{55}\right)\left(\frac{u'_{\Delta_0}}{s_L}\right)^2 , \tag{4.53}$$

$$f_{\Delta_o} = \left\{\frac{27C_K\pi^{4/3}}{110}\left[\left(\frac{\Delta_o}{\delta_L^*}\right)^{4/3} - 1\right]\right\}^{1/2} , \tag{4.54}$$

$$f_{Re} = \left[\frac{9}{55}\exp\left(-\frac{3}{2}C_K\pi^{4/3}Re_{\Delta_o}^{-1}\right)\right]^{1/2} Re_{\Delta_o}^{1/2} . \tag{4.55}$$

Here, C_K denotes the Kolmogorov constant ($C_K \approx 1.5$), $Re_{\Delta o}$ is the Reynolds number based on Δ_o and u'_{Δ_o}, and δ_L^* denotes the flame thickness employed to evaluate the function. The exponents a and b are given by

$$a = 0.60 + 0.20 \ \exp[-0.1(u'_{\Delta_o}/s_L)] - 0.20 \ \exp[-0.01(\Delta_o/\delta_L^*)], \quad b = 1.4 . \tag{4.56}$$

Since typically, $\Delta_o = F\delta_L$, the SFS wrinkling factor, $\Xi_{\Delta_o}(\Delta_o/\delta_L^1) = 1$. Therefore one can simply set $E_F = \Xi_{\Delta_o}(\Delta_o/\delta_L)$, as is done in the present work.

4.3   Flame Surface Density Model of Hawkes and Cant

Finally, a brief description of the transported FSD model of Hawkes & Cant [56] is also presented here. This model has been used for comparisons of different SFS models in the current LES studies. As it was discussed in Chapter 3, one approach to modelling of turbulent premixed flames is to ignore for the most part the internal structure of the flame and detailed chemical kinetics, and represent the combustion occurring at the flame front in terms of a reaction progress variable. The progress variable, c, is defined in terms of a normalized temperature or fuel mass fraction such that $c=0$ in the reactants and $c=1$ in the combustion products. The modelled

progress variable equation has the form

$$\frac{\partial (\bar{\rho}\tilde{c})}{\partial t} + \frac{\partial (\bar{\rho}\tilde{c}\tilde{u}_i)}{\partial x_i} = \frac{\partial}{\partial x_i} \left(\frac{\bar{\rho}\nu_t}{Sc_t} \frac{\partial \tilde{c}}{\partial x_i} \right) + \rho_r s_L \bar{\rho}\tilde{\Sigma},\tag{4.57}$$

where ρ_r is the reactants density, $\tilde{\Sigma}$ is the Favre-filtered flame surface area per unit mass of the mixture, and the product, $\bar{\rho}\tilde{\Sigma}$, is the flame surface area per unit volume or flame surface density (FSD).

The filtered quantity, $\tilde{\Sigma}$, includes contributions from the resolved FSD and the unresolved subfilter-scales. The latter must be modelled. The modelled transport equation for the FSD density that has been proposed by Hawkes and Cant [56] is given by

$$\frac{\partial(\bar{\rho}\tilde{\Sigma})}{\partial t} + \frac{\partial(\bar{\rho}\tilde{u}_i\tilde{\Sigma})}{\partial x_i} - \frac{\partial}{\partial x_i} \left(\frac{\bar{\rho}\nu_t}{Sc_t} \frac{\partial \tilde{\Sigma}}{\partial x_i} \right) = \Gamma_K \bar{\rho}\tilde{\Sigma} \frac{\sqrt{\tilde{k}_\Delta}}{\Delta} - \beta s_L \frac{(\bar{\rho}\tilde{\Sigma})^2}{1 - \tilde{c}} + (\delta_{ij} - n_{ij}) \bar{\rho}\tilde{\Sigma} \frac{\partial \tilde{u}_i}{\partial x_j}$$

$$- \frac{\partial}{\partial x_i} [s_L(1 + \tau\tilde{c}) M_i \bar{\rho}\tilde{\Sigma}] + s_L(1 + \tau\tilde{c}) \bar{\rho}\tilde{\Sigma} \frac{\partial M_i}{\partial x_i}, \tag{4.58}$$

where $\vec{M} = -\nabla\bar{c}/\tilde{\Sigma}$ is the flamelet model for the surface averaged normal ($\bar{c}$ is estimated using $\bar{c} = (1+\tau)\tilde{c}/(1+\tau\tilde{c})$), $\alpha = 1 - \vec{M}\cdot\vec{M}$, and $n_{ij} = M_i M_j + 1/3\alpha\delta_{ij}$. The variable $\tau = (T_{ad} - T_r)/T_r$ is the heat release parameter, where T_{ad} and T_r are the adiabatic and the reactants temperature, respectively, β is a model constant and must satisfy $\beta \geq 1$ for realisability requirements, α is a resolution factor, and Γ_K is an efficiency function [225]. The terms on the left hand side of the modelled FSD equation represent unsteady, convection and SFS transport effects, while the terms on the right hand side represent the production/destruction sources associated with SFS strain and curvature, resolved strain, resolved propagation and curvature. A more complete description of the FSD model used in the present work is provided in the recent thesis of Lin [168]. Application of the FSD model to LES of premixed turbulent flames for laboratory-scale burners is also discussed therein.

<div align="right">Chapter 5</div>

Parallel Adaptive Mesh Refinement Finite-Volume Scheme

The Favre-filtered governing equations introduced in previous chapters provide suitable formulations for performing LES predictions of premixed turbulent flames. A parallel adaptive mesh refinement finite-volume method, employed herein for the numerical solution of the various systems of filtered governing equations, is outlined and reviewed in this chapter.

5.1 Favre-Filtered Governing Equations in Vector Form

The systems of Favre-filtered governing equations introduced in the previous chapters can be expressed using matrix-vector notation as

$$\frac{\partial \boldsymbol{\mathcal{U}}}{\partial t} + \nabla \cdot \vec{\boldsymbol{\mathcal{F}}} = \boldsymbol{\mathcal{S}} \,, \tag{5.1}$$

where $\boldsymbol{\mathcal{U}}$ denotes the vector of conserved variables, $\vec{\boldsymbol{\mathcal{F}}}$ represents the flux dyad, and $\boldsymbol{\mathcal{S}}$ is the source term vector. The flux dyad $\vec{\boldsymbol{\mathcal{F}}}$ comprises both an inviscid component, $\vec{\boldsymbol{\mathcal{F}}}^{\mathbf{I}}$, and a viscous component, $\vec{\boldsymbol{\mathcal{F}}}^{\mathbf{V}}$. It can be written in terms of its vector components as

$$\begin{aligned}
\vec{\boldsymbol{\mathcal{F}}} &= (\boldsymbol{\mathcal{F}}_{\mathrm{x}}, \boldsymbol{\mathcal{F}}_{\mathrm{y}}, \boldsymbol{\mathcal{F}}_{\mathrm{z}}) \\
&= (\boldsymbol{\mathcal{F}}_{\mathrm{x}}^{\mathbf{I}} - \boldsymbol{\mathcal{F}}_{\mathrm{x}}^{\mathbf{V}}, \boldsymbol{\mathcal{F}}_{\mathrm{y}}^{\mathbf{I}} - \boldsymbol{\mathcal{F}}_{\mathrm{y}}^{\mathbf{V}}, \boldsymbol{\mathcal{F}}_{\mathrm{z}}^{\mathbf{I}} - \boldsymbol{\mathcal{F}}_{\mathrm{z}}^{\mathbf{V}}) \,, \tag{5.2}
\end{aligned}$$

where $\boldsymbol{\mathcal{F}}_{\mathrm{x}}^{\mathbf{I}}$, $\boldsymbol{\mathcal{F}}_{\mathrm{x}}^{\mathbf{V}}$, $\boldsymbol{\mathcal{F}}_{\mathrm{y}}^{\mathbf{I}}$, $\boldsymbol{\mathcal{F}}_{\mathrm{y}}^{\mathbf{V}}$, $\boldsymbol{\mathcal{F}}_{\mathrm{z}}^{\mathbf{I}}$, and $\boldsymbol{\mathcal{F}}_{\mathrm{z}}^{\mathbf{V}}$ are the components of inviscid and viscous flux vectors in the x-, y-, and z-coordinate directions, respectively. If one considers the Favre-filtered equations for the PCM-FPI model transporting N species, the vectors $\boldsymbol{\mathcal{U}}$, $\boldsymbol{\mathcal{F}}_{\mathrm{x}}^{\mathbf{I}}$, $\boldsymbol{\mathcal{F}}_{\mathrm{x}}^{\mathbf{V}}$, $\boldsymbol{\mathcal{F}}_{\mathrm{y}}^{\mathbf{I}}$, $\boldsymbol{\mathcal{F}}_{\mathrm{y}}^{\mathbf{V}}$, $\boldsymbol{\mathcal{F}}_{\mathrm{z}}^{\mathbf{I}}$, $\boldsymbol{\mathcal{F}}_{\mathrm{z}}^{\mathbf{I}}$, and

$\boldsymbol{\mathcal{S}}$ are given by

$$
\boldsymbol{\mathcal{U}} = \begin{bmatrix} \bar{\rho} \\ \bar{\rho}\tilde{u} \\ \bar{\rho}\tilde{v} \\ \bar{\rho}\tilde{w} \\ \bar{\rho}\tilde{E} \\ \bar{\rho}k_\Delta \\ \bar{\rho}\tilde{Y}_{\mathrm{c}} \\ \bar{\rho}Y_{\mathrm{c_v}} \\ \bar{\rho}\tilde{Y}_1 \\ \vdots \\ \bar{\rho}\tilde{Y}_N \end{bmatrix} , \tag{5.3}
$$

$$
\boldsymbol{\mathcal{F}}_{\mathrm{x}}^{\mathbf{I}} = \begin{bmatrix} \bar{\rho}\tilde{u} \\ \bar{\rho}\tilde{u}\tilde{u} + \bar{p} + \bar{\rho}k_\Delta \\ \bar{\rho}\tilde{u}\tilde{v} \\ \bar{\rho}\tilde{u}\tilde{w} \\ (\bar{\rho}\tilde{E} + \bar{p})\tilde{u} \\ \bar{\rho}k_\Delta\tilde{u} \\ \bar{\rho}\tilde{Y}_{\mathrm{c}}\tilde{u} \\ \bar{\rho}Y_{\mathrm{c_v}}\tilde{u} \\ \bar{\rho}\tilde{Y}_1\tilde{u} \\ \vdots \\ \bar{\rho}\tilde{Y}_N\tilde{u} \end{bmatrix} , \quad
\boldsymbol{\mathcal{F}}_{\mathrm{y}}^{\mathbf{I}} = \begin{bmatrix} \bar{\rho}\tilde{v} \\ \bar{\rho}\tilde{u}\tilde{v} \\ \bar{\rho}\tilde{v}\tilde{v} + \bar{p} + \bar{\rho}k_\Delta \\ \bar{\rho}\tilde{v}\tilde{w} \\ (\bar{\rho}\tilde{E} + \bar{p})\tilde{v} \\ \bar{\rho}k_\Delta\tilde{v} \\ \bar{\rho}\tilde{Y}_{\mathrm{c}}\tilde{v} \\ \bar{\rho}Y_{\mathrm{c_v}}\tilde{v} \\ \bar{\rho}\tilde{Y}_1\tilde{v} \\ \vdots \\ \bar{\rho}\tilde{Y}_N\tilde{v} \end{bmatrix} , \quad
\boldsymbol{\mathcal{F}}_{\mathrm{z}}^{\mathbf{I}} = \begin{bmatrix} \bar{\rho}\tilde{w} \\ \bar{\rho}\tilde{u}\tilde{w} \\ \bar{\rho}\tilde{v}\tilde{w} \\ \bar{\rho}\tilde{w}\tilde{w} + \bar{p} + \bar{\rho}k_\Delta \\ (\bar{\rho}\tilde{E} + \bar{p})\tilde{w} \\ \bar{\rho}k_\Delta\tilde{w} \\ \bar{\rho}\tilde{Y}_{\mathrm{c}}\tilde{w} \\ \bar{\rho}Y_{\mathrm{c_v}}\tilde{w} \\ \bar{\rho}\tilde{Y}_1\tilde{w} \\ \vdots \\ \bar{\rho}\tilde{Y}_N\tilde{w} \end{bmatrix} ,
\tag{5.4}
$$

$$\boldsymbol{\mathcal{F}}_{\mathrm{x}}^{\mathbf{V}} = \begin{bmatrix} 0 \\ \check{\tau}_{\mathrm{xx}} + \sigma_{\mathrm{xx}} \\ \check{\tau}_{\mathrm{xy}} + \sigma_{\mathrm{xy}} \\ \check{\tau}_{\mathrm{xz}} + \sigma_{\mathrm{xz}} \\ \tilde{u}(\check{\tau}_{\mathrm{xx}} + \sigma_{\mathrm{xx}}) + \tilde{v}(\check{\tau}_{\mathrm{xy}} + \sigma_{\mathrm{xy}}) + \tilde{w}(\check{\tau}_{\mathrm{xz}} + \sigma_{\mathrm{xz}}) - (\check{q}_{\mathrm{x}} + \theta_{\mathrm{x}}) \\ \bar{\rho}(\frac{\nu_{\mathrm{t}}}{\zeta^*} + \check{\nu})\frac{\partial k_\Delta}{\partial x} \\ \bar{\rho}(\check{\mathcal{D}}_{Y_{\mathrm{c}}} + \mathcal{D}_{\mathrm{t}})\frac{\partial \tilde{Y}_{\mathrm{c}}}{\partial x} \\ \bar{\rho}(\check{\mathcal{D}}_{Y_{\mathrm{c}}} + \mathcal{D}_{\mathrm{t}})\frac{\partial Y_{\mathrm{c_v}}}{\partial x} \\ \bar{\rho}(\check{\mathcal{D}}_{1} + \mathcal{D}_{\mathrm{t}})\frac{\partial \tilde{Y}_{1}}{\partial x} \\ \vdots \\ \bar{\rho}(\check{\mathcal{D}}_{N} + \mathcal{D}_{\mathrm{t}})\frac{\partial \tilde{Y}_{N}}{\partial x} \end{bmatrix}, \tag{5.5}$$

$$\boldsymbol{\mathcal{F}}_{\mathrm{y}}^{\mathbf{V}} = \begin{bmatrix} 0 \\ \check{\tau}_{\mathrm{xy}} + \sigma_{\mathrm{xy}} \\ \check{\tau}_{\mathrm{yy}} + \sigma_{\mathrm{yy}} \\ \check{\tau}_{\mathrm{yz}} + \sigma_{\mathrm{yz}} \\ \tilde{u}(\check{\tau}_{\mathrm{xy}} + \sigma_{\mathrm{xy}}) + \tilde{v}(\check{\tau}_{\mathrm{yy}} + \sigma_{\mathrm{yy}}) + \tilde{w}(\check{\tau}_{\mathrm{yz}} + \sigma_{\mathrm{yz}}) - (\check{q}_{\mathrm{y}} + \theta_{\mathrm{y}}) \\ \bar{\rho}(\frac{\nu_{\mathrm{t}}}{\zeta^*} + \check{\nu})\frac{\partial k_\Delta}{\partial y} \\ \bar{\rho}(\check{\mathcal{D}}_{Y_{\mathrm{c}}} + \mathcal{D}_{\mathrm{t}})\frac{\partial \tilde{Y}_{\mathrm{c}}}{\partial y} \\ \bar{\rho}(\check{\mathcal{D}}_{Y_{\mathrm{c}}} + \mathcal{D}_{\mathrm{t}})\frac{\partial Y_{\mathrm{c_v}}}{\partial y} \\ \bar{\rho}(\check{\mathcal{D}}_{1} + \mathcal{D}_{\mathrm{t}})\frac{\partial \tilde{Y}_{1}}{\partial y} \\ \vdots \\ \bar{\rho}(\check{\mathcal{D}}_{N} + \mathcal{D}_{\mathrm{t}})\frac{\partial \tilde{Y}_{N}}{\partial y} \end{bmatrix}, \tag{5.6}$$

$$\boldsymbol{\mathcal{F}}_{\mathrm{z}}^{\mathbf{V}} = \begin{bmatrix} 0 \\ \check{\tau}_{\mathrm{xz}} + \sigma_{\mathrm{xz}} \\ \check{\tau}_{\mathrm{yz}} + \sigma_{\mathrm{yz}} \\ \check{\tau}_{\mathrm{zz}} + \sigma_{\mathrm{zz}} \\ \tilde{u}(\check{\tau}_{\mathrm{xz}} + \sigma_{\mathrm{xz}}) + \tilde{v}(\check{\tau}_{\mathrm{yz}} + \sigma_{\mathrm{yz}}) + \tilde{w}(\check{\tau}_{\mathrm{zz}} + \sigma_{\mathrm{zz}}) - (\check{q}_{\mathrm{z}} + \theta_{\mathrm{z}}) \\ \bar{\rho}(\frac{\nu_{\mathrm{t}}}{\zeta^*} + \check{\nu})\frac{\partial k_\Delta}{\partial z} \\ \bar{\rho}(\check{\mathcal{D}}_{Y_{\mathrm{c}}} + \mathcal{D}_{\mathrm{t}})\frac{\partial \tilde{Y}_{\mathrm{c}}}{\partial z} \\ \bar{\rho}(\check{\mathcal{D}}_{Y_{\mathrm{c}}} + \mathcal{D}_{\mathrm{t}})\frac{\partial Y_{\mathrm{c_v}}}{\partial z} \\ \bar{\rho}(\check{\mathcal{D}}_{1} + \mathcal{D}_{\mathrm{t}})\frac{\partial \tilde{Y}_{1}}{\partial z} \\ \vdots \\ \bar{\rho}(\check{\mathcal{D}}_{N} + \mathcal{D}_{\mathrm{t}})\frac{\partial \tilde{Y}_{N}}{\partial z} \end{bmatrix}, \tag{5.7}$$

$$\boldsymbol{S} = \begin{bmatrix} 0 \\ \bar{\rho} g_{\mathrm{x}} \\ \bar{\rho} g_{\mathrm{y}} \\ \bar{\rho} g_{\mathrm{z}} \\ \bar{\rho}(\tilde{u} g_{\mathrm{x}} + \tilde{v} g_{\mathrm{y}} + \tilde{w} g_{\mathrm{z}}) \\ (\sigma_{\mathrm{xx}}\check{S}_{\mathrm{xx}} + \sigma_{\mathrm{yy}}\check{S}_{\mathrm{yy}} + \sigma_{\mathrm{zz}}\check{S}_{\mathrm{zz}} + 2\sigma_{\mathrm{xy}}\check{S}_{\mathrm{xy}} + 2\sigma_{\mathrm{xz}}\check{S}_{\mathrm{xz}} + 2\sigma_{\mathrm{yz}}\check{S}_{\mathrm{yz}}) - \frac{C_\epsilon \bar{\rho} k_\Delta^{3/2}}{\Delta} \\ \bar{\dot{\omega}}_{Y_{\mathrm{c}}} \\ 2\bar{\rho}\mathcal{D}_{\mathrm{t}}|\nabla \tilde{Y}_{\mathrm{c}}|^2 - 2\bar{s}_{\chi_{Y_{\mathrm{c}}}} + 2(\overline{Y_{\mathrm{c}}\dot{\omega}_{Y_{\mathrm{c}}}} - \tilde{Y}_{\mathrm{c}}\bar{\dot{\omega}}_{Y_{\mathrm{c}}}) \\ \bar{\dot{\omega}}_1 \\ \vdots \\ \bar{\dot{\omega}}_N \end{bmatrix} . \tag{5.8}$$

In addition, the vector of primitive variables, $\boldsymbol{\mathcal{W}}$, has the form

$$\boldsymbol{\mathcal{W}} = \left[\bar{\rho}, \tilde{u}, \tilde{v}, \tilde{w}, \bar{p}, k_\Delta, \tilde{Y}_{\mathrm{c}}, Y_{\mathrm{c_v}}, \tilde{Y}_1, \dots, \tilde{Y}_N \right]^{\mathrm{T}} . \tag{5.9}$$

In the above, θ denotes the SFS heat flux, $\check{S}$ is the strain rate evaluated in terms of the Favre-filtered velocity, and $\tilde{u}, \tilde{v}$, and $\tilde{w}$ are the Favre-filtered velocity components in the x-, y-, and z-coordinate directions, respectively.

5.2   Godunov Finite-Volume Method

5.2.1   Finite-Volume Formulation of the Governing Equations

By integrating the differential form of the preceding governing equations (Equation 5.1) over a control volume, V, and applying the divergence theorem, the following integral form is obtained

$$\frac{\mathrm{d}}{\mathrm{d}t} \int_{V(t)} \boldsymbol{\mathcal{U}} \, \mathrm{d}V + \oint_{\Omega(t)} \vec{n} \cdot \vec{\boldsymbol{\mathcal{F}}} \, \mathrm{d}\Omega = \int_{V(t)} \boldsymbol{S} \, \mathrm{d}V , \tag{5.10}$$

where Ω is the closed surface of the control volume, and $\vec{n}$ is the unit outward vector normal to the closed surface. The averaged values of $\boldsymbol{\mathcal{U}}$ and $\boldsymbol{S}$ for the control volume can be determined as follows:

$$\mathbf{U} = \frac{1}{V} \int_{V(t)} \boldsymbol{\mathcal{U}} \, \mathrm{d}V , \tag{5.11}$$

$$\mathbf{S} = \frac{1}{V} \int_{V(t)} \boldsymbol{S} \, \mathrm{d}V . \tag{5.12}$$

Equation 5.10 can then be rewritten using 5.11 and 5.12, leading to the following system of coupled integral equations for volume-averaged quantities

$$\frac{\mathrm{d}\mathbf{U}}{\mathrm{d}t} = -\frac{1}{V} \oint_{\Omega(t)} \vec{n} \cdot \vec{\boldsymbol{\mathcal{F}}} \, \mathrm{d}\Omega \, + \, \mathbf{S} \,. \tag{5.13}$$

The application of the above equation to a computational cell (i,j,k) of a three-dimensional, structured, multi-block, body-fitted mesh leads to the expression

$$\frac{\mathrm{d}\mathbf{U}_{i,j,k}}{\mathrm{d}t} = -\frac{1}{V_{i,j,k}} \sum_{l=1}^{N_\mathrm{f}} \left[\vec{n}_l \cdot \vec{\boldsymbol{\mathcal{F}}}_l A_l \right]_{i,j,k} + \mathbf{S}_{i,j,k}(\mathbf{U}) = \mathbf{R}_{i,j,k}(\mathbf{U}) \,, \tag{5.14}$$

where N_f denotes the number of cell faces, A_l is the surface area of face l, and $\mathbf{R}$ is the residual vector. This semi-discrete form of Equation 5.13 represents a set of coupled non-linear ordinary differential equations for cell-averaged quantities, $\mathbf{U}_{i,j,k}$, which can be solved by evaluating the flux integrals as well as source terms and using a time-stepping method. In the remainder of this chapter, various aspects of the finite-volume spatial discretization scheme employed herein to solve Equation 5.14 are described.

5.2.2 Inviscid Flux Evaluation

The scheme defined above requires the evaluation of the solution fluxes at the cell faces. The inviscid fluxes are discretized by applying a Godunov-type upwind finite-volume spatial discretization procedure. In Godunov-type finite-volume methods, the solution of a locally one-dimensional Riemann problem provides a means for evaluating the numerical inviscid flux at the cell boundaries. As first proposed by Godunov [226], the method preserves monotonicity allowing to capture solution discontinuities, such as shocks, without introducing oscillations in the solutions. Solution of the Riemann problem also provides natural upwinding of the solution content. The inviscid flux $\boldsymbol{\mathcal{F}}$ between cell (i, j, k) and cell $(i + 1, j, k)$ is then given at the cell interface $(i + \frac{1}{2}, j, k)$ by

$$\vec{\boldsymbol{\mathcal{F}}}_{i+\frac{1}{2},j,k} \cdot \vec{n}_{i+\frac{1}{2},j,k} = \boldsymbol{\mathcal{F}}(\mathcal{R}(\boldsymbol{\mathcal{U}}_\mathrm{L}, \boldsymbol{\mathcal{U}}_\mathrm{R})) = \boldsymbol{\mathcal{F}}(\mathcal{R}(\mathbf{U}_{i,j,k}, \mathbf{U}_{i+1,j,k})) \,, \tag{5.15}$$

where $\boldsymbol{\mathcal{U}}_\mathrm{L}$ and $\boldsymbol{\mathcal{U}}_\mathrm{R}$ are left and right conserved solution vectors, respectively, and $\mathcal{R}$ represents the solution of the Riemann problem. A first-order accurate solution in space can be obtained by solving Riemann problems using the cell averages as the left and right states when evaluating the face fluxes. For higher-order accuracy, a spatial reconstruction of the solution in each computational cell is required, which will be discussed in the following section. Exact

Riemann solvers, such as the one proposed by Gottlieb & Groth [227], can be used for the Euler equations for an ideal polytropic gas. For more complicated systems such as those under consideration here, efficient approximate Riemann solvers such as the Roe [228], Harten-Lax-van-Leer-Einfeldt (HLLE) [229] and Advection Upstream Splitting Method (AUSM$^+$-up) [230] schemes can be used. In particular, Roe and AUSM$^+$-up approximate Riemann solvers are utilized in this research. The AUSM$^+$-up approximate Riemann solver proposed by Liou [230] is used extensively, as it is valid for a wide range of flow speeds and low-Mach numbers encountered in the premixed reactive flows of interest here. Details of the two flux functions for the Favre-filtered equations governing premixed reactive flows are given in the sections to follow.

Piecewise Limited Linear Reconstruction

Extension of the discretization to second-order spatial accuracy requires sub-cell reconstruction of the solution. A linear least-squares method is used to determine the solution gradients within each cell based on information from adjacent cells [231]. The fluxes are then computed by solving a Riemann problem defined by the reconstructed solution states at the midpoint of each cell interface:

$$
\begin{aligned}
\mathbf{U}^{\mathrm{L}}_{i+\frac{1}{2},j,k} &= \mathbf{U}^{\mathrm{L}}_{i+\frac{1}{2},j,k}\left(\mathbf{W}_{i,j,k} + \mathbf{\Phi}_{i,j,k}\nabla\mathbf{W}_{i,j,k}\cdot\Delta\vec{\mathrm{x}}_{\mathrm{L}}\right), \\
\mathbf{U}^{\mathrm{R}}_{i+\frac{1}{2},j,k} &= \mathbf{U}^{\mathrm{R}}_{i+\frac{1}{2},j,k}\left(\mathbf{W}_{i+1,j,k} + \mathbf{\Phi}_{i+1,j,k}\nabla\mathbf{W}_{i+1,j,k}\cdot\Delta\vec{\mathrm{x}}_{\mathrm{R}}\right).
\end{aligned}
\tag{5.16}
$$

Here, $\mathbf{W}$ is the vector of primitive variables, $\mathbf{\Phi}$ is a vector of slope limiters, and $\Delta\vec{\mathrm{x}}_{\mathrm{L}}$ and $\Delta\vec{\mathrm{x}}_{\mathrm{R}}$ are respectively given by

$$
\begin{aligned}
\Delta\vec{\mathrm{x}}_{\mathrm{L}} &= \vec{\mathrm{x}} - \vec{\mathrm{x}}_{i,j,k}, \\
\Delta\vec{\mathrm{x}}_{\mathrm{R}} &= \vec{\mathrm{x}} - \vec{\mathrm{x}}_{i+1,j,k},
\end{aligned}
\tag{5.17}
$$

with $\vec{\mathrm{x}}$ being the location of the interface center. Slope limiters are used to preserve monotonicity of the solution near shocks and discontinuities. For an extensive analysis of limiters the reader is referred to the review by Waterson & Deconinck [232]. Here, the Barth-Jespersen [233] and the Venkatakrishnan [234] slope limiters have been implemented. The Barth-Jespersen limiter [233], which is used extensively in the thesis, has the form

$$
\mathbf{\Phi}_{i,j,k} = \begin{cases}
\min\left(1, \dfrac{\mathbf{W}_{\max}-\mathbf{W}_{i,j,k}}{\mathbf{W}_n-\mathbf{W}_{i,j,k}}\right), & \text{if } \mathbf{W}_n - \mathbf{W}_{i,j,k} > 0, \\[2mm]
\min\left(1, \dfrac{\mathbf{W}_{\min}-\mathbf{W}_{i,j,k}}{\mathbf{W}_n-\mathbf{W}_{i,j,k}}\right), & \text{if } \mathbf{W}_n - \mathbf{W}_{i,j,k} < 0, \\[2mm]
1, & \text{if } \mathbf{W}_n - \mathbf{W}_{i,j,k} = 0,
\end{cases}
\tag{5.18}
$$

where

$$\mathbf{W}_{\text{max}} = \max\left(\mathbf{W}_{i,j,k}, \mathbf{W}_{\text{neighbours}}\right),$$
$$\mathbf{W}_{\text{min}} = \min\left(\mathbf{W}_{i,j,k}, \mathbf{W}_{\text{neighbours}}\right). \tag{5.19}$$

In the expressions above, $\mathbf{W}_{\text{neighbours}}$ denotes the vector of primitive variables for neighbouring cells and $\mathbf{W}_n$ is the unlimited reconstructed solution at the nth flux quadrature point.

Approximate Riemann Solvers

As indicated above, Godunov-type finite-volume methods require the solution of locally one-dimensional Riemann problems at cell interfaces. One approach to solve the Riemann problem consists of using an exact solution procedure as performed by Gottlieb & Groth [227] for the Euler equations governing an ideal polytropic gas. However, an approximation often suffices for use in a finite-volume scheme. Approximate solvers can be efficient and easily extended to more complex systems of partial differential equations, such as the filtered LES equations previously introduced. The most detailed upwind approximation schemes are found in the solvers of Roe [228], which is based on a local linearization of the flow equations, and Osher [235], which replaces shock waves by inverted isotropic waves [236]. Since then, other solvers have been developed, for instance HLL [237], HLLE [229], and AUSM$^+$-up [230]. In this research, the Roe and AUSM$^+$-up flux functions have been implemented and used. Both flux functions for the filtered LES equations corresponding to the PCM-FPI formulation with transported species are described next.

Roe's approximate Riemann solver makes use of a local linearization of the governing equations. The linearized Riemann problem approximates all waves by discontinuous jumps. Consider the one-dimensional inviscid form of the filtered governing equations given by

$$\frac{\partial \boldsymbol{\mathcal{U}}}{\partial t} + \frac{\partial \boldsymbol{\mathcal{F}}}{\partial x} = \frac{\partial \boldsymbol{\mathcal{U}}}{\partial t} + \frac{\partial \boldsymbol{\mathcal{F}}}{\partial \boldsymbol{\mathcal{U}}}\frac{\partial \boldsymbol{\mathcal{U}}}{\partial x} \approx \frac{\partial \boldsymbol{\mathcal{U}}}{\partial t} + \hat{\mathcal{A}}(\hat{\boldsymbol{\mathcal{U}}})\frac{\partial \boldsymbol{\mathcal{U}}}{\partial x} = 0, \tag{5.20}$$

where $\hat{\mathcal{A}}(\hat{\boldsymbol{\mathcal{U}}})$ is the flux Jacobian evaluated at a reference state, $\hat{\boldsymbol{\mathcal{U}}}$, which is a function of the left and right solution states of the Riemann problem, $\boldsymbol{\mathcal{U}}_{\text{L}}$ and $\boldsymbol{\mathcal{U}}_{\text{R}}$. Since the approximate flux Jacobian contains constant coefficients, an analytic solution can be obtained for the intercell flux. The flux can be expressed as

$$\boldsymbol{\mathcal{F}}_{i+\frac{1}{2}} = \frac{1}{2}(\boldsymbol{\mathcal{F}}_{\text{L}} + \boldsymbol{\mathcal{F}}_{\text{R}}) - \frac{1}{2}\sum_m^{\mathcal{N}}\hat{\alpha}_m|\hat{\lambda}_m|\hat{\mathbf{R}}_m, \tag{5.21}$$

where $\mathcal{N}$ is the number of conservation laws in the system of equations. A suitable reference

state, $\hat{\boldsymbol{\mathcal{U}}}$, can be constructed for the evaluation of the eigenvalues, $\hat{\lambda}_m$, right eigenvectors, $\hat{\mathbf{R}}_m$, and wave-strengths, $\hat{\alpha}_m$, of the approximate flux Jacobian in terms of the left and right solution values. The reference state was designed such that the approximate flux Jacobian, $\hat{\mathcal{A}}$, satisfies the conditions: (i) $\hat{\mathcal{A}}$ has real eigenvalues with a complete set of linearly independent eigenvectors so that the system remains strictly hyperbolic; (ii) it should be consistent with the exact flux Jacobian, if $\boldsymbol{\mathcal{U}}_{\mathrm{R}} = \boldsymbol{\mathcal{U}}_{\mathrm{L}} = \boldsymbol{\mathcal{U}}$, then one should have $\hat{\mathcal{A}} = \frac{\partial \boldsymbol{\mathcal{F}}}{\partial \boldsymbol{\mathcal{U}}}|_{\boldsymbol{\mathcal{U}}}$; and (iii) it should ensure conservation across discontinuities, $\boldsymbol{\mathcal{F}}(\boldsymbol{\mathcal{U}}_{\mathrm{R}}) - \boldsymbol{\mathcal{F}}(\boldsymbol{\mathcal{U}}_{\mathrm{L}}) = \hat{\mathcal{A}}(\boldsymbol{\mathcal{U}}_{\mathrm{R}} - \boldsymbol{\mathcal{U}}_{\mathrm{L}})$ [228].

For the governing equations previously introduced, the Roe-averaged velocity components, $\hat{u}$, $\hat{v}$, and $\hat{w}$, sensible enthalpy, $\hat{h}_{\mathrm{s}}$, SFS turbulence kinetic energy, $\hat{k}_{\Delta}$, progress of reaction, $\hat{Y}_{\mathrm{c}}$, variance of the progress of reaction, $\hat{Y}_{\mathrm{c_v}}$, and the species mass fractions, $\hat{Y}_{\beta}$, are all given by the the relation

$$\hat{\boldsymbol{\Psi}} = \frac{\sqrt{\rho_{\mathrm{L}}}\boldsymbol{\Psi}_{\mathrm{L}} + \sqrt{\rho_{\mathrm{R}}}\boldsymbol{\Psi}_{\mathrm{R}}}{\sqrt{\rho_{\mathrm{L}}} + \sqrt{\rho_{\mathrm{R}}}}, \tag{5.22}$$

where $\boldsymbol{\Psi}_{\mathrm{L}}$ and $\boldsymbol{\Psi}_{\mathrm{R}}$ are the left and right state vectors of the quantities listed above, and the Roe-averaged density, $\hat{\rho}$, is determined by $\hat{\rho} = \sqrt{\rho_{\mathrm{L}}\rho_{\mathrm{R}}}$. The eigenvalues of the approximate Jacobian for the system considered here are given by

$$\hat{\lambda}_1 = \hat{u} - \hat{a}, \ \ \hat{\lambda}_{2,3,4} = \hat{u}, \ \ \hat{\lambda}_5 = \hat{u} + \hat{a}, \ \ \hat{\lambda}_{6,\dots,8+N} = \hat{u}, \tag{5.23}$$

where $\hat{a}$ is the Roe-averaged speed of sound.

Roe's approximate Riemann solver is valid for shock and contact waves. An entropy fix is necessary to account for the fact that the Roe's approximate Riemann solver cannot reasonably represent expansion waves associated with acoustic waves having wave speeds $\hat{\lambda}_1$ and $\hat{\lambda}_5$ in the vicinity of sonic points. The averaged eigenvalues, $|\hat{\lambda}_m|$, in Roe's flux function are replaced by Harten's entropy fix [238] to increase the magnitude of these two acoustic waves near sonic points such that $|\hat{\lambda}_m|^*$ is given by

$$|\hat{\lambda}_m|^* = \begin{cases} |\hat{\lambda}_m| & \text{if } |\hat{\lambda}_m| \geq \frac{\Delta\lambda_m}{2}, \\ \frac{\hat{\lambda}_m^2}{\Delta\lambda_m} + \frac{\Delta\lambda_m}{4} & \text{if } |\hat{\lambda}_m| < \frac{\Delta\lambda_m}{2}, \end{cases} \tag{5.24}$$

where $\Delta\lambda_m = \max\left(0, 4[\lambda_m(\boldsymbol{\mathcal{U}}_{\mathrm{R}}) - \lambda_m(\boldsymbol{\mathcal{U}}_{\mathrm{L}})]\right)$, with $m = 1, 5$. This procedure avoids the prediction of unphysical expansion shocks.

The AUSM$^+$-up scheme is valid at all speed regimes, including low-Mach number flows. In the AUSM-family of schemes the inviscid flux is split into convective and pressure contributions to the flux. Considering the one-dimensional inviscid fluxes for the PCM-FPI equations presented

above, the fluxes can be decomposed as

$$\mathcal{F} = \mathcal{F}_c + \mathcal{P} = \dot{m}\psi + \mathcal{P} = \bar{\rho}\tilde{u}
\begin{bmatrix}
1 \\
\tilde{u} \\
\tilde{v} \\
\tilde{w} \\
\tilde{H} \\
k_\Delta \\
\tilde{Y}_c \\
\tilde{Y}_{c_v} \\
\tilde{Y}_1 \\
\vdots \\
\tilde{Y}_N
\end{bmatrix}
+
\begin{bmatrix}
0 \\
\breve{p} \\
0 \\
0 \\
0 \\
0 \\
0 \\
0 \\
0 \\
\vdots \\
0
\end{bmatrix}, \tag{5.25}$$

where $\tilde{H}$ is the total Favre-filtered enthalpy ($\tilde{H} = \tilde{E} + \bar{p}/\bar{\rho}$) and $\breve{p}$ is a modified pressure given by $\breve{p} = \bar{p} + \bar{\rho}k_\Delta$. The numerical flux at the cell interface, $\mathcal{F}_{1/2}$, can be expressed in terms of the mass flux $\dot{m} = \bar{\rho}\tilde{u}$ and the vector of convected quantities, $\psi = [1, \tilde{u}, \tilde{v}, \tilde{w}, \tilde{H}, k_\Delta, \tilde{Y}_c, \tilde{Y}_{c_v}, \tilde{Y}_1, \ldots, \tilde{Y}_N]^T$, as

$$\mathcal{F}_{1/2} = \dot{m}_{1/2}\psi_{L/R} + \mathcal{P}_{1/2}, \tag{5.26}$$

where $\psi_{L/R}$ stands for the left or right vector of convected quantities, determined by a simple upwind scheme

$$\psi_{L/R} = \begin{cases} \psi_L, & \text{if } \dot{m}_{1/2} > 0, \\ \psi_R, & \text{otherwise}. \end{cases} \tag{5.27}$$

The mass flux, $\dot{m}_{1/2}$, is determined by

$$\dot{m}_{1/2} = u_{1/2}\rho_{L/R} = a_{1/2}M_{1/2} \begin{cases} \rho_L, & \text{if } u_{1/2} > 0, \\ \rho_R, & \text{otherwise}, \end{cases} \tag{5.28}$$

where $u_{1/2}$ is the interface convective velocity, $a_{1/2}$ is the interface speed of the sound, $M_{1/2}$ is the interface Mach number, and $\rho_{L/R}$ is the left or right density convected by $u_{1/2}$. The interface Mach number is computed in terms of the flow Mach number in the left and right neighbour cells, M_L and M_R, respectively, using

$$M_{1/2} = \mathfrak{M}^+_{(m)}(M_L) + \mathfrak{M}^-_{(m)}(M_R) + M_p. \tag{5.29}$$

The split Mach numbers, $\mathfrak{M}^\pm_{(m)}$, are polynomial functions of degree $m = 1, 2, 4$, as given in

Reference [239]. They have the form

$$\mathfrak{M}_{(4)}^{\pm}(M) = \begin{cases} \mathfrak{M}_{(1)}^{\pm}, & \text{if } |M| \geq 1, \\ \mathfrak{M}_{(2)}^{\pm}(1 \mp 16\xi\mathfrak{M}_{(2)}^{\mp}), & \text{otherwise}, \end{cases} \tag{5.30}$$

where

$$\mathfrak{M}_{(1)}^{\pm}(M) = \frac{1}{2}(M \pm |M|), \tag{5.31}$$

$$\mathfrak{M}_{(2)}^{\pm}(M) = \pm\frac{1}{4}(M \pm 1)^2. \tag{5.32}$$

The left or right Mach number, $M_{\text{L/R}}$, is defined by the left or right convective velocity, $u_{\text{L/R}}$, and the interface speed of sound, $a_{1/2}$, as follows:

$$M_{\text{L/R}} = \frac{u_{\text{L/R}}}{a_{1/2}}. \tag{5.33}$$

The pressure diffusion term, M_{p}, introduced to enhance low-speed or multi-phase flow calculations, is defined by

$$M_{\text{p}} = -\frac{K_{\text{p}}}{f_{\text{a}}}\max(1 - \sigma_{\text{p}}\check{M}^2, 0)\frac{p_{\text{R}} - p_{\text{L}}}{\rho_{1/2}a_{1/2}^2}, \tag{5.34}$$

where

$$\rho_{1/2} = \frac{\rho_{\text{L}} + \rho_{\text{R}}}{2}, \tag{5.35}$$

$$a_{1/2} = \frac{a_{\text{L}} + a_{\text{R}}}{2}, \tag{5.36}$$

and

$$\check{M}^2 = \frac{u_{\text{L}}^2 + u_{\text{R}}^2}{2a_{1/2}}, \tag{5.37}$$

with $0 \leq K_{\text{p}} \leq 1$ and $\sigma_{\text{p}} \leq 1$. The scaling factor, f_{a}, is defined in terms of the reference Mach number, M_0, by the relation

$$f_{\text{a}}(M_0) = M_0(2 - M_0) \in [0, 1], \tag{5.38}$$

where the reference Mach number is given by

$$M_0^2 = \min(1, \max(\check{M}^2, M_\infty^2)) \in [0, 1], \tag{5.39}$$

and M_∞ is a representative Mach number for the flow of interest. The formula for evaluating the pressure flux has the form

$$p_{1/2} = \mathfrak{P}_{(n)}^{+}(M_{\text{L}})p_{\text{L}} + \mathfrak{P}_{(n)}^{-}(M_{\text{R}})p_{\text{R}} + p_{\text{u}}, \tag{5.40}$$

where $n = 1, 3, 5$ corresponds to the degree of the polynomials $\mathfrak{P}^{\pm}$, as in $\mathfrak{M}^{\pm}$. The fifth-degree polynomials proposed by Liou [239] are preferred for more accurate solutions. They are also expressed in terms of the split Mach number and can be written as

$$
\mathfrak{P}^{\pm}_{(5)}(M) = \begin{cases} \frac{1}{M}\mathfrak{M}^{\pm}_{(1)}, & \text{if } |M| \geq 1, \\ \mathfrak{M}^{\pm}_{(2)}[(\pm 2 - M) \mp 16\Upsilon M\mathfrak{M}^{\mp}_{(2)}], & \text{otherwise}, \end{cases}
\tag{5.41}
$$

and the velocity diffusion term, p_{u}, is evaluated as

$$
p_{\mathrm{u}} = -K_{\mathrm{u}}\mathfrak{P}^{+}_{(5)}(M_{\mathrm{L}})\mathfrak{P}^{-}_{(5)}(M_{\mathrm{R}})(\rho_{\mathrm{L}} + \rho_{\mathrm{R}})(f_{\mathrm{a}}a_{1/2})(u_{\mathrm{R}} - u_{\mathrm{L}}),
\tag{5.42}
$$

employing the parameters

$$
\Upsilon = \frac{3}{16}(-4 + 5f_{\mathrm{a}}^{2}) \in \left[-\frac{3}{4}, \frac{3}{16}\right],
\tag{5.43}
$$

$$
\xi = \frac{1}{8},
\tag{5.44}
$$

with $0 \leq K_{\mathrm{u}} \leq 1$. In this research, $K_{\mathrm{p}} = 0.25$, $K_{\mathrm{u}} = 0.75$, and $\sigma_{\mathrm{p}} = 0.75$ are utilized.

5.2.3   Viscous Flux Evaluation

Evaluation of the viscous component of the numerical flux depends upon both the solution values and their gradients at the cell interface

$$
\vec{\mathcal{F}}_{i+\frac{1}{2},j,k} \cdot \vec{n}_{i+\frac{1}{2},j,k} = \mathcal{F}\left(\mathbf{W}_{i+\frac{1}{2},j,k}, \nabla\mathbf{W}_{i+\frac{1}{2},j,k}\right),
\tag{5.45}
$$

where $\mathbf{W}_{i+\frac{1}{2},j,k}$ is the solution vector of primitive variables at the cell interface, which is determined by averaging the reconstructed values of the left and right cells at the interface and given by

$$
\mathbf{W}_{i+\frac{1}{2},j,k} = \frac{\mathbf{W}_{\mathrm{L}} + \mathbf{W}_{\mathrm{R}}}{2}.
\tag{5.46}
$$

In this research, $\nabla\mathbf{W}_{i+\frac{1}{2},j,k}$ is calculated by employing the weighted cell-face gradient approach proposed by Mathur & Murthy [240]. In this approach, the cell-face gradient is determined using

$$
\nabla\mathbf{W}_{i+\frac{1}{2},j,k} = \frac{\mathbf{W}_{i+1,j,k} - \mathbf{W}_{i,j,k}}{ds}\frac{\vec{n}}{\vec{n} \cdot \vec{e}_s} + \left(\langle\nabla\mathbf{W}\rangle - \langle\nabla\mathbf{W}\rangle \cdot \vec{e}_s\frac{\vec{n}}{\vec{n} \cdot \vec{e}_s}\right),
\tag{5.47}
$$

with

$$
\langle\nabla\mathbf{W}\rangle = \vartheta\nabla\mathbf{W}_{i,j,k} + (1 - \vartheta)\nabla\mathbf{W}_{i+1,j,k}.
\tag{5.48}
$$

Here, ds is the distance between the two adjacent cell centres and $\vec{e}_s$ is the unit vector along the direction of ds. The weighting factor, ϑ, is based on cell volume ratios and has the form

$$\vartheta = \frac{V_{i,j,k}}{V_{i,j,k} + V_{i+1,j,k}} \, . \tag{5.49}$$

The procedure for the viscous flux evaluation is depicted in Figure 5.1 for a two-dimensional computational grid. The procedure is also directly applicable to the three-dimensional case. Furthermore, for a Cartesian grid, it can be shown that Equation 5.47 is equivalent to a second-order central difference approximation to the cell-face solution gradient.
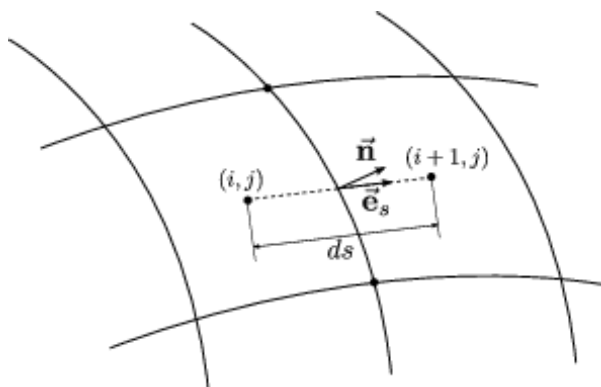
Figure 5.1: Weighted cell-face gradient approach for a two-dimensional grid.

5.2.4   Time Marching Scheme

The set of coupled non-linear ordinary differential equations (ODEs) resulting from the spatial discretization procedure given by Equation 5.14 can be solved by applying a time-marching scheme to advance the solution forward in time. Since a second-order accurate scheme is used in the spatial discretization, a time-marching scheme having the same order of accuracy is used for consistency. Various time-marching methods exist and are used for different purposes. For more information on time marching schemes, the reader is referred to the books by Lomax, Pulliam & Zingg [241], Ferziger & Perić [242], or Hirsch [243, 244]. For the unsteady LES calculations of interest here, the explicit second-order Runge-Kutta scheme is employed. This scheme provides the desired second-order accuracy, requiring low storage and computational operations per time step.

The time step is limited by the inviscid Courant-Friedrichs-Lewy (CFL) stability, viscous von Neumann stability, and chemical time-step constraints. The inverse of the maximum diagonal value of the chemical source term Jacobian is included in the time step calculation. A stable

time step, Δt, is then determined by

$$\Delta t = \min\left(\mathrm{CFL}\frac{\Delta l}{|\vec{\breve{u}}| + \breve{a}}\,,\, \frac{\alpha}{2}\frac{\Delta l^2}{\max(\breve{\nu}, \nu_\mathrm{t})}\,,\, \frac{\xi}{\max\left(\mathbf{J}_{ii}\right)}\right)\,, \tag{5.50}$$

where Δl is the characteristic cell-face length of a cell, $\breve{a}$ is the sound speed computed in terms of LES resolved quantities, and $\breve{\nu}$ and ν_t are the kinematic viscosity evaluated in terms of LES resolved quantities and the eddy viscosity, respectively. Additionally, $\mathbf{J} = \frac{\partial \mathbf{S}}{\partial \mathbf{U}}$ is the source term Jacobian. The coefficients α and ξ are appropriate scaling factors, which are applied to the viscous and chemistry-related constraints, respectively. The following values were employed in the computations: $\alpha = 2/3$ and $\xi = 1/2$.

5.3   Block-Based Adaptive Mesh Refinement

Adaptive mesh refinement (AMR) algorithms automatically adapt the mesh to the solution of the governing equations. AMR permits local mesh refinement and helps to minimize the number of computational cells required for a particular computation. Although the simulations reported herein did not employ AMR, the LES algorithms have been fully coupled with the AMR framework as part of this thesis work and will therefore be briefly described herein. A more detailed account can be found in the Ph.D. thesis by Gao [245]. The three-dimensional block-based AMR scheme has been implemented by Gao [246] and Northrup & Groth [247]. Based on the approach developed by Groth *et al.* [248, 249] for computational magnetohydro-dynamics, a flexible block-based hierarchical data structure is used to facilitate the automatic solution-directed mesh adaptation of a multi-block body-fitted mesh according to physics-based refinement criteria. In the AMR scheme, each of the structured blocks of the computational mesh consists of $N_\mathrm{x} \times N_\mathrm{y}$ quadrilateral cells in two space dimensions and $N_\mathrm{x} \times N_\mathrm{y} \times N_\mathrm{z}$ hexahedral cells in the three-dimensional case, where N_x, N_y and N_z are even but not necessarily equal integers. Mesh adaptation is achieved by dividing and coarsening grid blocks. In regions requiring higher cell resolution, a "parent" block is refined by dividing itself into four or eight "children" or "offspring" depending on the dimensionality. Each of the four or eight children of a parent block has the same number of cells as the parent. The refinement process can be reversed and four or eight children are coarsened or merged into a single parent block. Figure 5.2 displays two neighbouring hexahedral blocks of a three-dimensional mesh, the top block has undergone one level of refinement. The refined grid consists of nine blocks.

The refining and coarsening of blocks are directed using multiple physics-based refinement criteria [250]. The following refinement criteria can be used: density gradient, divergence of velocity, vorticity of the flow field, gradient of temperature, or gradient of species mass fractions. To
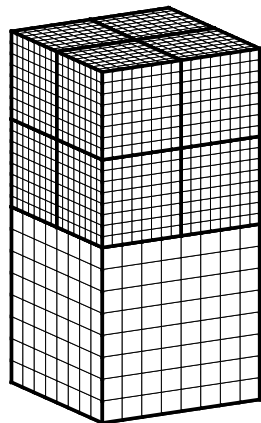
Figure 5.2: An example of two neighbouring $8 \times 8 \times 8$ hexahedral solution blocks. One has undergone refinement [246].

maintain the connectivity of the solution blocks in the multi-block mesh, quadtree and octree data structures are used in the two- and the three-dimensional cases, respectively. Figure 5.3(a) shows two-dimensional multi-block quadrilateral AMR mesh solution blocks at various levels of refinement. Figure 5.3(b) illustrates the corresponding quadtree data structure used to keep track of mesh refinement and the connectivity between solution blocks. Figure 5.4 depicts a three-dimensional multi-block hexahedral AMR mesh consisting of solution blocks at various levels of refinement and the associated octree data structure. The quadtree/octree data structure keeps track of the refinement level and connectivity between grid blocks during isotropic refinement processes. Although it is not strictly anisotropic, the refinement approach preserves original stretching of the mesh and allows for anisotropic mesh and improved treatment of thin boundary and shear layers.

To allow data to be exchanged between adjacent blocks having common interfaces, each block has additional layers of overlapping "ghost" cells, which contain solution information from neighbouring blocks. The information of the "ghost" cells between adjacent blocks is exchanged after each time step. Figures 5.5(a) and 5.5(b) show the ghost cells used for two- and three-dimensional solution blocks, respectively.

(a) Multi-block refinement
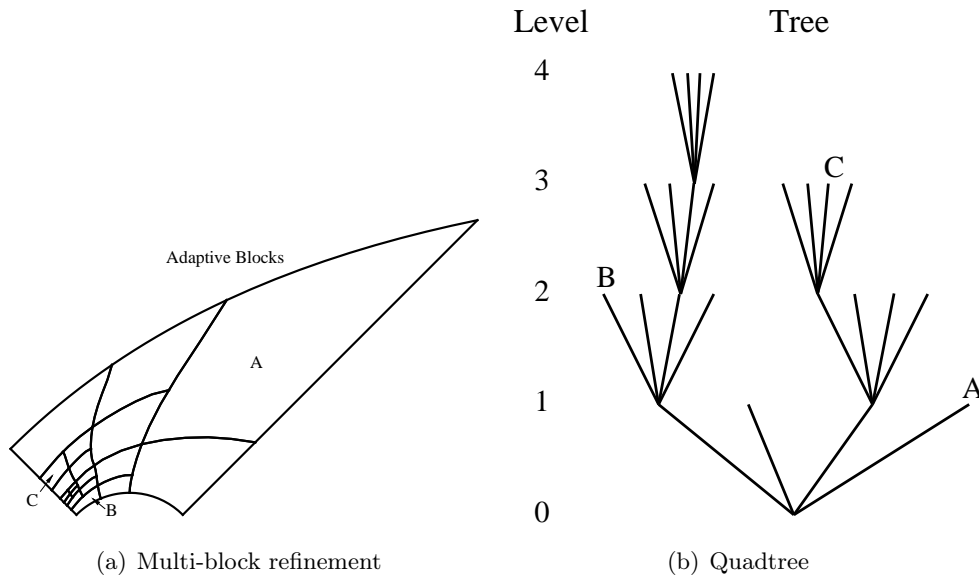
(b) Quadtree

Figure 5.3: Multi-block quadrilateral AMR mesh showing solution blocks at various levels of refinement and the corresponding quadtree data structure [246].
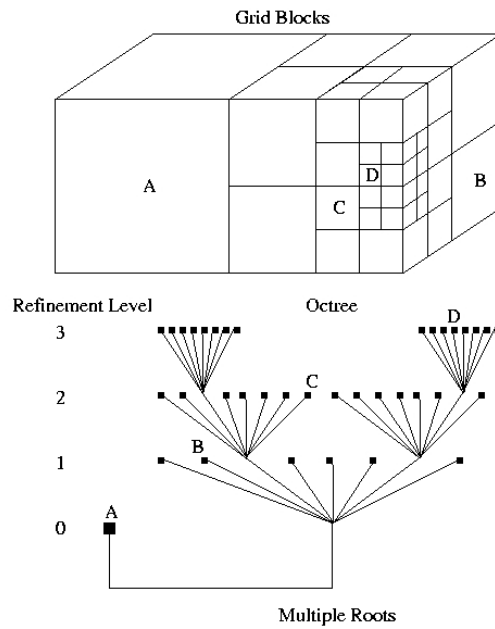
Figure 5.4: Multi-block hexahedral AMR mesh showing solution blocks at various levels of refinement and the corresponding octree data structure [246].

5.4 Domain Decomposition and Parallel Implementation

A parallel implementation of the block-based AMR finite-volume scheme has been performed utilizing the C++ programming language and the message passing interface (MPI) library [246,

(a) Two space dimensions   (b) Three space dimensions
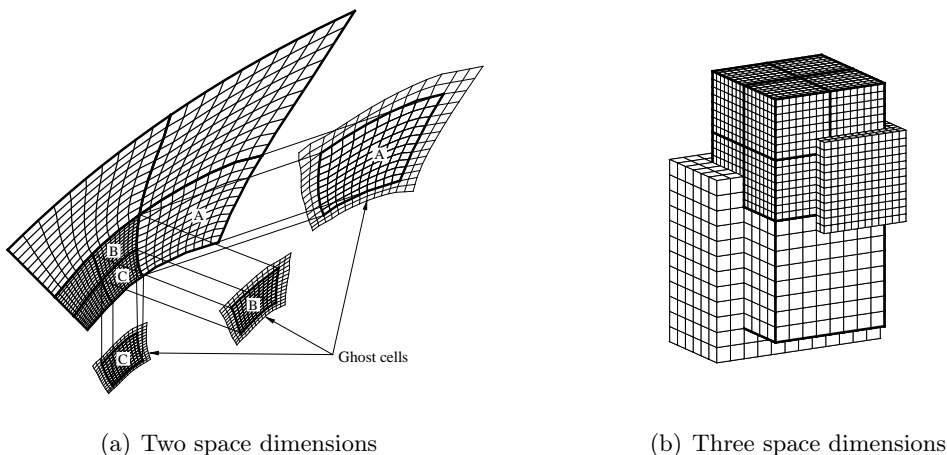
Figure 5.5: Two layers of overlapping "ghost" cells contain solution information from neighbouring blocks [246].

251]. Domain decomposition is carried out by distributing the computational solution blocks on separate processors, with more than one block permitted on each processor. For homogeneous architectures with multiple processors all of equal speed, an effective load balancing is accomplished by exploiting the self-similar nature of the solution blocks and distributing the blocks equally among the processors. Inter-processor communication is mainly related to block interfaces and involves the exchange of ghost-cell solution values and conservative flux corrections at every stage of the multi-stage time integration procedure. Message passing of the ghost-cell values and flux corrections are carried out in an asynchronous fashion with gathered wait states and message consolidation [252].

Chapter 6

Validation and Applications

In this chapter, numerical simulation results for the thickened flame and PCM-FPI models applied to the prediction of premixed flames in one, two, and three spatial dimensions are described and discussed. Freely propagating flames in isotropic decaying turbulence and Bunsen-type flames corresponding to stoichiometric and lean methane-air and lean hydrogen-enriched methane-air mixtures are considered. The predictions of the PCM-FPI model are compared to those obtained with the thickened flame model, which are further compared with FSD model predictions for two-dimensional methane-air flames. Comparisons of thickened flame and PCM-FPI predicted solutions are also made with experimental data and DNS results for a stoichiometric flame on a slot burner. Moreover, the thickened flame and PCM-FPI models have been applied to a Bunsen-type burner and the predictions are compared to FSD model numerical results and experimental data. Finally, the PCM-FPI model is applied to the prediction of lean hydrogen-enriched methane-air flames. Two-dimensional freely propagating flames in isotropic decaying turbulence and three-dimension Bunsen-type flames are studied. In addition, the computed Bunsen flame results are compared to experimental data. The numerical results provide validation of the LES methodology pursued in this research and demonstrate the predictive capabilities of the thickened flame and PCM-FPI models. In particular, the potential of the PCM-FPI model to predict observed behaviour of hydrogen-enriched methane-air flames is explored and examined. The conditions of all the cases that have been studied and examined are summarized in Table 6.1 and plotted in the premixed combustion regime diagram of Peters [113], which is shown in Figure 6.1.

The Favre-filtered transport equations associated with each model are solved on multi-block quadrilateral or hexahedral meshes employing the second-order accurate parallel finite-volume scheme that was outlined in Chapter 5. The inviscid flux at each cell face is evaluated using

Case	Flame configuration	Fuel	$\frac{n_{H_2}}{n_{H_2}+n_{CH_4}}$	ϕ	L_t (mm)	u' (m/s)	δ_L (mm)	s_L (m/s)
A	2D Freely propagating	CH_4	0	1	6.47	2.6	0.44	0.39
B	2D Freely propagating	CH_4	0	1	6.47	4.0	0.44	0.39
C	2D Freely propagating	CH_4	0	1	6.47	8.0	0.44	0.39
D	3D Slot	CH_4	0	1	5.2	0.3	0.44	0.39
E	3D Bunsen	CH_4	0	0.7	1.79	2.9	0.68	0.201
F	2D Freely propagating	CH_4	0	0.52	1.5	1.5	1.77	0.061
G	2D Freely propagating	H_2-CH_4	0.29	0.52	1.5	1.5	1.31	0.081
H	3D Bunsen	CH_4	0.0	0.6	3	0.17	0.99	0.117
I	3D Bunsen	H_2-CH_4	0.2	0.6	3	0.17	0.89	0.136

Table 6.1: Summary of conditions of the cases that have beed studied.

limited linear reconstruction and Riemann-solver based flux functions. Particularly, the Roe flux function with the Venkatakrishnan limiter were utilized for the computation of the steady-state solutions reported herein, while the AUSM$^+$-up flux function with the Barth-Jespersen limiter were used for unsteady solutions. The viscous fluxes were evaluated utilizing a diamond-path reconstruction in the one- and two-dimensional cases and a weighted cell-face gradient method in the three-dimensional cases. The explicit second-order Runge-Kutta scheme was used to time-march unsteady computations. Unless otherwise explicitly stated, a one-step chemical kinetic scheme was utilized in the thickened flame model simulations and the constant-coefficient one-equation eddy-viscosity model was used to determine the eddy-viscosity employed in the SFS modelling. The model coefficients C_ϵ, C_ν, and ζ^* were set to 0.845, 0.086, and 0.25, respectively. Additionally, the SFS Prandtl and Schmidt numbers used in the gradient approximation to the SFS scalar fluxes were set to 0.6 and 1.0, respectively.

Computations were carried out on a cluster of Intel Xeon E5540 (2.53 GHz) nodes interconnected with non-blocking 4x-DDR Infiniband. Computational parameters and CPU times for the performed three-dimensional LES simulations are summarized in Table 6.2. For the slot flame (case D), the CPU requirements of PCM-FPI without solving transport equations for the species mass fractions were 186% higher as compared to the thickened flame model. For the lean Bunsen flame (case E), the thickened flame model required the least amount of CPU time, while PCM-FPI was the most expensive approach when transport equations for the species mass fractions were solved, increasing the CPU time by a factor of 6.75 as compared to the thickened flame. Solving transport equations for the species mass fractions in the PCM-FPI model lead to a 103% increase in computational costs as compared to direct tabulation of species mass fractions. Finally, the computational costs associated with PCM-FPI transporting the species were higher than those associated with the FSD model by 55%.
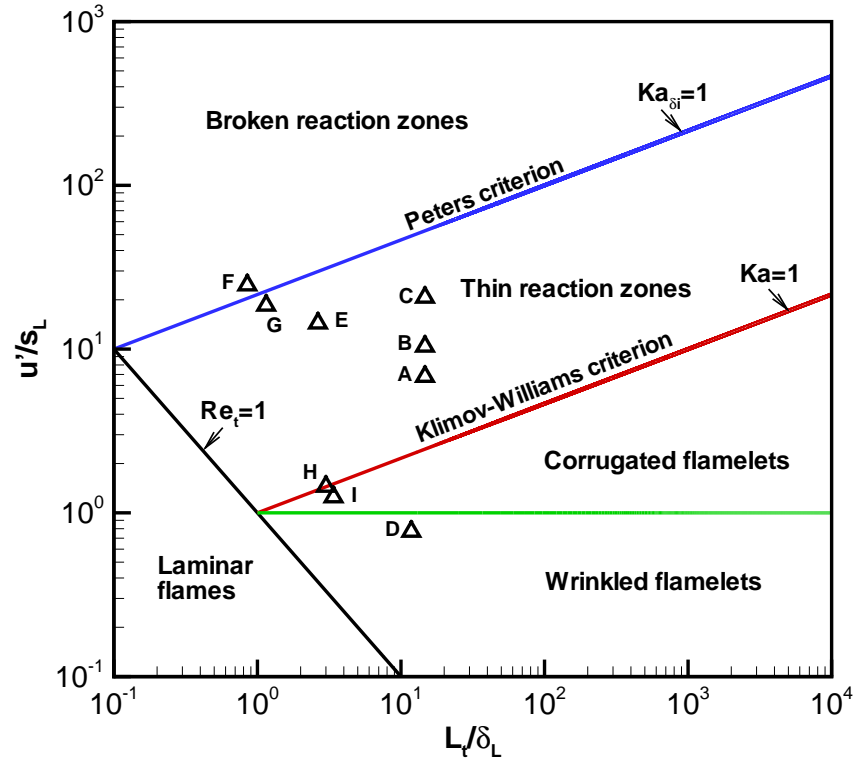
Figure 6.1: Turbulent premixed combustion regime diagram of Peters [113], showing the conditions of the cases that have been studied (empty triangles).

Case	Model	Number of species	Number of PDEs	Number of cells	Time (ms)	CPU time (hr)	Normalized CPU time
D	TF ($F=5$)	5	10	1,966,080	25	41,836	4.07
	PCM-FPI-SP	10	8	1,966,080	25	118,427	11.53
E	TF ($F=3$)	5	10	1,638,400	9	10,273	1.0
	FSD	5	8	1,638,400	9	44,735	4.35
	PCM-FPI-SP	10	8	1,638,400	9	34,012	3.31
	PCM-FPI-RR	10	17	1,638,400	9	69,375	6.75
H, I	PCM-FPI-RR	14	21	1,638,400	100	513,933	50.03

Table 6.2: Summary of computational parameters for the performed three-dimensional LES simulations. TF: thickened flame. PCM-FPI-SP: PCM-FPI approach, tabulating mass fractions directly from the look-up tables. PCM-FPI-RR: PCM-FPI approach, transporting the species and using reconstructed reaction rates.

6.1 One-Dimensional Laminar Methane-Air Flames

The validation of the thickened flame and PCM-FPI implementations was first examined for a one-dimensional laminar premixed flame under stoichiometric and atmospheric conditions. This

is a prototype problem that provides an initial test for the validity of the implemented models in the current LES computational framework with the parallel AMR finite-volume solution procedure. Since the flow under consideration was laminar, the LES filter width was set to zero and, thereby, the SFS scale terms in the Favre-filtered equations vanished.

A rectangular computational domain having a length of 0.05 m and a height of 0.000625 m was used. A base mesh consisting of 2 cells in the vertical direction and 200 cells in the horizontal direction (direction of flame propagation) was employed for unthickened flames. For thickened flames, thickening factors $F = 5$, $F = 10$ and $F = 20$ were utilized, with a decreased number of 160 cells in the direction of the flame propagation. Near the center of the domain, the meshes were stretched to cluster cells where the flame front was located. The inlet and outlet velocity and pressure were adjusted such that the mass flux remained constant throughout the domain and a stationary flame structure could be obtained. Other inlet initial conditions were held constant, whereas the remaining outlet properties were all extrapolated from the interior of the domain. Denoting inlet and outlet conditions with subscripts 1 and 2, respectively, the outlet pressure can be calculated using the relation $p_2 = p_1 - \rho_1 u_1 (u_1 - u_2)$.

The predicted temperature, velocity and pressure distributions of the stoichiometric thickened flames are shown in Figure 6.2. The predicted distributions computed with thickening factors $F = 5$, $F = 10$ and $F = 20$ are all in good agreement with the unthickened flame solution ($F = 1$). It should be noted that all of these solutions were obtained with a simple one-step reaction mechanism. The predicted flame speeds, $s_L = 0.38$ m/s, compare well with the flame speed obtained with Cantera and GRI-Mech 3.0, $s_L = 0.39$ m/s. However, the temperature in the burned gas is overpredicted by approximately 94 K. This overprediction is expected due to the simplified chemical kinetic scheme. The flame speeds and temperatures in the burned gas are summarized in Table 6.4. A pressure drop of approximately 1 Pa across the flame front is also verified [25]. The chemical structure of the thickened flames is depicted in Figure 6.3. The equilibrium values of all the species match those of the unthickened flame, despite the artificial thickening imposed by the model.

(a) Temperature distribution

(b) Velocity distribution

(c) Pressure distribution
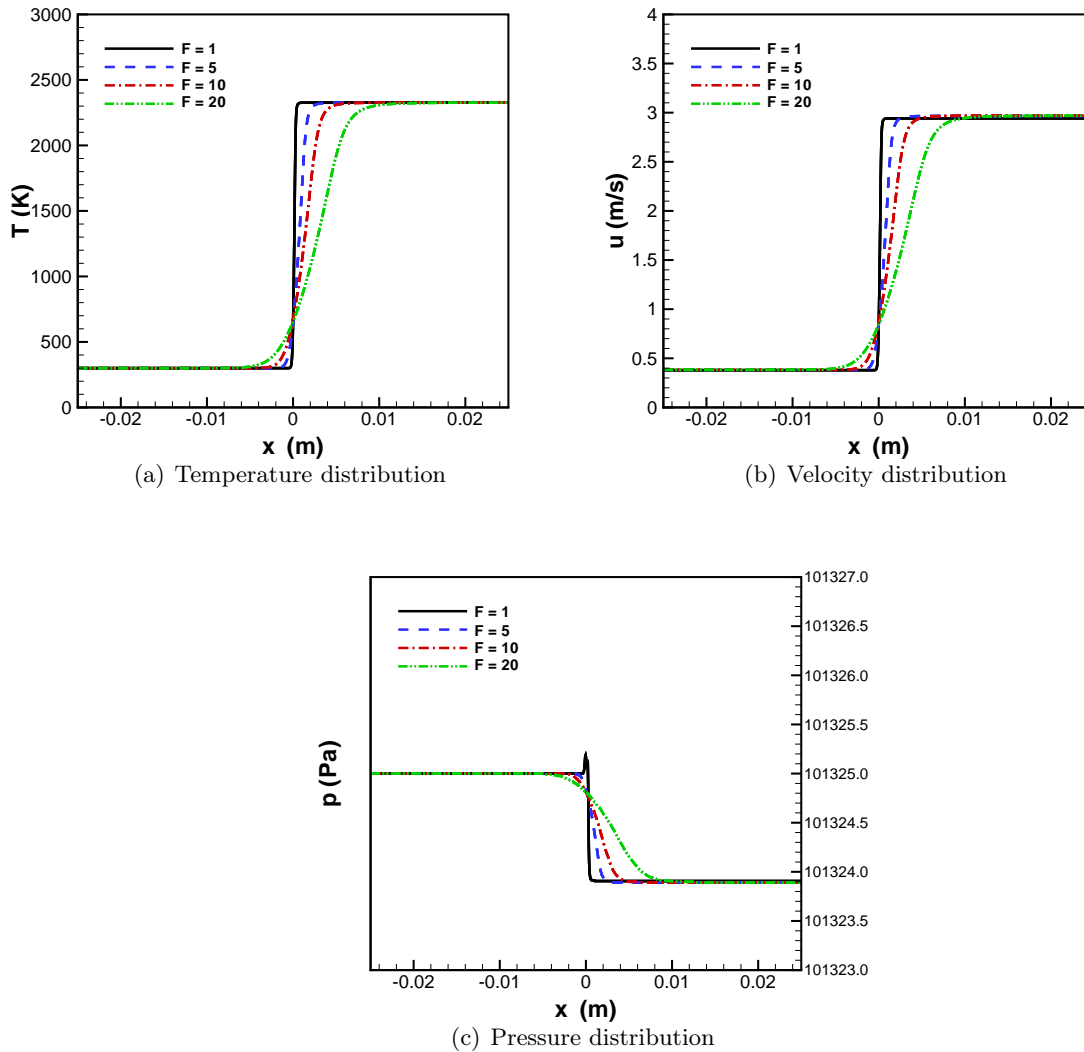
Figure 6.2: Temperature, velocity and pressure distribution of 1D steady-state stoichiometric methane-air thickened flames.

As for the PCM-FPI model, two approaches were tested. In the first approach, the values of the species mass fractions were directly updated from the look-up table. This approach is referred to as FPI-SP. In the second approach, the species were transported and the reactions rates were reconstructed using the method described in Chapter 4. This approach is referred to as FPI-RR. A reduced number of 10 species were selected and tabulated, as outlined in subsection 4.1.5 of Chapter 4, for methane-air flames. The species and their respective Schmidt numbers are given in Table 6.3.

The predicted pressure, velocity, and temperature distributions of the stoichiometric flames using the two PCM-FPI approaches are shown in Figure 6.4 and compared to the solution computed

(a) CH$_4$ mass fraction

(b) O$_2$ mass fraction

(c) CO$_2$ mass fraction

(d) H$_2$O mass fraction
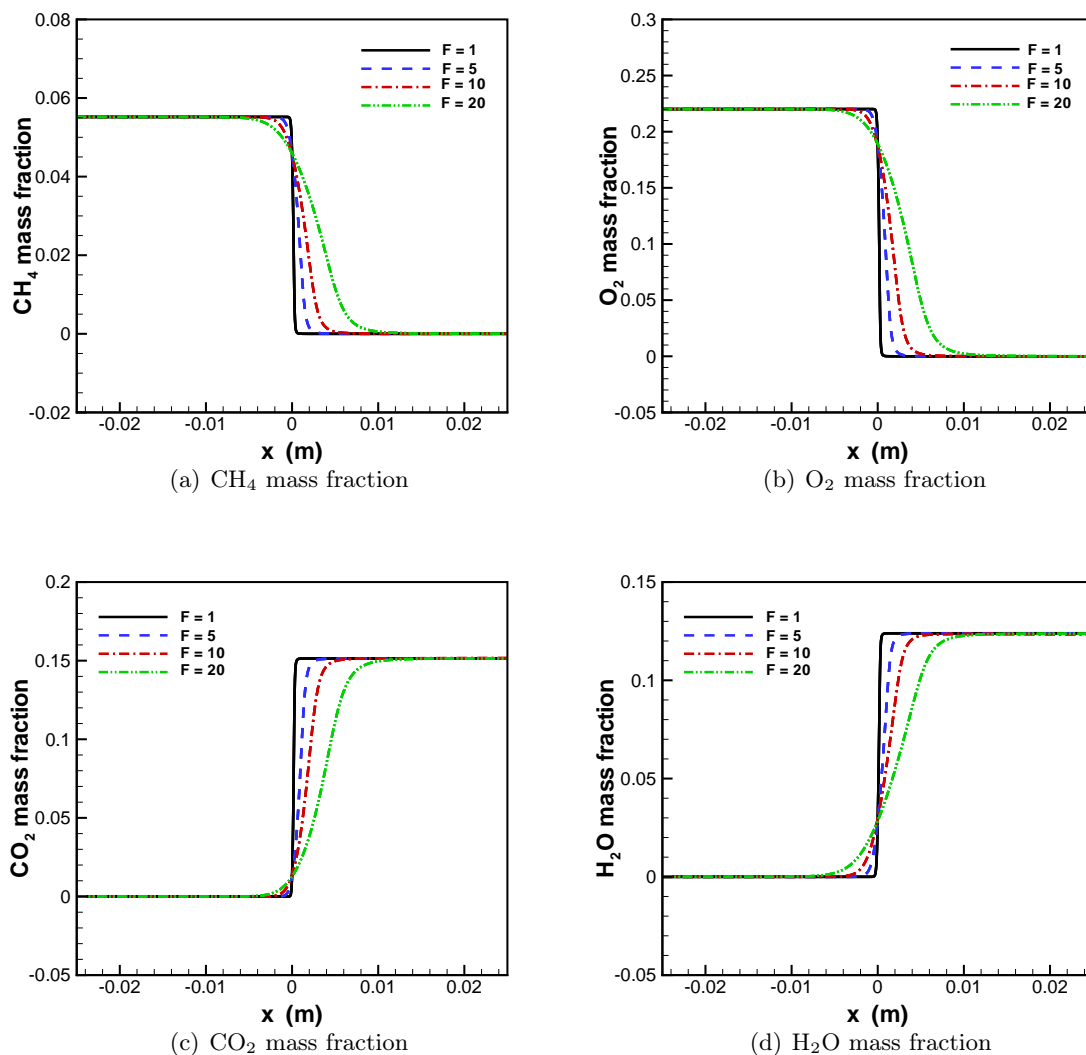
Figure 6.3: Structure of 1D steady-state stoichiometric methane-air thickened flames.

Schmidt numbers, $\phi = 1.0$									
CH$_4$	O$_2$	N$_2$	H$_2$O	CO$_2$	CO	H$_2$	H	OH	C$_2$H$_2$
0.685	0.746	0.734	0.551	0.956	0.757	0.208	0.124	0.494	0.893

Table 6.3: Schmidt numbers of the species for a stoichiometric methane-air premixed flame, taken from the Cantera solution in the burned gas.

with Cantera. The pressure drop of nearly 1 Pa is recovered in both PCM-FPI solutions, whereas Cantera assumes a constant pressure. The pressure jump leads to discrepancies in the flow velocity, in particular, in the burned gas. Nonetheless, the two flame speeds, $s_L = 0.4$ m/s, compare well with that obtained with Cantera and GRI-Mech 3.0, $s_L = 0.39$ m/s. The temperature in the burned gas differs to that of Cantera by only 5 K. The flame speeds
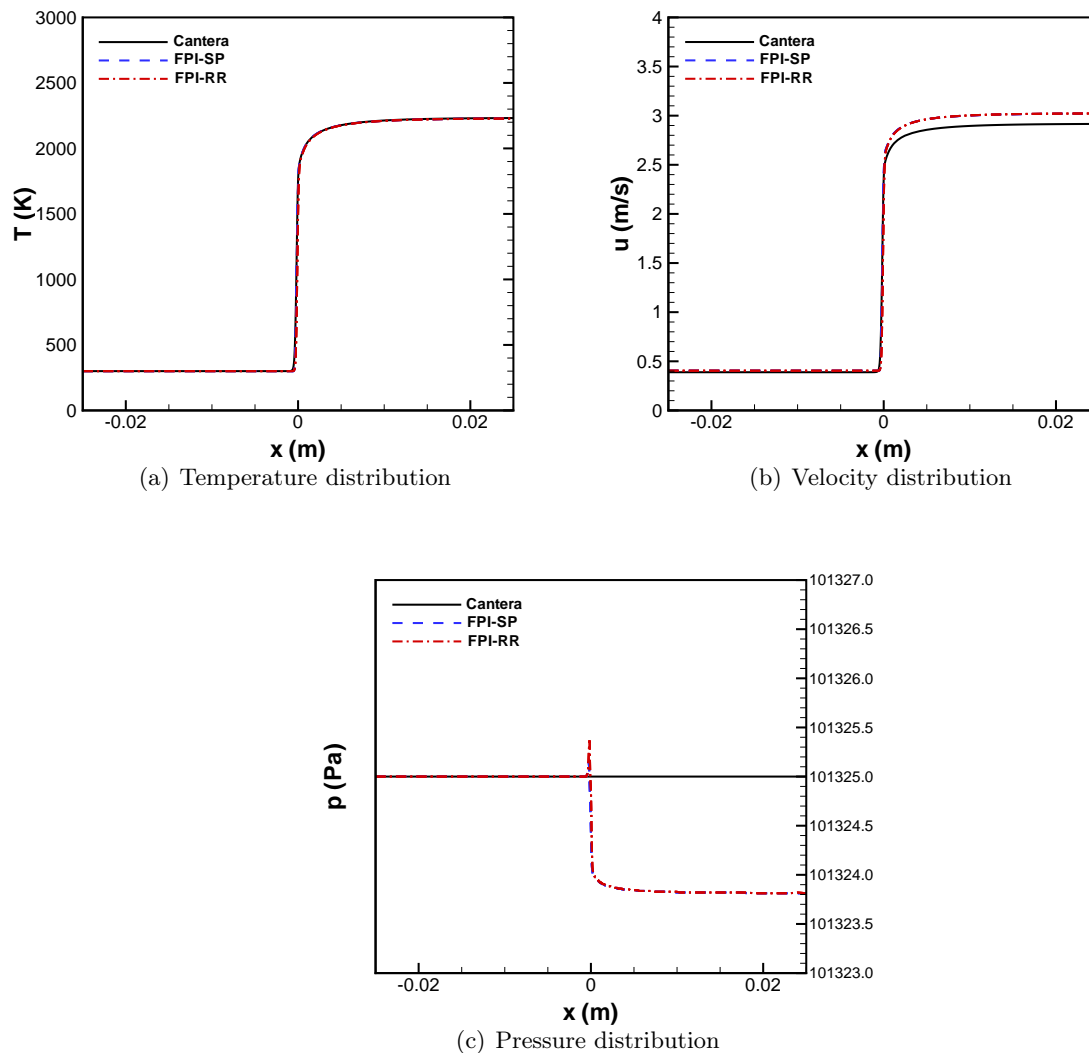
Figure 6.4:   Temperature, velocity and pressure distributions of 1D steady-state stoichiometric methane-air flames.

and temperatures in the burned gas are all summarized in Table 6.4. Overall, a rather good agreement is found for the predicted flame speeds and burned gas temperatures. The chemical structure of the flames computed with PCM-FPI is depicted in Figures 6.5 and 6.6. All in all, the predicted profiles of the species closely follow the profiles given by the Cantera solution with detailed chemistry, except for H_2. Discrepancies in the H_2 profiles are the result of tabulating chemistry with a reduced number of 10 species. As it was mentioned above, the mass fraction of H_2 was determined via the atom-balance for element H. To improve the prediction of H_2, more species containing H need to be included in the set of tabulated species. This will be considered for H_2-enrichment of methane, which has been discussed in Chapter 4.

(a) CH_4 mass fraction

(b) O_2 mass fraction

(c) CO_2 mass fraction

(d) H_2O mass fraction
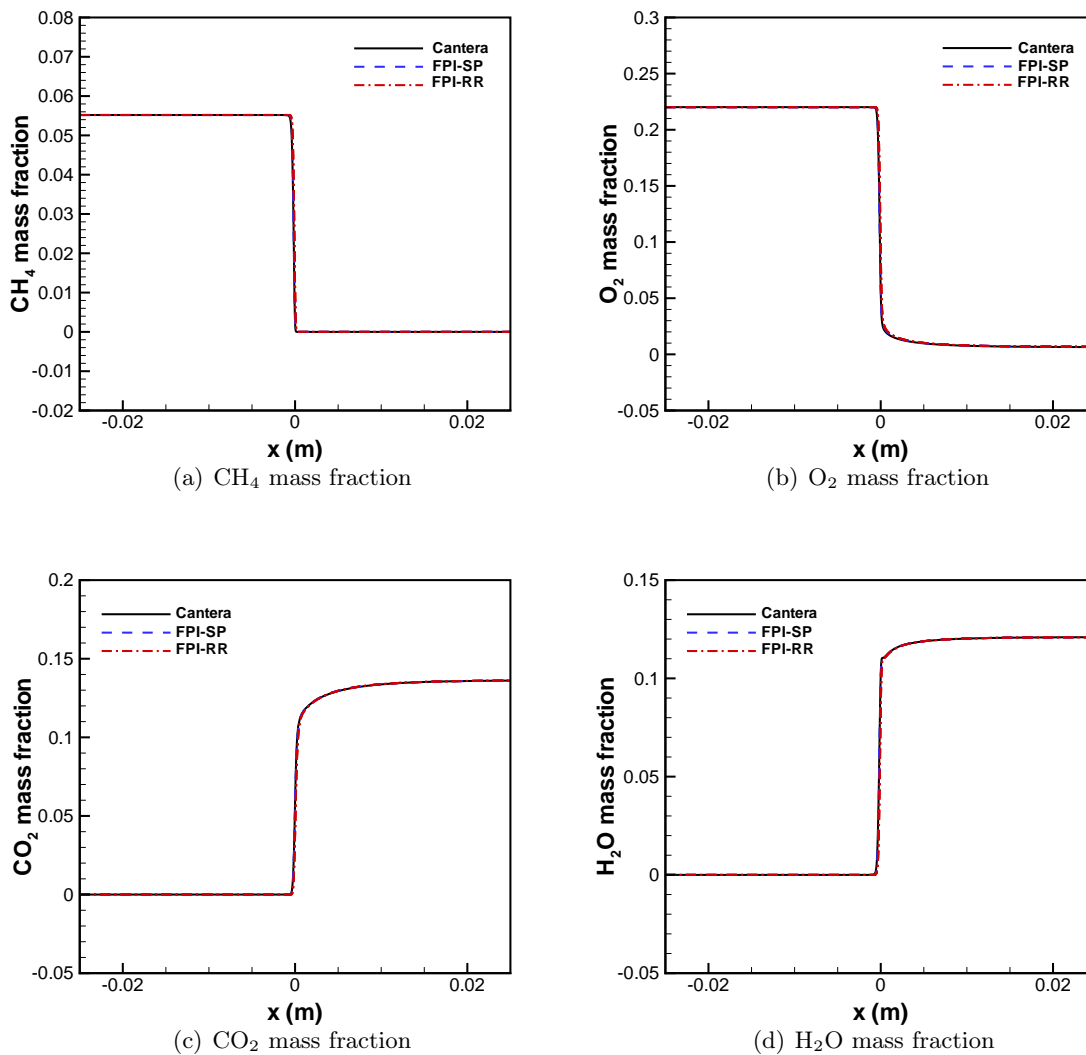
Figure 6.5: Major species of 1D steady-state stoichiometric methane-air flames.

	Cantera	Thickened Flame				PCM-FPI	
		$F=1$	$F=5$	$F=10$	$F=20$	FPI-SP	FPI-RR
s_L (m/s)	0.39	0.38	0.38	0.38	0.38	0.4	0.4
T_b (K)	2233	2327	2327	2327	2327	2228	2228

Table 6.4: Summary of predicted flame speeds and temperatures in the burned gas for a stoichiometric methane-air premixed flame. Thickened flame model with a one-step reaction mechanism and thickening factors $F=1$, $F=5$, $F=10$, and $F=20$. PCM-FPI model with 10 species reading mass fractions directly (FPI-SP) and transporting the species using reconstructed reaction rates (FPI-RR).

(a) CO mass fraction

(b) OH mass fraction

(c) H mass fraction

(d) H_2 mass fraction
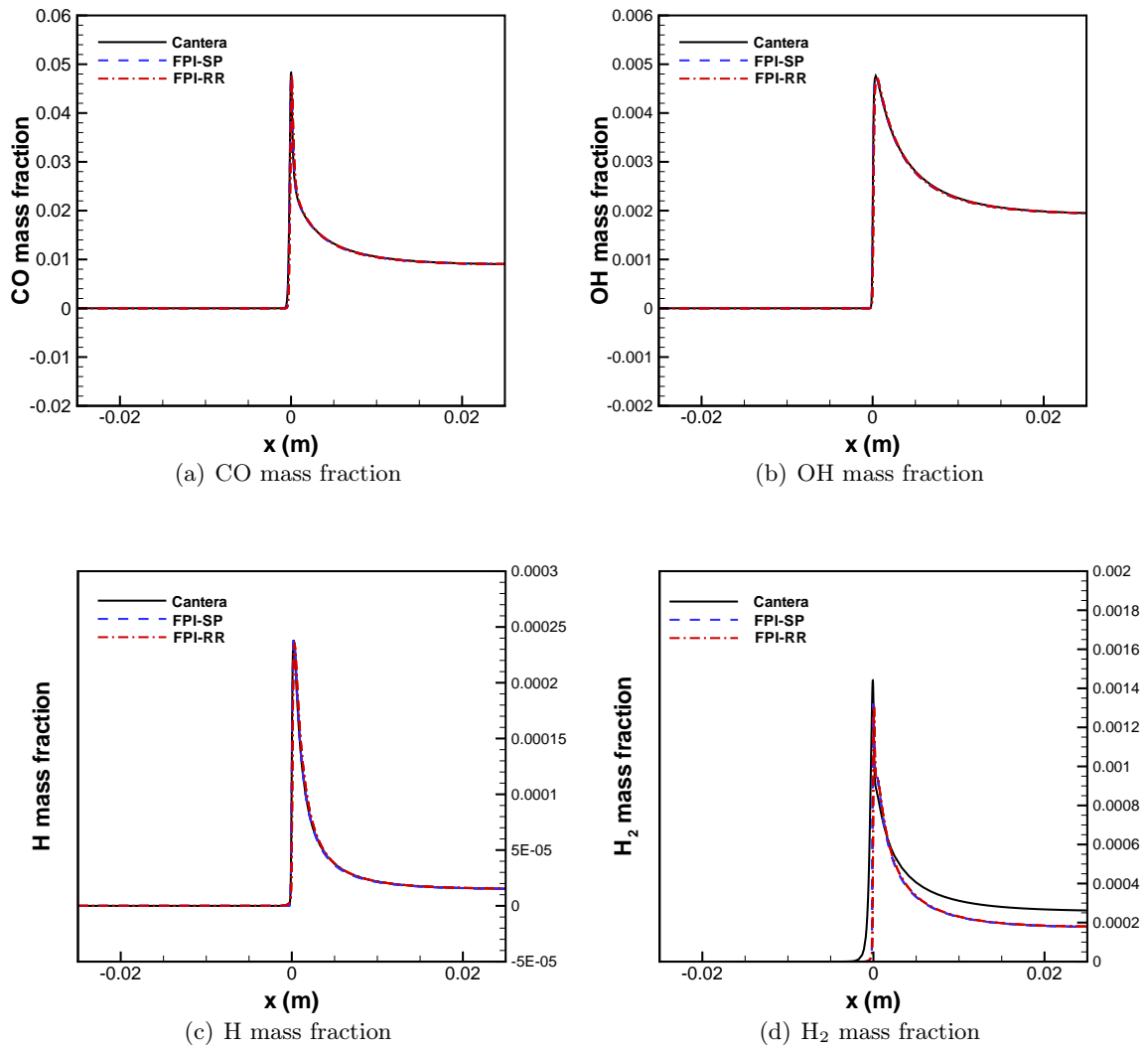
Figure 6.6: Minor species of 1D steady-state stoichiometric methane-air flames.

6.2   Decay of Three-Dimensional Homogeneous Isotropic Turbulence

As a starting point for validation of the multi-species LES implementation including all the SFS terms, the decay of three-dimensional homogeneous isotropic turbulence was considered. For this configuration, Kolmogorov's -5/3 law and a rate of decay of the turbulent kinetic energy proportional to $t^{-1.25\pm0.06}$ [253] are expected to be recovered. A cubic domain of size $2\pi \times 2\pi \times 2\pi$ m^3, discretized with $64 \times 64 \times 64 = 262,144$ hexahedral cells, was employed for the simulation. The mesh was uniform and periodic boundary conditions were utilized for all the boundaries of the domain. The filter width was $\Delta = 2h$, where h stands for the local mesh size ($h = 2\pi/64$). The fluid under consideration was air, treated as consisting of 21% oxygen (O_2) and 79% nitrogen (N_2) on a molar basis.

The turbulent velocity field was initialized by prescribing a synthetic turbulent kinetic energy spectrum and employing Rogallo's [254] procedure to generate an approximate homogeneous isotropic field, which is described in Appendix A. The energy spectrum was taken to have the form [255]

$$E(\kappa) = \frac{32}{2} \sqrt{\frac{2}{\pi}} \frac{u'^2}{\kappa_0} \left(\frac{\kappa}{\kappa_0}\right)^4 \exp\left(-2\left(\kappa/\kappa_0\right)^2\right) . \tag{6.1}$$

In the above expression, u' stands for the target rms velocity and κ_0 is the wavenumber corresponding to the peak of the energy spectrum. For the case under study, $\kappa_0 = 3.2$ m^{-1}. The initial turbulent field was characterized by an integral length scale $L_t = 0.66$ m and a turbulent intensity $u' = 10$ m/s. More than 9 integral length scales were then represented in the domain.

The initial turbulent kinetic energy spectrum as well as the turbulent kinetic energy spectrum of the solution after 50, 250, 500, and 1000 ms are all depicted in Figure 6.7. It can be seen that Kolmogorov's -5/3 law forms quickly after the initiation of the simulation and is maintained as time progresses, but the energy density lowers for the represented wavenumbers. The time evolution of the total, resolved, and SFS turbulent kinetic energy is shown in Figure 6.8(a). For a short period of time, the total, resolved, and SFS turbulent kinetic energy remain relatively constant, followed by a decrease in the total and resolved turbulent kinetic energy and an increase in the SFS turbulent kinetic energy, indicating a transfer of energy from resolved to SFS scales. After about 200 ms, the resolved and SFS turbulent kinetic energies start to decay and after approximately 250 ms, the asymptotic rate of decay is reached. For comparison, the line corresponding to a rate of decay $t^{-1.25}$ is also plotted. The predicted rate of decay of the turbulent kinetic energy is in close agreement with the $t^{-1.25}$ line. The relative contributions of the resolved and SFS components to the total turbulent kinetic energy are also displayed in

Figure 6.8(b). Once the asymptotic rate of decay is attained, the fractions of both components vary slightly, with more than 85% of turbulent kinetic energy being resolved.
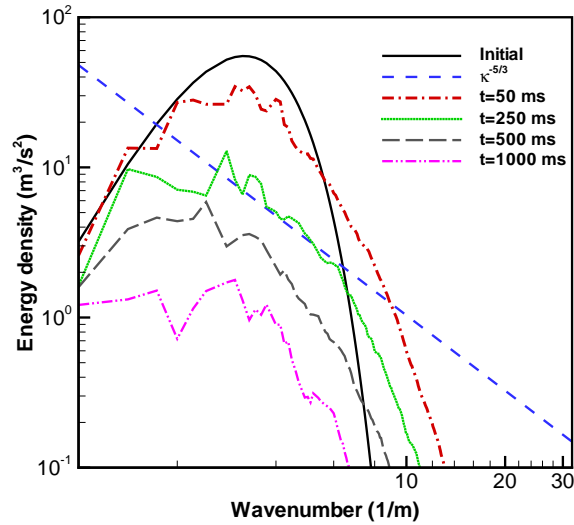
Figure 6.7: Evolution of the turbulence kinetic energy spectrum for the decay of homogeneous isotropic turbulence case.

To visualize the decay of turbulence, coherent structures of the turbulent flow field can also be identified and shown. For a review on criteria to detect coherent vortices, the reader is referred to Dubief & Delcayre [256]. The so called Q-criterion [257] is employed herein, which is defined

(a) Decay of turbulence kinetic energy

(b) Relative turbulence kinetic energy
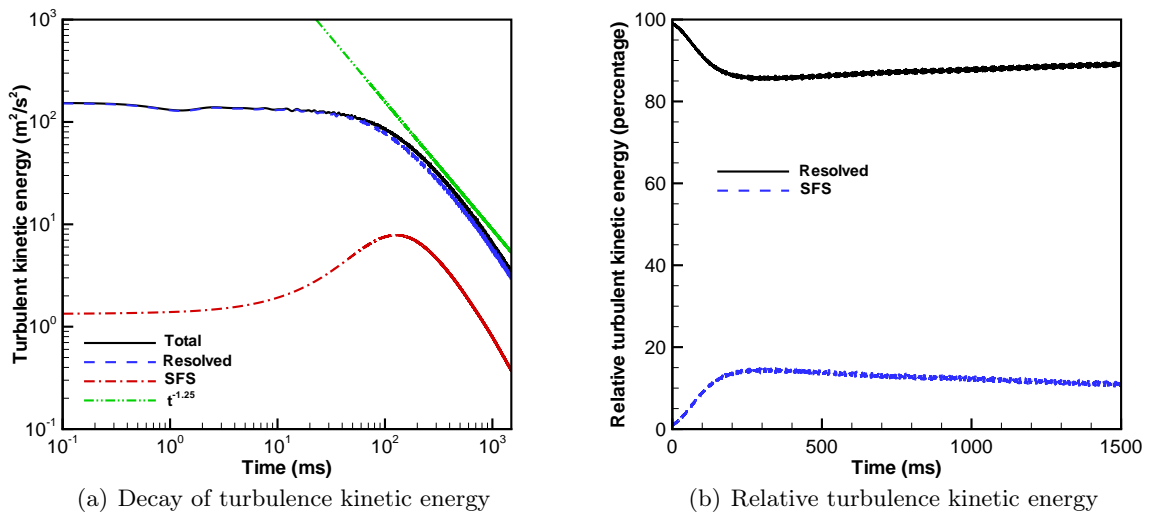
Figure 6.8: Evolution of turbulence kinetic energy for the decay of homogeneous isotropic turbulence case.

by

$$Q = \frac{1}{2}(\Omega_{ij}\Omega_{ij} - S_{ij}S_{ij}) = \frac{1}{4}(|\vec{\omega}|^2 - |S|)\,, \tag{6.2}$$

where S_{ij} and Ω_{ij} are the strain- and rotation-rate tensors, respectively, and $\vec{\omega}$ is the vorticity vector. The two tensors, evaluated in terms of the Favre-filtered velocity, are given by

$$\check{S}_{ij} = \frac{1}{2}\left(\frac{\partial \tilde{u}_i}{\partial x_j} + \frac{\partial \tilde{u}_j}{\partial x_i}\right)\,, \qquad \check{\Omega}_{ij} = \frac{1}{2}\left(\frac{\partial \tilde{u}_i}{\partial x_j} - \frac{\partial \tilde{u}_j}{\partial x_i}\right)\,. \tag{6.3}$$

Positive values of Q are associated with regions where vorticity dominates straining. The iso-surfaces corresponding to $Q = 0.5(u'/L_\mathrm{t})^2 \approx 115 \text{ s}^{-2}$ are illustrated in Figure 6.9 at $t = 50$, 250, 500, and 1000 ms of physical time for the simulation. It is evident that as time evolves, the turbulence decays and the number of coherent vortices decreases. In particular, coherent vortices are significantly dissipated once the asymptotic period of decay is achieved. Vortex stretching is clearly observed through the elongated turbulent structures. This behaviour is expected and has been reported in previous DNS results and experimental studies [130]. The preceding results provide some comfort in the ability of the proposed compressible flow solution method and modelling framework to perform LES.

6.3   Two-Dimensional Freely Propagating Methane-Air Flames

As a next step towards the validation of the implemented SFS modelling approaches for turbulent premixed combustion in three-dimensional configurations, numerical simulations of two-dimensional freely propagating turbulent premixed flames were performed. Even though it can be argued that two-dimensional turbulence considerably differs from three-dimensional turbulence, curvature statistics suggest that the three-dimensional topology of a propagating surface is mainly two-dimensional [258, 259]. In addition, the moderate computational cost associated with two-dimensional simulations, as compared to three-dimensional ones, allows to assess the influence of relevant parameters (e.g., filter width, mesh resolution, and so forth) on the predicted solutions. The two-dimensional simulations also provide a basis for analysing the subsequent three-dimensional results which will follow.

A freely propagating stoichiometric methane-air premixed flame was considered. The two-dimensional flame was initialized by introducing a one-dimensional laminar premixed flame on to a rectangular computational domain with isotropic turbulence and having dimensions $L_\mathrm{x} = 0.0366$ m and $L_\mathrm{y} = 0.0342$ m. The initial homogeneous isotropic turbulent flow field was generated by prescribing a specified synthetic energy spectrum [255] and using Rogallo's

(a) Time 50 ms

(b) Time 250 ms

(c) Time 500 ms

(d) Time 1000 ms
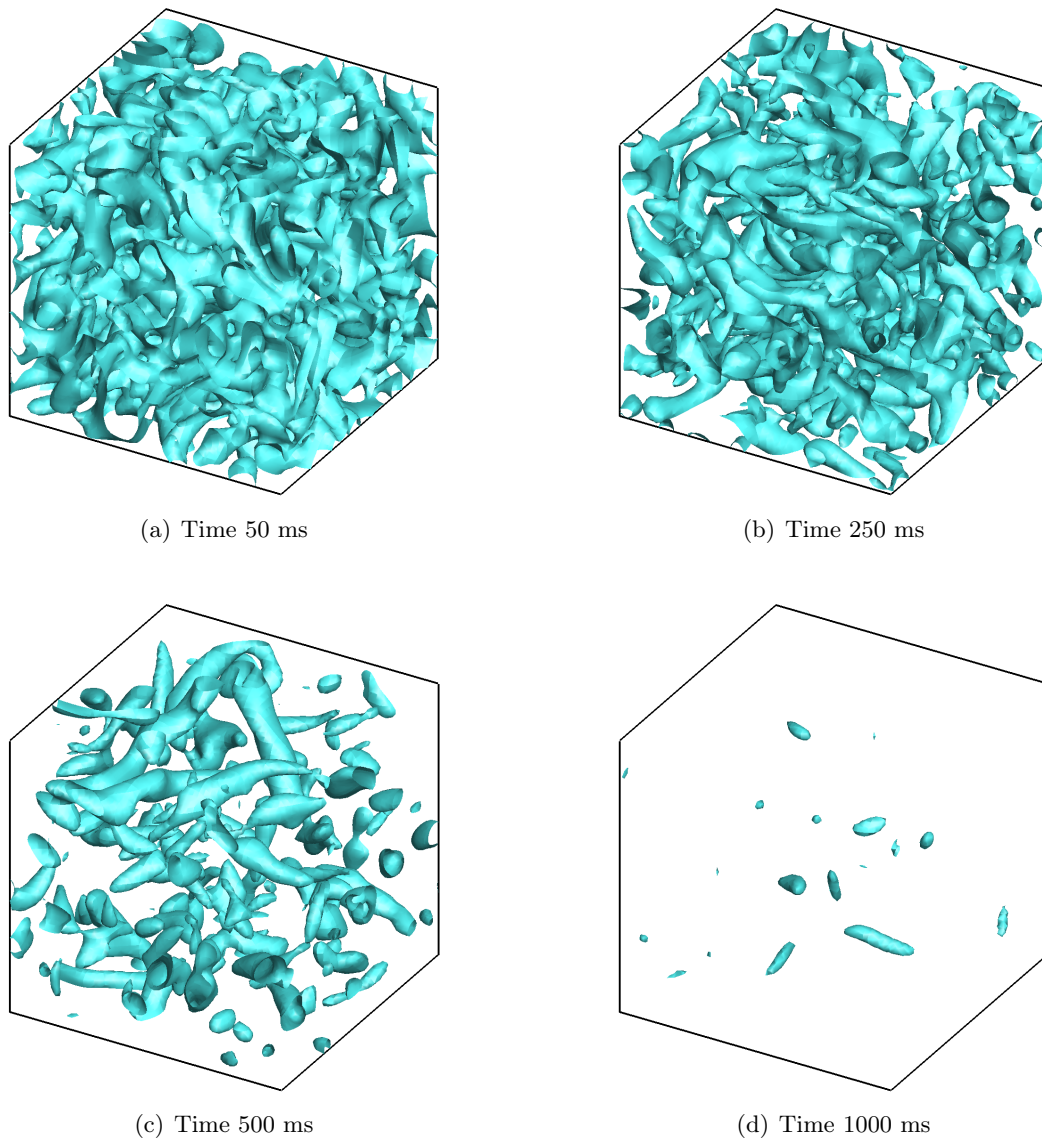
Figure 6.9: Q-criterion iso-surfaces corresponding to $Q\!=\!115\ \mathrm{s}^{-2}$ at 50, 250, 500, and 1000 ms. Decay of homogeneous isotropic turbulence case.

procedure [254]. The parameters characterizing the initial conditions for a reference turbulent flame are: turbulence intensity, $u'\!=\!2.6$ m/s; integral length scale, $L_\mathrm{t}\!=\!6.47$ mm; Taylor scale, $\lambda_\mathrm{T} = 0.832$ mm; Kolmogorov scale, $\eta = 0.06$ mm; and Reynolds number based on the Taylor scale, $Re_{\lambda_\mathrm{T}}\!=\!137$. Other parameters pertaining to the laminar methane-air flame are: laminar flame speed, $s_\mathrm{L} = 0.39$ m/s; and laminar flame thickness, $\delta_\mathrm{L} = 0.44$ mm. The computational domain contained approximately 5.6 integral length scales and 44 Taylor length scales in the direction of flame propagation at the beginning of the simulation. The flame propagated from the right to the left. Subsonic boundary conditions were prescribed at inflow (left) and outflow

(right) boundaries, and periodic boundary conditions were applied at the top and bottom of the domain.

First, the influence of the grid resolution on the predicted LES solution for the freely propagating flame was examined using three different grids having 64×50, 128×120, and 256×240 computational cells. The filter width was kept constant and corresponded to two times the grid spacing of the 128×120 mesh. To illustrate the effect of the grid on the solution, the predicted contours of methane mass fraction at 0.6 ms (approximately two eddy turnovers based on Taylor scale) and the time evolution of global burning rates based on fuel consumption are shown in Figure 6.10, for a thickened flame with a thickening factor $F = 5$. The global burning rate for this case is expressed as

$$s_{\mathrm{T}} = \frac{1}{\bar{\rho}_{\mathrm{r}} \tilde{Y}_{\mathrm{F_r}} L_{\mathrm{y}}} \int_A \tilde{\dot{\omega}}_{Y_{\mathrm{F}}} \, \mathrm{d}A \,, \qquad (6.4)$$

where $\bar{\rho}_{\mathrm{r}}$ is the filtered density of the reactants, $\tilde{Y}_{\mathrm{F_r}}$ is the Favre-filtered fuel mass fraction in the reactants, L_{y} is the height of the computational domain, and A stands for area. It can be seen that all of the predicted methane contours display a fairly similar flame structure. In particular, the contours corresponding to the two finer grids (128×120 and 256×240 cells) are in closer agreement with each other. As for the coarsest grid, the flame front is thicker and less wrinkling is resolved. The predicted burning rate associated with the coarsest grid is overpredicted as compared to those associated with the finer grids. From these observations it can be concluded that the 128×120 cell mesh provided enough resolution to obtain a grid-independent solution.

Next, a study of the filter width effect on the solution was conducted. A base grid of 128×120 cells was utilized with a reference filter width, Δ_0, equivalent to two times the grid spacing. Two other filter widths, one larger ($2\Delta_0$) and one smaller ($0.5\Delta_0$) than the reference filter width were used as well. Figure 6.11 depicts the predicted contours of methane mass fraction at a time corresponding to 0.6 ms and the time history of the decay of turbulence intensity, u'. No significant difference is observed from the fuel mass fraction contours, other than a slight thickening of the flame front when the largest filter width is employed. However, Figure 6.11(d) shows that as the filter width is increased, turbulence decays faster. This trend is expected, since an increase in the filter width leads to an increase in the eddy viscosity of the SFS modelling.

Predicted solutions of the thickened flame were also compared to the transported flame surface density (FSD) model of Hawkes & Cant [56], as implemented by Lin [168]. The same computational domain described above and base grid (128×120 cells) were employed for the comparison. Numerical results for three different levels of turbulence intensity are shown in Figure 6.12. The parameters characterizing the initial turbulent velocity field are: $u'/s_{\mathrm{L}} = 6.8$, 10.4, 20.7, $L_{\mathrm{T}} = 6.4$ mm, $\lambda_{\mathrm{T}} = 0.83$ mm. The predicted contours of methane mass fraction

(a) CH_4 mass fraction: 64×60 cells

(b) CH_4 mass fraction: 128×120 cells

(c) CH_4 mass fraction: 256×240 cells

(d) Burning rate comparison
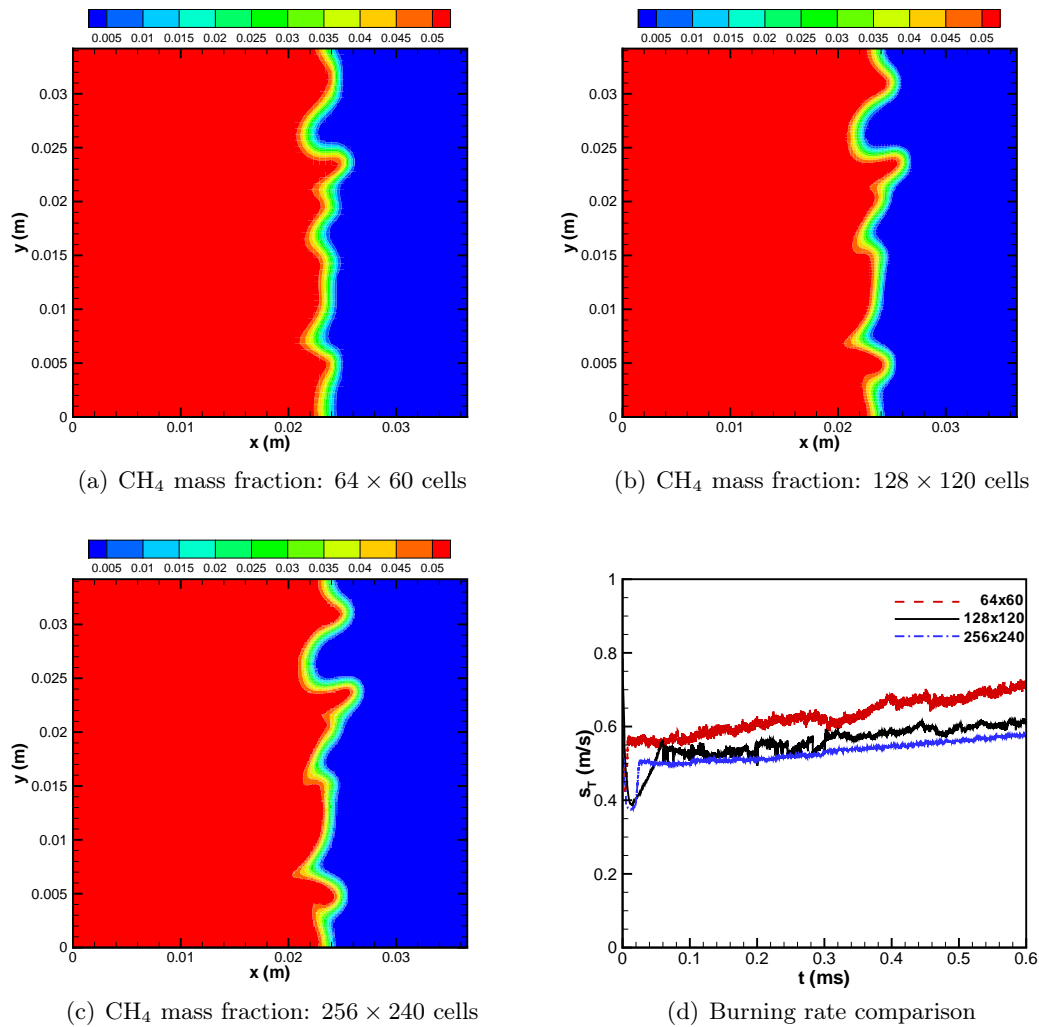
Figure 6.10: Mesh resolution influence on the solution of a 2D freely propagating turbulent premixed methane-air flame. Thickened flame model, $F = 5$.

at a time corresponding to 0.6 ms illustrate the strong influence of the turbulence intensity on the predicted flame structure. For both the thickened flame and FSD models, there is a significant increase in the resolved flame front wrinkling with turbulence intensity. Comparing the two models, the overall agreement between the predicted flames geometries is rather good. Differences are due to the fact that the flame front of the thickened model has been artificially thickened and a greater proportion of the flame wrinkling is therefore modelled. For brevity, two-dimensional results obtained with the thickened flame model have been discussed in this section only and compared to predictions of the FSD model. However, further validation and a comparison of the thickened flame and PCM-FPI models against experimental data and DNS simulations for a three-dimensional configuration follow in the next section.

(a) CH$_4$ mass fraction: filter size $2\Delta_0$

(b) CH$_4$ mass fraction: filter size Δ_0

(c) CH$_4$ mass fraction: $0.5\Delta_0$

(d) Turbulence intensity decay
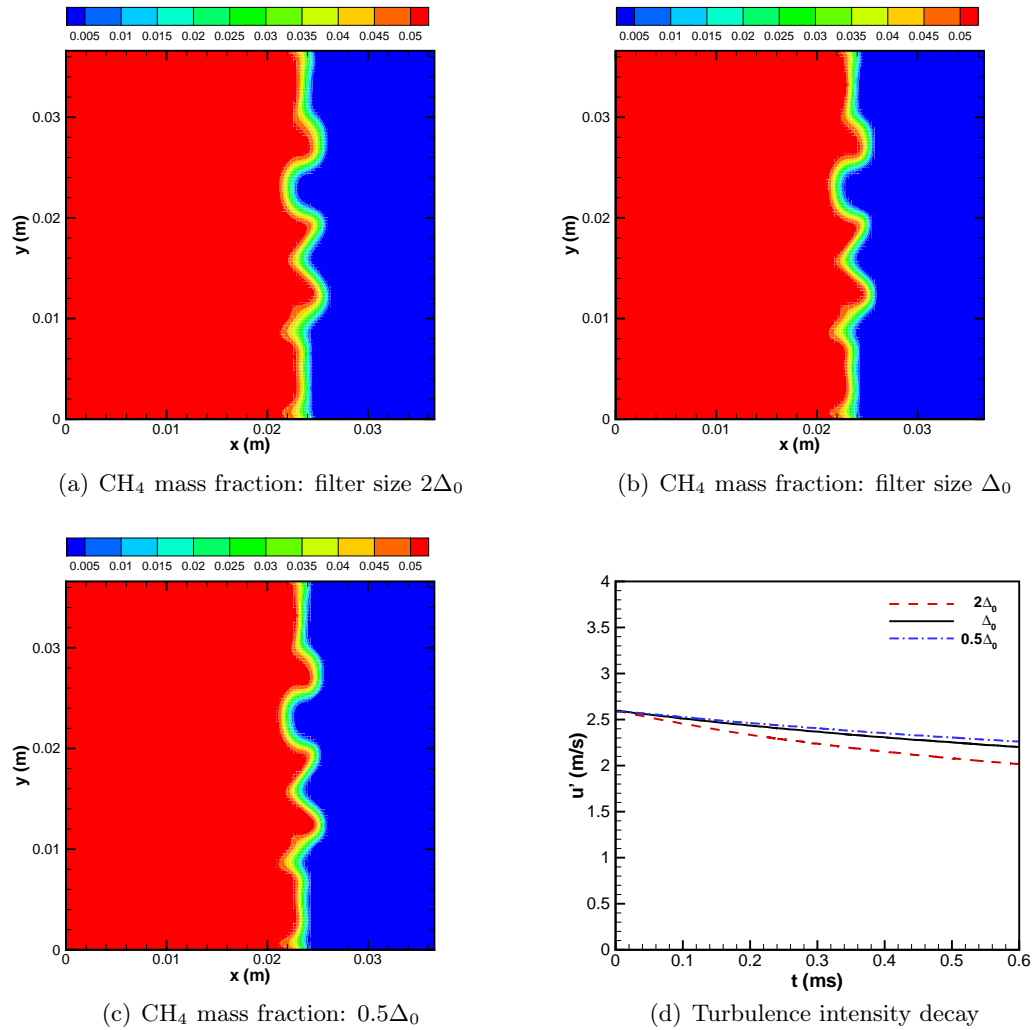
**Figure 6.11:** Filter width influence on the solution of a 2D freely propagating turbulent premixed methane-air flame. Thickened flame model, $F=5$.
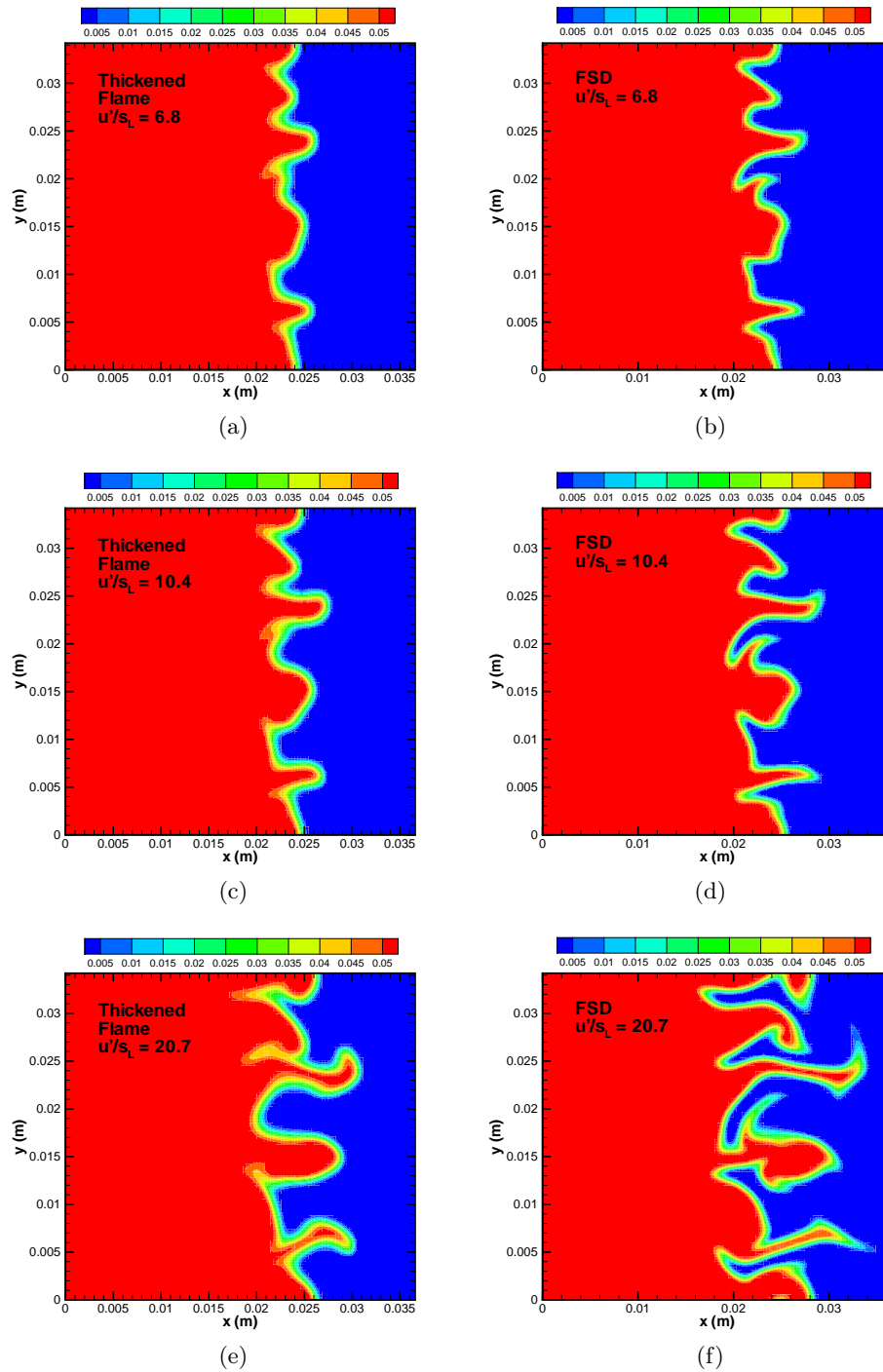
Figure 6.12: Comparison of predicted CH_4 mass fraction at 0.6 ms for 2D freely propagating turbulent premixed methane-air flames subject to different levels of turbulence intensity. Left: thickened flame model, $F = 5$. Right: FSD model.

6.4   Stoichiometric Methane-Air Flame for a Slot Burner

The configuration of the slot Bunsen flame experimentally investigated by Filatyev *et al.* [260] and numerically simulated by Bell *et al.* [261] was considered next for further validation of the thickened flame and PCM-FPI implementations. The slot Bunsen flame is categorized as an envelope flame [262] having an anchored base and is statistically two-dimensional. A schematic of the slot burner, taken from Filatyev *et al.*, is displayed in Figure 6.13. This configuration consists of a slot flanked by two pilot flames to anchor the central flame and shield it from the laboratory environment.

In the current simulations, as described and implemented in the previous numerical studies of Bell *et al.* [261], the two pilot flames were approximated by a uniform inflow of hot combustion products at a velocity of 7 m/s. For the central burner (slot with a width of 0.025 m), a uniform mean inflow of reactants at 3 m/s with superimposed turbulent fluctuations was prescribed. The velocity fluctuations were pre-generated using the procedure developed by Rogallo [254] and superimposed onto the mean inflow velocity using Taylor's hypothesis of frozen turbulence. The simulations were performed for a computational domain with dimensions $L_x = 0.05$ m, $L_y = 0.075$ m and $L_z = 0.1$ m. The domain was discretized with a grid of $N_x \times N_y \times N_z = 80 \times 128 \times 192 = 1,966,080$ cells. A total of 3072 blocks were used, each block having 640 cells. Subsonic outflow boundary conditions are specified on all the faces of the computational domain except for the bottom, for which subsonic inflow conditions are applied.

The fresh gas at the inflow is a methane-air premixed mixture at equivalence ratio $\phi = 1.0$ and temperature $T = 298$ K. The integral length scale of the inflow turbulence is $L_t = 0.0052$ m and the turbulence intensity $u' = 0.3$ m/s. The laminar flame speed and thickness of the stoichiometric methane-air flame are $s_L = 0.39$ m/s and $\delta_L = 0.44 \times 10^{-3}$ m. With these conditions, the flame pertains to the wrinkled flamelet regime of turbulent premixed combustion.

In the thickened flame simulation, methane-air chemistry was represented by a one-step reaction mechanism and a constant thickening factor $F = 5$ was utilized. In the PCM-FPI simulation, the species mass fractions were read directly from a look-up table that was generated from the steady-state solution of a one-dimensional laminar premixed flame obtained with Cantera and the GRI-Mech 3.0 mechanism. A reduced number of 10 species were selected and tabulated, as outlined in subsection 4.1.5 of Chapter 4. The species and their respective Schmidt numbers are given in Table 6.3. The tabulated species mass fractions and the terms $\tilde{\dot{\omega}}^*_{Y_c}$ and $\widetilde{Y_c \dot{\omega}^*_{Y_c}}$ were retrieved from the look-up table, which has 155 values of $\tilde{c}$ and 25 values of S_c.
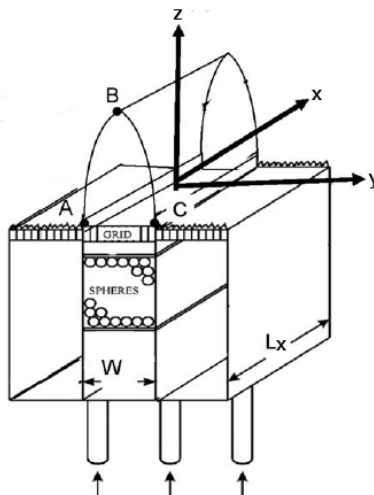
Figure 6.13: Schematic of slot burner showing flame configuration and piloted coflows [260].

Three-dimensional views of the instantaneous flame surface predicted by the thickened flame and PCM-FPI simulations are displayed in Figures 6.14(a) and 6.14(b), corresponding to time $t = 20$ ms. The flame surface is identified with the isotherm $\tilde{T} = 1300$ K. The premixed mixture coming from the central slot ignites on contact with the coflows of hot gas to form flame sheets anchored at the slot lips. Approximately 1 cm above the slot, the flames exhibit a cusped texture characteristic of premixed flames in low turbulence. For qualitative comparison, an instantaneous isotherm from the DNS of Bell *et al.* [261] is displayed in Figure 6.15. The image from the DNS shows a highly wrinkled flame with sharp ridges of negative curvature and large pockets of positive curvature (curvature is positive in regions convex towards the unburned gas). The PCM-FPI model would seem to capture similar qualitative features, with a lower degree of resolution. The thickened flame features the lowest degree of resolved wrinkling as a consequence of the modified interaction of the thickened flame front with turbulence. For a simulation with a low turbulence intensity, as in the present case, it appears that the thickening of the flame front significantly alters the interaction of the flame front with turbulence.

To quantitatively compare the predicted solutions by the PCM-FPI and thickened flame models with the experiment and the DNS, the flame brushes were computed using a temperature-based progress variable, as it was done in Bell *et al.* This progress variable is defined as $c_T = (T - T_u)/(T_b - T_u)$, where T is the local temperature, T_u is the unburnt gas temperature and T_b is the fully burnt gas temperature. For the thickened flame and PCM-FPI simulations, the solutions were time-averaged over 10 ms (from 15 ms to 25 ms) using 21 instantaneous snapshots of the solution. Then, a spatial averaging was performed along the x-direction (slot length). A similar procedure was used by Bell *et al.*, but they employed 88 snapshots separated by 125×10^{-6} s, resulting in a total averaging time of 11 ms. The experimental flame brush

(a) Isotherm $\tilde{T}=1300$ at 20 ms, thickened flame $F=5$ (b) Isotherm $\tilde{T}=1300$ at 20 ms, PCM-FPI
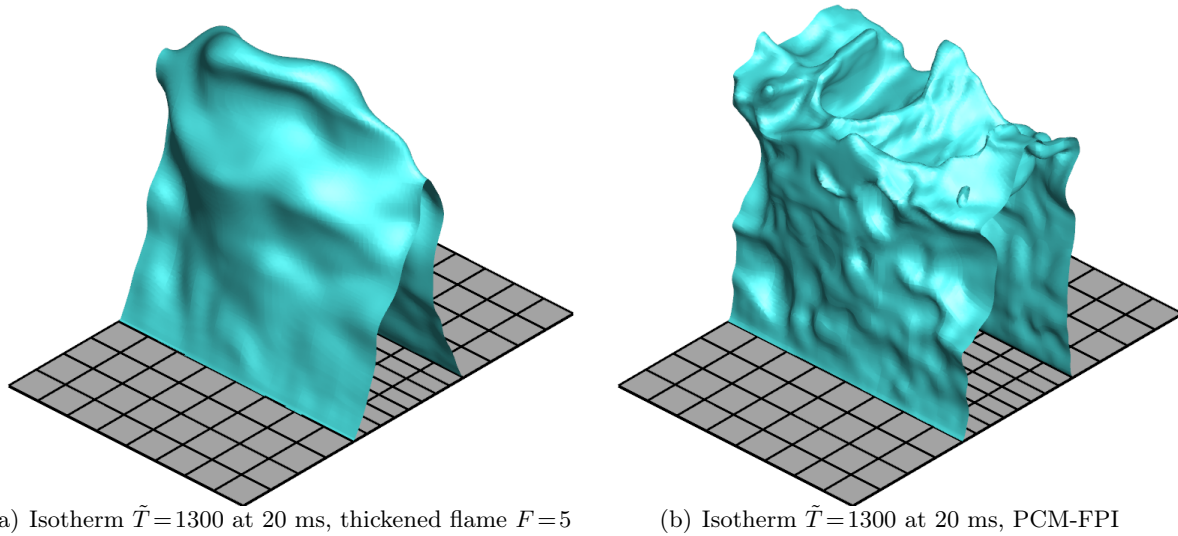
Figure 6.14: Instantaneous flame isotherms for the LES simulations of the Bunsen flame on a slot burner at 20 ms.
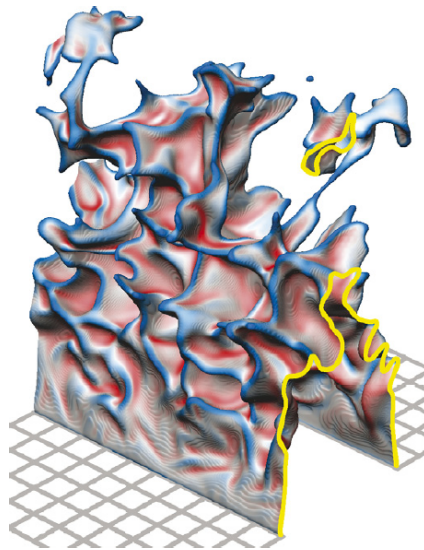
Figure 6.15: Instantaneous isotherm from the DNS of Bell *et al.* [261].

was calculated using 73 Mie scattering images of oil droplets seeded in the fresh mixture of reactants [261]. The flame brushes predicted by the thickened flame and PCM-FPI models are depicted in Figure 6.18. The flame brushes corresponding to the experiment and the DNS, taken from Reference [261], are also shown in Figure 6.17 for comparison.

The flanks of the experimental flame are more vertical as compared to all the simulated flames. The predicted brush by the PCM-FPI model appears to match better the flame flanks. The DNS brush displays a higher height for the flame tip, followed by the thickened flame model prediction. The height at the tip of the predicted PCM-FPI brush is closer to the experimental counterpart, but somewhat wider compared to the experiment and the other simulations. It is evident that noticeable differences exist between the experimental and simulated flame brushes. Nevertheless, considering that only two parameters were used to characterize the inflow turbulence (integral length scale and turbulence intensity) for the experiment and all the simulations, a remarkable agreement between the present LES flame brushes and those from the experiment and DNS was achieved. In particular, the flame heights based on the 0.5 contour of the averaged c_T map and evaluated at the slot centerline, are all around 4 cm. The heights from the experiment and DNS [261], as well as those obtained in the present LES simulations, are all summarized in Table 6.5 and the 0.5 contour of the averaged c_T maps for all the brushes is shown in Figure 6.16.

Flame heights based on the $\langle c_T \rangle = 0.5$ contour (cm)			
Experiment	DNS	Thickened flame, $F=5$	PCM-FPI
4.0	4.1	4.31	3.98

Table 6.5: Summary of flame heights obtained in the experiment and the DNS [261], thickened flame, and PCM-FPI simulations for the stoichiometric Bunsen flame on a slot burner.
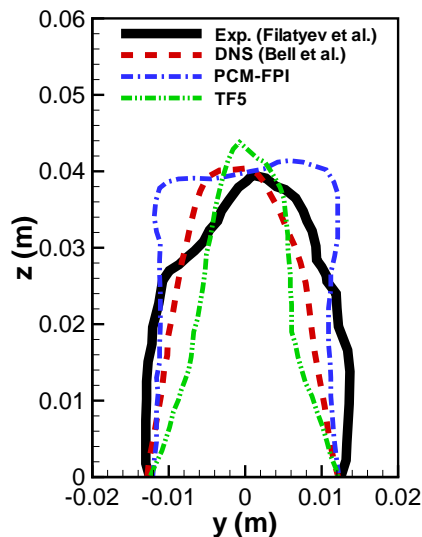
Figure 6.16: Flame brush contour $\langle c_T \rangle = 0.5$ for the present LES and the DNS and experiment reported in Reference [261].
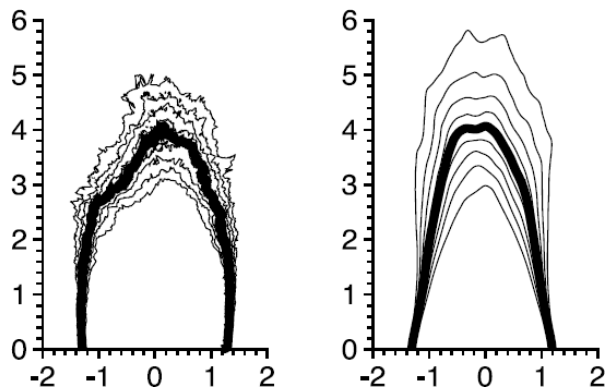
Figure 6.17: Flame brushes corresponding to the experiment and DNS [261] of the slot burner configuration. The thick lines correspond to the $\langle c_T \rangle = 0.5$ contour. The dimensions are in cm.
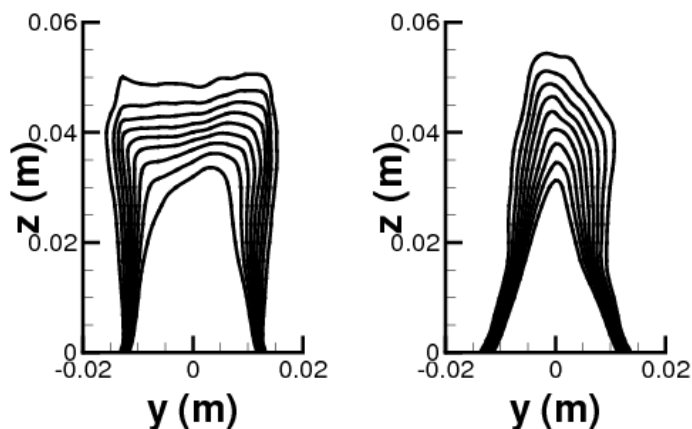
Figure 6.18: Flame brushes corresponding to the thickened flame and PCM-FPI simulations of the slot burner configuration.

6.5   Lean Methane-Air Bunsen Flame

In this section, three LES SFS modelling approaches for premixed turbulent combustion are compared and applied to a laboratory-scale turbulent Bunsen flame. Besides the thickened flame and PCM-FPI models, the transported FSD model of Hawkes & Cant [56] is again considered in the comparisons. Although a comparative study of Bunsen flames was performed recently in which LES predictions obtained using a modified thickened flame model were compared with experimental data and other Reynolds-Averaged Navier-Stokes (RANS) solutions [263], there have been in general few head-to-head comparative studies of SFS and LES modelling approaches. Such studies are needed to advance LES for premixed combustion and clearly identify the predictive capabilities and limitations of SFS models. A lean methane-air flame at equivalence ratio $\phi = 0.7$, which has been studied experimentally by Yuen & Gülder [264], is considered here.

Yuen & Gülder [264] used an axisymmetric Bunsen-type burner with an inner nozzle diameter of 11.2 mm to generate premixed turbulent conical flames stabilized by annular pilot flames. Flame front images were captured using planar Rayleigh scattering achieving a resolution of 45 μm/pixel. The Rayleigh scattering images were converted into temperature field and further processed to provide the temperature gradient and two-dimensional curvature. Particle image velocimetry was used to measure the instantaneous velocity field for the experimental conditions.
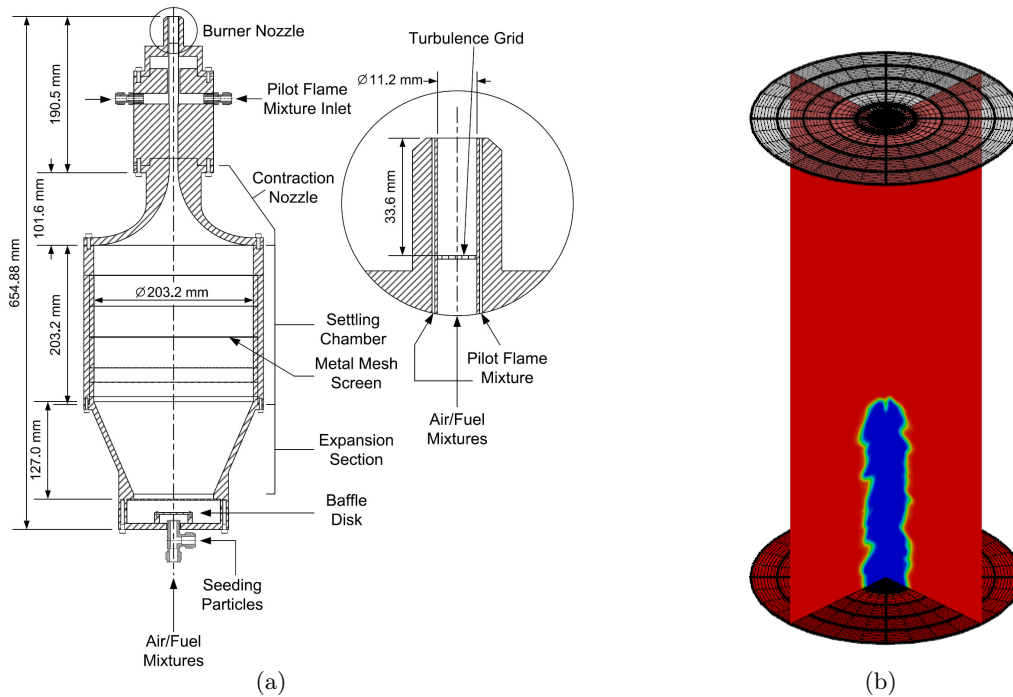
Figure 6.19: (a) Premixed Bunsen burner schematic [265]. (b) Computational domain for the premixed Bunsen flame.

The flame under study corresponds to a lean premixed methane-air flame at an equivalence ratio of $\phi = 0.7$ and atmospheric pressure. The turbulence at the burner exit was characterized by a non-dimensional turbulence intensity $u'/s_{\mathrm{L}} = 14.38$ and an integral length scale $L_{\mathrm{t}} = 1.79$ mm. The mixture of reactants was at a temperature of 300 K and its mean velocity was 15.58 m/s. The flame lies in the thickened wrinkled flame or thin reaction zone of the turbulent premixed combustion diagram and the corresponding turbulent Reynolds number is 324.

In the simulations, a cylindrical domain having a diameter of 0.05 m and a height of 0.1 m was employed and discretized with a grid consisting of 1,638,400 hexahedral cells. The pilot flame was approximated by a uniform inflow of hot combustion products at a velocity of 16.81 m/s. For the burner exit, a uniform mean inflow of reactants with superimposed turbulent fluctuations was prescribed. The velocity fluctuations were pre-generated using the procedure developed

by Rogallo [254] and superimposed onto the mean inflow velocity using Taylor's hypothesis of frozen turbulence. The same velocity fluctuations were used in all of the LES simulations.

In the thickened flame simulation, methane-air chemistry was represented by a one-step reaction mechanism as described by Westbrook and Dryer [108] and a constant thickening factor $F = 3$ was utilized. Two different simulations with the PCM-FPI model were run. In one case, species mass fractions were directly obtained from the look-up table. In the other one, the transport equations for species were solved, reconstructing the reaction rates based on the high Damköler number approximation outlined in Chapter 4. The chemistry look-up table for the PCM-FPI simulations was generated from the steady-state solution of a one-dimensional laminar premixed flame obtained with Cantera and the GRI-Mech 3.0 mechanism. A reduced number of 10 species was again selected and tabulated based on the species contributions to mixture mass and energy. The species are: $CH_4, O_2, CO_2, CO, H_2O, OH, H_2, H, C_2H_2$, and N_2. The tabulated species mass fractions and the terms $\tilde{\dot{\omega}}^*_{Y_c}$ and $\widetilde{Y_c \dot{\omega}^*_{Y_c}}$ were retrieved from the look-up table having 145 values of $\tilde{c}$ and 25 values of S_c. The Schmidt numbers of the species are given in Table 6.6.

Schmidt numbers, $\phi = 0.7$									
CH_4	O_2	CO_2	CO	H_2O	OH	H_2	H	C_2H_2	N_2
0.680	0.748	0.944	0.752	0.553	0.492	0.207	0.123	0.887	0.712

Table 6.6: Schmidt numbers of the species for a lean ($\phi = 0.7$) methane-air premixed flame, taken from the Cantera solution in the burned gas.

In what follows, the numerical solutions obtained with the different models will be identified as PCM-FPI-SP, PCM-FPI-RR, TF3 and C-FSD. The difference between the PCM-FPI-SP and PCM-FPI-RR is that the species mass fractions were transported and their reaction rates were reconstructed for PCM-FPI-RR, whereas species mass fractions were directly read from the look-up table for PCM-FPI-SP.

Three-dimensional views of the predicted instantaneous flame surface, identified by the isotherm $\tilde{T}$=1076 K, are displayed in Figure 6.20 corresponding to time $t = 4$ ms after the initiation of the simulation, for which a quasi-steady flame structure has been achieved in each case. The simulated flames exhibit a highly wrinkled surface and the scale of wrinkling becomes larger near the tips of the flames. Moreover, the overall predicted flame structure is quite similar for each of the SFS models, although the FSD model results would seem to exhibit the most wrinkling and the thickened flame shows considerably less resolved wrinkling than its counterparts. In the C-FSD case of Fig. 6.20(b), a more spread flame is observed. The PCM-FPI-SP (Fig. 6.20(a)) and PCM-FPI-RR (Fig. 6.20(c)) solutions display a nearly identical structure, whereas the artificially thickened flame (Fig. 6.20(d)) is considerably less wrinkled than those of the other
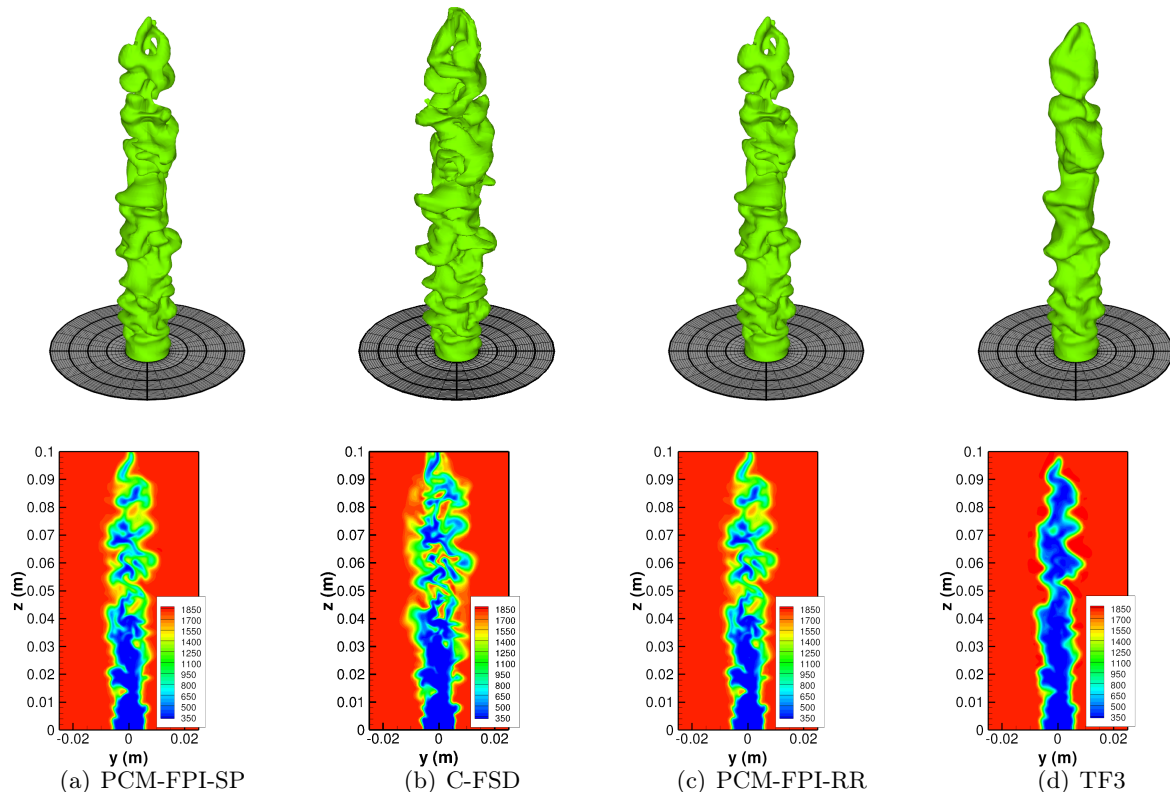
Figure 6.20: Instantaneous flame iso-surface $\tilde{T} = 1076$ K at 4 ms after the initiation of the simulations. Bunsen burner configuration.

models. This observation can be attributed to the fact that turbulent structures smaller than the flame front thickness are unable to wrinkle the thickened flame front.

More details of the internal structure of the flames can be seen in the lower part of Figure 6.20, where planar cuts of the four instantaneous solutions are shown. The solutions are in close agreement with each other up to nearly 3 cm above the bottom line. Further downstream, particularly in the region above 5 cm of the burner exit, clear differences are noticeable. Pockets of unburned reactants can be identified in Figures 6.20(a), 6.20(b) and 6.20(c), which are not present in Figure 6.20(d). For direct comparison, a filtered instantaneous image of the experimental flame is shown in Figure 6.21(a) obtained with a filter-width equal to that of the computations. As can be seen, the numerical simulations are able to reproduce, at least qualitatively, key features of the experimental flame front.

To extract the flame surface density from the experimental data, the Rayleigh scattering images were processed to obtain progress variable fields based on temperature. The two-dimensional (2D) maps of the FSD were computed by using the method developed by Shepherd [266], in which instantaneous flame front edges are superimposed onto the averaged c_T map to calculate

(a) Filtered image

(b) $\langle c_T \rangle = 0.5$
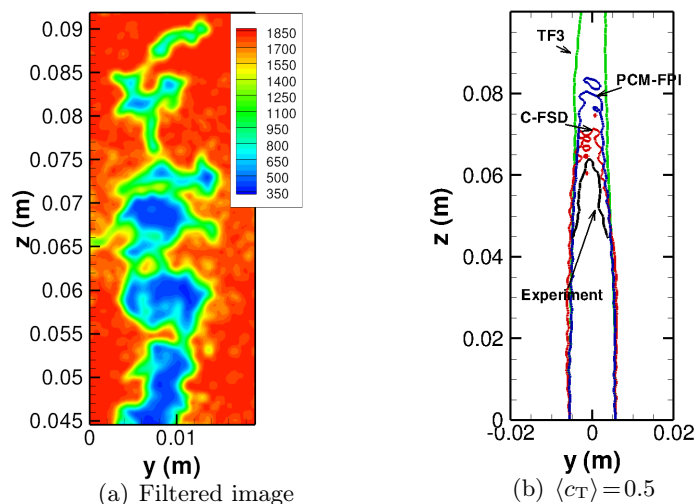
Figure 6.21: Instantaneous filtered temperature from the experiment and 0.5 contour of the averaged c_T map from the experiment and the simulations. Bunsen burner configuration.

the length over area ratio for a given c_T. For a detailed description of the procedure used to process the Rayleigh scattering images, the reader is referred to the theses by Yuen [265] and Lin [168]. The same procedure was then applied to 2D slices of the resolved temperature field obtained from the LES simulations. Since LES provides solutions of filtered variables, it is more appropriate to compare the numerical results with filtered experimental data. The experimental temperature images were therefore first filtered with a top-hat filter having a characteristic size of two times the average cell size of the LES computational grid. The total number of post-processed experimental images was 300 and, for each LES simulation, the 2D slices were extracted from 19 instantaneous snapshots of the numerical solution separated by 0.25 ms.

Predictions of the average map of $c_T = 0.5$ for the three SFS models are compared with the map obtained from the Rayleigh scattering images in Figure 6.21(b). Although it is quite evident that the thickened flame model over-predicts the average flame height by a considerable margin, both C-FSD and PCM-FPI models yield flame heights (7 cm and 7.75 cm respectively) that agree well with the experimental value, which is estimated to be about 6.5 cm based on the $c_T = 0.5$ contour.

The 2D FSD values extracted from the simulations and the experiment are compared in Figure 6.22. It can be seen that all the FSD profiles obtained from the simulations reproduce qualitatively the trends observed in the experimental data. In all the profiles the maximum FSD value is found around $c_T = 0.5$. The peak FSD values obtained from the simulations are
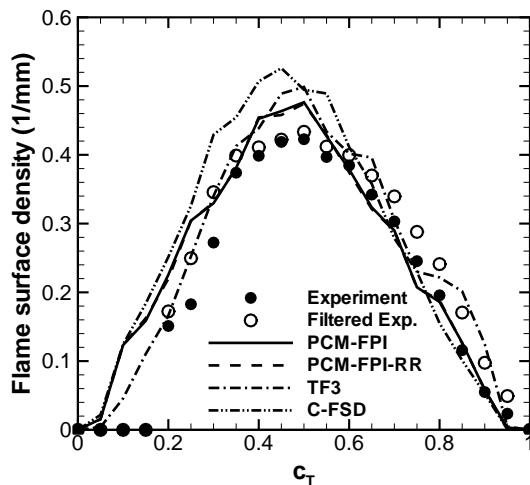
Figure 6.22: 2D Flame surface density extracted from the experimental data and LES simulations. Bunsen burner configuration.

higher than the experimental ones. Despite quantitative discrepancies observed, 2D FSD profiles obtained from the simulations show very good qualitative agreement with the experimental FSD profiles.

Two-dimensional curvature was also extracted from instantaneous experimental images and slices of the numerical solutions. The curvature PDFs of the experimental data, filtered experimental data and the different LES solutions, corresponding to $c_T = 0.5$ are shown in Figure 6.23. The PDFs display a Gaussian-type shape centred around zero. It can be highlighted that filtering the experimental data leads to a narrower PDF, which is due to the fact that filtering removes small-scale wrinkled structures having larger curvatures. All the LES solutions exhibit a narrow PDF as compared to the experimental ones. It can also be seen that the PDFs obtained from the C-FSD, PCM-FPI-SP and PCM-FPI-RR simulations nearly overlap with each other and the filtered experimental results, whereas the PDF obtained from the TF3 simulation is the most narrow. These trends indicate that more small-scale wrinkling is captured by the C-FSD and PCM-FPI models, as compared to the thickened flame model.

The present comparison of SFS model results for LES of a turbulent lean premixed methane-air Bunsen flame to the experimental results of Yuen & Gülder [264] has revealed a number of deficiencies in the thickened flame model, even with a relatively small value of 3 for the thickening factor. The flame height was significantly over-predicted, the instantaneous flame front exhibits noticeably less wrinkling than the actual experimental flame, and the resolved curvature of the flame front is under-predicted. These deficiencies would be even more pronounced if a large thickening factor were adopted as is more typically used. In contrast, the performance
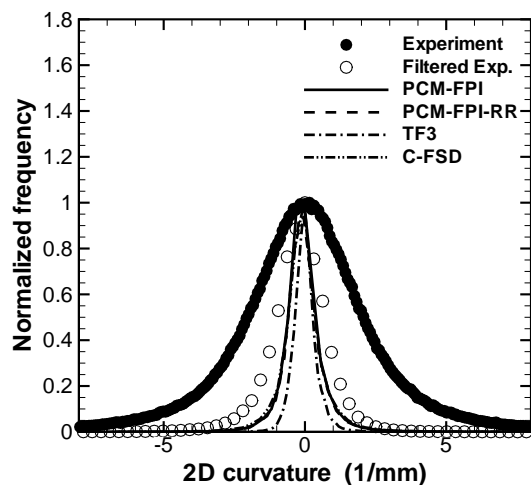
Figure 6.23: PDF of 2D curvature corresponding to a progress variable $c_{\mathrm{T}} = 0.5$. Bunsen burner configuration.

of the C-FSD and PCM-FPI models was found to be much better, with all three approaches providing predictions that agree both qualitatively and quantitatively with key aspects of the flame observed in the experiment. The resolved flame structure and wrinkling, average flame height, and resolved flame surface and curvature all compare well with experiment. The FSD model appears to be best suited for describing the evolution and dynamics of the flame surface, yielding slightly better predictions of these quantities, but is lacking in terms its connection of flame area to reaction rates. The PCM-FPI model seems more robust and can be applied more widely to premixed, non-premixed, and partially premixed flames, although at the expense of higher computational costs (computational costs of the PCM-FPI-RR simulation were about 55% more than those of the C-FSD model).

6.6   Hydrogen-Enriched Methane-Air Flames

In the previous sections of this chapter, the thickened flame and PCM-FPI model implementations have been systematically validated for one-, two-, and three-dimensional configurations. In particular, the two models were applied to the slot burner configuration that was experimentally studied by Filatyev *et al.* [260] and simulated by Bell *et al.* [261] using DNS with adaptive mesh refinement. The agreement of the predicted solutions by the thickened flame and PCM-FPI models with the experimental and DNS results provides assurance of the proper implementation of the models and reliance of the LES algorithm. Moreover, the models were also applied to the Bunsen flame configuration experimentally studied by Yuen & Gülder [264] (lean methane-air flame) and further compared to the FSD model of Hawkes & Cant [56]. Even

though all the numerical results obtained with the different models compared qualitatively well with the experiment, the comparison revealed deficiencies in thickened flame model. Based on the predictive capabilities of the models examined thus far, it is evident that the PCM-FPI approach is more suitable for the study of a more complicated combustion problem, such as hydrogen-enrichment of methane, which requires incorporation of complex chemistry, Lewis number effects, and preferential diffusion.

All of the numerical results obtained with the PCM-FPI model so far have involved a reduced number of 10 species without the inclusion of NO. Also, in section 6.1 it was pointed out that discrepancies in the predicted H_2 mass fraction profile of a 1D steady premixed flame were a consequence of determining H_2 via the atom-balance of H with a reduced number of 10 species. To improve the prediction of the H_2 mass fraction and allow for the prediction of NO in H_2-enriched methane-air flames, the number of species included in the look-up table has been increased to 13 and a suitable progress of reaction variable has been defined (Equation 4.40) in subsection 4.1.6 of Chapter 4.

6.6.1 Tabulated versus Directly Calculated Premixed H_2-Enriched Methane-Air Laminar Flames

Once the progress of reaction has been introduced to account for NO and a new set of selected species for tabulation has been defined, 1D steady-state laminar premixed flame cases corresponding to the conditions studied by Hawkes & Chen [93] are used as an initial test to apply the PCM-FPI model to H_2-enrichment of methane. Two flames at atmospheric pressure and having a fresh gas temperature of 300 K, both at equivalence ratio $\phi = 0.52$, are considered. One flame corresponds to a pure methane-air mixture and the other one to a hydrogen-methane-air mixture containing 29% H_2 (on a molar basis) in the blended fuel. The 13 tabulated species with their respective Schmidt numbers are given in Table 6.7. A rectangular computational domain having a length of 0.1 m and a height of 0.001 m, discretized with a mesh consisting of 2 cells in the vertical direction and 200 cells in the horizontal direction, is employed for these simulations.

The predicted temperature, velocity, pressure, and CO_2, CO, and NO mass fraction profiles of the 1D methane-air and hydrogen-methane-air flames are displayed in Figures 6.24 and 6.25, respectively. The predicted solutions with two PCM-FPI approaches (reading mass fractions directly and transporting the species with reconstructed reaction rates) are also compared to the Cantera solutions computed with the full GRI 3.0 mechanism. Pressure drops smaller than 0.1 Pa are obtained in both PCM-FPI solutions, whereas Cantera assumes a constant pressure. The pressure jumps lead to differences in the flow velocity, which are particularly noticeable in

Schmidt numbers, $\phi = 0.52$						
CH$_4$-air flame	CH$_4$	O$_2$	O	CO$_2$	CO	H$_2$O	N$_2$
	0.679	0.751	0.482	0.939	0.751	0.557	0.703
	OH	H$_2$	H	C$_2$H$_2$	NO	NH$_3$	
	0.491	0.206	0.123	0.887	0.757	0.608	
H$_2$-CH$_4$-air flame (29% H$_2$)	CH$_4$	O$_2$	O	CO$_2$	CO	H$_2$O	N$_2$
	0.681	0.753	0.483	0.939	0.753	0.558	0.710
	OH	H$_2$	H	C$_2$H$_2$	NO	NH$_3$	
	0.492	0.207	0.124	0.889	0.759	0.608	

Table 6.7: Schmidt numbers of the species for lean ($\phi = 0.52$) CH$_4$-air and H$_2$-CH$_4$-air premixed flames, taken from the Cantera solutions in the burned gas.

the burned gas. Nevertheless, the laminar flame speeds and burned gas temperatures compare well with those given by Cantera. The flame speeds and burned gas temperatures are summarized in Table 6.8. The predicted profiles of the species CO$_2$, CO, and NO closely follow the profiles given by the Cantera solutions. In particular, there is a remarkable agreement for the equilibrium NO levels, which are less than one part per million (ppm) in the two cases.

	Cantera		PCM-FPI			
			FPI-SP		FPI-RR	
$\varkappa$	0.0	0.29	0.0	0.29	0.0	0.29
s_{L} (m/s)	0.0612	0.0806	0.061	0.081	0.061	0.081
T_{b} (K)	1510.99	1523.89	1511.02	1526.9	1510.48	1525.9

Table 6.8: Summary of predicted flame speeds and temperatures in the burned gas for 1D steady-state CH$_4$-air and H$_2$-CH$_4$-air premixed flames at $\phi = 0.52$. PCM-FPI model with 13 species reading mass fractions directly (FPI-SP) and transporting the species using reconstructed reaction rates (FPI-RR).

6.6.2   Two-Dimensional H$_2$-Enriched Freely Propagating Turbulent Flame

The proposed progress variable for H$_2$-enriched methane combustion is now evaluated by considering a two-dimensional configuration. The LES prediction of a H$_2$-enriched methane-air freely propagating flame in a two-dimensional isotropic decaying turbulent field is considered. This flame is also compared to a pure methane-air flame with an identical initial turbulent velocity field. As for the H$_2$-enriched flame, the blended fuel contains 29% H$_2$ on a molar basis. The two flames are lean with an equivalence ratio $\phi = 0.52$. These cases were previously studied by Hawkes & Chen [93] with DNS. The parameters characterizing the initial turbulent field for the two flames are as follows: turbulence intensity, $u' = 1.5$ m/s; integral length scale, $L_{11} = 1.5$ mm; and turbulent Reynolds number, $Re_{\mathrm{L}_{11}} = 143$. A rectangular computational domain, having a
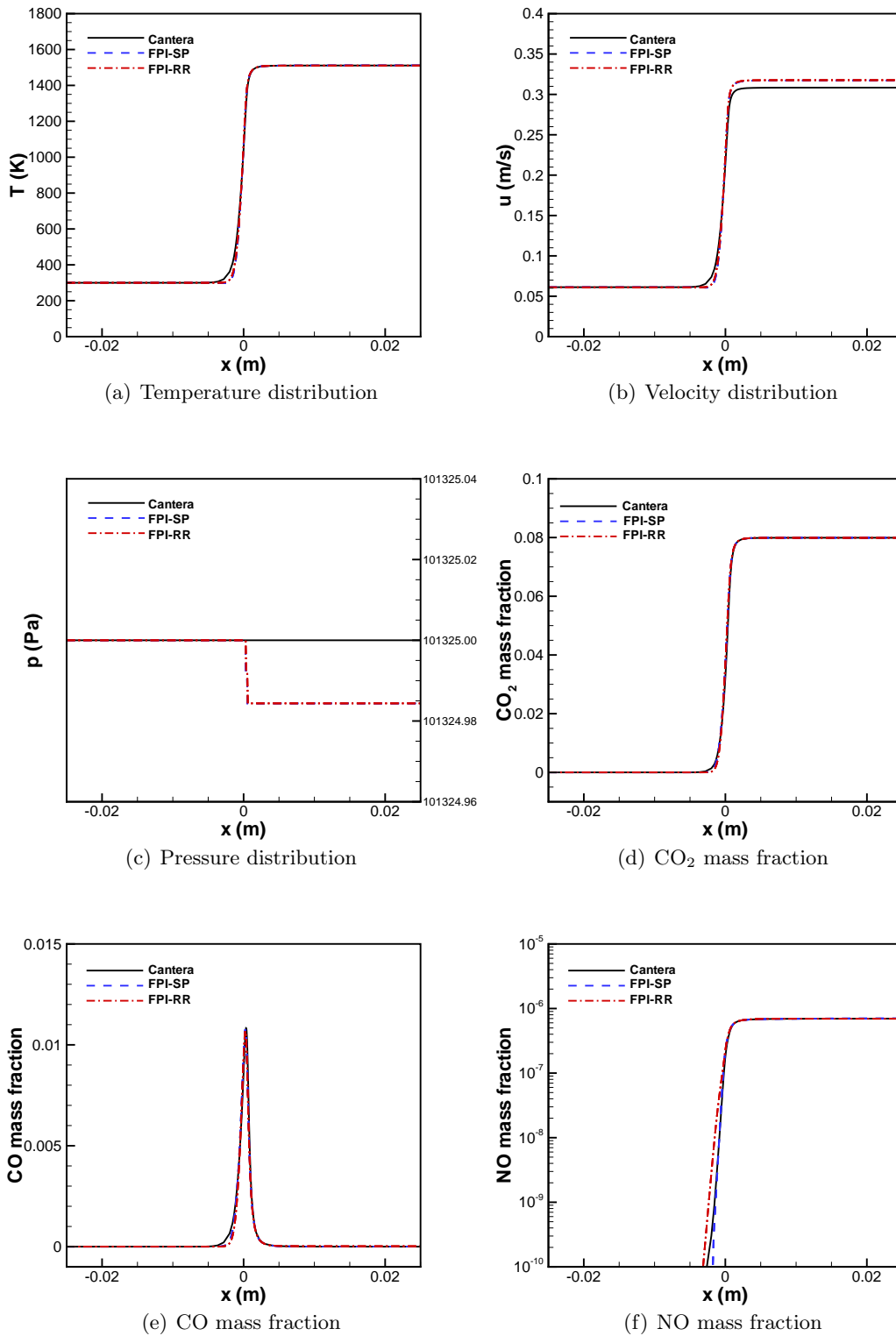
Figure 6.24: Temperature, velocity, pressure, and CO_2, CO, and NO mass fraction profiles of a 1D steady-state CH_4-air flame at $\phi = 0.52$, corresponding to the PCM-FPI model with $Y_c = Y_{CO_2} + Y_{NO}$ and 13 species. FPI-SP: reading mass fractions directly. FPI-RR: transporting the species using reconstructed reaction rates.

(a) Temperature distribution

(b) Velocity distribution

(c) Pressure distribution

(d) CO_2 mass fraction

(e) CO mass fraction
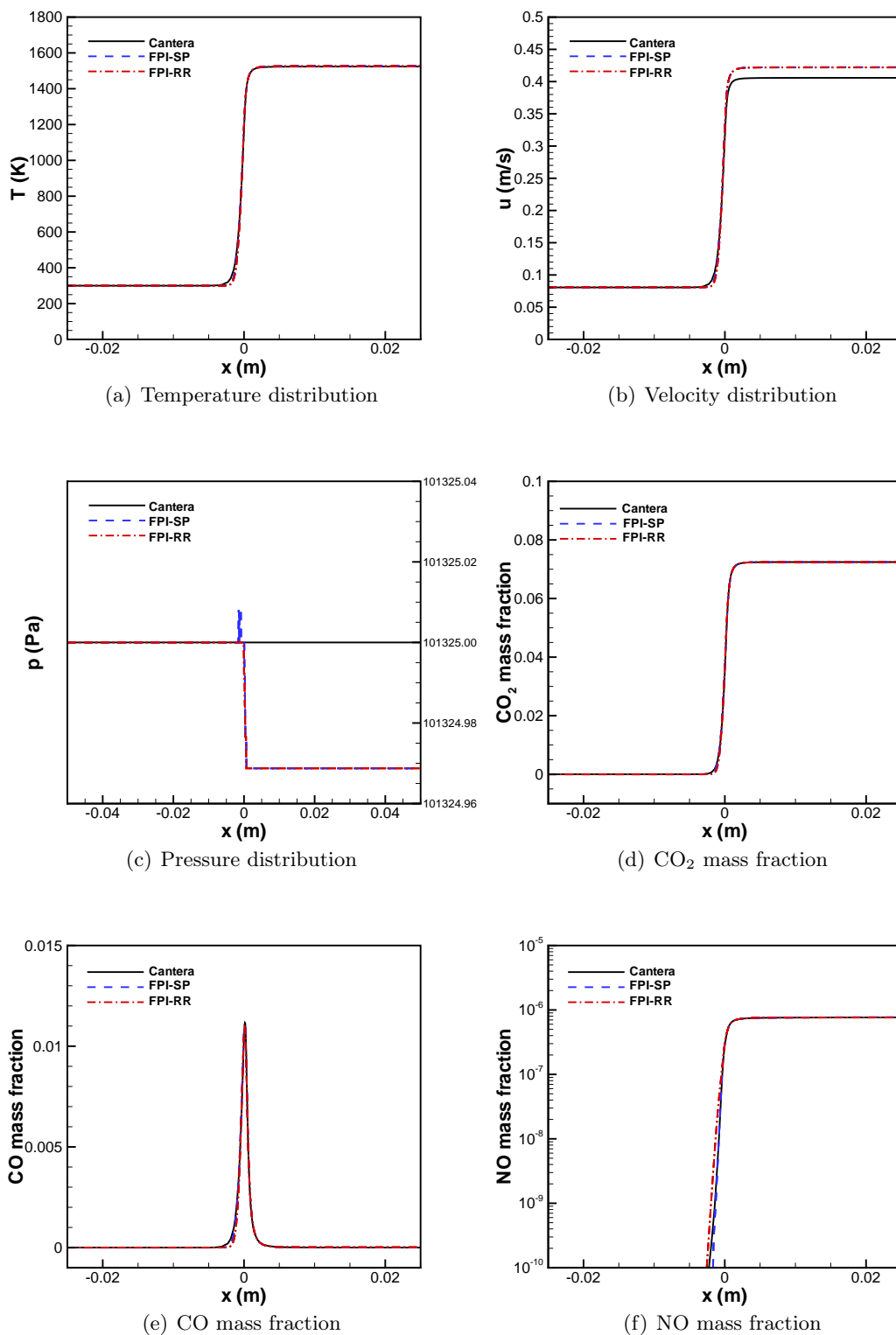
(f) NO mass fraction

Figure 6.25: Temperature, velocity, pressure, and CO_2, CO, and NO mass fraction profiles of a 1D steady-state H_2-CH_4-air flame (29% H_2 in the fuel) at $\phi = 0.52$, corresponding to the PCM-FPI model with $Y_c = Y_{CO_2} + Y_{NO}$ and 13 species. FPI-SP: reading mass fractions directly. FPI-RR: transporting the species using reconstructed reaction rates.

length of 0.012 m and a height of 0.03 m, was employed for the simulations. The numerical results were obtained using a uniform mesh and the computational domain was discretized with a $96 \times 240 = 23040$ cell mesh. In this configuration, the flames propagate to the left side of the domain. Subsonic inflow and outflow boundary conditions are imposed on the left and right boundaries, respectively, whereas the remaining boundaries are periodic. The look-up tables utilized for the LES simulations contained 138 values of $\tilde{c}$ and 25 values of S_c. The species used in the tabulation and their respective Schmidt numbers are given in Table 6.7.

Two sets of simulations were run to assess the importance of including diffusive effects by transporting the species with their appropriate molecular Schmidt numbers, and thereby, accounting for Lewis number effects, at least at the resolved LES level. This is of particular relevance for H_2, which is a light and highly diffusive molecule. Moreover, as it was discussed in section 2.9 of Chapter 2, preferential diffusion can lead to diffusive-thermal instability. Consequently, the H_2-enriched flame is expected to be less diffusive-thermally stable. The first set (enriched and non-enriched flames) corresponds to the PCM-FPI approach reading the species mass fractions of all the species directly (PCM-FPI-SP) and the second set corresponds to transporting the species with reconstructed reaction rates (PCM-FPI-RR).

For comparison, the H_2 mass fraction contours at 3.0 ms of physical time are displayed in Figure 6.26. This time corresponds to approximately 3.0 eddy turnovers based on the initial integral length scale and turbulent intensity. The contours obtained by direct tabulation of the species mass fractions are shown on the left and those obtained by transporting the species are shown on the right. Differences between the predicted contours are mainly observable in regions where the flame front is convex towards the mixture of reactants. In these regions, the solutions obtained by transporting H_2 exhibit smoother contours whereas the solutions obtained by reading H_2 mass fraction directly from the look-up table display somewhat distorted contours. The differences are more pronounced in the zone surrounding a long protrusion that has extended into the reactant side, as it can be seen from the lower part of each plot in Figure 6.26. It is clear that transporting H_2 results in a more accurate solution. In what follows, the solutions obtained by transporting the species with reconstructed reaction rates are further discussed.

Figure 6.27 depicts the CO_2, CO, and NO mass fraction contours of the pure and H_2-enriched methane-air flames at 3 ms. It is evident that the CO_2 concentration decreases with H_2 addition whereas the NO concentration increases. Although it should be noted that the NO mass fractions are smaller than 1 ppm in both cases. As for CO, the differences are not as clear as in CO_2 and NO, but it is apparent that more CO is produced in the long protrusion shown at the bottom of Figure 6.27(b) for the H_2-enriched flame. The protrusion is characterized by downstream interaction of flame front elements, where the production of CO is greater [93]. By

(a) H$_2$ mass fraction, PCM-FPI-SP   (b) H$_2$ mass fraction, PCM-FPI-RR
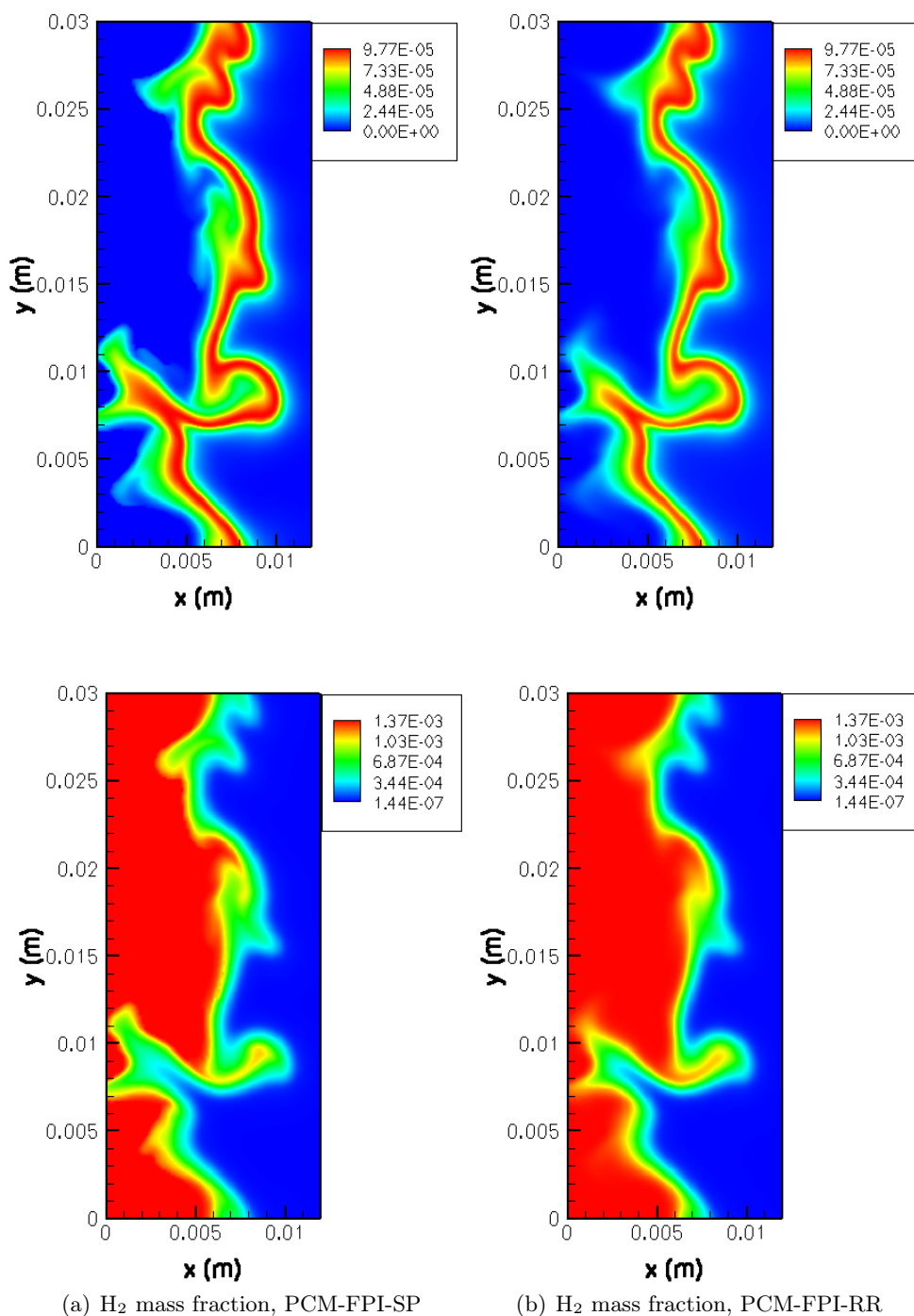
Figure 6.26: Predicted H$_2$ mass fraction contours of 2D freely-propagating flames at time $t=3.0$ ms, based on tabulating mass fractions directly from the look-up tables (PCM-FPI-SP) and transporting the species using reconstructed reaction rates (PCM-FPI-RR). Top: CH$_4$-air flame. Bottom: H$_2$-CH$_4$-air flame with 29% H$_2$ in the blended fuel.

integrating the production rate of CO over the entire domain ($\int \tilde{\omega}_{CO}\, dA$), the CO emissions can be further quantified and contrasted for the two flames under consideration. In Figure 6.29(b), the evolution of the integrated CO production rate per integrated methane consumption rate ($\int \tilde{\omega}_{CH_4}\, dA$) is shown. It can be observed that, after 1.4 ms, the enriched flame exhibits a lower global CO production rate per unit CH_4 consumption rate.

The oxidation of methane is characterized by the presence of the radicals H, O, and OH that are produced during the combustion process and diffuse upstream [104]. Furthermore, it has been documented that methane breakdown mainly proceeds through reactions with hydroxyl (OH) radicals in hydrogen-enriched methane-air blends [216, 267, 217]. The predicted mass fraction distributions of OH, O, and H are shown in Figure 6.28. Larger concentrations of radicals are encountered in the enriched flame, which is a trend consistent with the DNS results of Hawkes & Chen [93] and Dunstan & Jenkins [95]. A similar trend was observed in the experiments of Schefer *et al.* [20] for the OH radical. From the plots in Figure 6.28, it can also be observed that radicals exhibit a higher degree of penetration into the unburned mixture in the enriched flame, suggesting an enhancement of the flame resistance to extinction.

Another important quantity to compare is the global turbulent flame speed. Here, estimates of the global flame speed are based on the integrated reaction rate of the progress of reaction variable and evaluated via the following expression:

$$s_{\mathrm{T}} = \frac{1}{\bar{\rho}_{\mathrm{r}} Y_{\mathrm{c}}^{\mathrm{Eq}} L_{\mathrm{y}}} \int_A \tilde{\omega}_{Y_{\mathrm{c}}}\, dA\,. \tag{6.5}$$

In the above expression, $\bar{\rho}_{\mathrm{r}}$ is the filtered density of the reactants, L_{y} is the height of the computational domain, and A stands for area. Figure 6.29(a) displays the estimated flame speeds (or burning rates) for the two flames. It is apparent that the burning rate is considerably increased by the addition of H_2 to methane. A similar trend was obtained in 2D DNS of planar flames [93] and burning kernels [95], where the consumption rates of methane were used to compute the global turbulent flame speeds. In the case of the planar flames, Hawkes & Chen [93] ascribed the increase in the turbulent flame speed of the enriched flame to a faster laminar flame speed, a larger flame surface area (the flame is less diffusive-thermally stable and more resistant to strain), and a higher local burning rate per unit area due to preferential diffusion of H_2.

All in all, the LES simulation of the H_2-enriched flame with the proposed PCM-FPI approach predicts similar trends to those found in the corresponding DNS [93] of the configuration under study. A greater estimated turbulent flame speed, a lower global CO production rate per unit CH_4 consumption rate, decreased CO_2 emissions, increased NO emissions, and higher

(a) CO_2 mass fraction   (b) CO mass fraction   (c) NO mass fraction
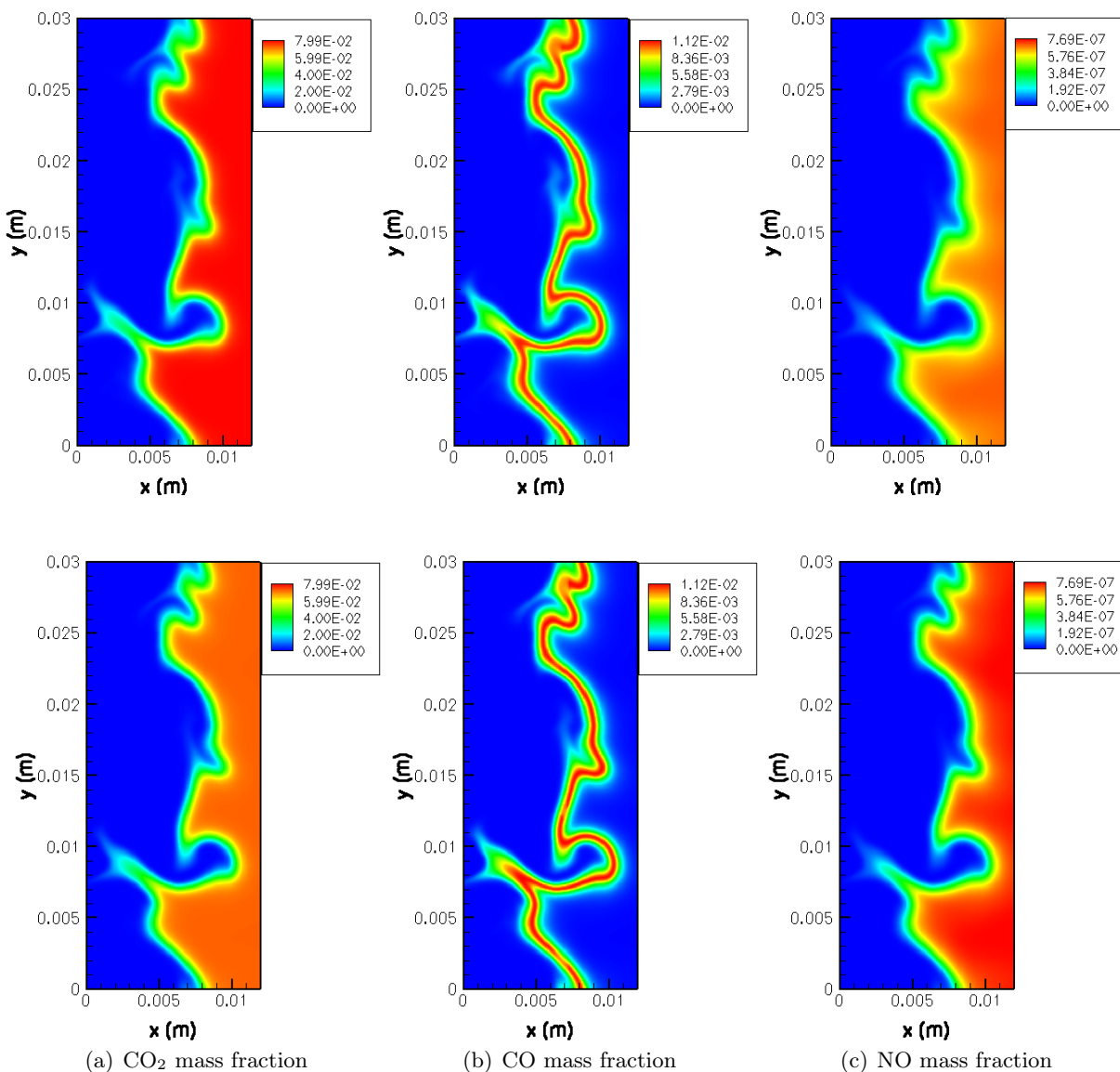
Figure 6.27: Predicted CO_2, CO, and NO mass fraction contours of 2D freely-propagating flames at time $t = 3.0$ ms. Top: CH_4-air flame. Bottom: H_2-CH_4-air flame with 29% H_2 in the blended fuel.

concentrations of OH radicals were predicted for the enriched flame when compared to the pure methane case.

6.6.3   Three-Dimensional H_2-Enriched Methane-Air Turbulent Bunsen Flame

In this subsection, a final evaluation of the proposed PCM-FPI approach in the context of H_2-CH_4 blending is carried out. LES of 3D Bunsen-type turbulent premixed methane-air and

(a) OH mass fraction   (b) O mass fraction   (c) H mass fraction
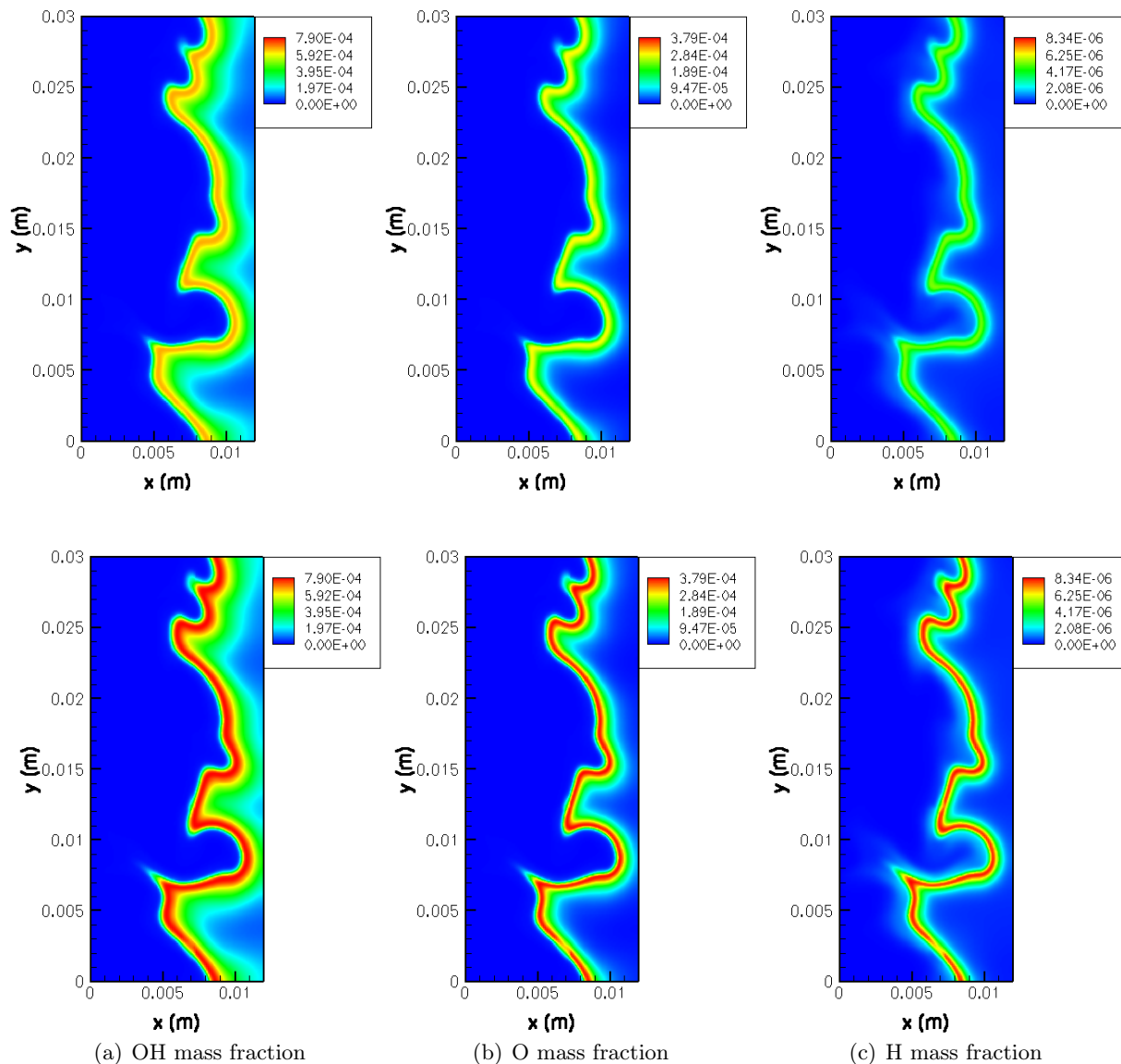
Figure 6.28: Predicted OH, O, and H mass fraction contours of 2D freely-propagating flames at time $t = 3.0$ ms. Top: CH_4-air flame. Bottom: H_2-CH_4-air flame with 29% H_2 in the blended fuel.

H_2-enriched methane-air flames have been performed. The predicted solutions of both flames are examined and further compared to measured data from the experiments of Halter *et al.* [268]

The Bunsen flames under study correspond to lean premixed turbulent conditions at an equivalence ratio of $\phi = 0.6$ and atmospheric pressure. For the enriched flame, H_2 represented 20% of the blended fuel on a molar basis ($\varkappa = 0.2$). Flames with these conditions have been studied experimentally by Halter and co-workers [269, 268]. An axisymmetric Bunsen-type burner with an inner nozzle diameter of 25 mm was used to generate the premixed turbulent conical flames

(a) Estimated global burning rates

(b) Ratio $\int \tilde{\dot{\omega}}_{\mathrm{CO}} \, \mathrm{d}A / \int \tilde{\dot{\omega}}_{\mathrm{CH}_4} \, \mathrm{d}A$
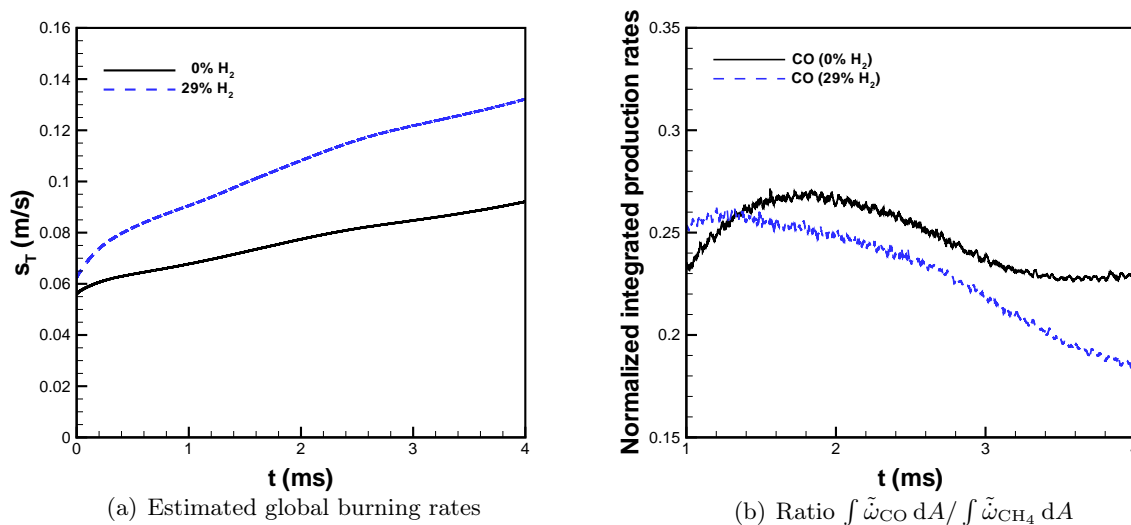
Figure 6.29: Estimated global turbulent flame speeds based on the integrated $\tilde{\dot{\omega}}_{Y_c}$ term and integrated CO production rate per integrated CH_4 consumption rate for 2D freely-propagating CH_4-air and H_2-CH_4-air flames. The H_2-CH_4-air mixture contained 29% H_2 in the blended fuel.

stabilized by annular pilot flames. The turbulence at the burner exit was characterized by a turbulence intensity $u' = 0.17$ m/s and an integral length scale $L_t = 3$ mm. The mixtures of reactants had a temperature of 300 K and their mean inflow velocity was 2.1 m/s. In the simulations, a cylindrical domain having a diameter of 0.05 m and a height of 0.1 m was employed and discretized with a grid consisting of 1,638,400 hexahedral cells. The pilot flames were approximated by a uniform inflow of hot combustion products at a velocity of 2.73 m/s. For the burner exit, a uniform mean inflow of reactants with superimposed turbulent fluctuations was prescribed, as outlined in section 6.5. The same velocity fluctuations were used for both the H_2-enriched methane and pure methane flame simulations.

In the LES simulations, the transport equations for species were solved using reconstructed filtered reaction rates from the look-up tables. In addition to the 13 species previously selected for the simulation the 2D freely propagating H_2-enriched flame, CH_3 was included in the set of chosen species for tabulation. The selected species with their respective Schmidt numbers are given in Table 6.9. The tabulated species mass fractions and the terms $\tilde{\dot{\omega}}_{Y_c}^*$ and $\widetilde{Y_c \dot{\omega}_{Y_c}^*}$ were retrieved from the look-up tables, which had 138 values of $\tilde{c}$ and 25 values of S_c.

Three-dimensional views of the predicted instantaneous flame surface, identified by the isotherm $\tilde{T} = 650$ K, are depicted in Figure 6.30 corresponding to a physical time $t = 56$ ms, for which a quasi-steady flame structure has been achieved in each case. The simulated flames exhibit a wrinkled surface having a similar structure up to 5 cm above the burner exit. Further down-

Schmidt numbers, $\phi = 0.6$							
CH$_4$-air flame	CH$_4$	CH$_3$	O$_2$	O	CO$_2$	CO	H$_2$O
	0.679	0.675	0.749	0.482	0.941	0.751	0.555
	N$_2$	OH	H$_2$	H	C$_2$H$_2$	NO	NH$_3$
	0.707	0.491	0.206	0.123	0.887	0.758	0.607
H$_2$-CH$_4$-air flame (20% H$_2$)	CH$_4$	CH$_3$	O$_2$	O	CO$_2$	CO	H$_2$O
	0.681	0.677	0.751	0.483	0.941	0.753	0.556
	N$_2$	OH	H$_2$	H	C$_2$H$_2$	NO	NH$_3$
	0.712	0.492	0.207	0.124	0.889	0.759	0.608

Table 6.9: Schmidt numbers of the species for lean ($\phi = 0.6$) CH$_4$-air and H$_2$-CH$_4$-air premixed flames, taken from the Cantera solutions in the burned gas.

stream, the hydrogen enriched flame displays a higher degree of wrinkling with sharper ridges of negative curvature (curvature is negative in regions that are concave with respect to the unburned gas) and larger pockets of positive curvature, which are more pronounced near the flame tip.

In Figure 6.31, the same isotherm (light grey) is shown interacting with turbulent structures identified by the iso-value $Q = 1606$ s^{-2} (cyan). The vortical structures are similar in shape and number near the burner exit for both flames. Further downstream, the number of the coherent vortices decreases significantly for the pure methane-air flame, whereas a large number of turbulent structures is observed for the H$_2$-enriched flame, particularly in the highly wrinkled region around the flame tip. The addition of H$_2$ would seem to modify the interaction between the flame front and the turbulent field, which can be related to the less diffusive-thermally stable character of the H$_2$-enriched flame. It has been suggested that the diffusive-thermal instability could lead to self-turbulization of flames [270].

More details of the internal structure of the flames can be seen in Figures 6.32 and 6.33, where planar cuts of the two instantaneous temperature fields and the mass fraction distributions of representative species are respectively shown. It is evident that the enriched flame is shorter, which can be ascribed to a faster consumption of the blended fuel. The enriched flame displays slightly higher temperatures, particularly in regions convex towards the combustible mixture of gases. In addition, more and sharper cusps that protrude the burned gas are observed in the enriched flame. The planar cuts of CO$_2$ mass fraction reveal reduced levels of CO$_2$ emissions in the enriched flame (see Figures 6.33(a) and 6.33(b)). In contrast, the planar cuts of NO mass fractions display larger amounts of NO in the enriched flame. Areas of larger NO concentrations are localized downstream regions of positive curvature (convex towards the unburned gas) for the enriched case, as it can be seen in Figure 6.33(f). These regions also coincide with areas of

(a) Iso-surface $\tilde{T}=650$ K, $\varkappa=0$ (b) Iso-surface $\tilde{T}=650$ K, $\varkappa=0.2$
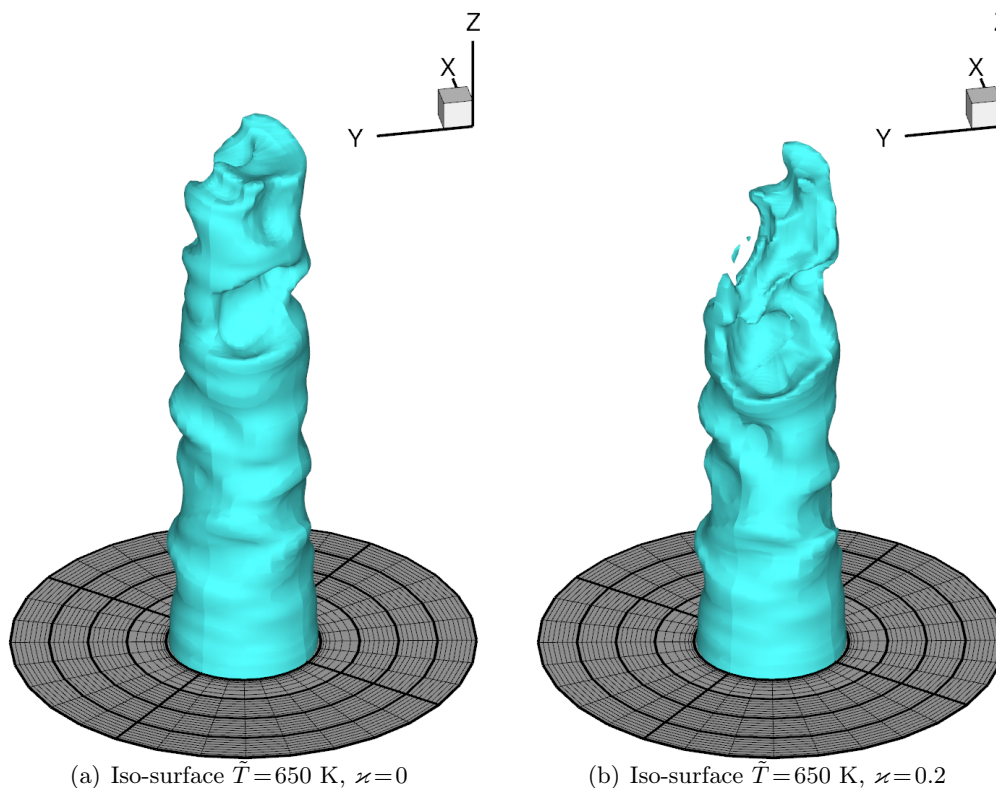
Figure 6.30: Instantaneous iso-surface $\tilde{T}=650$ K of the Bunsen-type flames at 56 ms. Left: CH$_4$-air flame. Right: H$_2$-CH$_4$-air flame.

high temperature (see Figure 6.30(b)). The planar cuts of CO mass fractions show an intensified production of CO for the enriched flame in the highly wrinkled region near the flame tip, around the centerline (see Figure 6.33(d)). However, no significant difference of CO levels is noticeable in the fully burned gas zones of the two flames from these contours. Further details on the variation of CO can be seen in Figure 6.34, where radial profiles of CO mass fraction are compared at different locations above the burner exit. A greater magnitude of peak values of CO mass fraction (see Figure 6.34(c)) and a slight increase of CO levels in zones of fully burned gas are found in the enriched flame.

To compare the numerical results with the experimental data, a time-average of the LES solutions was performed over 70 ms (from 30 ms to 100 ms) using 71 instantaneous snapshots of each solution. Moreover, 2D slices of the resolved LES temperature field were extracted and processed to calculate progress variable fields based on temperature, following the procedure described in section 6.5. On the other hand, the experimental flame brush was calculated using 500 Mie scattering images of oil droplets seeded in the fresh mixture of reactants [268]. The images were binarised and an edge-finding algorithm was applied to each instantaneous image to determine the progress variable maps. The resolution of the Mie scattering imaging procedure

(a) Isotherm $\tilde{T}=650$ K, $Q=1606$ s^{-2}, $\varkappa=0$ (b) Isotherm $\tilde{T}=650$ K, $Q=1606$ s^{-2}, $\varkappa=0.2$
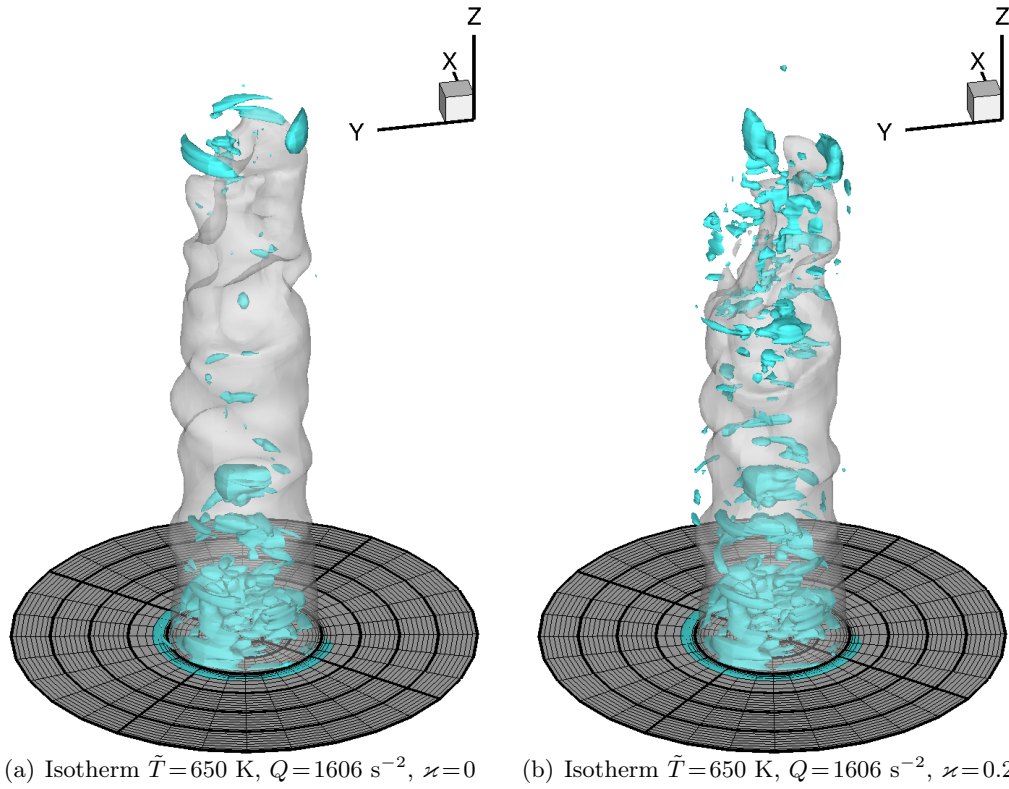
Figure 6.31: Instantaneous iso-surface $\tilde{T}=650$ K of the Bunsen-type flames (light grey) interacting with vortical structures (cyan) identified by $Q=0.5(u'/L_{\mathrm{t}})^2=1606$ s^{-2} at 56 ms. Left: CH$_4$-air flame. Right: H$_2$-CH$_4$-air flame.

(a) Temperature, $\varkappa=0$ (b) Temperature, $\varkappa=0.2$
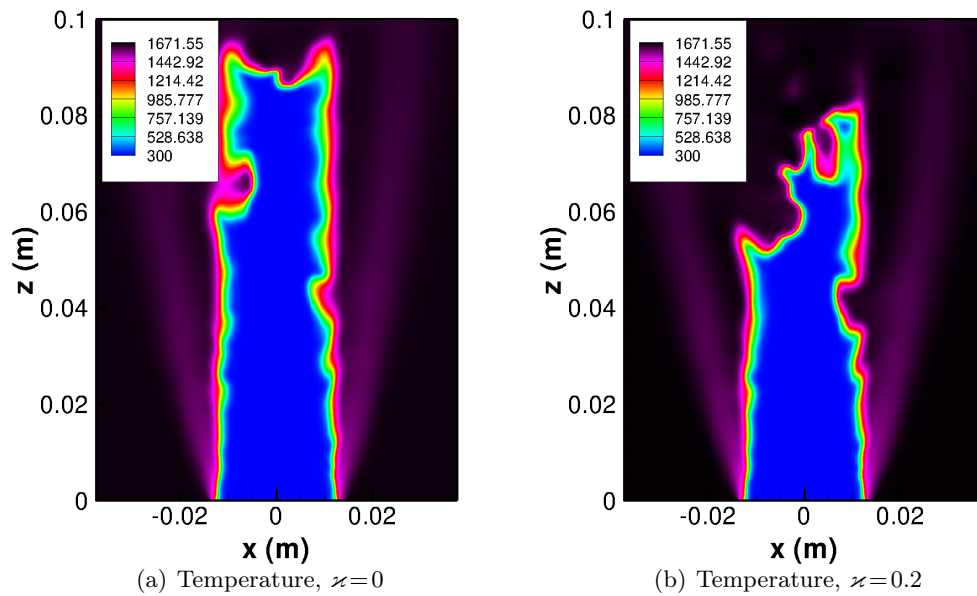
Figure 6.32: Temperature planar cuts of the Bunsen-type flames at 56 ms. Plane $y=0$. Left: CH$_4$-air flame. Right: H$_2$-CH$_4$-air flame.

(a) CO_2 mass fraction, $\varkappa = 0$

(b) CO_2 mass fraction, $\varkappa = 0.2$

(c) CO mass fraction, $\varkappa = 0$

(d) CO mass fraction, $\varkappa = 0.2$

(e) NO mass fraction, $\varkappa = 0$

(f) NO mass fraction, $\varkappa = 0.2$
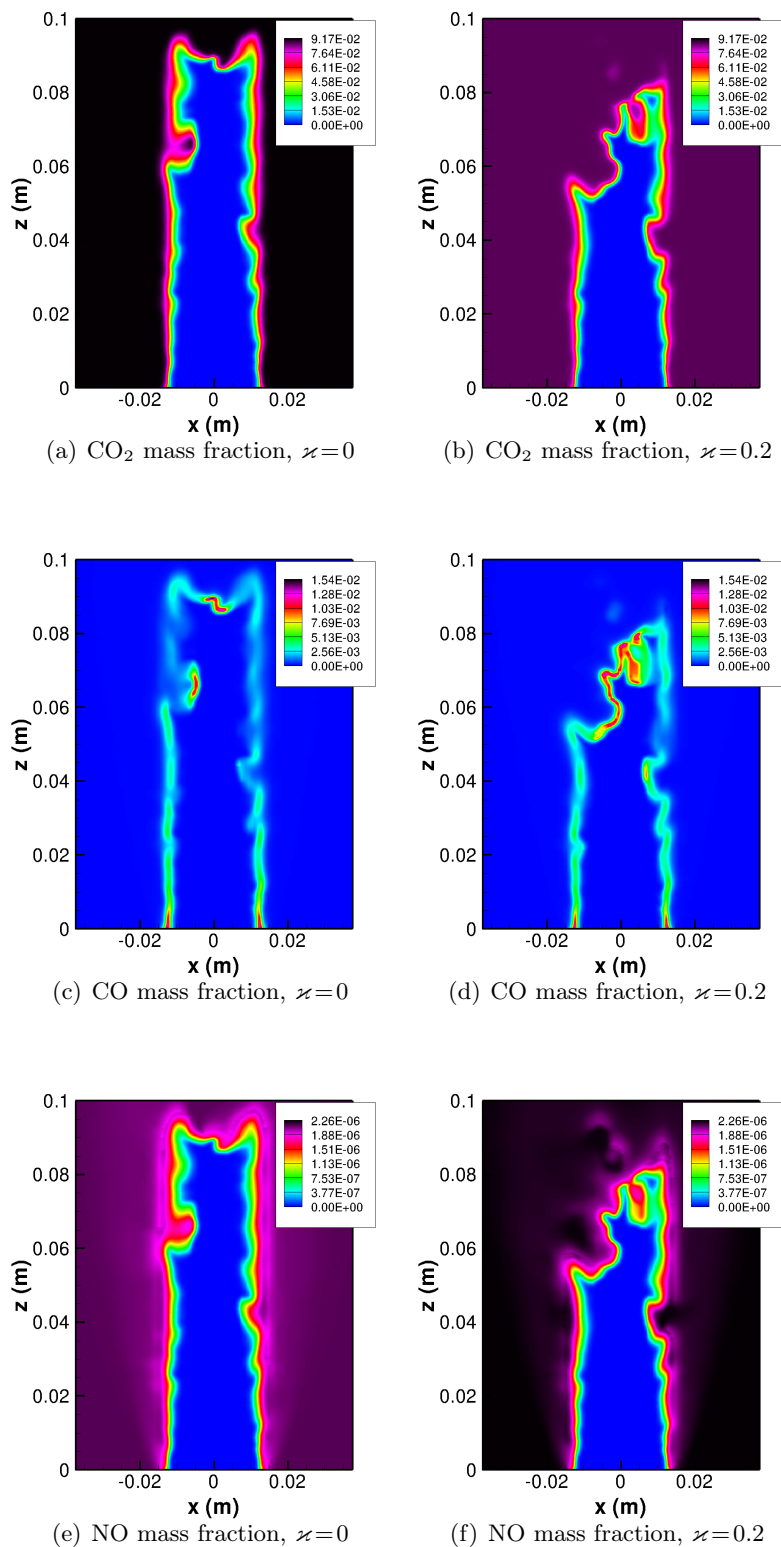
Figure 6.33: Planar cuts of the instantaneous CO_2, CO, and NO mass fraction distributions of the Bunsen-type flames at 56 ms. Plane $y = 0$. Left: CH_4-air flame. Right: H_2-CH_4-air flame.
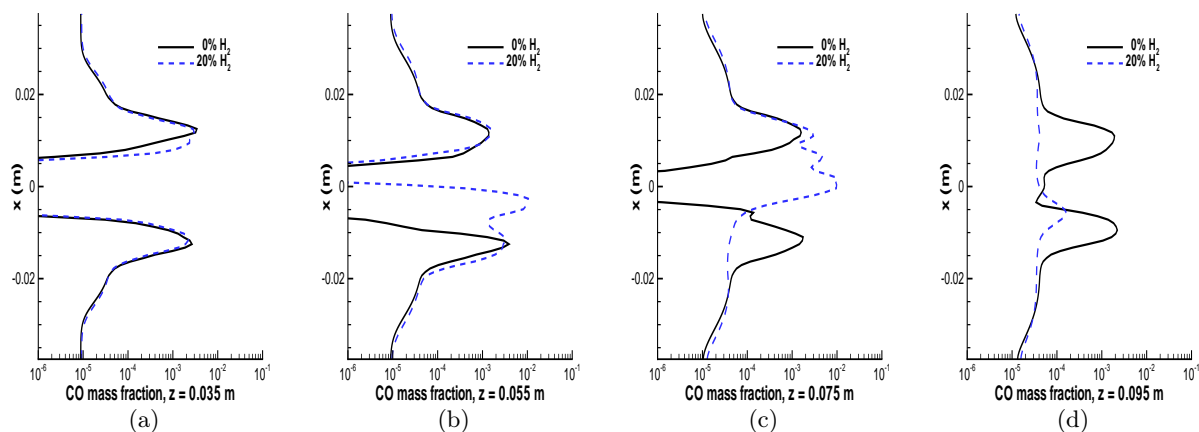
Figure 6.34: Radial profiles of the instantaneous CO mass fraction distribution of the Bunsen-type flames at 56 ms. Plane $y=0$.

was 110 μm/pixel. It is important to note that the experimental flame brushes were computed from unfiltered images. The author did not have access to raw data from the experiments, so filtering could not be carried out, as done previously for the methane Bunsen flame of section 6.5.

The experimental and numerical flame brushes are displayed in Figure 6.35. Although clear differences between the experimental and numerical results can be seen, both the experiments and the simulations show a decrease in the flame height (36% and 18%, respectively, based on the $c_T=0.1$ contour and evaluated at the centerline [268]) when hydrogen is added to methane, indicating a higher global burning rate for the enriched flame. It can also be observed that the predicted flames are taller that their experimental counterparts. It is worth noting that pockets of unburned gas were neglected (i.e., they were treated as burned gas) in the image analysis of Halter [269]. The presence of pockets of unburned gas near and above the flame tip in the instantaneous images would increase the height of the ensemble-averaged flame front. Therefore, the actual flame brushes are expected to be taller than those shown in Figures 6.35(a) and 6.35(b), which correspond to the experiments.

Two-dimensional curvature was also extracted from instantaneous unfiltered experimental images and slices of the numerical solutions. The curvature PDFs from the experimental data and the LES solutions associated to $c_T=0.5$ contour are shown in Figure 6.36. The PDFs display a Gaussian-type shape centred around zero, with the PDF corresponding to the predicted enriched flame being slightly skewed towards negative values of curvature. The PDFs corresponding to the LES simulations are narrower, owing to a smaller resolution of the flame front as compared to the experimental flame front images. It is apparent that the addition of hydrogen leads to slightly broader PDFs, in both the experiments and the simulations, with higher probabilities of

(a) Experimental CH$_4$-air flame

(b) Experimental H$_2$-CH$_4$-air flame

(c) Predicted CH$_4$-air flame

(d) Predicted H$_2$-CH$_4$-air flame
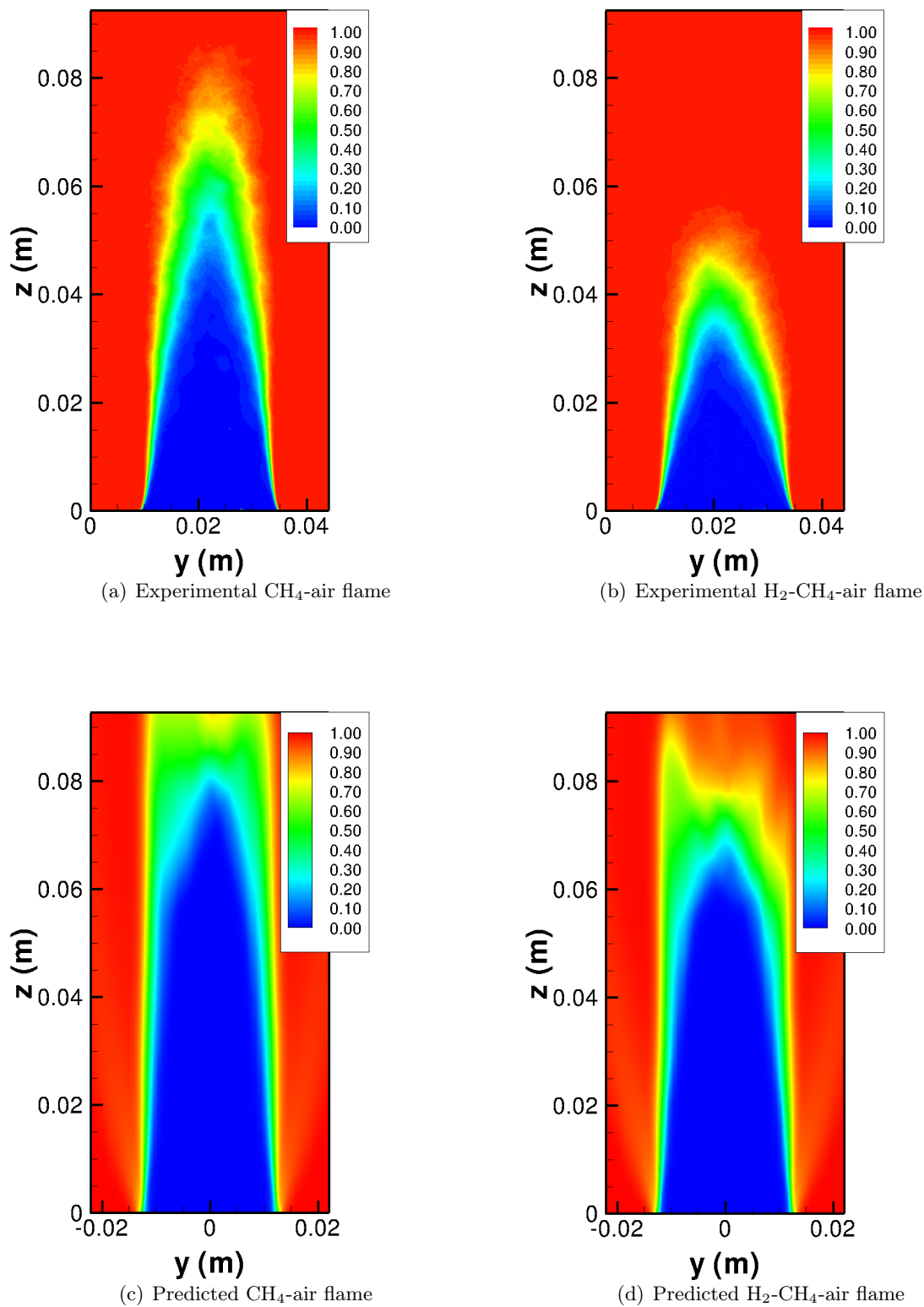
Figure 6.35: Comparison of experimental and predicted temperature-based flame brushes for the Bunsen-type CH$_4$-air and H$_2$-CH$_4$-air flames.
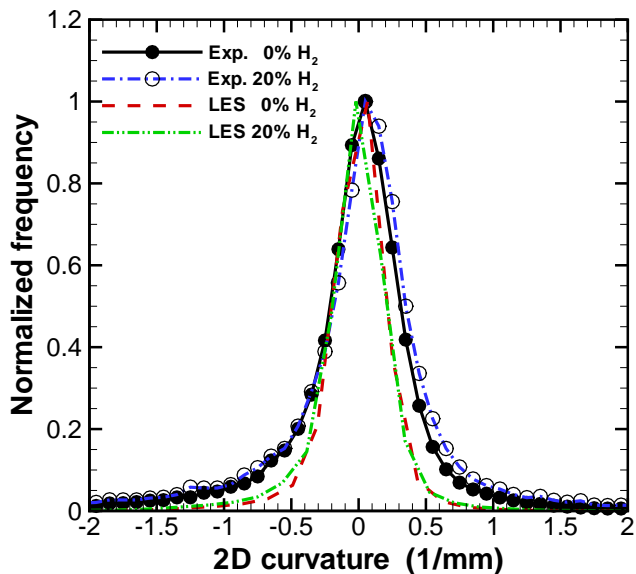
Figure 6.36: PDF of 2D curvature corresponding to a progress variable $c_T = 0.5$ for the Bunsen-type CH_4-air and H_2-CH_4-air flames.

finding larger curvatures for the enriched flame. This indicates that more small-scale wrinkling is present in the enriched flame.

In what follows, the predicted time-averaged mass fractions of relevant species are contrasted and discussed. In Figure 6.37 planar cuts of the time-averaged CO_2, CO, and NO mass fraction distributions are shown. Similar trends to those encountered in the instantaneous cuts are discernible for CO_2 and NO. Reduced levels of CO_2 and increased levels of NO are observed in the enriched flame. The planar cuts of the time-averaged CO mass fractions show that, away from the burner exit, more CO can be found in a region surrounding the centerline above 0.06 m and 0.07 m of the burner exit (see Figure 6.37(c) and Figure 6.37(d)) for the the H_2-enriched and pure methane flames, respectively. In the enriched flame, the region extends further upstream. Radial profiles of CO mass fraction are also displayed for different locations above the burner exit. A slight increase in the CO levels in areas of fully burned gas is exhibited in the enriched flame and a decreased margin between peak CO mass fraction values for the two flames is visible, as compared to the instantaneous plots.

In summary, the LES simulations of 3D Bunsen-type turbulent premixed methane-air and H_2-enriched methane-air flames predicted similar qualitative trends to those found in the experiments of Halter *et al.* [268] for the flame height and two-dimensional curvature. The enriched flame was shorter, which is attributed to a faster consumption of the blended fuel. The 2D curvature PDFs displayed a Gaussian-type shape centred around zero. In both the experiments

(a) CO$_2$ mass fraction, $\varkappa=0$ (b) CO$_2$ mass fraction, $\varkappa=0.2$

(c) CO mass fraction, $\varkappa=0$ (d) CO mass fraction, $\varkappa=0.2$

(e) NO mass fraction, $\varkappa=0$ (f) NO mass fraction, $\varkappa=0.2$
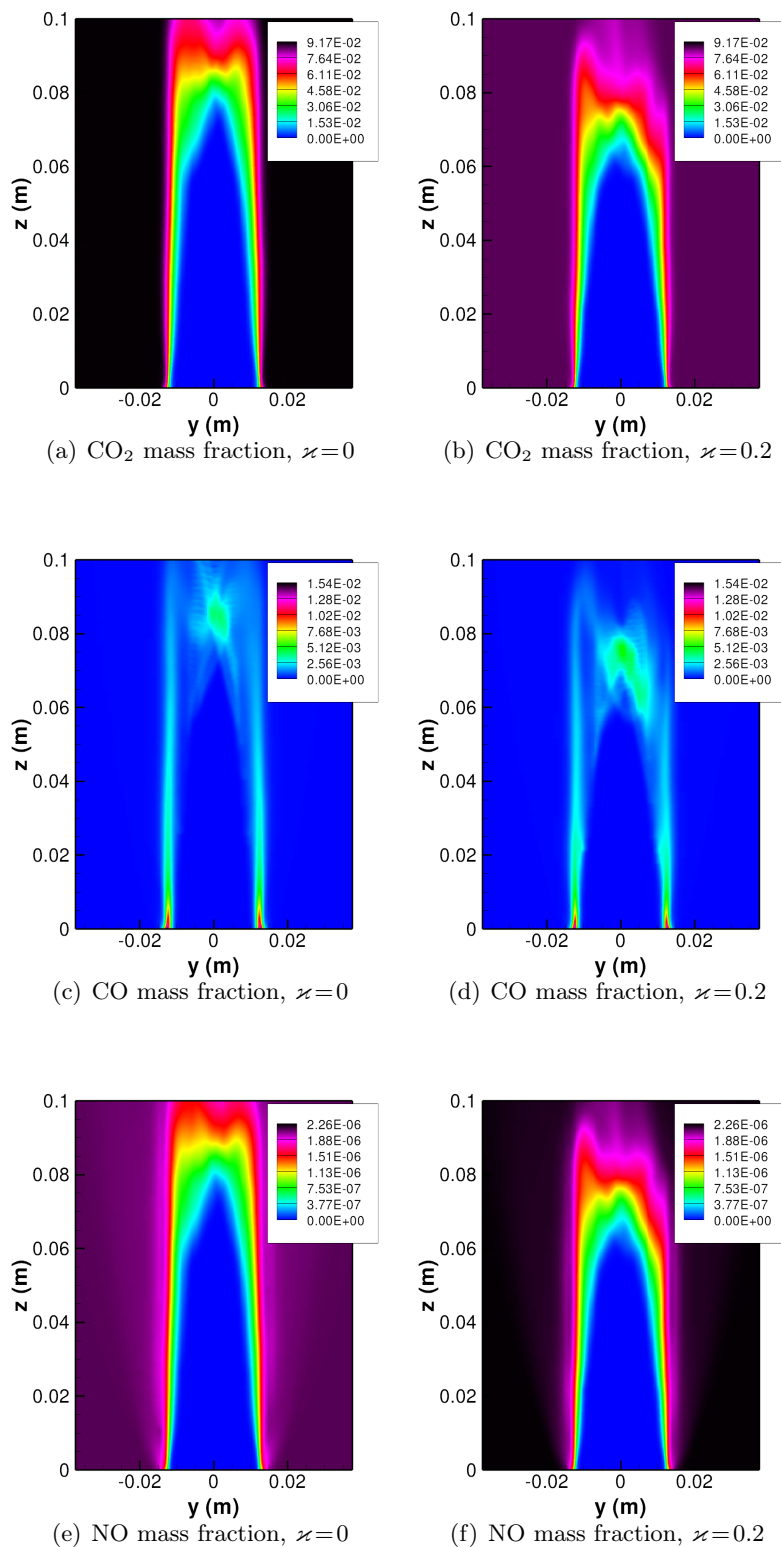
Figure 6.37: Planar cuts of the time-averaged CO$_2$, CO, and NO mass fraction distributions of the Bunsen-type flames. Plane $x=0$. Left: CH$_4$-air flame. Right: H$_2$-CH$_4$-air flame.
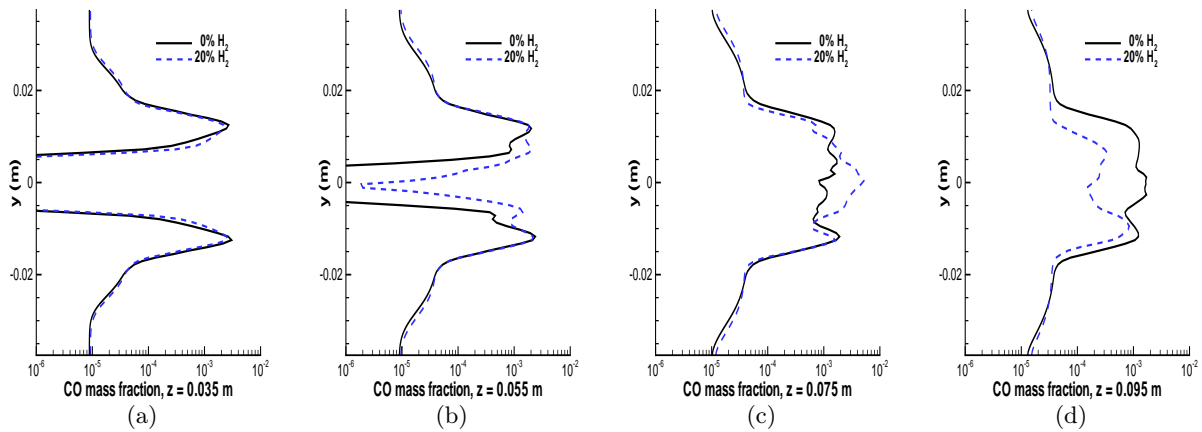
Figure 6.38: Radial profiles of the time-averaged CO mass fraction distribution of the Bunsen-type flames. Plane $x = 0$.

and the simulations, the addition of hydrogen lead to slightly broader PDFs. Furthermore, the hydrogen enriched flame displayed a higher degree of wrinkling with sharper ridges of negative curvature and larger pockets of positive curvature, which were more pronounced near the flame tip. This behaviour has been associated with preferential diffusion effects and the less diffusive-thermally stable character of the H_2-enriched flame. In addition, reduced levels of CO_2 and increased levels of NO emissions were predicted for the enriched flame, and a slight increase in the CO levels in areas of fully burned gas was exhibited in the predicted enriched flame.

Chapter 7

Conclusions and Future Directions

7.1 Conclusions

In this thesis research, subfilter-scale (SFS) modelling for large-eddy simulation (LES) of lean and H_2-enriched methane-air turbulent premixed combustion has been investigated. Two- and three-dimensional fully-compressible LES solvers for a thermally perfect reactive mixture of gases were developed and systematically validated. The SFS stresses were modelled using constant-coefficient versions of the Smagorinsky and one-equation eddy-viscosity type models and gradient approximations were employed to model the SFS scalar fluxes. Two modelling strategies for the chemistry-turbulence interaction were pursued: the artificially thickened flame model [66] coupled with a power-law SFS wrinkling approach [60] and the presumed conditional moment (PCM) SFS modelling approach [51] coupled with the flame prolongation of intrinsic low-dimensional manifold (FPI) [208] chemistry tabulation technique. Two versions of the PCM-FPI approach, as outlined by Galpin *et al.* [209], were investigated. The first one consists in reading species mass fractions directly from a look-up table and the second consists in transporting the species and reconstructing the reaction rates from a look-up table of species mass fractions.

A parallel, block-based adaptive mesh refinement (AMR), finite-volume scheme was developed for the numerical solutions of the Favre-filtered Navier-Stokes equations along with the additional equations for the thickened flame and PCM-FPI models. The Favre-filtered transport equations were solved on multiblock quadrilateral or hexahedral meshes employing a second-order accurate scheme in both time and space. The inviscid flux at each cell face was evaluated using limited linear reconstruction and Riemann-solver based flux functions. Particularly, the Roe [228] flux function with the Venkatakrishnan [234] limiter were utilized for the computation

of steady-state solutions, while the AUSM$^+$-up [230] flux function with the Barth-Jespersen [233] limiter were used for unsteady solutions. The viscous fluxes were evaluated utilizing a diamond-path reconstruction [271] in one- and two-dimensional computations and a weighted cell-face gradient method [240] in three-dimensional cases.

Validation of the LES solvers were carried out by comparing predicted solutions with experimental data and other published numerical results. Numerical simulation results for the thickened flame and PCM-FPI models applied to the prediction of premixed flames in one, two, and three spatial dimensions were described and discussed. Freely propagating flames in isotropic decaying turbulence and Bunsen-type flames corresponding to stoichiometric and lean methane-air and lean hydrogen-enriched methane-air mixtures were considered.

In particular, the thickened flame and PCM-FPI models were applied to the slot burner configuration that was experimentally studied by Filatyev *et al.* [260] and simulated by Bell *et al.* [261] using direct numerical simulation (DNS) with adaptive mesh refinement. The agreement of the predicted flame heights and brushes by the thickened flame and PCM-FPI models with the experimental and DNS results provided assurance of the proper implementation of the models and reliance of the LES algorithm.

The two models were also applied to the Bunsen flame configuration experimentally studied by Yuen & Gülder [264] (lean methane-air flame) and further compared to the transported flame surface density (FSD) model of Hawkes & Cant [56]. Even though all the numerical results obtained with the different models compared qualitatively well with the experiment, the comparison revealed deficiencies in thickened flame formulation employed herein, even with a relatively small value of 3 for the thickening factor. The flame height was significantly over-predicted, the instantaneous flame front exhibited noticeably less wrinkling than the actual experimental flame, and the resolved curvature of the flame front was under-predicted. These deficiencies would be even more pronounced if a large thickening factor were adopted as is more typically used. In contrast, the performance of the FSD and PCM-FPI models was found to be better, with both approaches providing predictions that agreed both qualitatively and quantitatively with key aspects of the flame observed in the experiment. The resolved flame structure and wrinkling, average flame height, and resolved flame surface and curvature all compared well with experiment. The FSD model appears to be well suited for describing the evolution and dynamics of the flame surface, yielding slightly better predictions of these quantities, but is lacking in its ability to connect the flame area to reaction rates. The PCM-FPI model seems more robust and can be applied more widely to premixed, non-premixed, and partially premixed flames, although at the expense of higher computational costs.

Based on the predictive capabilities of the models examined, the PCM-FPI model was selected for the study of hydrogen-enrichment of methane, which requires incorporation of complex chemistry, Lewis number effects, and preferential diffusion. A new progress of reaction variable was proposed to account for NO, namely $Y_c = Y_{CO_2} + Y_{NO}$. The importance of transporting species with different diffusion coefficients was demonstrated, in particular for H_2. The PCM-FPI model, with the proposed progress of reaction variable for H_2-enriched methane flames, was then applied to the Bunsen flame configuration studied experimentally by Halter [268] *et al.* The LES simulations of three-dimensional Bunsen-type turbulent premixed methane-air and H_2-enriched methane-air flames predicted similar qualitative trends to those found in the experiments of Halter *et al.* [268] for the flame height and two-dimensional curvature. The enriched flame was shorter, which is attributed to a faster consumption of the blended fuel. The two-dimensional curvature PDFs displayed a Gaussian-type shape centred around zero. In both the experiments and the simulations, the addition of hydrogen lead to slightly broader PDFs. The H_2-enriched flame displayed a higher degree of wrinkling with sharper ridges of negative curvature and larger pockets of positive curvature, which were more pronounced near the flame tip. This behaviour has been associated with preferential diffusion effects and the less diffusive-thermally stable character of the H_2-enriched flame. Furthermore, reduced levels of CO_2 and increased levels of NO emissions were predicted for the enriched flame, and a slight increase in the CO levels in areas of fully burned gas was exhibited in the predicted enriched flame. Unfortunately, experimental data for CO_2, CO, and NO were not available from the measurements of Halter *et al.* [268] to compare the predicted levels of these quantities.

7.2   Original Contributions

The contributions of this thesis work can be summarized as follows:

- Development of a fully compressible LES framework for a thermally perfect reactive mixture of gases in two and three spatial dimensions, focused on premixed combustion. The LES solution algorithm was written in C++ and parallelized using the MPI library. In addition, post-processing tools were developed specifically for the unsteady LES solutions and comparison with experimental measurements using the Python scripting language and Octave package.

- Two modelling formulations for LES of premixed combustion were implemented: the thickened flame model coupled with a power-law SFS flame wrinkling approach, and the presumed conditional moment (PCM) SFS modelling approach coupled with the flame prolongation of intrinsic low-dimensional manifold (FPI) chemistry tabulation technique.

Three variants of the latter formulation were implemented: (i) retrieving the species mass fractions directly from a look-up table; (ii) transporting the species and retrieving their reactions rates directly from a look-up table; and (iii) transporting the species and reconstructing their reactions rates from a look-up table of species mass fractions.

- Development of a computational framework for look-up table generation based on the Cantera package, C++ and Python, in addition to a look-up table manager for both premixed and non-premixed combustion. The look-up table manager and the two-dimensional LES solver include the mixture fraction and its SFS variance variables as well. Besides the two aforesaid variables together with the progress variable and its SFS variance, the look-up table supports an additional variable to characterize the FPI manifold, which could be the temperature of the fresh combustible mixture.

- Head-to-head comparisons of SFS models for turbulent premixed combustion. The comparisons represent some of the first direct comparisons of multiple SFS models to laboratory-scale flame data and this permitted identification and highlighting of weaknesses and strengths of several popular SFS models for premixed combustion, including the thickened flame model, the PCM-FPI approach, and a transported FSD model.

- Deficiencies of the thickened flame model with the power-law SFS wrinkling approach used herein were identified. For a lean methane-air flame in the thin reaction zone regime, the flame height was over-predicted, the instantaneous flame front exhibited noticeably less wrinkling than the actual experimental flame, and the resolved curvature of the flame front was under-predicted.

- In general, it is a common practice to compare predicted LES results with unfiltered experimental data. In this research, comparison of numerical solutions with both filtered and unfiltered experimental data were performed. Differences between the curvature statistics of filtered and unfiltered experimental data were clearly shown, suggesting that filtered experimental data should be used when carrying out such comparisons.

- The first LES of H_2-enriched methane-air turbulent premixed flames were performed:

  - leading to the introduction of a novel progress of reaction variable that was specifically defined to account for NO in the PCM-FPI model;

  - showing the importance of transporting species with different diffusion coefficients (in particular H_2), and thereby, accounting for Lewis number and differential diffusion effects, at least at the resolved LES level.

- First direct comparison of LES predictions for H_2-enriched methane-air flames to experimental data, which reproduced observed behaviour in the experiments, particularly for the flame heights and statistics of two-dimensional curvature.

7.3 Recommendations for Future Directions

The proposed LES framework appears to be promising for the simulation of turbulent premixed combustion. In particular, encouraging results were obtained with the PCM-FPI SFS modelling approach and the proposed progress of reaction variable for hydrogen-enrichment of lean methane-air flames. Nevertheless, further research is required to make the proposed approach practical for application to realistic combustion devices. Among the many possible areas for improvement and future research, the following work is suggested:

- Direct comparisons of predicted CO_2, CO, and NO should be made with measured data. Also, radiative heat losses should be included to improve the predictions of temperature and species concentrations, particularly those of NO.

- The SFS modelling in the current LES framework makes use of an eddy-viscosity heavily, which is determined using constant-coefficient models. Variable-coefficient versions of the Smagorinsky [135] and one-equation [139] models could be implemented to improve the accuracy of the eddy-viscosity type SFS modelling.

- The SFS power-law approach that was used in conjunction with the thickened flame model assumes equilibrium between production and destruction of flame surface at the SFS level, and a constant power was employed throughout this research. A transport equation for the SFS wrinkling factor, as proposed by Weller *et al.* [58] and Fureby [59], could be used and investigated for improved accuracy of the thickened flame model.

- The PCM-FPI model used herein assumes a beta distribution for the SFS PDF of the progress variable. Alternative shapes of the presumed PDF could be utilized and further assessed. For instance, the laminar flame based PDF proposed by Bray *et al.* [272] and modified by Grout & Bushe [273] would seem quite promising.

- The proposed progress of reaction variable definition is valid only for lean and stoichiometric hydrogen-methane premixed combustion. More investigation could be done to define a more general progress of reaction variable.

- In the PCM-FPI approach, the method to reconstruct reaction rates assumes equal molecular diffusivities of species and Y_c and a large Damköhler number. The high Damköhler

number approximation can be relaxed by including the second-order term in Equation 4.41. The assumption of equal molecular diffusivities of species and Y_c needs further investigation.

- Non-gradient transport modelling should be investigated, particularly for flames with $Le <$ 1. Using DNS with simple chemistry, Chakraborty & Cant [274] have shown that flames with a global $Le < 1$ exhibit non-gradient transport.

- Recently, Grcar *et al.* [275] showed that the Soret effect significantly changes the burning characteristics of two-dimensional freely propagating lean hydrogen-air laminar flames. Whether the Soret effect is important in lean H_2-enriched hydrocarbon flames is a topic that requires research.

- The present three-dimensional LES framework uses an explicit time marching scheme. It would be interesting to assess the use of an implicit scheme for improving the efficiency of the time integration procedure. An implicit NKS algorithm with a dual time-stepping (DTS) procedure, which has been developed by Northrup & Groth [247], was adapted to the two-dimensional LES framework. The NKS-DTS procedure can be readily implemented in the three-dimensional LES framework.

- Future research should involve the investigation of adaptive mesh refinement to LES of turbulent premixed flames using the PCM-FPI approach.

- Additional improvements to the LES framework may be possible by means of high-order finite-volume schemes together with high-order explicit commutative filters, which have been recently studied by Ivan [276] and Deconinck [277], respectively.

References

[1] "Key World Energy Statistics 2009." International Energy Agency, 2009.

[2] "CO$_2$ Emissions from Fuel Combustion 2009 (Highlights)." International Energy Agency, 2009.

[3] D. N. Anderson, "Effect of hydrogen injection on stability and emissions of an experimental premixed prevaporized propane burner." NASA Technical Memorandum TM X-3301, 1975.

[4] R. M. Clayton, "Hydrogen enrichment for low-emission jet combustion," *Advances in Chemistry Series*, vol. 166, pp. 267–286, 1978.

[5] B. Nagalingam, F. Duebel, and K. Schmillen, "Performance study using natural gas, hydrogen-supplemented natural gas and hydrogen in AVL research engine," *International Journal of Hydrogen Energy*, vol. 8, pp. 715–720, 1983.

[6] G. A. Karim, I. Wierzba, and Y. Al-Alousi, "Methane-hydrogen mixtures as fuels," *International Journal of Hydrogen Energy*, vol. 21, pp. 625–631, 1996.

[7] S. R. Bell and M. Gupta, "Extension of the lean operating limit for natural gas fueling of spark ignited engine using hydrogen blending," *Combustion Science and Technology*, vol. 123, pp. 23–48, 1997.

[8] J. D. Morris, R. A. Symonds, F. L. Ballard, and A. Banti in *ASME International Gas Turbine and Aeroengine Congress and Exhibition, Paper 98-GT-359*, 1998.

[9] C. G. Bauer and T. Forest, "Efect of hydrogen addition on the performance of methane-fueled vehicles. Part I: efect on S.I. engine performance," *International Journal of Hydrogen Energy*, vol. 26, pp. 71–77, 2001.

[10] M. S. Kumar, A. Ramesh, and B. Nagalingam, "Use of hydrogen to enhance the performance of a vegetable oil fuelled compression ignition engine," *International Journal of Hydrogen Energy*, vol. 28, pp. 1143–1154, 2003.

[11] M. A. S. Al-Baghdadi, "Hydrogen-ethanol blending as an alternative fuel of spark ignition engines," *Renewable Energy*, vol. 28, pp. 1471–1478, 2003.

[12] F. Ma, Y. Wang, H. Liu, Y. Li, J. Wang, and S. Zhao, "Experimental study on thermal efficiency and emission characteristics of a lean burn hydrogen enriched natural gas engine," *International Journal of Hydrogen Energy*, vol. 32, pp. 5067–5075, 2007.

[13] G. Yu, C. K. Law, and C. K. Wu, "Laminar flame speeds of hydrocarbon + air mixtures with hydrogen addition," *Combustion and Flame*, vol. 63, pp. 339–347, 1986.

[14] J. L. Gauducheau, B. Denet, and G. Searby, "A numerical study of lean $CH_4/H_2/Air$ premixed flames at high pressure," *Combustion Science and Technology*, vol. 137, pp. 81–99, 1998.

[15] J.-Y. Ren, W. Qin, F. N. Egolfopoulos, and T. T. Tsotsis, "Strain-rate effects on hydrogen-enhanced lean premixed combustion," *Combustion and Flame*, vol. 124, pp. 717–720, 2001.

[16] C. Uykur, P. Henshaw, D.-K. Ting, and R. Barron, "Effects of addition of electrolysis products on methane/air premixed laminar combustion," *International Journal of Hydrogen Energy*, vol. 26, pp. 265–273, 2001.

[17] C. J. Sung, Y. Huang, and J. A. Eng, "Effects of reformer gas addition on the laminar flame speeds and flammability limits of n-butane and iso-butane flames," *Combustion and Flame*, vol. 126, pp. 1699–1713, 2001.

[18] G. S. Jackson, R. Sai, J. M. Plaia, C. M. Boggs, and K. T. Kiger, "Influence of H_2 on the response of lean premixed CH_4 flames to high strained flows," *Combustion and Flame*, vol. 132, pp. 503–511, 2003.

[19] H. Guo, G. J. Smallwood, F. Liu, Y. Ju, and O. L. Gülder, "The effect of hydrogen addition on flammability limit and NO_x emission in ultra-lean counterflow CH_4/Air premixed flames," in *Proceedings of the Combustion Institute*, vol. 30, pp. 303–311, The Combustion Institute, 2005.

[20] R. W. Schefer, D. M. Wicksall, and A. K. Agrawal, "Combustion of hydrogen-enriched methane in a lean premixed swirl-stabilized burner," in *Proceedings of the Combustion Institute*, vol. 29, pp. 843–851, The Combustion Institute, 2002.

[21] R. W. Schefer, "Hydrogen enrichment for improved lean flame stability," *International Journal of Hydrogen Energy*, vol. 28, pp. 1131–1141, 2003.

[22] H. S. Kim, V. K. Arghode, and A. K. Gupta, "Flame characteristics of hydrogen-enriched methane-air premixed swirling flames," *International Journal of Hydrogen Energy*, vol. 34, pp. 1063–1073, 2009.

[23] N. Peters, *Turbulent Combustion*. Cambridge University Press, 2000.

[24] D. Veynante and L. Vervisch, "Turbulent combustion modeling," *Progress in Energy and Combustion Science*, vol. 28, pp. 193–266, 2002.

[25] T. Poinsot and D. Veynante, *Theoretical and Numerical Combustion*. R.T. Edwards Inc., 2005.

[26] P. Givi, "Model free simulations of turbulent reactive flows," *Progress in Energy and Combustion Science*, vol. 15, pp. 1–107, 1989.

[27] T. Poinsot, "Using direct numerical simulations to understand premixed turbulent combustion," in *Proceedings of the Combustion Institute*, vol. 26, pp. 219–232, The Combustion Institute, 1996.

[28] T. Poinsot, S. Candel, and A. Trouvé, "Applications of direct numerical simulations to premixed turbulent combustion," *Progress in Energy and Combustion Science*, vol. 21, pp. 531–576, 1996.

[29] T. Baritaud, T. Poinsot, and M. Baum, *Direct numerical simulation for turbulent reacting flows.* Technip, 1996.

[30] L. Vervisch and T. Poinsot, "Direct numerical simulation of non-premixed turbulent flames," *Annual Review of Fluid Mechanics*, vol. 30, pp. 655–691, 1998.

[31] D. Wilcox, *Turbulence Modeling for CFD.* DCW Industries, 2006.

[32] H. Pitsch, "Large-eddy simulation of turbulent combustion," *Annual Review of Fluid Mechanics*, vol. 38, pp. 453–482, 2006.

[33] A. Leonard, "Energy cascade in large-eddy simulations of turbulent fluid flows," *Advances in Geophysics*, vol. 18, pp. 237–248, 1974.

[34] F. T. M. Nieuwstadt and J. P. Meeder, "Large-eddy simulation of air pollution dispersion: a review," in *New tools in turbulence modelling* (O. Métais and J. H. Ferziger, eds.), pp. 264–280, Les Editions de Physique - Springer Verlag, 1997.

[35] C. Fureby and C. Löfström, "Large eddy simulations of bluff body stabilized flames," in *Proceedings of the Combustion Institute*, vol. 25, pp. 1257–1264, The Combustion Institute, 1994.

[36] C. Fureby and S.-I. Möller, "Large eddy simulation of reacting flows applied to bluff body stabilized flames," *AIAA Journal*, vol. 33, no. 12, pp. 2339–2347, 1995.

[37] P. E. DesJardin and S. H. Frankel, "Large eddy simulation of a nonpremixed reacting jet: Application and assessment of subgrid-scale combustion models," *Physics of Fluids*, vol. 10, pp. 2298–2314, 1998.

[38] F. A. Jaberi and S. James, "A dynamic similarity model for large eddy simulation of turbulent combustion," *Physics of Fluids*, vol. 10, pp. 1775–1777, 1998.

[39] F. Gao and E. E. O'Brien, "A large-eddy simulation scheme for turbulent reacting flows," *Physics of Fluids A*, vol. 5, pp. 1282–1284, 1993.

[40] S. H. Frankel, V. Adumitroaie, C. K. Madnia, and P. Givi, "Large eddy simulation of turbulent reacting flows by assumed PDF methods," in *Engineering Applications of Large Eddy Simulations* (S. A. Ragab and U. Piomelli, eds.), pp. 81–101, ASME, 1993.

[41] A. W. Cook and J. J. Riley, "A subgrid model for equilibrium chemistry in turbulent flows," *Physics of Fluids*, vol. 6, pp. 2868–2870, 1994.

[42] S. I. Möller, E. Lundgren, and C. Fureby, "Large eddy simulations of unsteady combustion," in *Proceedings of the Combustion Institute*, vol. 26, pp. 241–248, The Combustion Institute, 1996.

[43] A. W. Cook, J. J. Riley, and G. Kosály, "A laminar flamelet approach to sub-grid scale chemistry in turbulent flows," *Combustion and Flame*, vol. 109, pp. 332–341, 1997.

[44] P. J. Colucci, F. A. Jaberi, P. Givi, and S. B. Pope, "Filtered density function for large eddy simulation of turbulent reacting flows," *Physics of Fluids*, vol. 10, pp. 499–515, 1998.

[45] F. A. Jaberi, P. J. Colucci, S. James, P. Givi, and S. B. Pope, "Filtered mass density function for large-eddy simulation of turbulent reacting flows," *Journal of Fluid Mechanics*, vol. 41, pp. 85–121, 1999.

[46] H. Pitsch and H. Steiner, "Large-eddy simulation of a turbulent piloted methane/air diffusion flame (Sandia flame D)," *Physics of Fluids*, vol. 12, pp. 2541–2554, 2000.

[47] C. D. Pierce and P. Moin, "Progress-variable approach for large-eddy simulation of nonpremixed turbulent combustion," *Journal of Fluid Mechanics*, vol. 504, pp. 73–97, 2004.

[48] W. K. Bushe and H. Steiner, "Conditional moment closure for large eddy simulation of nonpremixed turbulent reacting flows," *Physics of Fluids*, vol. 11, pp. 1896–1906, 1999.

[49] S. H. Kim and H. Pitsch, "Conditional filtering method for large-eddy simulation of turbulent nonpremixed combustion," *Physics of Fluids*, vol. 17, 2005.

[50] S. Navarro-Martinez, A. Kronenburg, and F. di Mare, "Conditional moment closure for large eddy simulations," *Flow, Turbulence and Combustion*, vol. 75, pp. 245–274, 2005.

[51] P. Domingo, L. Vervisch, S. Payet, and R. Hauguel, "DNS of a premixed turbulent V flame and LES of a ducted flame using a FSD-PDF subgrid scale closure with FPI-tabulated chemistry," *Combustion and Flame*, vol. 143, pp. 566–586, 2005.

[52] P. Domingo, L. Vervisch, and D. Veynante, "Large-eddy simulation of a lifted methane jet flame in a vitiated coflow," *Combustion and Flame*, vol. 152, pp. 415–432, 2008.

[53] M. Boger, D. Veynante, H. Boughanem, and A. Trouvé, "Direct numerical simulation analysis of flame surface density concept for large eddy simulation of turbulent premixed combustion," in *Proceedings of the Combustion Institute*, vol. 27, pp. 917–925, The Combustion Institute, 1998.

[54] F. Charlette, A. Trouvé, M. Boger, and D. Veynante, "A flame surface density model for large eddy simulations of turbulent premixed flames," in *Proceedings of the Combustion Institute Joint Meeting of the British, German and French Sections*, (Nancy, France), 1999.

[55] E. R. Hawkes and R. S. Cant, "A flame surface density approach to large-eddy simulation of premixed turbulent combustion," in *Proceedings of the Combustion Institute*, vol. 28, pp. 51–58, The Combustion Institute, 2000.

[56] E. R. Hawkes and R. S. Cant, "Implications of a flame surface density approach to large eddy simulation of premixed turbulent combustion," *Combustion and Flame*, vol. 126, pp. 1617–1629, 2001.

[57] R. Knikker, D. Veynante, and C. Meneveau, "A priori testing of a similarity model for large eddy simulations of turbulent premixed combustion," in *Proceedings of the Combustion Institute*, vol. 29, pp. 2105–2111, The Combustion Institute, 2002.

[58] H. G. Weller, G. Tabor, A. D. Gosman, and C. Fureby, "Application of flame-wrinkling LES combustion model to a turbulent mixing layer," in *Proceedings of the Combustion Institute*, vol. 27, pp. 899–907, The Combustion Institute, 1998.

[59] C. Fureby, "Large eddy simulation of combustion instabilities in a jet engine afterburner model," *Combustion Science and Technology*, vol. 161, pp. 213–243, 2000.

[60] F. Charlette, C. Meneveau, and D. Veynante, "A power-law flame wrinkling model for LES of premixed turbulent combustion, part I: non-dynamic formulation and initial tests," *Combustion and Flame*, vol. 131, pp. 159–180, 2002.

[61] F. Charlette, C. Meneveau, and D. Veynante, "A power-law flame wrinkling model for LES of premixed turbulent combustion, part II: dynamic formulation," *Combustion and Flame*, vol. 131, pp. 181–197, 2002.

[62] C. Fureby, "A fractal flame-wrinkling large eddy simulation model for premixed turbulent combustion," in *Proceedings of the Combustion Institute*, vol. 30, pp. 593–601, The Combustion Institute, 2005.

[63] H. Pitsch and L. Duchamp de Lageneste, "Large-eddy simulation of premixed turbulent combustion using a level-set approach," in *Proceedings of the Combustion Institute*, vol. 29, pp. 2001–2008, The Combustion Institute, 2002.

[64] H. Pitsch, "A consistent level set formulation for large-eddy simulation of premixed turbulent combustion," *Combustion and Flame*, vol. 143, pp. 587–598, 2005.

[65] C. Angelberger, D. Veynante, and T. Poinsot, "Large eddy simulations of combustion instabilities in premixed flames." Proceedings of the Summer Program, Center for Turbulence Research, 1998.

[66] O. Colin, F. Ducros, D. Veynante, and T. Poinsot, "A thickened flame model for large eddy simulations of turbulent premixed combustion," *Physics of Fluids*, vol. 12, pp. 1843–1863, 2000.

[67] J. P. Legier, T. Poinsot, and D. Veynante, "Dynamically thickened flame LES model for premixed and non-premixed turbulent combustion," in *Proceedings of the Summer Program*, Center for Turbulence Research, 2000.

[68] P. A. McMurtry, S. Menon, and A. R. Kerstein, "Linear eddy sub-grid model for turbulent reacting flows: application to hydrogen–air combustion," in *Proceedings of the Combustion Institute*, vol. 24, pp. 271–278, The Combustion Institute, 1992.

[69] S. Menon, P. McMurtry, and A. R. Kerstein, "A linear eddy mixing model for large eddy simulation of turbulent combustion," in *LES of Complex Engineering and Geophysical Flows* (B. Galperin and S. Orszag, eds.), Cambridge University Press, 1993.

[70] S. Menon and W. H. Calhoon, "Subgrid mixing and molecular transport modeling for large eddy simulations of turbulent reacting flows," in *Proceedings of the Combustion Institute*, vol. 26, pp. 59–66, The Combustion Institute, 1996.

[71] T. Smith and S. Menon, "Model simulations of freely propagating turbulent premixed flames," in *Proceedings of the Combustion Institute*, vol. 26, pp. 229–306, The Combustion Institute, 1996.

[72] V. K. Chakravarthy and S. Menon, "Subgrid modeling of premixed flames in the flamelet regime," *Flow, Turbulence and Combustion*, vol. 65, pp. 133–161, 2000.

[73] F. di Mare, W. P. Jones, and K. R. Menzies, "Large eddy simulation of a model gas turbine," *Combustion and Flame*, vol. 137, pp. 278–294, 2004.

[74] W.-W. Kim, S. Menon, and H. C. Mongia, "Large-eddy simulation of a gas turbine combustor flow," *Combustion Science and Technology*, vol. 143, pp. 25–62, 1999.

[75] P. Moin, "Advances in large eddy simulation methodology for complex flows," *International Journal of Heat and Fluid Flow*, vol. 23, pp. 710–720, 2002.

[76] D. C. Haworth and K. Jansen, "Large-eddy simulation on unstructured deforming meshes: towards reciprocating IC engines," *Computers & Fluids*, vol. 29, pp. 493–524, 2000.

[77] L. Selle, G. Lartigue, T. Poinsot, R. Koch, K. U. Schildmacher, W. Krebs, B. Prade, P. Kaufmann, and D. Veynante, "Compressible large eddy simulation of turbulent combustion in complex geometry on unstructured meshes," *Combustion and Flame*, vol. 137, pp. 489–505, 2004.

[78] Y. Sommerer, D. Galley, T. Poinsot, S. Ducruix, F. Lacas, and D. Veynante, "Large eddy simulation and experimental study of flashback and blow-off in a lean partially premixed swirled burner," *Journal of Turbulence*, vol. 5, no. 37, 2004.

[79] C. Stone and S. Menon, "Open-loop control of combustion instabilities in a model gas turbine combustor," *Journal of Turbulence*, vol. 4, no. 20, 2003.

[80] C. Angelberger, D. Veynante, and F. Egolfopoulos, "LES of chemical and acoustic forcing of a premixed dump combustor," *Flow, Turbulence and Combustion*, vol. 65, pp. 205–222, 2000.

[81] J. Shinjo, Y. Mizobuchi, and S. Ogawa, "LES of unstable combustion in a gas turbine combustor," in *High Performance Computing: 5th International Symposium*, pp. 234–244, 2003.

[82] C. Wall and P. Moin, "Numerical methods for large eddy simulations of acoustic combustion instabilities," Tech. Rep. TF-91, Stanford University, 2005.

[83] J. B. Bell, R. K. Cheng, M. S. Day, and I. G. Shepherd, "Numerical simulation of Lewis number effects on lean premixed turbulent flames," in *Proceedings of the Combustion Institute*, vol. 31, pp. 1309–1317, The Combustion Institute, 2007.

[84] B. Bédat and R. K. Cheng, "Experimental study of premixed flames in intense isotropic turbulence," *Combustion and Flame*, vol. 100, pp. 485–494, 1995.

[85] Y. C. Chen and R. W. Bilger, "Experimental investigation of three-dimensional flame-front structure in premixed turbulent combustion—I: hydrocarbon/air Bunsen flames," *Combustion and Flame*, vol. 131, pp. 400–435, 2002.

[86] Y. C. Chen and R. W. Bilger, "Experimental investigation of three-dimensional flame-front structure in premixed turbulent combustion II. lean hydrogen/air Bunsen flames," *Combustion and Flame*, vol. 138, pp. 155–174, 2004.

[87] B. Bregeon, A. S. Gordon, and F. A. Williams, "Near-limit downward propagation of hydrogen and methane flames in oxygen–nitrogen mixtures," *Combustion and Flame*, vol. 33, pp. 33–45, 1978.

[88] T. Mitani and F. A. Williams, "Studies of cellular flames in hydrogen–oxygen–nitrogen mixtures," *Combustion and Flame*, vol. 39, pp. 169–190, 1980.

[89] M. Mizomoto, Y. Asaka, S. Ikai, and C. K. Law, "Effects of preferential diffusion on the burning intensity of curved flames," in *Proceedings of the Combustion Institute*, vol. 20, pp. 1933–1939, The Combustion Institute, 1985.

[90] V. R. Katta and W. M. Roquemore, "Numerical studies on the structure of two-dimensional H_2/air premixed jet flame," *Combustion and Flame*, vol. 102, pp. 21–40, 1995.

[91] M. Day, J. Bell, P.-T. Bremer, V. Pascucci, V. Beckner, and M. Lijewski, "Turbulent effects on cellular burning structures in lean premixed hydrogen flames," *Combustion and Flame*, vol. 156, pp. 1035–1045, 2009.

[92] A. N. Lipatnikov and J. Chomiak, "Molecular transport effects on turbulent flame propagation and structure," *Progress in Energy and Combustion Science*, vol. 31, pp. 1–73, 2005.

[93] E. R. Hawkes and J. H. Chen, "Direct numerical simulation of hydrogen-enriched lean premixed methane-air flames," *Combustion and Flame*, vol. 138, pp. 405–436, 2004.

[94] A. Mameri and I. Gökalp, "Numerical simulation of turbulent methane premixed flames enriched by hydrogen," in *Proceedings of the European Combustion Meeting*, 2007.

[95] T. D. Dunstan and K. W. Jenkins, "The efects of hydrogen substitution on turbulent premixed methane-air kernels using direct numerical simulation," *International Journal of Hydrogen Energy*, vol. 34, pp. 8389–8404, 2009.

[96] M. S. Day, X. Gao, and J. B. Bell, "Properties of lean turbulent methane-air flames with significant hydrogen addition," in *Proceedings of the Combustion Institute*, vol. 33, pp. 1601–1608, The Combustion Institute, 2011.

[97] A. W. Vreman, J. A. van Oijen, L. P. H. de Goey, and R. J. M. Bastiaans, "Direct numerical simulation of hydrogen addition in turbulent premixed Bunsen flames using flamelet-generated manifold reduction," *International Journal of Hydrogen Energy*, vol. 34, pp. 2778–2788, 2009.

[98] J.-Y. Ren, F. N. Egolfopoulos, and T. T. Tsotsis, "NO_x emission control of lean methane-air combustion with addition of methane reforming products," *Combustion Science and Technology*, vol. 174, pp. 181–205, 2002.

[99] F. A. Williams, *Combustion Theory*. Benjamin Cummings, 1985.

[100] K. K. Kuo, *Principles of Combustion*. John Wiley & Sons, 1986.

[101] S. Gordon and B. J. McBride, "Computer program for calculation of complex chemical equilibrium compositions and applications I. Analysis," Reference Publication 1311, NASA, 1994.

[102] B. J. McBride and S. Gordon, "Computer program for calculation of complex chemical equilibrium compositions and applications II. Users manual and program description," Reference Publication 1311, NASA, 1996.

[103] J. O. Hirschfelder, C. F. Curtiss, and R. B. Bird, *Molecular Theory of Gases and Liquids.* John Wiley, 1954.

[104] C. K. Law, *Combustion Physics.* Cambridge University Press, 2006.

[105] C. R. Wilke, "A viscosity equation for gas mixtures," *Journal of Chemical Physics*, vol. 18, pp. 517–519, 1950.

[106] W. C. Gardiner, *Combustion Chemistry.* Boca Raton: Springer-Verlag New York Inc., 1984.

[107] G. P. Smith, D. M. Golden, M. Frenklach, N. W. Moriarty, B. Eiteneer, M. Goldenberg, C. T. Bowman, R. K. Hanson, S. Song, W. C. Gardiner, V. V. Lissianski, and Z. Qin, "GRI-Mech 3.0." Available at http://www.me.berkeley.edu/gri_mech/.

[108] C. K. Westbrook and F. L. Dryer, "Simplified reaction mechanisms for the oxidation of hydrocarbon fuels in flames," *Combustion Science and Technology*, vol. 27, pp. 31–43, 1981.

[109] N. Peters and F. A. Williams, "The asymptotic structure of a stoichiometric methane–air flame," *Combustion and Flame*, vol. 68, pp. 185–207, 1987.

[110] S. B. Pope, *Turbulent Flows.* Cambridge University Press, 2000.

[111] R. Borghi, "On the structure and morphology of turbulent premixed flames," in *Recent Advances in the Aerospace Science* (C. Casci, ed.), pp. 117–138, New York: Springer, 1985.

[112] N. Peters, "Laminar flamelet concepts in turbulent combustion," in *Proceedings of the Combustion Institute*, vol. 21, pp. 1231–1250, The Combustion Institute, 1986.

[113] N. Peters, "The turbulent burning velocity for large-scale and small-scale turbulence," *Journal of Fluid Mechanics*, vol. 384, pp. 107–132, 1999.

[114] R. G. Abdel-Gayed and D. Bradley, "Combustion regimes and the straining of turbulent premixed flames," *Combustion and Flame*, vol. 76, pp. 213–218, 1989.

[115] T. Poinsot, D. Veynante, and S. Candel, "Quenching processes and premixed turbulent combustion diagrams," *Journal of Fluid Mechanics*, vol. 228, pp. 561–605, 1991.

[116] M. Düsing, A. Sadiki, and J. Janicka, "Towards a classification of models for the numerical simulation of premixed combustion based on a generalized regime diagram," *Combustion Theory and Modelling*, vol. 10, no. 1, pp. 105–132, 2006.

[117] C. Kortschik, T. Plessing, and N. Peters, "Laser optical investigation of turbulent transport of temperature ahead of the preheat zone in a premixed flame," *Combustion and Flame*, vol. 136, pp. 43–50, 2004.

[118] Y. B. Zeldovich, ed., *Theory of Combustion and Detonation in Gases.* Acad. Sci. USSR, 1944.

[119] C. Meneveau and J. Katz, "Scale-invariance and turbulence models for large-eddy simulation," *Annual Review of Fluid Mechanics*, vol. 32, pp. 1–32, 2000.

[120] S. Ghosal and P. Moin, "The basic equations for the large eddy simulation of turbulent flows in complex geometry," *Journal of Computational Physics*, vol. 118, pp. 24–37, 1995.

[121] O. V. Vasilyev, T. S. Lund, and P. Moin, "A general class of commutative filters for LES in complex geometries," *Journal of Computational Physics*, vol. 146, pp. 82–104, 1998.

[122] J. W. Deardorff, "A numerical study of three-dimensional turbulent channel flow at large Reynolds numbers," *Journal of Fluid Mechanics*, vol. 41, pp. 453–480, 1970.

[123] A. Scotti, C. Meneveau, and D. K. Lilly, "Generalized Smagorinsky model for anisotropic grids," *Physics of Fluids A*, vol. 5, pp. 2306–2308, 1993.

[124] A. Scotti, C. Meneveau, and M. Fatica, "Dynamic Smagorinsky model on anisotropic grids," *Physics of Fluids*, vol. 9, pp. 1856–1858, 1997.

[125] B. Vreman, B. Geurts, and H. Kuerten, "Subgrid-modeling in LES of compressible flow," *Applied Scientific Research*, vol. 54, pp. 191–203, 1995.

[126] M. P. Martín, U. Piomelli, and G. V. Candler, "Subgrid-scale models for compressible large-eddy simulations," *Theoretical and Computational Fluid Dynamics*, vol. 13, pp. 361–376, 2000.

[127] D. Knight, G. Zhou, N. Okong'o, and V. Shukla, "Compressible large eddy simulation using unstructured grids," Paper 98-0535, AIAA, January 1998.

[128] R. S. Rogallo and P. Moin, "Numerical simulation of turbulent flows," *Annual Review of Fluid Mechanics*, vol. 16, pp. 99–137, 1984.

[129] M. Lesieur and O. Métais, "New trends in large-eddy simulations of turbulence," *Annual Review of Fluid Mechanics*, vol. 28, pp. 45–82, 1996.

[130] U. Piomelli, "Large-eddy simulation: achievements and challenges," *Progress in Aerospace Sciences*, vol. 35, pp. 335–362, 1999.

[131] C. Fureby, N. Alin, N. Wikström, S. Menon, N. Svanstedt, and L. Persson, "Large-eddy simulation of high-Reynolds-number wall-bounded flows," *AIAA Journal*, vol. 42, no. 3, pp. 457–468, 2004.

[132] P. Sagaut, *Large Eddy Simulation for Incompressible Flows*. Berlin: Springer, 2004.

[133] J. Smagorinski, "General circulation experiments with the primitive equations. I: The basic experiment," *Monthly Weather Review*, vol. 91, no. 3, pp. 99–165, 1979.

[134] U. Schumann, "Subgrid scale model for finite difference simulation of turbulent flows in plane channels and annuli," *Journal of Computational Physics*, vol. 18, pp. 376–404, 1975.

[135] M. Germano, U. Piomelli, P. Moin, and W. H. Cabot, "A dynamic subgrid-scale eddy viscosity model," *Physics of Fluids A*, vol. 3, pp. 1760–1765, 1991.

[136] D. K. Lilly, "A proposed modification of the Germano subgrid-scale closure model," *Physics of Fluids A*, vol. 4, pp. 633–635, 1992.

[137] S. Ghosal, T. S. Lund, P. Moin, and K. Akselvoll, "A dynamic localization model for large eddy simulation of turbulent flows," *Journal of Fluid Mechanics*, vol. 286, pp. 229–255, 1995.

[138] C. Meneveau, T. S. Lund, and W. H. Cabot, "A Lagrangian dynamic subgrid-scale model of turbulence," *Journal of Fluid Mechanics*, vol. 319, pp. 353–385, 1996.

[139] W.-W. Kim and S. Menon, "A new dynamic one equation subgrid scale model for large eddy simulations," Paper 95-0356, AIAA, January 1995.

[140] J. Bardina, J. H. Ferziger, and W. C. Reynolds, "Improved subgrid scale models for large-eddy simulation," Paper 80-1357, AIAA, January 1980.

[141] J. W. Deardorff, "The use of subgrid transport equations in a three-dimensional model of atmospherical turbulence," *ASME Transactions, Journal of Fluids Engineering*, vol. 95, pp. 429–438, 1973.

[142] T. S. Lund and E. A. Novikov, "Parametrization of subgrid scale stress by velocity gradient tensor," in *Annual Research Briefs*, pp. 27–43, Center for Turbulence Research, 1994.

[143] J. P. Boris, F. F. Grinstein, E. S. Oran, and R. L. Kolbe, "New insights into large eddy simulation," *Fluid Dynamics Research*, vol. 10, pp. 199–228, 1992.

[144] C. Fureby and F. F. Gristein, "Large eddy simulation of high Reynolds number free and wall bounded flows," *Journal of Computational Physics*, vol. 181, pp. 68–97, 2002.

[145] S. Stolz, N. A. Adams, and L. Kleiser, "An approximate deconvolution model for large-eddy simulation of incompressible flows," *Physics of Fluids*, vol. 11, pp. 1699–1701, 1999.

[146] N. A. Adams and S. Stolz, "Deconvolution methods for subgrid-scale approximation in LES," in *Modern Simulation Strategies for Turbulent Flows* (B. J. Geurts, ed.), (Philadelphia), p. 21, Edwards, 2001.

[147] K. Kemenov and S. Menon, "TLS: a new two level simulation methodology for high-Reynolds LES," Paper 2002-0287, AIAA, January 2002.

[148] K. Kemenov and S. Menon, "A two-level simulation of high-Reynolds number non-homogeneous turbulent flows," Paper 2003-0084, AIAA, January 2003.

[149] L. Persson, C. Fureby, and N. Svanstedt, "On homogenisation based methods for large eddy simulation," *Journal of Fluids Engineering*, vol. 124, pp. 892–903, 2002.

[150] A. Yoshizawa, "Statistical theory for compressible turbulent shear flows, with the application to subgrid modeling," *Physics of Fluids A*, vol. 29, pp. 2152–2164, 1986.

[151] C. G. Speziale, G. Erlebacher, T. A. Zang, and M. Y. Hussaini, "The subgrid-scale modeling of compressible turbulence," *Physics of Fluids A*, vol. 31, pp. 940–942, 1988.

[152] A. Yoshizawa and K. Horiuti, "A statistically-derived subgrid-scale kinetic energy model for large-eddy simulation of turbulent flows," *Journal of the Physical Society of Japan*, vol. 54, pp. 2834–2839, 1985.

[153] D. K. Lilly, "The representation of small-scale turbulence in numerical simulation experiments," in *Proceedings of the IBM Scientific Computing Symposium on Environmental Sciences*, pp. 195–210, IBM Form No. 321–1951, 1967.

[154] H. Schmidt and U. Schumann, "Coherent structure of the convective boundary layer derived from large-eddy simulations," *Journal of Fluid Mechanics*, vol. 200, pp. 511–562, 1989.

[155] S. Menon, P.-K. Yeung, and W.-W. Kim, "Effect of subgrid models on the computed interscale energy transfer in isotropic turbulence," *Computers & Fluids*, vol. 25, pp. 165–180, 1996.

[156] C. Fureby, G. Tabor, H. Weller, and D. Gosman, "A comparative study of subgrid scale models in homogeneous isotropic turbulence," *Physics of Fluids*, vol. 9, pp. 1416–1429, 1997.

[157] J. Janicka and A. Sadiki, "Large eddy simulation of turbulent combustion systems," in *Proceedings of the Combustion Institute*, vol. 30, pp. 537–547, The Combustion Institute, 2005.

[158] T. M. Eidson, "Numerical simulation of the turbulent Rayleigh–Bénard problem using subgrid modelling," *Journal of Fluid Mechanics*, vol. 158, pp. 245–268, 1985.

[159] P. Moin, K. Squires, W. Cabot, and S. Lee, "A dynamic subgrid-scale model for compressible turbulence and scalar transport," *Physics of Fluids A*, vol. 3, pp. 2746–2757, 1991.

[160] P. Domingo, L. Vervisch, and K. Bray, "Partially premixed flamelets in LES of non-premixed turbulent combustion," *Combustion Theory and Modelling*, vol. 6, pp. 529–551, 2002.

[161] V. Sankaran and S. Menon, "LES of scalar mixing in supersonic mixing layers," in *Proceedings of the Combustion Institute*, vol. 30, pp. 2835–2842, The Combustion Institute, 2005.

[162] I. Porumbel and S. Menon, "Large eddy simulation of bluff body stabilized premixed flame," Paper 2006-0152, AIAA, January 2006.

[163] G. Erlebacher, M. Y. Hussaini, C. G. Speziale, and T. A. Zang, "Toward the large eddy simulation of compressible turbulent flows," *Journal of Fluid Mechanics*, vol. 238, pp. 155–185, 1992.

[164] K.-J. Nogenmyr, C. Fureby, X. Bai, P. Petersson, R. Collin, and M. Linne, "Large eddy simulation and laser diagnostic studies on a low swirl stratified premixed flame," *Combustion and Flame*, vol. 156, pp. 25–36, 2009.

[165] D. Veynante, A. Trouvé, K. N. C. Bray, and T. Mantel, "Gradient and countergradient scalar transport in turbulent premixed flames," *Journal of Fluid Mechanics*, vol. 332, pp. 263–293, 1997.

[166] S. Tullis and R. S. Cant, "Scalar transport modeling in large eddy simulation of turbulent premixed flames," in *Proceedings of the Combustion Institute*, vol. 29, pp. 2097–2104, The Combustion Institute, 2003.

[167] G. Damköhler, "Der einfluβ der turbulenz auf flammengeschwindigkeit in gasgemischen," *Z. Elektrochem*, vol. 46, pp. 601–652, 1947. English translation NASA Technical Memorandum 1112.

[168] W. Lin, *Large-Eddy Simulation of Premixed Turbulent Combustion Using Flame Surface Density Approach.* PhD thesis, University of Toronto, 2010.

[169] G. H. Markstein, ed., *Nonsteady Flame Propagation.* Pergamon Press, 1964.

[170] H. G. Im, T. S. Lund, and J. H. Ferziger, "Large eddy simulation of turbulent front propagation with dynamic subgrid models," *Physics of Fluids*, vol. 9, pp. 3826–3833, 1997.

[171] J. Piana, F. Ducros, and D. Veynante, "Large eddy simulations of turbulent premixed flames based on the G-equation and a flame front wrinkling description," in 11th *Symposium on Turbulent Shear Flows*, (Grenoble, France), 1997.

[172] M. Oberlack, H. Wenzel, and N. Peters, "On symmetries and averaging of the G-equation for premixed combustion," *Combustion Theory and Modelling*, vol. 5, pp. 1–20, 2001.

[173] V. Moureau, B. Fiorina, and H. Pitsch, "A level set formulation for premixed combustion LES considering the turbulent flame structure," *Combustion and Flame*, vol. 156, pp. 801–812, 2009.

[174] R. W. Bilger, S. B. Pope, K. N. C. Bray, and J. F. Driscoll, "Paradigms in turbulent combustion research," in *Proceedings of the Combustion Institute*, vol. 30, pp. 21–42, The Combustion Institute, 2005.

[175] T. D. Butler and P. J. O'Rourke, "A numerical method for two dimensional unsteady reacting flows," in *Proceedings of the Combustion Institute*, pp. 1503–1515, The Combustion Institute, 1977.

[176] D. Veynante and T. Poinsot, "Large eddy simulation of combustion instabilities in turbulent premixed burners," in *Annual Research Briefs*, pp. 253–274, Center for Turbulence Research, 1997.

[177] S. Roux, G. Lartigue, T. Poinsot, U. Meier, and C. Bérat, "Studies of mean and unsteady flow in a swirled combustor using experiments, acoustic analysis, and large eddy simulations," *Combustion and Flame*, vol. 141, pp. 40–54, 2005.

[178] M. Boileau, G. Staffelbach, B. Cuenot, T. Poinsot, and C. Bérat, "LES of an ignition sequence in a gas turbine engine," *Combustion and Flame*, vol. 154, pp. 2–22, 2008.

[179] A. R. Kerstein, "A linear-eddy model of turbulent scalar transport and mixing," *Combustion Science and Technology*, vol. 60, pp. 391–421, 1988.

[180] A. R. Kerstein, "Linear-eddy modeling of turbulent transport. II: Application to shear layer mixing," *Combustion and Flame*, vol. 75, pp. 397–413, 1989.

[181] A. R. Kerstein, "Linear-eddy modeling of turbulent transport. Part 3. Mixing and differential molecular diffusion in round jets," *Journal of Fluid Mechanics*, vol. 216, pp. 411–435, 1990.

[182] A. R. Kerstein, "Linear-eddy modeling of turbulent transport. Part 6. Microstructure of diffusive scalar mixing fields," *Journal of Fluid Mechanics*, vol. 231, pp. 361–394, 1991.

[183] A. R. Kerstein, "Linear eddy modeling of turbulent transport. Part 4. Structure of diffusion flames," *Combustion Science and Technology*, vol. 81, pp. 75–96, 1992.

[184] A. R. Kerstein, "Linear-eddy modeling of turbulent transport. Part 7. Finite-rate chemistry and multi-stream mixing," *Journal of Fluid Mechanics*, vol. 240, pp. 289–313, 1992.

[185] V. K. Chakravarthy and S. Menon, "Linear-eddy simulations of Reynolds and Schmidt number dependencies in turbulent scalar mixing," *Physics of Fluids*, vol. 13, pp. 488–499, 2001.

[186] W. H. Calhoon, S. Menon, and G. Goldin, "Comparison of reduced and full chemical mechanisms for nonpremixed turbulent H_2-air jet flames," *Combustion Science and Technology*, vol. 104, pp. 115–141, 1995.

[187] V. Sankaran and S. Menon, "Subgrid combustion modeling of 3-D premixed flames in the thin-reaction-zone regime," in *Proceedings of the Combustion Institute*, vol. 30, pp. 575–582, The Combustion Institute, 2005.

[188] G. Eggenspieler and S. Menon, "Combustion and emission modelling near lean blow-out in a gas turbine engine," *Progress in Computational Fluid Dynamics*, vol. 5, pp. 281–297, 2005.

[189] E. E. O'Brien, "The probability density function (PDF) approach to reacting turbulent flows," in *Turbulent Reacting Flows* (P. A. Libby and F. A. Williams, eds.), (London), pp. 185–218, Academic Press, 1980.

[190] S. B. Pope, "PDF methods for turbulent reactive flows," *Progress in Energy and Combustion Science*, vol. 11, pp. 119–192, 1985.

[191] S. B. Pope, "Computations of turbulent combustion: progress and challenges," in *Proceedings of the Combustion Institute*, vol. 23, pp. 591–612, The Combustion Institute, 1990.

[192] C. K. Madnia and P. Givi, "Direct and Large Eddy Simulation of reacting homogeneous turbulence," in *Large Eddy Simulation of Complex Engineering and Geophysical Flows* (B. Galperin and S. A. Orzag, eds.), (Cambridge, U. K.), pp. 315–346, Cambridge University Press, 1993.

[193] A. W. Cook and J. J. Riley, "Subgrid scale modelling for turbulent flows," *Combustion and Flame*, vol. 112, pp. 593–606, 1998.

[194] J. Jiménez, A. Linan, M. M. Rogers, and F. J. Higuera, "A priori testing of subgrid models for chemically reacting non-premixed turbulent shear flows," *Journal of Fluid Mechanics*, vol. 349, pp. 149–171, 1997.

[195] J. Réveillon and L. Vervisch, "Dynamic sub-grid PDF modelling for nonpremixed turbulent combustion," in *Direct and Large Eddy Simulation* (J. P. Chollet, P. R. Voke, and L. Kleiser, eds.), vol. II, (Amsterdam), pp. 311–320, Kluwer Academic Publishers, 1997.

[196] J. Réveillon and L. Vervisch, "Response of the dynamic LES model to heat release induced effects," *Physics of Fluids*, vol. 8, pp. 2248–2250, 1996.

[197] C. Wall, B. Boersma, and P. Moin, "An evaluation of the assumed beta PDF subgrid-scale model for LES of nonpremixed, turbulent combustion with heat release," *Physics of Fluids*, vol. 12, pp. 2522–2529, 2000.

[198] C. Tong, "Measurements of conserved scalar filtered density function in a turbulent jet," *Physics of Fluids*, vol. 13, pp. 2923–2937, 2001.

[199] A. Y. Klimenko, "Multicomponent diffusion of various scalars in turbulent flow," *Fluid Dynamics*, vol. 25, pp. 327–334, 1990.

[200] R. W. Bilger, "Conditional moment closure for turbulent reacting flow," *Physics of Fluids A*, vol. 5, pp. 436–444, 1993.

[201] A. Y. Klimenko and R. W. Bilger, "Conditional moment closure for turbulent combustion," *Progress in Energy and Combustion Science*, vol. 25, pp. 595–687, 1999.

[202] N. Swaminathan and R. W. Bilger, "Analyses of conditional moment closure for turbulent premixed flames," *Combustion Theory and Modelling*, vol. 5, pp. 241–260, 2001.

[203] M. Wang, J. Huang, and W. K. Bushe, "Simulation of turbulent non-premixed flame using conditional source-term estimation with trajectory generated low-dimensional manifold," in *Proceedings of the Combustion Institute*, vol. 31, pp. 1701–1709, The Combustion Institute, 2006.

[204] R. Grout, W. K. Bushe, and C. Blair, "Predicting the ignition delay of turbulent methane jets using conditional source-term estimation," *Combustion Theory and Modelling*, vol. 11, pp. 1009–1028, 2007.

[205] J. Huang and W. K. Bushe, "Simulation of an igniting methane jet using conditional source-term estimation with a trajectory generated low-dimensional manifold," *Combustion Theory and Modelling*, vol. 11, pp. 977–1008, 2007.

[206] B. Jin, R. Grout, and W. K. Bushe, "Conditional source-term estimation as a method for chemical closure in premixed turbulent reacting flow," *Flow, Turbulence and Combustion*, vol. 81, pp. 563–582, 2008.

[207] L. Vervisch, R. Hauguel, P. Domingo, and M. Rullaud, "Three facets of turbulent combustion modelling: DNS of premixed V-flame, LES of lifted nonpremixed flame and RANS of jet-flame," *Journal of Turbulence*, vol. 5, pp. 1–36, 2004.

[208] O. Gicquel, N. Darabiha, and D. Thévenin, "Laminar premixed hydrogen/air counterflow flame simulations using Flame Prolongation of ILDM with differential diffusion," in *Proceedings of the Combustion Institute*, vol. 28, pp. 1901–1908, The Combustion Institute, 2000.

[209] J. Galpin, A. Naudin, L. Vervisch, C. Angelberger, O. Colin, and P. Domingo, "Large-eddy simulation of a fuel-lean premixed turbulent swirl-burner," *Combustion and Flame*, vol. 155, pp. 247–266, 2008.

[210] J. A. van Oijen, F. A. Lammers, and L. P. H. de Goey, "Modeling of complex premixed burner systems by using flamelet-generated manifolds," *Combustion and Flame*, vol. 127, pp. 2124–2134, 2001.

[211] B. Fiorina, R. Baron, O. Gicquel, D. Thévenin, S. Carpentier, and N. Darabiha, "Modelling non-adiabatic partially premixed flames using flame-prolongation of ILDM," *Combustion Theory and Modelling*, vol. 7, pp. 449–470, 2003.

[212] L. Vervisch, "Study and modeling of finite rate chemistry effects in turbulent non-premixed flames," in *Annual Research Briefs*, pp. 411–429, Center for Turbulence Research, 1992.

[213] R. S. Barlow and J. H. Frank, "Effects of turbulence on species mass fractions in methane/air jet flames," in *Proceedings of the Combustion Institute*, vol. 27, pp. 1087–1095, The Combustion Institute, 1998.

[214] J. Galpin, *Modélisation LES de la combustion avec une prise en compte des effets de cinétique detaillée et en perspective d'application moteur.* PhD thesis, INSA de Rouen, December 2007.

[215] D. Goodwin and H. K. Moffat, "Cantera." Available at http://code.google.com/p/cantera/.

[216] J.-Y. Ren, W. Qin, F. N. Egolfopoulos, H. Mak, and T. T. Tsotsis, "Methane reforming and its potential effect on the efficiency and pollutant emissions of lean methane–air combustion," *Chemical Engineering Science*, vol. 56, pp. 1541–1549, 2001.

[217] V. di Sarli and A. di Benedetto, "Laminar burning velocity of hydrogen–methane/air premixed flames," *International Journal of Hydrogen Energy*, vol. 32, pp. 637–646, 2007.

[218] D. Bradley, P. H. Gaskell, X. J. Gu, M. Lawes, and M. J. Scott, "Premixed turbulent flame instability and NO formation in a lean-burn swirl burner," *Combustion and Flame*, vol. 115, pp. 515–538, 1998.

[219] G. Godel, P. Domingo, and L. Vervisch, "Tabulation of NO_x chemistry for large-eddy simulation of non-premixed turbulent flames," in *Proceedings of the Combustion Institute*, vol. 32, pp. 1555–1561, The Combustion Institute, 2009.

[220] S. C. Hill and L. D. Smoot, "Modeling of nitrogen oxides formation and destruction in combustion systems," *Progress in Energy and Combustion Science*, vol. 26, pp. 417–458, 2000.

[221] A. Frassoldati, S. Frigerio, E. Colombo, F. Inzoli, and T. Faravelli, "Determination of NO_x emissions from strong swirling confined flames with an integrated CFD-based procedure," *Chemical Engineering Science*, vol. 60, pp. 2851–2869, 2005.

[222] F. Biagioli and F. Güthe, "Effect of pressure and fuel-air unmixedness on NO_x emissions from industrial gas turbine burners," *Combustion and Flame*, vol. 151, pp. 274–288, 2007.

[223] Reaction Design, *CHEMKIN 4.0, Theory Manual*, 2004.

[224] P. J. O'Rourke and F. V. Bracco, "Two scaling transformations for the numerical computation of multidimensional unsteady laminar flames," *Journal of Computational Physics*, vol. 33, pp. 185–203, 1979.

[225] C. Meneveau and T. Poinsot, "Stretching and quenching of flamelets in premixed turbulent combustion," *Combustion and Flame*, vol. 86, pp. 311–332, 1991.

[226] S. K. Godunov, "Finite-difference method for numerical computations of discontinuous solutions of the equations of fluid dynamics," *Matematicheskii Sbornik*, vol. 47, pp. 271–306, 1959.

[227] J. J. Gottlieb and C. P. T. Groth, "Assessment of Riemann solvers for unsteady one-dimensional inviscid flows of perfect gases," *Journal of Computational Physics*, vol. 78, pp. 437–458, 1988.

[228] P. L. Roe, "Approximate Riemann solvers, parameter vectors, and difference schemes," *Journal of Computational Physics*, vol. 43, pp. 357–372, 1981.

[229] B. Einfeldt, "On Godunov-type methods for gas dynamics," *SIAM Journal on Numerical Analysis*, vol. 25, pp. 294–318, 1988.

[230] M.-S. Liou, "A sequel to AUSM, part ii: AUSM$^+$-up for all apeeds," *Journal of Computational Physics*, vol. 214, pp. 137–170, 2006.

[231] T. J. Barth, "Recent developments in high order k-exact reconstruction on unstructured meshes," Paper 93-0668, AIAA, January 1993.

[232] N. Waterson and H. Deconinck, "Design principles for bounded hight-order convection schemes–a unified approach," *Journal of Computational Physics*, vol. 224, pp. 128–207, 2007.

[233] T. J. Barth and D. C. Jespersen, "The design and application of upwind schemes on unstructured meshes," Paper 89-0366, AIAA, January 1989.

[234] V. Venkatakrishnan, "On the accuracy of limiters and convergence to steady state solutions," Paper 93-0880, AIAA, January 1993.

[235] S. Osher and F. Solomon, "Upwind difference schemes for hyperbolic systems of conservation laws," *Mathematics of Computation*, vol. 38, no. 158, pp. 339–374, 1982.

[236] B. van Leer, "On the relation between the upwind-difference schemes of Godunov's engquist osher and roe," *SIAM Journal for Scientific and Statistical Computing*, vol. 5, pp. 1–20, 1984.

[237] A. Harten, P. D. Lax, and B. van Leer, "On upstream differencing and Godunov-type schemes for hyperbolic conservation laws," *SIAM Review*, vol. 25, no. 1, pp. 35–61, 1983.

[238] A. Harten, "On a class of high resolution total-variation-stable finite-difference schemes," *SIAM Journal on Numerical Analysis*, vol. 21, pp. 1–23, 1984.

[239] M.-S. Liou and C. J. Steffen, "A new flux splitting scheme," *Journal of Computational Physics*, vol. 107, pp. 23–39, 1993.

[240] S. R. Mathur and J. Y. Murthy, "A pressure-based method for unstructured meshes," *Numerical Heat Transfer*, vol. 31, pp. 191–215, 1997.

[241] H. Lomax, T. H. Pulliam, and D. W. Zingg, *Fundamentals of Computational Fluid Dynamics*. Springer-Verlag Berlin Heidelberg, 2001.

[242] J. H. Ferziger and M. Perić, *Computational Methods for Fluid Dynamics*. Springer-Verlag Berlin Heidelberg NewYork, 2002.

[243] C. Hirsch, *Numerical Computation of Internal and External Flows, Volume 1, Fundamentals of Numerical Discretization*. Toronto: John Wiley & Sons, 1989.

[244] C. Hirsch, *Numerical Computation of Internal and External Flows, Volume 2, Computational Methods for Inviscid and Viscous Flows.* Toronto: John Wiley & Sons, 1990.

[245] X. Gao, *A Parallel Solution-Adaptive Method for Turbulent Non-Premixed Combusting Flows.* PhD thesis, University of Toronto, August 2008.

[246] X. Gao and C. P. T. Groth, "Parallel adaptive mesh refinement scheme for three-dimensional turbulent non-premixed combustion," Paper 2008-1017, AIAA, January 2008.

[247] S. A. Northrup and C. P. T. Groth, "Prediction of unsteady laminar flames using a parallel implicit adaptive mesh refinement algorithm," in *Proceedings of the 6th U.S. National Combustion Meeting, Ann Arbor, MI, USA*, May 18–21, 2009.

[248] C. P. T. Groth, D. L. D. Zeeuw, K. G. Powell, T. I. Gombosi, and Q. F. Stout, "A parallel solution-adaptive scheme for ideal magnetohydrodynamics," Paper 99-3273, AIAA, June 1999.

[249] C. P. T. Groth, D. L. De Zeeuw, T. I. Gombosi, and K. G. Powell, "Global three-dimensional MHD simulation of a space weather event: CME formation, interplanetary propagation, and and interaction with the magnetosphere," *Journal of Geophysical Research*, vol. 105, no. A11, pp. 25,053–25,078, 2000.

[250] K. G. Powell, P. L. Roe, and J. Quirk, "Adaptive-mesh algorithms for computational fluid dynamics," in *Algorithmic Trends in Computational Fluid Dynmaics* (M. Y. Hussaini, A. Kumar, and M. D. Salas, eds.), pp. 303–337, New York: Springer-Verlag, 1993.

[251] W. Gropp, E. Lusk, and R. Thakur, *Using MPI-2.* Cambridge, Massachussets: MIT Press, 1999.

[252] S. A. Northrup, "A parallel adaptive-mesh refinement scheme for predicting laminar diffusion flames," Master's thesis, University of Toronto, 2004.

[253] A. A. Townsend, *The Structure of Turbulent Shear Flow.* Cambridge, England: Cambridge University Press, 1976.

[254] R. S. Rogallo, "Numerical experiments in homogeneous turbulence." NASA Technical Memorandum 81315, 1981.

[255] D. C. Haworth and T. J. Poinsot, "Numerical simulations of Lewis number effects in turbulent premixed flames," *Journal of Fluid Mechanics*, vol. 244, pp. 405–436, 1992.

[256] Y. Dubief and F. Delcayre, "On coherent-vortex identification in turbulence," *Journal of Turbulence*, vol. 1, no. 11, pp. 1–22, 2000.

[257] J. C. R. Hunt, A. A. Wray, and P. Moin, "Eddies, stream, and convergence zones in turbulent flows," in *Annual Research Briefs*, Center for Turbulence Research, 1988.

[258] R. S. Cant, C. J. Rutland, and A. Trouvé, "Statistics for laminar modeling," in *Proceedings of the Summer Program*, pp. 271–279, Center for Turbulence Research, 1990.

[259] S. S. Girimaji and S. B. Pope, "Propagating surfaces in isotropic turbulence," *Journal of Fluid Mechanics*, vol. 234, pp. 247–277, 1992.

[260] S. A. Filatyev, J. F. Driscoll, C. D. Carter, and J. M. Donbar, "Measured properties of turbulent premixed flames for model assessment, including burning velocities, stretch rates, and surface densities," *Combustion and Flame*, vol. 141, pp. 1–21, 2005.

[261] J. B. Bell, M. S. Day, J. F. Grcar, M. J. Lijewski, J. F. Driscoll, and S. A. Filatyev, "Numerical simulation of a laboratory-scale turbulent slot flame," in *Proceedings of the Combustion Institute*, vol. 31, pp. 1299–1307, The Combustion Institute, 2007.

[262] R. K. Cheng and I. G. Shepherd, "The influence of burner geometry on premixed turbulent flame propagation," *Combustion and Flame*, vol. 85, pp. 7–26, 1991.

[263] A. De and S. Acharya, "Large eddy simulation of a premixed bunsen flame using a modified thickened-flame model at two Reynolds number," *Combustion Science and Technology*, vol. 181, pp. 1231–1272, 2009.

[264] F. T. C. Yuen and O. L. Gülder, "Premixed turbulent flame front structure investigation by Rayleigh scattering in the thin reaction zone regime," in *Proceedings of Combustion Institute*, vol. 32, pp. 1747–1754, 2009.

[265] F. Yuen, *Experimental Investigation of the Dynamics and Structure of Lean-Premixed Turbulent Combustion.* PhD thesis, University of Toronto, August 2009.

[266] I. Shepherd, "Flame surface density and burning rate in premixed turbulent flames," in *Proceedings of Combustion Institute*, vol. 26, pp. 373–379, 1996.

[267] P. Dagaut and A. Nicolle, "Experimental and detailed kinetic modeling study of hydrogen-enriched natural gas blend oxidation over extended temperature and equivalence ratio ranges," in *Proceedings of the Combustion Institute*, vol. 30, pp. 2631–2638, The Combustion Institute, 2005.

[268] F. Halter, C. Chauveau, and I. Gökalp, "Characterization of the effects of hydrogen addition in premixed methane/air flames," *International Journal of Hydrogen Energy*, vol. 32, pp. 2585–2592, 2007.

[269] F. Halter, *Caractérisation des effets de l'ajout d'hydrogène et de la haute pression dans les flammes turbulentes de prémélange méthane/air.* PhD thesis, Université d'Orléans, October 2005.

[270] G. I. Sivashinsky, "Instabilities, pattern formation, and turbulence in flames," *Annual Review of Fluid Mechanics*, vol. 15, pp. 179–199, 1983.

[271] W. J. Coirier, *An Adaptively-Refined, Cartesian, Cell-Based Scheme for the Euler and Navier-Stokes Equations.* PhD thesis, University of Michigan, 1994.

[272] K. N. C. Bray, M. Champion, P. A. Libby, and N. Swaminathan, "Finite rate chemistry and presumed PDF models for premixed turbulent combustion," *Combustion and Flame*, vol. 146, pp. 665–673, 2006.

[273] B. J. R. Grout and W. K. Bushe, "Conditional source-term estimation as a method for chemical closure in premixed turbulent reacting flow," *Flow, Turbulence and Combustion*, vol. 81, pp. 563–582, 2008.

[274] N. Chakraborty and R. S. Cant, "Effects of Lewis number on turbulent scalar transport and its modelling in turbulent premixed flames," *Combustion and Flame*, vol. 156, pp. 1427–1444, 2009.

[275] J. F. Grcar, J. B. Bell, and M. S. Day, "The Soret effect in naturally propagating, premixed, lean, hydrogen–air flames," in *Proceedings of the Combustion Institute*, vol. 32, pp. 1173–1180, The Combustion Institute, 2009.

[276] L. Ivan and C. P. T. Groth, "High-order central eno finite-volume scheme with adaptive mesh refinement," Paper 2007-4323, AIAA, June 2007.

[277] W. Deconinck, "Design and application of discrete explicit filters for large-eddy simulation of compressible turbulent flows," Master's thesis, University of Toronto, March 2008.

[278] T. S. Lund, X. Wu, and K. D. Squires, "Generation of turbulent inflow data for spatially-developing boundary layer simulations," *Journal of Computational Physics*, vol. 140, pp. 233–258, 1998.

Initialization of 3D Homogeneous Isotropic Turbulence

The initialization of the flow is significantly important as if realistic initial conditions are not prescribed, the establishment of a fully developed turbulence can require very long execution times. For this reason, it is necessary to initialize the flow field with some form of perturbation to provide appropriate initial turbulent conditions.

One approach consists in applying a separate flow solver with periodic boundary conditions [278]; however, it may be too expensive in terms of computer resources. An alternative approach is to generate Fourier harmonics with the appropriate statistics, assembled into a random flow field. The procedure employed in this research to initialize the flow field is similar to that of Rogallo [254]. It generates an approximately isotropic and homogeneous turbulent field having a specified energy spectrum. The field is generated in Fourier space subject to the constraint of continuity for incompressible flow, and inverse Fourier transformed to obtain the velocity components in physical space.

In wavenumber space, the divergence of velocity is given by

$$\mathcal{F}\left\{\frac{\partial u_j}{\partial x_j}\right\} = \kappa_j \hat{u}_j = \boldsymbol{\kappa} \cdot \hat{\mathbf{u}}\,, \tag{A.1}$$

where $\boldsymbol{\kappa}$ is the wavenumber vector, $\hat{\mathbf{u}}$ is the velocity vector in Fourier space, and $\mathcal{F}$ is the Fourier transform operator. The continuity equation for an incompressible flow indicates that $\hat{\mathbf{u}}$ is normal to $\boldsymbol{\kappa}$:

$$\boldsymbol{\kappa} \cdot \hat{\mathbf{u}} = 0\,. \tag{A.2}$$

The Fourier coefficients of velocity can take the form

$$\hat{\mathbf{u}} = \hat{u}_j \mathbf{e}_j = \alpha(\boldsymbol{\kappa})\mathbf{e}_1' + \beta(\boldsymbol{\kappa})\mathbf{e}_2' \,, \tag{A.3}$$

where $\mathbf{e}_j'$ is any vector basis having $\mathbf{e}_3'$ parallel to $\boldsymbol{\kappa}$ and α and β are complex functions. Rogallo proposed the following form for the complex functions α and β:

$$\alpha = \left(\frac{E(\kappa)}{4\pi\kappa^2}\right) e^{i\theta_1} \cos\phi\,, \qquad \beta = \left(\frac{E(\kappa)}{4\pi\kappa^2}\right) e^{i\theta_2} \sin\phi\,. \tag{A.4}$$

In the above expressions, θ_1, θ_2, and ϕ are uniformly distributed random numbers in the interval $(0, 2\pi)$, and $E(\kappa)$ is the energy density associated with the scalar wave number κ. This form results from the constraint

$$E(\kappa) = (\alpha\alpha^* + \beta\beta^*) \int \mathrm{d}\mathbf{A}(\kappa). \tag{A.5}$$

The vector basis can be chosen such that

$$\mathbf{e}_1' \cdot \mathbf{e}_3 = 0\,, \tag{A.6}$$

leading to

$$\hat{\mathbf{u}} = \frac{\alpha\kappa\kappa_2 + \beta\kappa_1\kappa_3}{\kappa(\kappa_1^2 + \kappa_2^2)^{1/2}}\mathbf{e}_1 + \frac{\beta\kappa_2\kappa_3 - \alpha\kappa\kappa_1}{\kappa(\kappa_1^2 + \kappa_2^2)^{1/2}}\mathbf{e}_2 - \frac{\beta(\kappa_1^2 + \kappa_2^2)^{1/2}}{\kappa}\mathbf{e}_3\,. \tag{A.7}$$

A turbulent homogeneous velocity field generated with the implemented procedure of Rogallo in three dimensions is shown below. An artificial turbulence energy spectrum having the form [255]

$$E(\kappa) = \frac{32}{2}(2/\pi)^{1/2}\frac{u'^2}{\kappa_{\mathrm{p}}}\left(\frac{\kappa}{\kappa_{\mathrm{p}}}\right)^4 e^{-2(\kappa/\kappa_{\mathrm{p}})^2}\,, \tag{A.8}$$

was employed. The spectrum function depends on the wave number, κ, the most energetic wave number, κ_{p}, which is associated with the size of the most energetic eddies, and the turbulence intensity, u'. Figure A.1 displays the iso-surfaces of vorticity corresponding to $u' = 2.5$ m/s and $\kappa_{\mathrm{p}} = 4$ m^{-1} in a cubic domain of size 2π m in each of the three spatial coordinates. The domain was discretized using 64^3 cells.
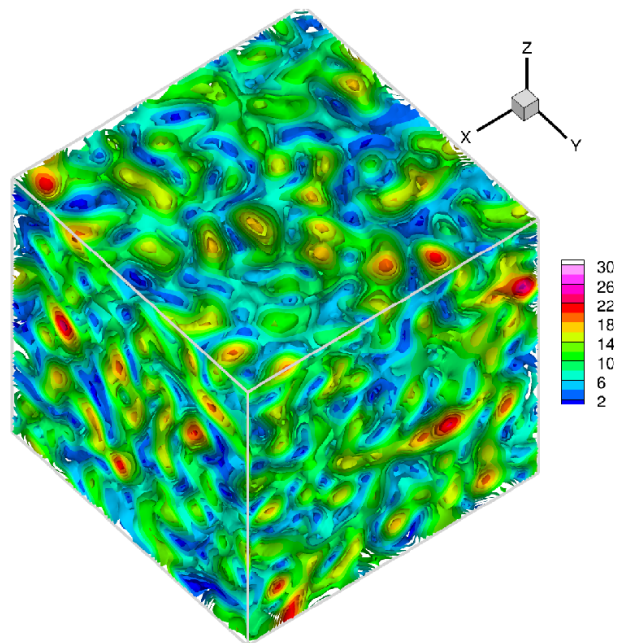
Figure A.1: Example of a homogeneous turbulent field artificially generated: iso-vorticity surfaces.

Derivation and Modelling of the Transport Equations for $\tilde{Y}_\text{c}$ and Y_{C_V}

B.1 Transport Equation for Y_c

As outlined in Chapter 4, the progress of reaction variable can be defined as a linear combination of species mass fractions, which is expressed as

$$Y_\text{c} = \sum_{\alpha=1}^{N} a_\alpha Y_\alpha \,, \tag{B.1}$$

where N is the number of species, a_α is a real-valued constant coefficient associated with species α, and Y_α is the mass fraction of species α. Assuming Fick's law of diffusion to be valid to represent the mass diffusion of the species, the conservation equation for species α has the form

$$\frac{\partial(\rho Y_\alpha)}{\partial t} + \frac{\partial(\rho Y_\alpha u_i)}{\partial x_i} = \frac{\partial}{\partial x_i}\left(\rho \mathcal{D}_\alpha \frac{\partial Y_\alpha}{\partial x_i}\right) + \dot{\omega}_\alpha \,. \tag{B.2}$$

Multiplying Equation B.2 by a_α and adding together the resulting equations for scaled mass fractions, $a_\alpha Y_\alpha$, yields

$$\frac{\partial}{\partial t}\left(\rho \sum_{\alpha=1}^{N} a_\alpha Y_\alpha\right) + \frac{\partial}{\partial x_i}\left(\rho u_i \sum_{\alpha=1}^{N} a_\alpha Y_\alpha\right) = \frac{\partial}{\partial x_i}\left(\rho \sum_{\alpha=1}^{N} a_\alpha \mathcal{D}_\alpha \frac{\partial Y_\alpha}{\partial x_i}\right) + \sum_{\alpha=1}^{N} a_\alpha \dot{\omega}_\alpha \,, \tag{B.3}$$

which can be re-written as

$$\boxed{\frac{\partial(\rho Y_\text{c})}{\partial t} + \frac{\partial(\rho u_i Y_\text{c})}{\partial x_i} = \frac{\partial}{\partial x_i}\left(\rho \mathcal{D}_{Y_\text{c}} \frac{\partial Y_\text{c}}{\partial x_i}\right) + \dot{\omega}_{Y_\text{c}} \,,} \tag{B.4}$$

with

$$\mathcal{D}_{Y_{\rm c}} = \frac{\sum_{\alpha=1}^{N} a_\alpha \mathcal{D}_\alpha \frac{\partial Y_\alpha}{\partial x_i}}{\frac{\partial Y_{\rm c}}{\partial x_i}} \tag{B.5}$$

and

$$\dot{\omega}_{Y_{\rm c}} = \sum_{\alpha=1}^{N} a_\alpha \dot{\omega}_\alpha \,. \tag{B.6}$$

Note that Equation B.4 can also be written as

$$\rho \frac{\partial Y_{\rm c}}{\partial t} + \rho u_i \frac{\partial Y_{\rm c}}{\partial x_i} = \frac{\partial}{\partial x_i}\left(\rho \mathcal{D}_{Y_{\rm c}} \frac{\partial Y_{\rm c}}{\partial x_i}\right) + \dot{\omega}_{Y_{\rm c}} \,. \tag{B.7}$$

It is useful to derive a transport equation for $Y_{\rm c}^2$, which will be needed in the derivation of the transport equation for $Y_{\rm c_v}$. First, Equation B.4 is multiplied by $Y_{\rm c}$, obtaining

$$\frac{\partial(\rho Y_{\rm c}^2)}{\partial t} - \rho Y_{\rm c} \frac{\partial Y_{\rm c}}{\partial t} + \frac{\partial(\rho u_i Y_{\rm c}^2)}{\partial x_i} - \rho u_i Y_{\rm c} \frac{\partial Y_{\rm c}}{\partial x_i} = Y_{\rm c} \frac{\partial}{\partial x_i}\left(\rho \mathcal{D}_{Y_{\rm c}} \frac{\partial Y_{\rm c}}{\partial x_i}\right) + Y_{\rm c}\dot{\omega}_{Y_{\rm c}} \,. \tag{B.8}$$

Next, Equation B.7 is multiplied by $Y_{\rm c}^2$, yielding

$$\rho Y_{\rm c} \frac{\partial Y_{\rm c}}{\partial t} + \rho u_i Y_{\rm c} \frac{\partial Y_{\rm c}}{\partial x_i} = Y_{\rm c} \frac{\partial}{\partial x_i}\left(\rho \mathcal{D}_{Y_{\rm c}} \frac{\partial Y_{\rm c}}{\partial x_i}\right) + Y_{\rm c}\dot{\omega}_{Y_{\rm c}} \,. \tag{B.9}$$

Adding together Equation B.8 and Equation B.9, and re-arranging terms gives

$$\boxed{\frac{\partial(\rho Y_{\rm c}^2)}{\partial t} + \frac{\partial(\rho u_i Y_{\rm c}^2)}{\partial x_i} = \frac{\partial}{\partial x_i}\left(\rho \mathcal{D}_{Y_{\rm c}} \frac{\partial Y_{\rm c}^2}{\partial x_i}\right) - 2\rho \mathcal{D}_{Y_{\rm c}} \frac{\partial Y_{\rm c}}{\partial x_i}\frac{\partial Y_{\rm c}}{\partial x_i} + 2Y_{\rm c}\dot{\omega}_{Y_{\rm c}} \,.} \tag{B.10}$$

B.2   Transport Equation for $\tilde{Y}_{\rm c}$

In what follows, its is assumed that filtering and differentiation commute and differences between filtered diffusive fluxes and diffusive fluxes evaluated in terms of filtered quantities are negligible. After filtering Equation B.4, one obtains the following equation for the Favre-filtered progress of reaction variable:

$$\frac{\partial(\bar{\rho}\tilde{Y}_{\rm c})}{\partial t} + \frac{\partial(\bar{\rho}\tilde{u}_i\tilde{Y}_{\rm c})}{\partial x_i} = -\frac{\partial\sigma_{Y_{\rm c}}}{\partial x_i} + \frac{\partial}{\partial x_i}\left(\bar{\rho}\check{\mathcal{D}}_{Y_{\rm c}} \frac{\partial\tilde{Y}_{\rm c}}{\partial x_i}\right) + \bar{\dot{\omega}}_{Y_{\rm c}} \,, \tag{B.11}$$

where $\sigma_{Y_{\rm c}} = \bar{\rho}(\widetilde{u_i Y_{\rm c}} - \tilde{u}_i\tilde{Y}_{\rm c})$ is the SFS transport of $Y_{\rm c}$. The above equation can also be written as

$$\bar{\rho}\frac{\partial\tilde{Y}_{\rm c}}{\partial t} + \bar{\rho}\tilde{u}_i\frac{\partial\tilde{Y}_{\rm c}}{\partial x_i} = -\frac{\partial\sigma_{Y_{\rm c}}}{\partial x_i} + \frac{\partial}{\partial x_i}\left(\bar{\rho}\check{\mathcal{D}}_{Y_{\rm c}} \frac{\partial\tilde{Y}_{\rm c}}{\partial x_i}\right) + \bar{\dot{\omega}}_{Y_{\rm c}} \,. \tag{B.12}$$

By using a gradient approximation to model the SFS transport term, Equation B.11 takes the form

$$\boxed{\frac{\partial(\bar{\rho}\tilde{Y}_c)}{\partial t} + \frac{\partial(\bar{\rho}\tilde{u}_i\tilde{Y}_c)}{\partial x_i} = \frac{\partial}{\partial x_i}\left[\bar{\rho}(\check{\mathcal{D}}_{Y_c} + \mathcal{D}_t)\frac{\partial\tilde{Y}_c}{\partial x_i}\right] + \bar{\dot{\omega}}_{Y_c}.}$$

(B.13)

B.3 Transport Equation for Y_{c_v}

To derive a transport equation for Y_{c_v}, first it is necessary to derive transport equations for $\widetilde{Y_c^2}$ and $\tilde{Y}_c^2$, since, by definition, $Y_{c_v} = \widetilde{Y_c^2} - \tilde{Y}_c^2$. By filtering Equation B.10, the following equation is obtained:

$$\frac{\partial(\bar{\rho}\widetilde{Y_c^2})}{\partial t} + \frac{\partial(\bar{\rho}\tilde{u}_i\widetilde{Y_c^2})}{\partial x_i} = -\frac{\partial\sigma_{Y_c^2}}{\partial x_i} + \frac{\partial}{\partial x_i}\left(\bar{\rho}\check{\mathcal{D}}_{Y_c}\frac{\partial\widetilde{Y_c^2}}{\partial x_i}\right) - 2\overline{\rho\mathcal{D}_{Y_c}\frac{\partial Y_c}{\partial x_i}\frac{\partial Y_c}{\partial x_i}} + 2\overline{Y_c\dot{\omega}_{Y_c}},$$

(B.14)

where $\sigma_{Y_c^2} = \bar{\rho}(\widetilde{u_iY_c^2} - \tilde{u}_i\widetilde{Y_c^2})$.

To derive a transport equation for $\tilde{Y}_c^2$, Equations B.11 and B.12 are both multiplied by $\tilde{Y}_c$ and the resulting equations are added together to yield

$$\begin{aligned}
\frac{\partial(\bar{\rho}\tilde{Y}_c^2)}{\partial t} + \frac{\partial(\bar{\rho}\tilde{u}_i\tilde{Y}_c^2)}{\partial x_i} &= -\frac{\partial}{\partial x_i}\left(2\tilde{Y}_c\sigma_{Y_c}\right) + 2\sigma_{Y_c}\frac{\partial\tilde{Y}_c}{\partial x_i} + \frac{\partial}{\partial x_i}\left(\bar{\rho}\check{\mathcal{D}}_{Y_c}\frac{\partial\tilde{Y}_c^2}{\partial x_i}\right) \\
&\quad - 2\bar{\rho}\check{\mathcal{D}}_{Y_c}\frac{\partial\tilde{Y}_c}{\partial x_i}\frac{\partial\tilde{Y}_c}{\partial x_i} + 2\tilde{Y}_c\bar{\dot{\omega}}_{Y_c}.
\end{aligned}$$

(B.15)

Finally, by subtracting Equation B.15 from Equation B.14, one arrives at a the following transport equation for Y_{c_v}:

$$\begin{aligned}
\frac{\partial(\bar{\rho}Y_{c_v})}{\partial t} + \frac{\partial(\bar{\rho}\tilde{u}_iY_{c_v})}{\partial x_i} &= \frac{\partial}{\partial x_i}\left(\bar{\rho}\check{\mathcal{D}}_{Y_c}\frac{\partial Y_{c_v}}{\partial x_i}\right) - \frac{\partial}{\partial x_i}\left(\sigma_{Y_c^2} - 2\tilde{Y}_c\sigma_{Y_c}\right) + 2\bar{\rho}\check{\mathcal{D}}_{Y_c}\frac{\partial\tilde{Y}_c}{\partial x_i}\frac{\partial\tilde{Y}_c}{\partial x_i} \\
&\quad - 2\sigma_{Y_c}\frac{\partial\tilde{Y}_c}{\partial x_i} - 2\overline{\rho\mathcal{D}_{Y_c}\frac{\partial Y_c}{\partial x_i}\frac{\partial Y_c}{\partial x_i}} + 2(\overline{Y_c\dot{\omega}_{Y_c}} - \tilde{Y}_c\bar{\dot{\omega}}_{Y_c}),
\end{aligned}$$

(B.16)

where $\sigma_{Y_c} = \bar{\rho}(\widetilde{u_iY_c} - \tilde{u}_i\tilde{Y}_c)$ and $\sigma_{Y_c^2} = \bar{\rho}(\widetilde{u_iY_c^2} - \tilde{u}_i\widetilde{Y_c^2})$ are SFS transport terms associated with Y_c and Y_c^2, respectively. By employing gradient approximations to model these SFS terms, Equation B.16 takes the form

$$\boxed{\begin{aligned}
\frac{\partial(\bar{\rho}Y_{c_v})}{\partial t} + \frac{\partial(\bar{\rho}\tilde{u}_iY_{c_v})}{\partial x_i} &= \frac{\partial}{\partial x_i}\left[\bar{\rho}(\check{\mathcal{D}}_{Y_c} + \mathcal{D}_t)\frac{\partial Y_{c_v}}{\partial x_i}\right] + 2\bar{\rho}(\check{\mathcal{D}}_{Y_c} + \mathcal{D}_t)\frac{\partial\tilde{Y}_c}{\partial x_i}\frac{\partial\tilde{Y}_c}{\partial x_i} \\
&\quad - 2\overline{\rho\mathcal{D}_{Y_c}\frac{\partial Y_c}{\partial x_i}\frac{\partial Y_c}{\partial x_i}} + 2(\overline{Y_c\dot{\omega}_{Y_c}} - \tilde{Y}_c\bar{\dot{\omega}}_{Y_c}).
\end{aligned}}$$

(B.17)

As discussed in subsection 4.1.3 of Chapter 4, the scalar dissipation rate of Y_c, $\bar{\chi}_{Y_c} = \overline{2\rho\mathcal{D}_{Y_c}\frac{\partial Y_c}{\partial x_i}\frac{\partial Y_c}{\partial x_i}}$, can be decomposed into resolved and unresolved parts [51], as follows:

$$\overline{\rho\mathcal{D}_{Y_c}\frac{\partial Y_c}{\partial x_i}\frac{\partial Y_c}{\partial x_i}} = \bar{\rho}\check{\mathcal{D}}_{Y_c}\frac{\partial \tilde{Y}_c}{\partial x_i}\frac{\partial \tilde{Y}_c}{\partial x_i} + \bar{s}_{\chi Y_c} \,. \tag{B.18}$$

The SFS component, $\bar{s}_{\chi Y_c}$, can be modelled using a linear relaxation hypothesis [51] or a combined linear relaxation hypothesis and bimodal limit closure [52].

B.4   Further Considerations

In this section, the determination of $\check{\mathcal{D}}_{Y_c}$ and initialization of Y_{c_v} are discussed. The diffusive coefficient associated with Y_c can be determined by prescribing the corresponding Schmidt number. The latter can be computed using Equation B.5, expressed in terms of the Schmidt numbers of the species, as follows:

$$\frac{1}{Sc_{Y_c}} = \frac{\sum_{\alpha=1}^{N}\frac{a_\alpha}{Sc_\alpha}\frac{\partial Y_\alpha}{\partial x_i}}{\frac{\partial Y_c}{\partial x_i}} \,. \tag{B.19}$$

In this research, Sc_{Y_c} values were calculated from one-dimensional premixed flame solutions obtained using Cantera and included in the look-up tables.

As for the initialization of Y_{c_v}, by assuming equilibrium between the production and dissipation of Y_{c_v}, and neglecting SFS contributions related to chemistry in Equation B.17, the following expression is obtained:

$$2\bar{\rho}(\check{\mathcal{D}}_{Y_c} + \mathcal{D}_t)\frac{\partial \tilde{Y}_c}{\partial x_i}\frac{\partial \tilde{Y}_c}{\partial x_i} = 2\overline{\rho\mathcal{D}_{Y_c}\frac{\partial Y_c}{\partial x_i}\frac{\partial Y_c}{\partial x_i}} \,. \tag{B.20}$$

Decomposing the filtered dissipation term into resolved and SFS parts, and using a linear relaxation hypothesis [51] to model the SFS component leads to

$$2\bar{\rho}(\check{\mathcal{D}}_{Y_c} + \mathcal{D}_t)\frac{\partial \tilde{Y}_c}{\partial x_i}\frac{\partial \tilde{Y}_c}{\partial x_i} = \bar{\rho}\check{\mathcal{D}}_{Y_c}\frac{\partial \tilde{Y}_c}{\partial x_i}\frac{\partial \tilde{Y}_c}{\partial x_i} + C_D\bar{\rho}Y_{c_v}\frac{\mathcal{D}_t}{\Delta^2} \,. \tag{B.21}$$

It follows that

$$Y_{c_v} = C_{Y_{c_v}}\Delta^2\left(\frac{\partial \tilde{Y}_c}{\partial x_i}\right)^2 = C_{Y_{c_v}}\Delta^2|\nabla\tilde{Y}_c|^2 \,, \tag{B.22}$$

where $C_{Y_{c_v}} = 1/C_D$. In this research, after some preliminary tests, a value of 0.25 was adopted for $C_{Y_{c_v}}$.